Applications of Spectrally-Resolved Photoluminescence in Silicon Photovoltaics

Hieu Trong Nguyen

November 2016

Australian
National
University

A thesis submitted for the degree of
Doctor of Philosophy
of The Australian National University

For my love

Truc Thuy Nguyen

Declaration

I certify that this thesis does not incorporate without acknowledgement any material previously submitted for a degree or diploma in any university, and that, to the best of my knowledge, it does not contain any material previously published or written by another person except where due reference is made in the text. The work in this thesis is my own, except for the contributions made by others as described in the Acknowledgement. The thesis is a compilation of 12 manuscripts, all of which I am the corresponding author. The manuscript details are given as below.

Manuscript 1 is presented as Chapter 2 in this thesis.

- Title: Temperature dependence of the band-band absorption coefficient in crystalline silicon from photoluminescence.
- Authors: Hieu T. Nguyen, Fiacre E. Rougieux, Bernhard Mitchell, and Daniel Macdonald
- Current status: published in Journal of Applied Physics, volume 115, 043710, 2014.
- Contributions: DM designed and supervised the project, and helped with the data analysis. HTN prepared the samples, performed all measurements, developed the modeling, and analyzed the data. FER helped with the sample preparation and data analysis. BM established the independent confirmation of the absorption coefficient presented in Figure 11 in the manuscript. HTN wrote the manuscript and other authors reviewed it.
- Declaration signed from a senior author:

Manuscript 2 is presented as Chapter 3 in this thesis.

- Title: Temperature dependence of the radiative recombination coefficient in crystalline silicon from photoluminescence.
- Authors: Hieu T. Nguyen, Simeon C. Baker-Finch, and Daniel Macdonald.
- Current status: published in Applied Physics Letters, volume 104, 112105, 2014.
- Contributions: DM designed and supervised the project, and helped with the data analysis. HTN prepared the samples, performed all measurements, developed the modeling, and analyzed the data. SCBF helped with the data analysis. HTN wrote the manuscript and other authors reviewed it.
- Declaration signed from a senior author:

Manuscript 3 is presented as Chapter 4 in this thesis.

- Title: Impact of carrier profile and rear-side reflection on photoluminescence spectra in planar crystalline silicon wafers at different temperatures.
- Authors: Hieu T. Nguyen, Fiacre E. Rougieux, Simeon C. Baker-Finch, and Daniel Macdonald.
- Current status: published in IEEE Journal of Photovoltaics, volume 5, 77, 2014.
- Contributions: HTN conceived and designed the project, prepared the samples, performed all measurements, developed the modeling, and analyzed the data. DM supervised the project and helped with the data analysis. FER and SCBF helped with the data analysis. HTN wrote the manuscript and other authors reviewed it.
- Declaration signed from a senior author:

Manuscript 4 is presented as Chapter 5 in this thesis.

- Title: Micrometer-scale deep-level spectral photoluminescence from dislocations in multicrystalline silicon.
- Authors: Hieu T. Nguyen, Fiacre E. Rougieux, Fan Wang, Hoe Tan, and Daniel Macdonald
- Current status: published in IEEE Journal of Photovoltaics, volume 5, 799, 2015.
- Contributions: HTN conceived and designed the project, prepared the samples, performed all measurements, developed the modeling, and analyzed the data. DM supervised the project and helped with the data analysis. FER, FW and HT helped with the sample preparation, experimental setup, and data analysis. HTN wrote the manuscript and other authors reviewed it.
- Declaration signed from a senior author:

Manuscript 5 is presented as Chapter 6 in this thesis.

- Title: Micro-photoluminescence spectroscopy on heavily-doped layers of silicon solar cells
- Authors: Hieu T. Nguyen, Di Yan, Fan Wang, Peiting Zheng, Young Han, and Daniel Macdonald.
- Current status: published in Physica Status Solidi-Rapid Research Letters, volume 9, 230, 2015.
- Contributions: HTN conceived and designed the project, prepared the samples, performed all measurements, developed the modeling, and analyzed the data. DM supervised the

project and helped with the data analysis. DY, FW, PZ, and YH helped with the sample preparation and experimental setup. HTN wrote the manuscript and other authors reviewed it.

- Declaration signed from a senior author:

Manuscript 6 is presented as Chapter 7 in this thesis.

- Title: Dislocations in laser-doped silicon detected by micro-photoluminescence spectroscopy.
- Authors: Hieu T. Nguyen, Young Han, Marco Ernst, Andreas Fell, Evan Franklin, and Daniel Macdonald.
- Current status: published in Applied Physics Letters, volume 107, 022101, 2015.
- Contributions: HTN conceived and designed the project, prepared the samples, performed all measurements, developed the modeling, and analyzed the data. DM supervised the project and helped with the data analysis. YH, ME, AF, and EF helped with the sample preparation and experimental setup. HTN wrote the manuscript and other authors reviewed it.
- Declaration signed from a senior author:

Manuscript 7 is presented as Chapter 8 in this thesis.

- Title: Characterizing amorphous silicon, silicon nitride, and diffused layers in crystalline silicon solar cells using micro-photoluminescence spectroscopy.
- Authors: Hieu T. Nguyen, Fiacre E. Rougieux, Di Yan, Yimao Wan, Sudha Mokkapati, Silvia Martin de Nicolas, Johannes Peter Seif, Stefaan De Wolf, and Daniel Macdonald.
- Current status: published in Solar Energy Materials and Solar Cells, volume 145, 403, 2016
- Contributions: HTN conceived and designed the project, prepared the samples, performed all measurements, developed the modeling, and analyzed the data. DM supervised the project and helped with the data analysis. FER, DY, YW, SM, SMN, JPS, and SDW helped with the sample preparation and experimental setup. HTN wrote the manuscript and other authors reviewed it.
- Declaration signed from a senior author:

Manuscript 8 is presented as Chapter 9 in this thesis.

- Title: Photoluminescence excitation spectroscopy of diffused layers on crystalline silicon wafers.
- Authors: Hieu T. Nguyen, Sieu Pheng Phang, Jennifer Wong-Leung, and Daniel Macdonald
- Current status: published in IEEE Journal of Photovoltaics, volume 6, 746, 2016.
- Contributions: HTN conceived and designed the project, prepared the samples, performed all measurements, developed the modeling, and analyzed the data. DM supervised the project and helped with the data analysis. SPP helped with the sample preparation. JWL assisted with the microscopic experiment and analysis. HTN wrote the manuscript and other authors reviewed it.
- Declaration signed from a senior author:

Manuscript 9 is presented as Chapter 10 in this thesis.

- Title: Investigation of enhanced diffusion in multicrystalline silicon wafers with micro-photoluminescence excitation spectroscopy.
- Authors: Hieu T. Nguyen, Sudha Mokkapati, and Daniel Macdonald.
- Current status: under review by IEEE Journal of Photovoltaics, submitted on 31st May 2016.
- Contributions: HTN conceived and designed the project, prepared the samples, performed all measurements, developed the modeling, and analyzed the data. DM supervised the project and helped with the data analysis. SM assisted with the experimental setup. HTN wrote the manuscript and other authors reviewed it.
- Declaration signed from a senior author:

Manuscript 10 is presented as Chapter 11 in this thesis.

- Title: On the composition of luminescence spectra from heavily doped p-type silicon under low and high excitation.
- Authors: Hieu T. Nguyen and Daniel Macdonald.
- Current status: published in Journal of Luminescence, volume 181, 223, 2017.
- Contributions: HTN conceived and designed the project, prepared the samples, performed all measurements, developed the modeling, and analyzed the data. DM supervised the project and helped with the data analysis. HTN wrote the manuscript and DM reviewed it.
- Declaration signed from a senior author:

Manuscript 11 is presented as an Appendix in this thesis.

- Title: Effects of solar cell processing steps on dislocation luminescence in multicrystalline silicon.
- Authors: Hieu T. Nguyen, Fiacre E. Rougieux, Fan Wang, and Daniel Macdonald.
- Current status: presented at 5th International Conference on Silicon Photovoltaics, Germany, 2015; and published in Energy Procedia, volume 77, 619, 2015.
- Contributions: HTN conceived and designed the project, prepared the samples, performed all measurements, developed the modeling, and analyzed the data. DM supervised the project and helped with the data analysis. FER and FW assisted with the sample preparation and experimental setup. HTN wrote the manuscript and other authors reviewed it.
- Declaration signed from a senior author:

Manuscript 12 is presented as an Appendix in this thesis.

- Title: Evaluating depth distributions of dislocations in silicon wafers using micro-photoluminescence excitation spectroscopy.
- Authors: Hieu T. Nguyen, Sieu Pheng Phang, and Daniel Macdonald.
- Current status: presented at 6th International Conference on Silicon Photovoltaics, France, 2016; and published in Energy Procedia, volume 92, 145, 2016.
- Contributions: HTN conceived and designed the project, prepared the samples, performed all measurements, developed the modeling, and analyzed the data. DM supervised the project and helped with the data analysis. SPP helped with the sample preparation. HTN wrote the manuscript and other authors reviewed it.
- Declaration signed from a senior author:

Acknowledgement

First, I would like to express my deepest gratitude to my supervisor, Assoc. Prof. Daniel Macdonald, for originally stimulating my interest in photovoltaic research, for his unfailing enthusiasm and guidance during my PhD, and for doing so much to foster my research capabilities. He always makes himself available for discussions and is an outstanding source of knowledge.

I would like to thank Dr. Fiacre Rougieux and Prof. Andres Cuevas for being part of my supervisory panel. Fiacre guided me through the very first experiments at ANU and provided much technical assistance and many useful discussions, whereas Andres gave many stimulating discussions with his immense knowledge in the field. I also would like to thank Prof. Hoe Tan of EME at RSPhysSE for his generosity for allowing me to use the micro-PLS system during my PhD.

The technical team in the ANU solar lab was of immeasurable assistance. Dr. Nina De Caritat, James Cotsett, Mark Saunders, Bruce Condon, Maureen Brauers, and Dr. Beatriz Velasco kept the solar cleanroom, characterization lab, and other equipment running smoothly. This thesis could not be finished without their support.

Chris Samundsett, Dr. Sudha Mokkapati, Dr. Fan Wang, Dr. Sarchin Surve are greatly acknowledged for their assistance with many experimental setups in this thesis. Assoc. Prof. Jennifer Wong-Leung of EME was kindly acknowledged for her support with TEM analysis and her useful discussions. Mark Lockrey and Li Li of EME are also acknowledged for assisting with SEM and FIB. Felipe Kremer of CAM was appreciated for his assistance and knowledge of TEM analysis.

I would like to thank Pheng Sieu Phang, AnYao Liu, Kelvin Sio, The Duong, James Bullock, Tom Allen, Tom Ratcliff, Peiting Zheng, Di Yan, Ryan Sun, Chog Barugkin, Teck Kong, Teng Kho, Heping Shen, Daniel Water, Jin Jin Cong, Xiao Fu, Ingrid Haedrich, Eric Wang, Louis Yang, Yimao Wan, Andy Thomson, Mohsen Goodarzi, Young Han, Marco Ernst, Azul Mayon, Yiliang Wu, Marco Ernst and many other friends that I forgot to put their names here, for being my friends. You all made this journey enjoyable.

Finally, I would like to thank my parents for their love and continuous support. I wish I could show them just how much I love and appreciate them. I would like to thank my wife Truc Thuy Nguyen for her encouragement and companion throughout my PhD.

Abstract

In broad terms, this thesis is devoted to measuring and interpreting the photoluminescence spectra emitted from different structures in crystalline silicon wafers and solar cells. Based on the knowledge accumulated, it also establishes a variety of applications of photoluminescence spectroscopy in silicon photovoltaics. The thesis may be divided into 3 main categories: band-to-band luminescence from wafers, deep-level luminescence from defects and impurities, and composite luminescence from different structures and layers in solar cells.

First, this thesis utilizes band-to-band photoluminescence spectra emitted from planar silicon wafers to determine the values of the band-to-band absorption coefficient and the radiative recombination coefficient as a function of temperature with high precision. Parameterizations of these two coefficients are established to allow convenient calculations. Based on the newly established temperature data, the impacts of surface geometries and excess carrier profiles on luminescence spectra emitted from various silicon wafers are investigated via both modeling and experiments as a function of temperature. The results suggest that, the accuracy of many photoluminescence-based techniques, established mainly at room temperature in the literature, can be further improved by performing the measurements at higher temperatures due to the increasing impacts of surface reflectivities and excess carrier profiles on luminescence spectra with rising temperatures. These applications highlight the significance of the established data of the two coefficients for spectral fitting techniques.

Next, the thesis investigates the deep-level luminescence from defects and impurities distributed around sub-grain boundaries in multicrystalline silicon wafers. The thesis shows that, the dislocations at sub-grain boundaries and the defects and impurities trapped around the dislocations emit separate luminescence peaks at low temperatures. The luminescence intensity of the trapped defects and impurities is found to be altered significantly after phosphorus gettering, whereas the dislocation luminescence is not changed throughout different solar cell processing steps. Also, the trapped defects and impurities are found to be preferentially distributed on one side of the sub-grain boundaries due to the asymmetric distribution of their luminescence intensity across the sub-grain boundaries. In addition, the thesis also demonstrates that the damage induced by laser doping is related to dislocations, since its deep-level luminescence spectrum has similar properties to those emitted from dislocations in multicrystalline silicon wafers. The interface between the laser-doped and un-doped regions is found to contain more damage than the laser-doped regions.

Furthermore, the thesis reports a new photoluminescence-based method to separate the luminescence signatures from different layers and structures in a single silicon substrate, courtesy of the well-resolved luminescence peaks at low temperatures from different layers. In

particular, the technique is applied to characterize the doping level of both locally-diffused and laser-doped regions on various silicon solar cells and cell precursors, utilizing band-gap narrowing effects in heavily-doped silicon. The results show that, the interface between the laser-doped and un-doped regions is much more heavily-doped that the doped regions. In addition, the technique is also applied to evaluate and the parasitic absorption of different surface passivation films on finished solar cells, due to the correlation between the sub band-gap luminescence intensity from these passivation films and the optical absorption in the films. The technique is contactless and nondestructive, requires minimal sample preparation, and provides micron-scale spatial resolutions.

Finally, the thesis combines the advantages of spectrally-resolved photoluminescence (PLS) and photoluminescence excitation spectroscopy (PLE) to develop a PLS-PLE-combined technique for characterizing wafers and solar cells. In particular, the entire photoluminescence spectrum from a silicon wafer or solar cell is captured and monitored while the excitation energy is varied. This technique allows us to quantitatively evaluate both the doping level and the junction depth of various diffused silicon wafers, the defects induced by the post-diffusion thermal treatment at different depths below the wafer surface, and the enhanced diffusion at grain boundaries and sub-grain boundaries in multicrystalline silicon wafers. The results show that, the enhanced diffusion happens at both grain boundaries and sub-grain boundaries.

Table of Contents

INTRODUCTION **1**
Spectrally-resolved photoluminescence 2
Thesis outline 4

CHAPTER 1: PHOTOLUMINESCENCE IN CRYSTALLINE SILICON **11**
1.1 Generation of band-to-band photoluminescence from silicon 12
1.2 Band-to-band photoluminescence emitted from silicon wafers 15
1.3 Deep-level photoluminescence from defects and impurities 16
1.4 Separation of PL signal from various layers at low temperatures 17
1.5 Photoluminescence spectroscopy systems 18
1.6 Summary 21

CHAPTER 2: TEMPERATURE DEPENDENCE OF BAND-TO-BAND APSORPTION COEFFICIENT **23**

CHAPTER 3: TEMPERATURE DEPENDENCE OF RADIATIVE RECOMBINATION COEFFICIENT **33**

CHAPTER 4: IMPACT OF CARRIER PROFILE AND REAR SIDE REFLECTION ON PHOTOLUMINESCENCE SPECTRA **39**

CHAPTER 5: DEEP-LEVEL PHOTOLUMINESCENCE SPECTROSCOPY FROM DISLOCATIONS IN MULTICRYSTALLINE SILICON **47**

CHAPTER 6: CHARACTERIZATION OF HEAVILY-DOPED LAYERS IN SOLAR CELLS BY PHOTOLUMINESCENCE SPECTROSCOPY **55**

CHAPTER 7: CHARACTERIZATION OF DISLOCATIONS IN LASER-DOPED SILICON BY PHOTOLUMINESCENCE SPECTROSCOPY **63**

CHAPTER 8: CHARACTERIZATION OF a-Si, SiN_x, AND HEAVILY-DOPED LAYERS IN SOLAR CELLS **71**

CHAPTER 9: SPECTRALLY-RESOLVED MICRO-PHOTOLUMINESCENCE EXCITATION SPECTROSCOPY **83**

CHAPTER 10: INVESTIGATION OF ENHANCED DIFFUSION AT GRAIN BOUNDARIES IN MULTICRYSTALLINE SILICON WAFERS **93**

CHAPTER 11: COMPOSITION OF LUMINESCENCE SPECTRA FROM HEAVILY-DOPED p-TYPE SILICON UNDER LOW AND HIGH EXCITATION **105**

CHAPTER 12: SUMMARY AND FUTURE WORK **123**

LIST OF OTHER PUBLICATIONS **129**

APPENDIX **131**

Introduction

Crystalline silicon (c-Si) accounts for more than 90% of the photovoltaic market share [1]. Over the past decades, c-Si has been the material of choice for industrial production due to its clear advantages over other semiconductors. First, silicon is the second most abundant element on the planet. Second, c-Si wafers have stable electronic properties, a band gap well-suited for high efficiency photovoltaic cells, and are nontoxic. Most importantly, c-Si has been the workhorse for microelectronic industries and research for more than a half of century. Therefore, the material's properties have been investigated extensively. Also, fabrication processes as well as characterization methods for c-Si have been well developed. Many of these processes and methods, as well as much of the developed knowledge, can be readily applied to silicon photovoltaic applications.

To date, the highest confirmed efficiency of a homo-junction silicon solar cell is 25.6% [2]. However, most industrial cells have lower efficiencies due to a combination of both the material itself and the device fabrication process. Many types of defects and impurities are already present in the starting material during the crystal growth process. Some of them are electrically active even in the as-cut wafers, and some of them can be activated during the cell fabrication or operation. In addition, the fabrication process itself can induce both optical and electrical losses. A great deal of work has been performed at both laboratory and industrial settings in order to optimize the cell fabrication process as well as to mitigate the impacts of the grown-in defects and impurities. Although much knowledge of silicon properties and characterization techniques developed for microelectronics can be reused, characterization techniques specifically designed for photovoltaic applications are required due to the different fabrication process and the unique requirements of solar cells, compared to those of microelectronic devices.

Optical spectroscopy has been widely used to study the physics and properties of many semiconductors. Optical measurements are attractive since they are contactless and non-destructive, and often require less effort in sample preparation than other characterization techniques. Spectrally-resolved photoluminescence or photoluminescence spectroscopy (PLS) is a subfield of optical spectroscopy. From a thermo-dynamical point of view, photoluminescence (PL) is a non-equilibrium phenomenon since materials need to be supplied with extra energy from a light source. The luminescence spectra detected contain fingerprints of material

properties, defects and impurities, device architectures, and fabrication processes. Therefore, PLS has great potential for device characterization in silicon photovoltaics.

Generally speaking, PLS-based methods have been employed as a precise, contactless, and non-destructive characterization tool in silicon photovoltaic research for many decades. The applications are varied from fundamental properties of the material, such as band gap [3-5], doping levels [6], band-to-band absorption coefficient [7-9], or radiative recombination coefficient [9,10], to device properties, such as diffusion lengths of minority carriers in wafers and solar cells [11-13], surface recombination in wafers [14,15], or light trapping capability of plasmonic structures [16], to name a few. In the intervening years, with the advent of a micro-photoluminescence system, PLS-based techniques have been further advanced significantly. Courtesy of high spatial resolutions, the techniques have been employed to pinpoint micron-scale features of wafers and finished devices, including dislocations [17], iron precipitates [18], laser-doped regions [19,20], and recombination and stress around grain boundaries [21].

This thesis is based on the photoluminescence phenomenon from crystalline silicon. It is devoted to understanding the photoluminescence spectra emitted from a variety of silicon wafers and solar cells. Based on these properties, it reports a range of new applications of spectrally-resolved photoluminescence in silicon photovoltaics, ranging from material studies to finished solar cell characterization.

Spectrally-resolved photoluminescence

If a semiconductor is illuminated with a light source having an appropriate energy, the incoming light will be absorbed in the semiconductor. The energy of the absorbed light can excite electrons in the valence band into empty states in the conduction band. These excited electrons will then be thermalized almost immediately to the lowest energy states in the conduction band. After that, the thermalized electrons will fall back to the valence band either indirectly via energy states inside the band gap of the semiconductor, or directly, and recombine with free holes in the valence band. The excess energy of the free electrons can be released in the form of heat (i.e. phonons), or light (i.e. photons), or both. In the case where photons are emitted, the phenomenon is called photoluminescence. Spectrally-resolved photoluminescence techniques measure the energy distribution of these emitted photons. Many properties of materials, defects and impurities, and fabrication processes can be extracted by systematically and carefully analyzing this energy distribution.

In general, the emission rate correlates with the absorption rate. However, there are still some fundamental differences between the two processes. Technically, compared to the absorption spectrum, the emission spectrum reflects the operating principle of silicon solar cells

more closely since it directly involves free electrons and holes, which contribute to the photo-induced current. On the other hand, the absorption spectrum consists of the band-to-band absorption and other parasitic absorption mechanisms. Only the former contributes to the photo-induced current of silicon solar cells. The parasitic absorption generates heat inside solar cells, and thus reduces their performance. Furthermore, the absorption could be associated with all energy states, and thus its spectrum is often very broad. On the other hand, the emission involves narrow bands of energy states in the conduction and valence bands, and as such the emission spectrum is much narrower than the absorption spectrum.

Properties of the luminescence spectrum are generally determined by two quantities: the band gap and the band structure of the semiconductor. The first quantity is the minimum energy difference between the conduction and valence bands, and it determines the overall position of the spectrum. The latter quantity determines the intensity, shape, and overall properties of the spectrum. In a direct semiconductor, the momentum difference between the conduction band minimum and the valence band maximum is zero (see Figure 1a), and as such the luminescence spectrum is very sharp and strong. On the other hand, in an in-direct semiconductor (silicon, for example), the momentum difference is non-zero (see Figure 1b), and the emission must involve the participation of phonons in order to satisfy momentum conservation. Due to the participation of phonons in the luminescence process, the emission spectrum from silicon is broader and contains various components corresponding to different types of phonons. The rich features of luminescence spectra from silicon are, in fact, foundations of many photoluminescence-based techniques established to characterize silicon solar cells. However, the luminescence efficiency of silicon is very low compared to that of direct band-gap materials. Therefore, in luminescence experiments on silicon, a high excitation power and sensitive spectroscopic equipment are critical requirements.

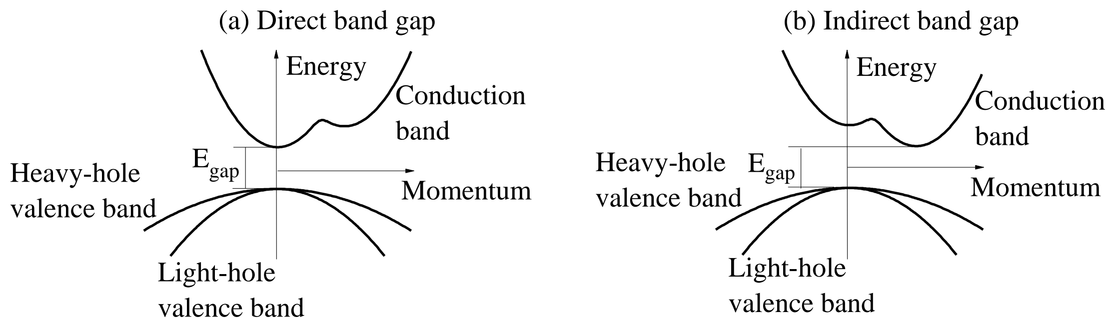

Figure 1: *Illustration of band structures of direct (a) and indirect (b) semiconductors, adapted from Gilliland [22].*

Thesis outline

Chapter 1 provides a brief overview of the luminescence theory from crystalline silicon wafers, which serves as a foundation for all spectrally-resolved photoluminescence-based techniques developed in this thesis. In particular, various photoluminescence mechanisms in silicon wafers, which are important for solar cell characterization, are explained from a physical point of view. The chapter consists of five sections. The first section explains the generation process of band-to-band photons, which are emitted spontaneously from a volume element inside a silicon wafer. This spontaneous generation is determined solely by intrinsic electronic properties of the material. The second section continues to explain loss mechanisms of these spontaneously generated photons when they move towards the wafer surface and escape the semiconductor. These loss mechanisms alter the original shape of the luminescence spectra due to their different dependences at different photon energies. The third section focuses on the deep-level luminescence emitted from defects and impurities, which are present in silicon wafers and occupy energy levels inside the forbidden gap of silicon. The fourth section describes a new technique, which can separate the luminescence signal from individual materials and structures buried underneath the wafer surface. Finally, experimental setups of the conventional photoluminescence spectroscopy and micro-photoluminescence spectroscopy systems, which were employed to capture all PL spectra in this thesis, are described in detail.

Chapter 2 is concerned with the band-to-band absorption coefficient in crystalline silicon, one important parameter in device modeling and characterization. Due to the significance of this coefficient, numerous experimental works have been performed to determine its values at different temperatures and wavelengths in the literature. However, around room temperature, the established data of this coefficient are not dense enough to cover the practical working temperature range of silicon solar cells, and thus there is still a lack of information on this coefficient for device modeling and characterization. This chapter first presents the evolution of luminescence spectra captured from silicon wafers between 79 and 363 K, in particular with a step of 10 K in the range of 249 – 363 K. Based on these spectra, the band-to-band absorption coefficient is extracted at different temperatures for wavelengths from 990 to 1300 nm, a wavelength range which is important for spectral fitting methods. Furthermore, by comparing the data around room temperature, the values of the coefficient are found to vary significantly even though the temperature changes only a few degrees, which in turn affects the spectral shape. This finding motivates correct usage of exact temperatures for the band-to-band absorption coefficient in device modeling, rather than approximate room temperature values, which can vary significantly from, for example, 291 K (18 ^{o}C) to 300 K (27 ^{o}C). Finally, a parameterization is established, giving a convenient way to calculate the values of the band-to-

band absorption coefficient at a given temperature in the working temperature range of silicon solar cells.

Chapter 3 utilizes the dense temperature data of the band-to-band absorption coefficient established in Chapter 2 to extract the radiative recombination coefficient of crystalline silicon, which is another important parameter in device modeling and characterization. Applying the generalized Planck's law, an aggregate quantity of the radiative recombination coefficient and the intrinsic carrier density was determined as a function of temperature. This combination allows the data established to be independent of the intrinsic carrier density model, which is still controversial in the literature. A parameterization of this combined quantity is then extracted in order to provide quick calculations of this coefficient at different temperatures. After that, the data are compared with the results established in the literature, and are found to agree with them well. Finally, the data show a saturation of the radiative recombination coefficient at room temperature and above, a conclusion which could not be made based on the sparse data available in the literature.

Chapter 4 is concerned with the impacts of internal surface reflectance and carrier profiles on the PL spectral shape from crystalline silicon wafers. The dataset of the band-to-band absorption coefficient established in Chapter 2 is applied to model PL spectra emitted from silicon wafers under various surface conditions. In practice, changes in excess carrier profiles and optical properties of wafers and solar cells often occur simultaneously, and thus their effects on the shape of the spectrum measured are confounded. Based on both modeling and experiments, individual effects of internal surface reflectivities, as well as of inhomogeneous carrier profiles varying across the wafer thickness due to an increased surface recombination, are investigated as a function of temperature. The results suggest that the accuracy of many existing PL-based techniques could be improved by performing measurements at higher temperatures, rather than room temperature, due to the increasing impact of carrier profiles and surface reflectivities with rising temperatures. Furthermore, the possible impact of variations in internal reflectivities at long wavelengths, for which measured reflectivities are often affected by the escaping infrared light, on the established values of the band-to-band absorption coefficient is examined and found to be insignificant in practice.

Chapter 5 focuses on another class of photoluminescence spectroscopy. It deals with the electronic and optical properties of deep levels situated inside the band gap of silicon at microscopic scales. In particular, utilizing micron-scale spatial resolutions of a micro-photoluminescence spectroscopy system equipped with confocal optics, luminescence properties of dislocations in multicrystalline silicon (mc-Si) wafers, as well as of defects and impurities decorating around them, are investigated separately. First, individual deep-level emission lines from these defects (both dislocations and trapped defects) and impurities are examined and demonstrated to have different spatial distributions around sub-grain boundaries, suggesting the different origins of these luminescence centers. After that, their behaviors after

different processing steps are examined, including phosphorus diffusion gettering, high-temperature annealing, and controlled contamination with iron. The results show that, the luminescence intensity from the defects and impurities trapped around the dislocations varies significantly, whereas that from the dislocations themselves is not altered, suggesting that the structure of the dislocations formed during the ingot growth and cooling is unchanged after different processing steps. Furthermore, the defects and impurities are found to be preferentially trapped at one side of the sub-grain boundaries due to the asymmetric intensity distribution of their luminescence across the sub-grain boundaries both before and after the processing steps.

Chapter 6 reports a new technique to separate luminescence signals from heavily-doped layers and an underlying crystalline silicon substrate. In heavily-doped silicon, the band gap is narrowed and the band-to-band luminescence spectrum is shifted to longer wavelengths, i.e. lower energies. If an appropriate excitation wavelength is employed, the laser light will be absorbed in both the heavily-doped layer and the silicon substrate, yielding different luminescence peaks associated with the two layers. However, the individual signatures of the two layers are not discernible at room temperature due to thermal broadening effects, causing different spectral components to be overlapped together. This chapter utilizes the distinctly sharp features of luminescence spectra from crystalline silicon at low temperatures to separate the emission signals from the individual layers, thus allowing us to investigate luminescence properties of thin diffused layers by just capturing spectra from above the wafer surface. Moreover, taking the advantages of the micron-scale spatial resolution from the micro-photoluminescence spectroscopy system, this technique is then applied to assess the dopant level of various localized diffused regions, whose diameters are only a few tens of micrometers, on solar cell precursors. The technique is also applied to laser-doped samples, revealing an interesting finding on the dopant concentration at the micron-scale region between the laser-doped and un-doped regions.

Chapter 7 continues to report another application of the micro-PLS technique to characterize laser-doped regions on silicon wafers. In solar cell fabrications, although laser doping is more precise and simpler than thermal diffusion and ion implantation, this doping technique is known to introduce a high level of crystal damage, which in turn has detrimental impacts on final cell efficiencies. This chapter shows that, the laser-induced damage can emit strong sub band-gap PL signals at low temperatures. Based on similarities in the luminescence properties and energy levels with those of dislocations, the damage is demonstrated to be related to dislocations. Moreover, by comparing PL spectra from various locations in the laser-doped region, the interface between the laser-processed and normal regions is found to contain much more crystal damage than the laser-doped region itself. Finally, the observed excitation power dependence of the PL intensity from the laser-induced damage is also reported and explained.

Chapter 8 studies luminescence spectra from c-Si wafers passivated with hydrogenated amorphous silicon (a-Si) and hydrogenated silicon nitride (SiN_x) films. First, luminescence

spectra from a-Si under various deposition and measurement conditions are reported separately. After that, the combined luminescence from a-Si/c-Si stacks is investigated. Luminescence spectra from c-Si wafers passivatied with SiN_x films are then examined and demonstrated to have similar properties to those from wafers passivated with a-Si films. The work shows a correlation between the luminescence intensity from the SiN_x films and the a-Si component inside these films, whose presence is confirmed with Raman spectroscopy measurements. The results also indicate that, even though the SiN_x films are aimed to improve the surface passivation quality, and thus improve the photocurrent, the internal absorption of the films can in fact reduce the blue response of silicon solar cells, and thus adversely impact the final photocurrent. Furthermore, when combining with the ability to detect the luminescence from the heavily-doped layer in silicon wafers (reported in Chapter 7), this PLS-based technique is applied to unambiguously separate individual luminescence signatures from different layers on a single substrate including the SiN_x passivation film, the heavily-doped layer, and the c-Si substrate. Finally, this technique is applied to evaluate the parasitic absorption inside the passivation films, and the doping level of the heavily-doped regions on various finished solar cells.

Chapter 9 introduces another new PL-based characterization technique combining both spectrally-resolved photoluminescence (PLS) and photoluminescence excitation spectroscopy (PLE) at low temperatures. The PLS-based method captures the entire spectrum from the material with a single excitation wavelength, whereas the PLE-based method monitors the PL intensity at a certain wavelength with varying excitation wavelengths. With this combined PLS-PLE technique, the evolution of the entire PL spectrum versus excitation wavelength from different materials and structures can be observed. This spectrally-resolved PLE-based technique is established based on the fact that, recombination mechanisms among various materials and structures inside a c-Si wafer are often different from each other, giving different distinct PL peaks at low temperatures. In addition, in case the materials and structures are distributed at different depths underneath the wafer surface, the fraction of the excitation light absorbed in each material and structure is changed with varying excitation wavelengths. Therefore, not only can the electronic and optical properties of the materials and structures be probed, but also the depth distributions of these features can be evaluated. This newly developed technique is then applied to evaluate doping densities and junction depths of different diffused c-Si wafers. It is also applied to detect and separate the depth distribution of various defects induced by the post-diffusion thermal treatment in c-Si wafers.

Chapter 10 is, in general terms, the culmination of the previous chapters. It brings together all characterization methods established for the deep-level centers in Chapter 5, the heavily-doped layers in Chapter 6, and the separation of luminescence signals from different layers at various depths in c-Si wafers in Chapter 9, to investigate the enhanced diffusion of dopant atoms in mc-Si wafers. The enhanced diffusion has been reported in the literature for certain

types of grain boundaries in mc-Si wafers using electron beam induced current (EBIC) or light beam induced current (LBIC) techniques. However, these techniques require contact formation and a cross-sectioning or an angle lapping of the samples. This chapter shows that, by performing PL measurements from above the wafer surface, the enhanced diffusion in mc-Si wafers can be detected without much sample preparation. The results show that the enhanced diffusion occurs at numerous types of grain boundaries, rather than just some specific types as reported in the literature. In addition, by applying the spectrally-resolved PLE technique developed in Chapter 9, defects and impurities decorating around sub-grain boundaries are demonstrated to be uniformly distributed along the wafer thickness. The results suggest that, the defects and impurities trapped around the sub-grain boundaries do not hinder the preferential diffusion of the dopant atoms. Therefore, the sub-grain boundaries are not only recombination active but also promote preferential diffusion of dopant atoms. This conclusion could not be made based on EBIC and LBIC measurements since the defects and impurities and the dopants have opposing effects on the induced current.

Chapter 11 focuses on a more fundamental understanding of luminescence spectra emitted from heavily-doped c-Si. In particular, the chapter looks into the impact of both dopant and excitation levels on the PL spectral shape at different temperatures. Numerous phenomena are known to occur in the band structure of heavily-doped c-Si, which in turn affect the shape of the luminescence spectra. Nevertheless, these phenomena are often characterized by two simple quantities of the spectra: the shifting of the peak and the broadening of the width. This chapter investigates and elucidates the separate effects of individual parameters including the band gap, Fermi level, band tails, and neutral dopant band on the luminescence spectra emitted from heavily-doped c-Si by both modeling and experiments. The results show that, in heavily-doped c-Si, the reduction of the band gap simply shifts the band-to-band luminescence peak to lower energies without changing the spectral shape; the increasing band tails simply broaden the band-to-band luminescence spectrum, causing different spectral components to be overlapped; and the increasing Fermi level not only shifts the band-to-band luminescence peak towards higher energies, but also broadens the spectral width. These results help explain why the relative luminescence peak shift is always smaller than the amount of band-gap narrowing in heavily-doped c-Si; and why the spectral width is broadened with increasing doping densities more quickly once the semiconductor becomes degenerate. Finally, the evolutions of the dopant band and the band tails with increasing doping densities are empirically demonstrated, and the difference in the spectra between low and high excitation levels is clarified.

References

[1] "International Technology Roadmap for Photovoltaics (ITRPV)," 7th Edition, March 2016.

[2] K. Masuko, M. Shigematsu,T. Hashiguchi, D. Fujishima, M. Kai, N. Yoshimura, T. Yamaguchi, Y. Ichihashi, T. Mishima, N. Matsubara, T. Yamanishi, T. Takahama, M. Taguchi, E. Maruyama, S. Okamoto, "Achievement of more than 25% conversion efficiency with crystalline silicon heterojunction solar cell," IEEE J. Photovoltaics, vol. 4, pp. 1433-1435, 2014.

[3] W. Bludau, A. Onton, and W. Heinke, "Temperature dependence of the band gap of silicon," J. Appl. Phys., vol. 45, pp. 1846-1848, 1974.

[4] W. P. Dumke, "Comparison of band-gap shrinkage observed in luminescence from n+-si with that from transport and optical absorption measurements," Appl. Phys. Lett., vol. 42, pp. 196-198, 1983.

[5] J. Wagner, "Photoluminescence and excitation spectroscopy in heavily doped n- and p-type silicon," Phys. Rev. B, vol. 29, pp. 2002-2009, 1984.

[6] M. Tajima, "Determination of boron and phosphorus concentration in silicon by photoluminescence analysis," Applied Physics Letters, vol. 32, pp. 719-721, 1978.

[7] E. Daub and P. Würfel, "Ultralow values of the absorption coefficient of Si obtained from luminescence," Phys. Rev. Lett., vol. 74, pp. 1020-1023, 1995.

[8] E. Daub and P. Würfel, "Ultralow values of the absorption coefficient for band–band transitions in moderately doped Si obtained from luminescence," J. Appl. Phys., vol. 80, pp. 5325-5331, 1996.

[9] T. Trupke, M. A. Green, P. Würfel, P. P. Altermatt, A. Wang, J. Zhao, and R. Corkish, "Temperature dependence of the radiative recombination coefficient of intrinsic crystalline silicon," J. Appl. Phys., vol. 94, pp. 4930-4937, 2003.

[10] P. P. Altermatt, F. Geelhaar, T. Trupke, X. Dai, A. Neisser, and E. Daub, "Injection dependence of spontaneous radiative recombination in crystalline silicon: Experimental verification and theoretical analysis," Appl. Phys. Lett., vol. 88, pp. 261901-1 -261901-3, 2006.

[11] P. Würfel, T. Trupke, T. Puzzer, E. Schäffer, W. Warta, and S. W. Glunz, "Diffusion lengths of silicon solar cells from luminescence images," J. Appl. Phys., vol. 101, pp. 123110-1–123110-10, 2007.

[12] J. A. Giesecke, M. Kasemann, and W. Warta, "Determination of local minority carrier diffusion lengths in crystalline silicon from luminescence images," J. Appl. Phys., vol. 106, pp. 014907-1–014907-8, 2009.

[13] B. Mitchell, M. K. Juhl,M.A.Green, and T. Trupke, "Full spectrum photoluminescence lifetime analyses on silicon bricks," IEEE J. Photovoltaics, vol. 3, pp. 962–969, 2013.

[14] J. A. Giesecke, M. Kasemann, M. C. Schubert, P. Würfel, and W. Warta, "Separation of local bulk and surface recombination in crystalline silicon from luminescence reabsorption," Prog. Photovoltaics: Res. Appl., vol. 18, pp. 10–19, 2011.

[15] M. P. Peloso, J. S. Lew, T. Trupke, M. Peters, R. Utama, and A. G. Aberle, "Evaluating the electrical properties of silicon wafer solar cells using hyperspectral imaging of luminescence," Appl. Phys. Lett., vol. 99, pp. 221915-1–221915-3, 2011.

[16] C. Barugkin, Y. Wan, D. Macdonald, and K. R. Catchpole, "Evaluating plasmonic light trapping with photoluminescence," IEEE J. Photovoltaics, vol. 3, pp. 1292–1297, 2013.

[17] M. Tajima, Y. Iwata, F. Okayama, H. Toyota, H. Onodera, and T. Sekiguchi, "Deep-level photoluminescence due to dislocations and oxygen precipitates in multicrystalline Si," J. Appl. Phys., vol. 111, pp. 113523-1 – 113523-6, 2012.

[18] P. Gundel, M. C. Schubert, W. Kwapil, J. Schön, M. Reiche, H. Savin, M. Yli-Koski, J. A. Sans, G. Martinez-Criado, W. Seifert, W. Warta, and E. R. Weber, "Micro-photoluminescence spectroscopy on metal precipitates in silicon," Physica Status Solidi RRL, vol. 3, pp. 230-232, 2009.

[19] R. Woehl, P. Gundel, J. Krause, K. Rühle, F. D. Heinz, M. Rauer, C. Schmiga, M. C. Schubert, W. Warta, and D. Biro, "Evaluating the aluminum-alloyed p+-layer of silicon solar cells by emitter saturation current density and optical microspectroscopy measurements," IEEE Trans. Elec. Devices, vol. 58, pp. 441-447, 2011.

[20] P. Gundel, D. Suwito, U. Jäger, F. D. Heinz, W. Warta, and M. C. Schubert, "Comprehensive microscopic analysis of laser-induced high doping regions in silicon," IEEE Trans. Elec. Devices, vol. 58, pp. 2874-2877, 2011.

[21] P.Gundel, M.C.Schubert, and W.Warta, "Simultaneous stress and defect luminescence study on silicon," Phys. Status Solidi A, vol. 207, pp. 436-441, 2010.

[22] G. D. Gilliland, "Photoluminescence spectroscopy of crystalline semiconductors," Materials Science and Engineering, vol. R18, pp. 99-400, 1997.

CHAPTER 1

Photoluminescence in Crystalline Silicon

In simple terms, luminescence in a semiconductor is the emission of photons from the material when electrons from higher energy states make transitions to lower energy states. Depending on the mechanism employed to excite the electrons, there are various types of luminescence. Among them, the three types which are most commonly used as characterization tools in silicon photovoltaics (Si-PV) are cathodoluminescence (CL), electroluminescence (EL), and photoluminescence (PL). In CL, the excitation is achieved by bombarding samples with a high energy electron beam from cathode rays, which can potentially damage the sample regions under measurements. In EL, the excitation is achieved by applying an electric potential across or electric current through the samples, and thus requires contact formation. In principle, these two techniques involve both electrical and optical phenomena, and thus are not considered as a purely optical characterization technique. On the other hand, the PL technique excites the

electrons with a primary incident photon beam, and hence has all the advantages of optical spectroscopy such as being contactless and non-destructive, and requires minimal sample preparation.

In crystalline silicon (c-Si), the PL phenomenon consists of both band-to-band and deep-level luminescence. The band-to-band emission is due to radiative transitions of free electrons in the conduction band to empty states in the valence band, and it reflects the intrinsic properties of silicon. On the other hand, the deep-level emission is due to the radiative recombination of electrons and/or holes trapped by defect and impurity centers occupying energy levels inside the silicon band gap, and thus it reflects the properties of defects and impurities within the host material. Although the PL signal is emitted by the material itself, the PL spectrum detected outside the material is a complex combination of numerous phenomena which are both intrinsic and extrinsic to the material properties. In particular, PL spectra from c-Si wafers are determined by:

(i) The material properties.

(ii) The energy and power of the excitation source, and the surface recombination. These properties determine excess carrier profiles inside the silicon wafers, which generally affect the PL spectral shape.

(iii) The optical properties of the wafer surface, which determine the escape probability of the generated photons.

(iv) The spectral response of the spectroscopic equipment employed to capture the PL spectra.

Therefore, this chapter provides a theoretical background on the PL emission from c-Si wafers from a physical point of view, which is essential for understanding the rich information embedded in the captured PL spectra discussed throughout the course of this thesis.

1.1 Generation of band-to-band photoluminescence from silicon

Band-to-band photons are generated due to the radiative recombination of free electrons and holes in the conduction and valence bands of silicon, respectively. Generally speaking, the generation of these photons from a volume element of c-Si is determined by two quantities: the ability of the semiconductor itself to emit photons and the capability of the surrounding environment to accept them. The former is related to the numbers of free electrons and holes, whereas the latter is described by the energy distribution of photons.

The ability to emit photons, denoted as P_{emit}, is determined by the relationship [1-3]:

$$P_{emit} \propto \int_0^\infty f_e(E_e) D_e(E_e) f_h(E_h) D_h(E_h) dE_e \,. \tag{1}$$

f_e, D_e, and E_e (f_h, D_h, and E_h), respectively, are the distribution function, density of states, and amount of energy above the conduction band edge E_C (below the valence band edge E_V) of free electrons (holes). The energy distribution of photons is a product of the distribution function (f_γ) and density of states (D_γ) of photons, and is given by [4]:

$$f_\gamma(\hbar\omega) \times D_\gamma(\hbar\omega) \propto (\hbar\omega)^2 \times \exp\left(-\frac{\hbar\omega}{kT}\right), \tag{2}$$

where $\hbar\omega$ and kT are the energy of emitted photons and the thermal energy, respectively. Therefore, the spectral shape of the generated photons from a silicon volume element in the dark should be determined by the following relationship:

$$I_{dark}(\hbar\omega) \propto \left[\int_0^\infty f_e(E_e) D_e(E_e) f_h(E_h) D_h(E_h) dE_e\right] \times \left[(\hbar\omega)^2 \times \exp\left(-\frac{\hbar\omega}{kT}\right)\right]. \tag{3}$$

Since silicon is an indirect semiconductor, the photon emission also requires the participation of phonons whose energy is E_P. The energy relationship among free electrons and holes, phonons, and emitted photons is illustrated in Figure 1.1, and is given by:

$$\hbar\omega \pm E_P = E_e + E_h + E_G, \tag{4}$$

where E_G is the silicon band gap. '+/-' denotes the emission/absorption of phonons.

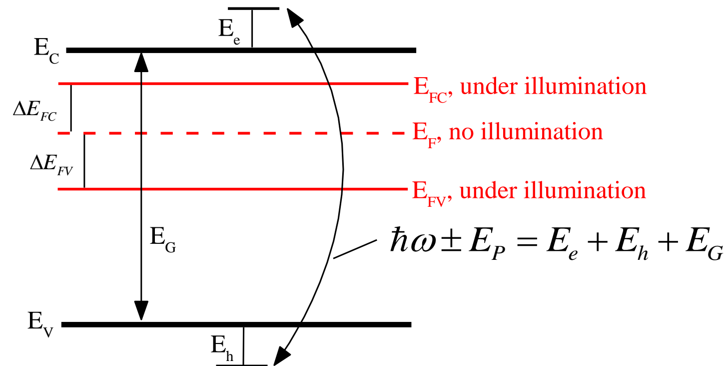

Figure 1.1: *Illustration of the energy relationship among emitted photons $\hbar\omega$, phonons E_P ('+' denotes a phonon emission event, whereas '-' denotes a phonon absorption event), free holes E_h, and free electrons E_e in n-type silicon under illumination. See the text for descriptions of the symbols.*

However, under illumination, the Fermi level E_F is split into two separate levels $E_{FC} = E_F + \Delta E_{FC}$ and $E_{FV} = E_F - \Delta E_{FV}$ for electrons and holes, respectively. Therefore, the distribution functions of electrons and holes under illumination, $f_{e,illum}$ and $f_{h,illum}$, become:

$$f_{e,illum}(E_e) = \frac{1}{1+\exp\left(\frac{E_e - (E_F + \Delta E_{FC})}{kT}\right)} \tag{5a}$$

and

$$f_{h,illum}(E_h) = \frac{1}{1+\exp\left(\frac{(E_F - \Delta E_{FV}) - E_h}{kT}\right)}. \tag{5b}$$

In non-degenerate semiconductors, under low excitation levels in which the quasi-Fermi levels are far enough from the band edges, i.e. $E_e - (E_F + \Delta E_{FC})$ and $(E_F - \Delta E_{FV}) - E_h$ are several times larger than kT, we can rewrite $f_{e,illum}$ and $f_{h,illum}$ as:

$$f_{e,illum}(E_e) = f_e(E_e) \times \exp\left(\frac{\Delta E_{FC}}{kT}\right) \tag{6a}$$

and

$$f_{h,illum}(E_e) = f_h(E_h) \times \exp\left(\frac{\Delta E_{FV}}{kT}\right). \tag{6b}$$

Therefore, Eq. (3) becomes:

$$I_{illum}(\hbar\omega) \propto \left[\int_0^\infty f_e(E_e) D_e(E_e) f_h(E_h) D_h(E_h) dE_e\right] \times \left[(\hbar\omega)^2 \times \exp\left(-\frac{\hbar\omega - (\Delta E_{FC} + \Delta E_{FV})}{kT}\right)\right] \tag{7}$$

Eq. (7) is, in fact, similar to the generalized Planck's law which describes the spontaneous generation rate of photons from a volume element due to band-to-band transitions in a non-

degenerate semiconductor. According to this law, the spontaneous generation rate from silicon is given by [5,6]:

$$R_{sp}(\hbar\omega) \propto \alpha_{BB} \times (\hbar\omega)^2 \times \exp\left(-\frac{\hbar\omega}{kT}\right) \times \exp\left(\frac{\Delta E_{FC} + \Delta E_{FV}}{kT}\right). \quad (8)$$

α_{BB} is the band-to-band absorption coefficient of silicon, and reflects intrinsic properties of the material. It incorporates both the distribution functions and densities of states of electrons and holes, and the participation of phonons. Therefore, in principle, this parameter is closely related to the first square bracket in Eq. (7). The two formulas in (7) and (8) can both be used to describe the shape of the band-to-band luminescence spectra from silicon at low temperatures, at which the reabsorption of the spontaneously generated photons is negligible.

1.2 Band-to-band photoluminescence emitted from silicon wafers

After the photons are spontaneously generated, in order to escape the semiconductor, they have to overcome two loss mechanisms, which are illustrated in Figure 1.2. First, these photons have to survive reabsorption on the way to the wafer surface. This reabsorption is characterized by the absorption coefficient α_{BB}, in which case the band-to-band absorption is assumed to be the dominating phenomenon. Second, the photons have to arrive at the surface at an incident angle which is smaller than the critical angle θ_c. Otherwise, they will be totally reflected back and do not have any chance to escape. The fraction of the spontaneously generated photons within the critical angle is one out of $4n^2$ [7], in which n is the refractive index of silicon. At the surface, after the reabsorption, the remaining photons within the critical angle can be either reflected back or transmitted into the outside environment.

Accounting for the phenomena described above, the photon flux emitted from a silicon wafer is then given by [7-9]:

$$PL = \left[\int_0^w \frac{R_{sp}}{4n^2} \times \exp(-\alpha_{BB} x) dx\right] \times A . \quad (9)$$

w is the wafer thickness and A is determined by the geometry and internal reflectivities on both wafer surfaces. The following relationship also holds for the Fermi level separation under illumination [4]:

$$\exp\left(\frac{\Delta E_{FC} + \Delta E_{FV}}{kT}\right) = \frac{n \times p}{n_i^2} \approx \frac{(N_{dopant} + \Delta n) \times \Delta n}{n_i^2} . \quad (10)$$

n and p are the free carrier densities of electrons and holes, respectively. N_{dopant} and Δn are the doping density and the excess carrier density, respectively. n_i is the intrinsic carrier density of silicon. Therefore, combining (8), (9), and (10), one can model the band-to-band PL spectra emitted from silicon wafers at a given temperature if the band-to-band absorption coefficient α_{BB}, surface geometry and reflectivities, and excess carrier profile are known. On the other hand, these properties of the silicon wafers can be studied using the emitted PL spectra.

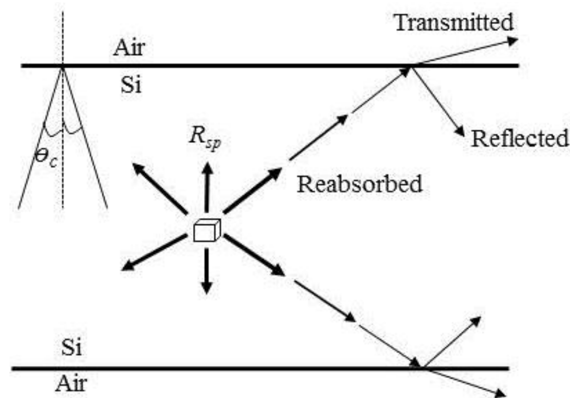

Figure 1.2: *Loss mechanisms of spontaneously generated photons inside a silicon wafer. First, the generated photons can be reabsorbed on the way to the surface. Second, only photons arriving at the surface at an angle less than the critical angle* θ_c *have opportunities to escape the wafer. The remaining photons also suffer from the internal reflection at the surface. Note that the incident, reflected, transmitted, and critical angles in this figure are not presented in actual scales.*

1.3 Deep-level photoluminescence from defects and impurities

When a c-Si wafer contains defects and impurities which occupy energy levels within the forbidden gap of c-Si, these centers can trap free electrons and holes. The trapped electrons and holes can then radiatively recombine, resulting in deep-level PL. Compared to the band-to-band PL peak, the energy of the deep-level PL peak is shifted towards lower energies, i.e. longer wavelengths. Figure 1.3 illustrates the three most common mechanisms of deep-level radiation. Type 1 and type 2 deep-level radiations involve only one trapping level, and the energy difference between the deep-level and band-to-band PL lines directly reflects the energy level of the trapping state in the band gap. On the other hand, type 3 requires the participation of two trapping levels – one for holes and one for electrons. For this type of deep-level radiation, we cannot determine the trap energy levels based on the energy difference between the band-to-band and deep-level PL lines directly.

However, if the defect or impurity luminescence involving two trapping levels (type 3) consists of a deep state (far from a band edge) and a shallow state (near the other band edge),

the luminescence will display a strong thermal quenching rate. The reason is that, at high temperatures the thermal energy can excite the carriers trapped at the shallow state back to the nearest band edge, thus reducing the PL intensity. The thermal activation energy E_A of the defects or impurities is the energy difference between the shallow state and its nearest band edge, and is determined by fitting the equation below with the experimental data [10,11]:

$$I(T) = \frac{I_0}{1 + CT^{3/2} \exp\left(-\frac{E_A}{kT}\right)}, \tag{11}$$

where $I(T)$ is the PL intensity at a certain absolute temperature T, I_0 is a constant, C is a fitting parameter, and k is Boltzmann's constant. Based on the value of E_A and the energy difference between the band-to-band and deep-level lines, one can then extract the energy level of the deep state.

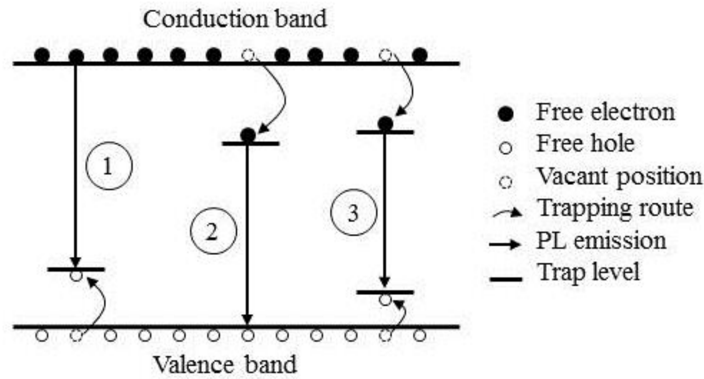

Figure 1.3: *Illustration of recombination schemes of deep-level luminescence from defects and impurities in c-Si wafers. See the text for descriptions of the three recombination types.*

1.4 Separation of PL signal from various layers at low temperatures

When different layers of various materials are stacked together, if we employ an appropriate excitation wavelength, the excitation light will be absorbed in all layers (Figure 1.4a). Each of these layers will then emit its own PL spectrum. Since different materials have their unique band gaps, absorption coefficients, and radiative recombination mechanisms, the PL spectrum emitted from each layer is distinct. Therefore, the total spectrum captured contains signatures of all layers. However, at room temperature, either the PL spectrum is very broad due to thermal broadening, or some spectral components are reduced in intensity significantly due to thermal quenching. Therefore, we cannot distinguish the signatures of the individual layers on the

detected spectrum. On the other hand, at low temperatures the PL spectrum is sharp and the thermal quenching does not impact the luminescence intensity significantly, and thus we can observe different PL lines associated with different layers unambiguously, as illustrated in Figure 1.4b.

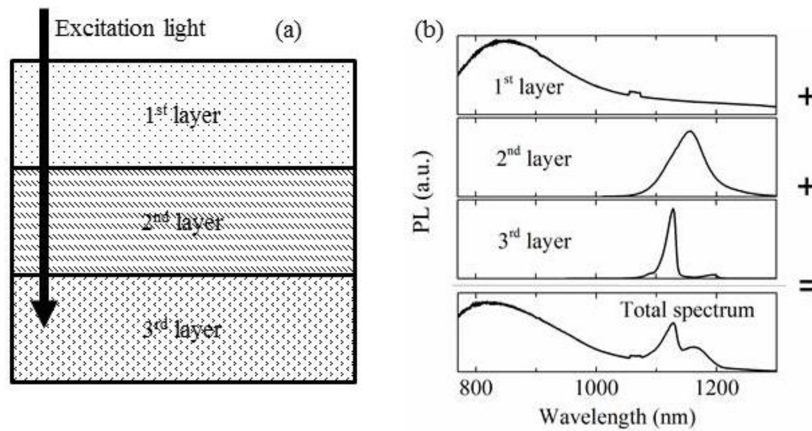

Figure 1.4: *(a) Different layers absorb the excitation light. (b) Illustration of the individual spectra emitted from each layer and the total spectrum detected at low temperatures.*

1.5 Photoluminescence spectroscopy systems

In this thesis, PL spectra are captured using two experimental systems: a conventional PL spectroscopy system in which the on-sample illuminated spot size is several millimeters in diameter, and a micro-PL spectroscopy system equipped with confocal optics yielding an on-sample spot size of about one micrometer in diameter. A schematic of the conventional PL spectroscopy system is given in Figure 1.5. Samples under investigation are excited with a laser light. The emitted PL signal is focused through a focusing mirror, and then directed into a double-monochromator and captured by an InGaAs detector. A standard lock-in technique is employed in order to improve the signal-to-noise ratio. This system allows us to capture the luminescence signal from silicon wafers with a dynamic range of up to five orders of magnitude. However, due to the large illuminated spot size, the spatial resolution of this system is limited and the properties of features smaller than one millimeter are often confounded with those of surrounding regions.

On the other hand, the micro-PL spectroscopy system can overcome the spatial limitation of the conventional system. A schematic of this system is plotted in Figure 1.6. A collimated light source is focused onto a submicron spot on the sample surface through confocal optics. The emitted PL signal is then collected with the same confocal path, directed into the entrance slit of a monochromator, and detected with an InGaAs detector. The illuminated spot size can be

controlled by changing the objective lens. The sample stage is equipped with an X-Y mapping system which has a minimum step size of 0.3 micrometers. Furthermore, an optical camera is also installed on the sample stage in order to help locate the area of interest. The system enables us to examine the luminescence properties of sub-micron structures in c-Si wafers and solar cells. However, since the PL signal is collected from such a small area on the samples and there is no lock-in amplification of the signal, the signal-to-noise ratio is reduced significantly compared to that of the conventional PL spectroscopy system.

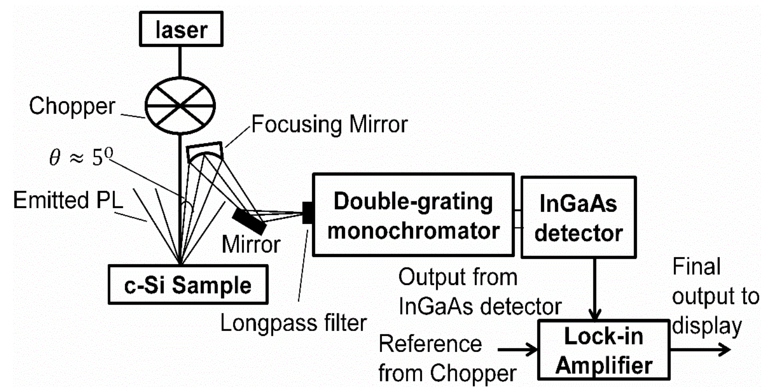

Figure 1.5: *Schematic of the conventional PL spectroscopy system employed in this thesis, adapted from Nguyen et al. [12].*

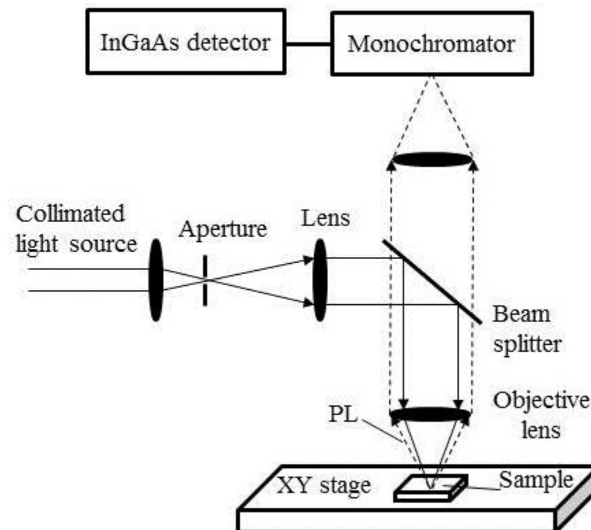

Figure 1.6: *Schematic of the micro-PL spectroscopy system employed in this thesis. Courtesy of confocal optics, the illuminated spot size is on the order of micrometers in diameter.*

The components in these two PL spectroscopy systems, including the optics and detectors, are always non-ideal, and thus the emitted spectra are always distorted after passing through them. Therefore, the detected PL spectra are altered from the real spectra emitted by the c-Si wafers and solar cells. As shown in Figure 1.7 and Figure 1.8 for the conventional and micro-

PL spectroscopy systems respectively, the measured spectra from a calibrated tungsten-halogen light source are remarkably deviated from its expected spectrum. Therefore, in order to have reliable interpretations on the PL spectra captured, they must be corrected for the spectral responses of the two systems. These correction factors can be extracted by taking the ratio between the expected and measured spectra from the calibrated light source in Figure 1.7 and Figure 1.8. The detected signal is then multiplied with the corresponding correction factor of each spectroscopic system.

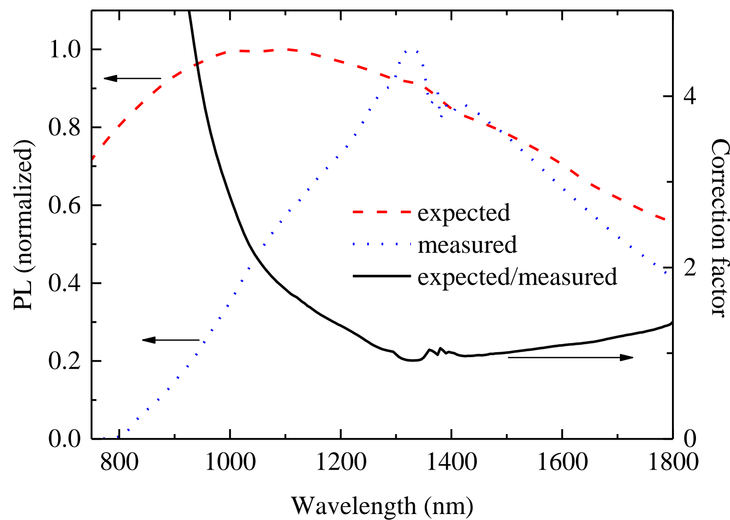

Figure 1.7: *Normalized expected and measured spectra of the calibrated tungsten-halogen light source from the conventional PL spectroscopy system. The correction factor is derived from the ratio between the expected and measured signals.*

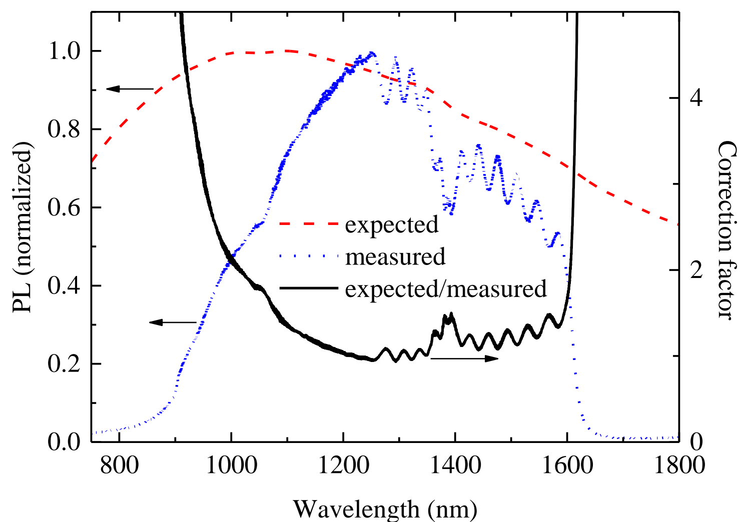

Figure 1.8: *Normalized expected and measured spectra of the calibrated tungsten-halogen light source from the micro-PL spectroscopy system. The correction factor is derived from the ratio between the expected and measured signals. The oscillation pattern between 1200 and 1600 nm is caused by the interference in the optical path of the experimental system.*

1.6 Summary

In summary, the photoluminescence signal captured is a complicated combination of numerous phenomena occurring in both the silicon wafers and spectroscopic equipment. The emitted spectrum itself is determined by the intrinsic properties of silicon, defects and impurities in the host material, experimental conditions, and surface optics. The detected spectrum is then affected by the spectral responses of the photoluminescence spectroscopy systems. However, viewed from a different perspective, these relationships are, in fact, opportunities for exploring potential applications of spectrally-resolved photoluminescence. By systematically controlling and monitoring the parameters which can potentially affect the detected spectra, certain properties of silicon wafers and solar cells can be evaluated. The next chapters will exploit these complications to establish different applications of spectrally-resolved photoluminescence-based techniques for silicon photovoltaics.

References

[1] R. R. Parsons, "On the origin of photoluminescence in heavily-doped silicon," Solid State Communications, vol. 29, pp. 763-766, 1979.

[2] W. P. Dumke, "Comparison of band-gap shrinkage observed in luminescence from n+-si with that from transport and optical absorption measurements," Appl. Phys. Lett., vol. 42, pp. 196-198, 1983.

[3] J. Wagner, "Photoluminescence and excitation spectroscopy in heavily doped n- and p-type silicon," Phys. Rev. B, vol. 29, pp. 2002-2009, 1984.

[4] P. Würfel, Physics of Solar Cells: From Basic Principles to Advanced Concepts, Wiley-VCH, 2009.

[5] P. Würfel , "The chemical potential of radiation," J. Phys. C: Solid State Phys., vol. 15, pp. 3967-3985, 1982.

[6] P. Würfel, S. Finkbeiner, and E. Daub, "Generalized Planck's radiation law for luminescence via indirect transitions," Appl. Phys. A, vol. 60, pp. 67-70, 1995.

[7] K. Schick, E. Daub, S. Finkbeiner, and P. Würfel, "Verification of a generalized Planck law for luminescence radiation from silicon solar cells," Appl. Phys. A, Solids Surfaces, vol. 54, pp. 109–114, 1992.

[8] T. Trupke, E. Daub, and P. Würfel, "Absorptivity of silicon solar cells obtained from luminescence," Sol. Energy Mater. Sol. Cells, vol. 53, pp. 103–114, 1998.

[9] P. Würfel, T. Trupke, T. Puzzer, E. Sch¨affer, W. Warta, and S. W. Glunz, "Diffusion lengths of silicon solar cells from luminescence images," J. Appl. Phys., vol. 101, pp. 123110-1–123110-10, 2007.

[10] M. Suezawa, Y. Sasaki, and K. Sumino, “Dependence of photoluminescence on temperature in dislocated silicon crystals,” Phys. Status Solidi A, vol. 79, pp. 173-181, 1983.

[11] M. C. Schubert, P. Gundel,M. The,W.Warta,M. Romero, S. Ostapenko, and Tz. Arguirov, “Spatially resolved luminescence spectroscopy on multicrystalline silicon,” in Proceedings of 23rd EU-PVSEC, Valencia, pp. 17-23, 2008.

[12] H. T. Nguyen, F. E. Rougieux, B. Mitchell, and D. Macdonald, “Temperature dependence of the band-band absorption coefficient in crystalline silicon from photoluminescence,” J. Appl. Phys., vol. 115, pp. 043710-1 -043710-8, 2014.

CHAPTER 2

Temperature Dependence of Band-to-Band Absorption Coefficient

The absorption of light in a silicon sample can either generate heat inside the sample since some of the light's energy is converted to lattice vibrations, or promote electrons located in the valence band to the conduction band. Only the latter case of absorption generates free electrons and holes, which contribute to the photo-generated current of a silicon solar cell. This absorption is called band-to-band absorption. On the other hand, only the free electrons and holes can give rise to band-to-band photoluminescence spectra. Therefore, the band-to-band photoluminescence spectra and the band-to-band absorption are closely related together, and to some extent, directly reflect the material quality and the performance of final silicon solar cells.

The band-to-band absorption is characterized by the band-to-band absorption coefficient. This coefficient is a key parameter in modeling and characterizing semiconductor devices. Due to its significance, the value of this coefficient has received great attention from many researchers over the past several decades. Numerous efforts have been made to determine the precise value of the coefficient at different temperatures and wavelengths using different methods, such as the conventional transmission and reflection technique, spectral response measurements on a silicon solar cell, and spectrally-resolved photoluminescence data. However,

none of the established works has densely covered the practical working temperature range of silicon solar cells. Therefore, this chapter is devoted to re-examining the established data of the band-to-band absorption coefficient. It also fills in the gap in the temperature data of this coefficient around room temperature, in particular from 249 to 363 K with a step of 10 K, a region in which there are relatively sparse experimental data in the literature.

In more specific terms, the chapter utilizes the generalized Planck's law, which describes the spontaneous generation rate of photons from a silicon volume element. In principle, the absorption coefficient could be directly extracted from the spontaneous photoluminescence spectrum. However, around room temperature, it is never possible to capture the actual spontaneous shape of the spectrum. Due to the reabsorption of these generated photons and the different values of the absorption coefficient at different wavelengths, various parts of the spectrum itself are affected non-uniformly by the reabsorption. As discussed in section 1.2, the band-to-band absorption coefficient, excess carrier distribution inside the wafer, and surface optics all play critical roles on the final spectrum detected. Therefore, at a given temperature, if the excess carrier profile and surface optics are well controlled, the values of the absorption coefficient versus wavelength can be extracted accurately from the spectrum captured.

This work has been published. However, a very important point, which was not discussed in the publication, is the impact of excess carriers on the apparent band gap of silicon. Under high injection, the band gap of silicon will be effectively narrowed, leading to higher values of the absorption coefficient across all wavelengths. According to the literature [1,2], the simulated excess carrier density of ~8×10^{16} cm^{-3} in this publication could reduce the apparent band gap of silicon by ~10 meV. However, the simulation was done for the worst case scenario, in which the peak intensity of the Gaussian-shape laser beam was considered to be the average intensity and the lateral carrier diffusion was assumed to be negligible. Therefore, the actual impact of excess carriers on the band gap of silicon must be less than the value mentioned above. In fact, the luminescence spectrum reconstructed from an unpassivated silicon brick, using the absorption values established in this work, is matched with the spectrum reported by Mitchell *et al.* [3] very well (Figure 11 in this publication). The average injection level in Mitchell *et al.*'s work is ~2×10^{14} cm^{-3}. Therefore, the impact of excess carriers on the established absorption data is unlikely to be significant.

References

[1] D. B. M. Klaassen, J. W. Slotboom, and H. C. de Graaff, Solid-State Electron., vol. 35, pp. 125-129, 1992.

[2] A. Schenk, J. Appl. Phys., vol. 84, pp. 3684-3695, 1998.

[3] B. Mitchell, M. K. Juhl, M. A. Green, and T. Trupke, IEEE J. Photovolt., vol. 3, pp. 962-969, 2013.

JOURNAL OF APPLIED PHYSICS 115, 043710 (2014)

Temperature dependence of the band-band absorption coefficient in crystalline silicon from photoluminescence

Hieu T. Nguyen,[1,a)] Fiacre E. Rougieux,[1] Bernhard Mitchell,[2] and Daniel Macdonald[1]
[1]*Research School of Engineering, College of Engineering and Computer Science, The Australian National University, Canberra, ACT 0200, Australia*
[2]*Australian Centre for Advanced Photovoltaics, School of Photovoltaic and Renewable Energy Engineering, University of New South Wales, Sydney, NSW 2052, Australia*

(Received 14 November 2013; accepted 9 January 2014; published online 27 January 2014)

The band-band absorption coefficient in crystalline silicon has been determined using spectral photoluminescence measurements across the wavelength range of 990–1300 nm, and a parameterization of the temperature dependence has been established to allow interpolation of accurate values of the absorption coefficient for any temperature between 170 and 363 K. Band-band absorption coefficient measurements across a temperature range of 78–363 K are found to match well with previous results from MacFarlane *et al.* [Phys. Rev. **111**, 1245 (1958)], and are extended to significantly longer wavelengths. In addition, we report the band-band absorption coefficient across the temperature range from 270–350 K with 10 K intervals, a range in which most practical silicon based devices operate, and for which there are only sparse data available at present. Moreover, the absorption coefficient is shown to vary by up to 50% for every 10 K increment around room temperature. Furthermore, the likely origins of the differences among the absorption coefficient of several commonly referenced works by Green [Sol. Energy Mater. Sol. Cells **92**, 1305 (2008)], Daub and Würfel [Phys. Rev. Lett. **74**, 1020 (1995)], and MacFarlane *et al.* [Phys. Rev. **111**, 1245 (1958)] are discussed. © *2014 AIP Publishing LLC*. [http://dx.doi.org/10.1063/1.4862912]

I. INTRODUCTION

Numerous experimental studies[1–7] have reported measurements of the band-band absorption coefficient in crystalline silicon in the wavelength range near the energy band-gap. Among them, MacFarlane *et al.*[1] used the transmission and reflection characteristics of silicon to establish data at different temperatures, but in a relatively limited wavelength range. Weakliem and Redfield[2] applied the same method but with elevated temperatures up to 475 K and down to wavelengths as small as 460 nm. Green and Keevers,[3] later updated by Green,[4] and Daub and Würfel[6] produced their data independently at 300 K and 295 K, respectively, with a broader wavelength range compared with MacFarlane *et al.* These latter data sets are commonly used today although there is some deviation between them. Green[4] extracted the data from both the transmission and reflection method and the spectral response of high-efficiency silicon solar cells[3–5] while Daub and Würfel[6] analyzed photoluminescence (PL) spectra emitted from optically excited silicon. Later, Trupke *et al.*[7] again utilized this PL-based method to extract data at temperatures covered in the experiment of Ref. 1, but for longer wavelengths.

Recently, there have been some new applications[8,9] relating to silicon solar cells based on fitting photoluminescence spectra. Schinke *et al.*[8] modeled the emitted spectra for silicon wafers with different surface geometries, while Mitchell *et al.*[9] extracted the bulk lifetime of minority carriers in silicon bricks using a fitting of the full PL spectra. These techniques require the band-band absorption coefficient as a key input parameter. They were carried out at 295 K, and both found that the spectra could be fitted better with Daub and Würfel's data (Ref. 6) rather than Green's (Ref. 4). There is significant disagreement in these data sets at wavelengths between 1180–1250 nm, a region which is important for the fitting procedures of the techniques above. However, to date there has been no direct reassessment of the band-band absorption coefficient in order to verify the data at these wavelengths and at this temperature. Moreover, temperatures in experiments of MacFarlane *et al.* and Trupke *et al.* do not densely cover the range in which practical solar cells and microelectronic devices usually operate, and thus there is still a lack of information on the band-band absorption coefficient in crystalline silicon.

The PL-based approach has been demonstrated to have some advantages over the conventional reflection and transmission approach. Previous works[6,7] have shown that it is possible to determine values of the band-band absorption coefficient as low as $10^{-7}\,\text{cm}^{-1}$ at room temperature (RT) via PL measurements, courtesy of the direct relationship between the band-band absorption and emission processes.[11–13] Such sensitivity is not possible with the reflection and transmission method, since impractically thick samples would be required. In any case, free carrier absorption would mask the band-band absorption processes at longer wavelengths in such a transmission experiment,[7] while PL-based data are largely unaffected by free carrier absorption.[10] Therefore, in this study, we again take advantage of this PL-based technique to empirically determine the band-band absorption coefficient in crystalline silicon. First, we perform the measurements at different temperatures and establish a tabulated data set from 78–363 K, especially in the range from 270–350 K with a step of 10 K,

a)Author to whom correspondence should be addressed. Electronic mail: hieu.nguyen@anu.edu.au.

 © 2014 AIP Publishing LLC

[This article is copyrighted as indicated in the article. Reuse of AIP content is subject to the terms at: http://scitation.aip.org/termsconditions. Downloaded to] IP: 150.203.210.78 On: Tue, 03 Nov 2015 08:10:49

which covers the typical operation temperature of silicon based devices. Next, we investigate the impact of temperature in this temperature range around RT on the band-band absorption coefficient. In addition, we provide a parameterization of the temperature dependence of the absorption coefficient for wavelengths from 990–1300 nm, from which values can be calculated for any temperature between 170 and 363 K. Furthermore, we elucidate the inconsistencies of the absorption data among MacFarlane *et al.*,[1] Daub and Würfel,[6] and Green.[4] Finally, we extend the data up to the wavelength of 1500 nm at 297 K.

II. THEORY AND METHOD

The spontaneous generation rate of photons per volume and energy interval due to band-band transitions in an excited non-degenerate semiconductor is described by the generalized Planck law[11–13]

$$dr_{sp} = C(\hbar\omega)^2 \alpha_{BB}(\hbar\omega)\exp\left(\frac{-\hbar\omega}{kT}\right)\exp\left(\frac{\Delta\eta}{kT}\right)d(\hbar\omega), \quad (1)$$

with $\alpha_{BB}(\hbar\omega)$ the band-band absorption coefficient, k Boltzmann's constant, and T the absolute temperature of the sample. C is given by $n^2/(\pi^2\hbar^3 c_0^2)$, with n the refractive index of silicon and c_0 the speed of light in vacuum. As measured in Ref. 14, the refractive index varies approximately 0.5% for every 100 nm wavelength increment around the band-gap, and less than 0.03% for every 10 K increment. Hence, C is usually considered as a constant in Eq. (1). $\Delta\eta$ is the difference between the quasi-Fermi levels of electrons and holes under illumination. Since $\Delta\eta$ is independent of wavelength, the $\exp(\Delta\eta/kT)$ factor is also a constant for a fixed injection level at a particular temperature.

To obtain the total photon flux outside the sample, one has to integrate Eq. (1) over its thickness and account for the reabsorption of emitted photons within it. For planar samples excited by monochromatic light, the photon flux, in this case called the PL signal, emitted outside these samples per energy interval is given by[6,7,10,11]

$$\begin{aligned} PL &= \frac{dr_{sp}A(\hbar\omega)}{4\alpha_{BB}n^2} \\ &= \frac{1}{4\pi^2\hbar^3 c_0^2}(\hbar\omega)^2 A(\hbar\omega)\exp\left(\frac{-\hbar\omega}{kT}\right)\exp\left(\frac{\Delta\eta}{kT}\right)d(\hbar\omega), \end{aligned} \quad (2)$$

with $A(\hbar\omega)$ the absorptivity at a given energy, which is approximated via the following formula after multiple incoherent reflections between two surfaces are included[6,7,10,11]

$$A(\hbar\omega) = \frac{[1-R_f(\hbar\omega)][1-e^{-\alpha_{BB}(\hbar\omega)d}][1+R_b(\hbar\omega)e^{-\alpha_{BB}(\hbar\omega)d}]}{1-R_f(\hbar\omega)R_b(\hbar\omega)e^{-2\alpha_{BB}(\hbar\omega)d}}, \quad (3)$$

with d the sample thickness, R_f and R_b the reflectivity of the front and back surfaces relative to the illuminated side. As simulated with the OPAL optical simulator developed by McIntosh and Baker-Finch[15,16] at wavelengths 1100 and 1200 nm, the internal reflectivity of emitted luminescence at the silicon/SiN/air interface varies less than 10% relative for incident angles less than the critical angle for the sample investigated in this study. Based on this modeling, we conclude that the internal reflectivity is effectively independent of the angle of incidence for rays that contribute to the PL signal, and equal to the externally measured reflectance for a normally incident beam.

In order for Eqs. (2) and (3) to be valid, the charge carrier profile must be homogeneous through the sample thickness, and the reabsorption of emitted photons is assumed to be dominated by the band-band absorption,[6,7] rather than other processes such as free carrier absorption. The first point is true for samples whose diffusion lengths are several times larger than their thicknesses, while the second assumption was justified by Trupke *et al.*[10] for wavelengths below 1300 nm for silicon wafers with standard background doping levels in solar cell applications, in which the free carrier density is less than $2 \times 10^{17}\,\mathrm{cm}^{-3}$.

An advantage of this photoluminescence technique is that one can avoid the need to measure the absolute values of PL spectra, which is difficult in practice. The PL signal is instead measured in relative units using an optical spectrometer, from which the relative absorptivity is calculated by dividing the PL signal by the $(\hbar\omega)^2\exp(-\hbar\omega/kT)$ term, in accordance with Eq. (2). A scaling factor is then obtained from one absolute value of the absorptivity, calculated from Eq. (3) together with one literature value of α_{BB} from Ref. 1 at 1065 nm (for 78 and 90 K) or 1110 nm (for other temperatures), and the relative one. The reason for choosing these two wavelengths will be explained in Sec. IV A. This scaling factor is used to convert all relative data of the absorptivity into absolute data. Finally, Eq. (3) is solved to acquire α_{BB} for all wavelengths.

Note that further reference to the absorption coefficient in this paper refers to band-band transitions only.

III. EXPERIMENTAL DETAILS

Figure 1 shows the schematic of our experiment. Our sample was illuminated from the front by a mechanically chopped monochromatic laser diode, and the emitted PL signal was detected from the same side. The laser beam was perpendicular to the sample surface. The laser had a wavelength of 785 nm, on-sample power of 250 mW, and beam diameter of 2.2 mm. The emitted signal was focused onto the entrance port of a double-grating monochromator with blazed gratings of 600 grooves/mm and 1000 nm blaze by a

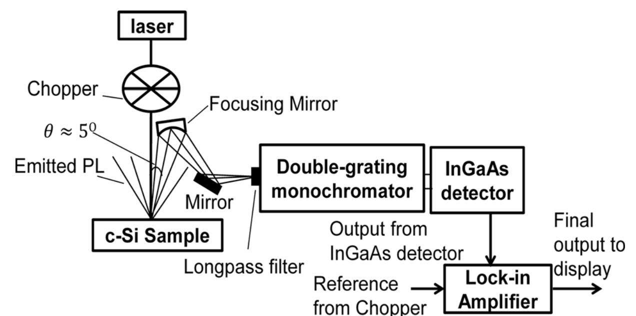

FIG. 1. Schematic of the photoluminescence spectroscopy system used to capture the PL spectra emitted from silicon.

[This article is copyrighted as indicated in the article. Reuse of AIP content is subject to the terms at: http://scitation.aip.org/termsconditions. Downloaded to] IP: 150.203.210.78 On: Tue, 03 Nov 2015 08:10:49

focusing mirror whose central point, along with the illuminated spot, created an angle of about 5° relative to the laser beam (this angle is denoted by θ in Figure 1). The signal was then captured by a liquid-nitrogen-cooled InGaAs detector with a 1 mm^2 active area. The detector output, along with a reference signal from the optical chopper, was fed into a digital lock-in amplifier where the PL spectrum was measured with a modulation frequency of 500 Hz. The final output was connected to a pre-amplifier before being displayed by a computer. A long-pass filter was located in front of the monochromator to avoid the laser light being reflected directly towards the detector. A liquid-nitrogen-cooled cryostat was used to control the sample temperature precisely from 78 to 363 K. The spectra were measured at wavelength intervals of 5 nm and a typical integration time of 10 s. The slit width was adjusted to allow a wavelength integration interval of 5 nm for each data point.

The investigated silicon sample was a high quality phosphorus-doped n-type float zone wafer, 220 μm thick, whose two sides were chemically polished to achieve planar surfaces. The resistivity was 3 Ωcm, corresponding to a background doping level of 1.6×10^{15} cm^{-3}. Both surfaces were passivated by a 75 nm thick layer of silicon nitride (SiN) deposited by plasma-enhanced chemical-vapor deposition (PECVD). The external reflectivity of both sides was measured accurately by a spectrophotometer with a built-in 150 mm integrating sphere and automated reflectance and transmittance analyzer. Before the PL measurement, the sample was irradiated for two hours and the temperature was monitored with a thermocouple mounted behind the illuminated spot. The temperature increased less than 1.5 K, allowing us to neglect the heating effect on the illuminated spot.

Under the high injection conditions that prevail during the PL measurements in this study, the passivation quality of the SiN films may be quantified via the so-called emitter saturation current density J_{Oe}.[17] This quantity was measured with the transient photo-conductance decay technique[18] under high injection, and was found to have a value of 11 fA/cm^2 for both sides combined. Typically, this parameter is used to characterize the surface recombination associated with diffused layers, however, it is also applicable to surfaces under high injection passivated by dielectric films with high fixed charge densities, such as the SiN films used here. The fixed charge induces a charge separation layer just below the surface, which acts in a similar manner to a diffused region in terms of recombination. From this value of the saturation current density, the carrier profile as a function of depth was simulated with the simulation spreadsheet developed by Cuevas.[19,20] Klaassen's mobility model[21,22] was used to estimate the carrier mobilities in this simulation, and the Auger lifetime was estimated via the model of Kerr and Cuevas.[23] The laser has an average intensity of 60 suns and a spatial Gaussian distribution. The simulation was carried out under a generation rate of 120 suns, which is equivalent to the peak intensity of the laser at the center of the illuminated spot.

Figure 2 shows the simulated excess carrier profile at the center of the illuminated spot through the thickness of the investigated wafer at RT. The difference between the front and back surfaces is less than 15%, indicating an almost uniform carrier distribution. Outside this central point, the minority carrier lifetime, and therefore the diffusion length, will be even larger, due to the lower local injection level, thus the carrier profile will be more uniform than the center. Therefore the conditions for which Eq. (2) is valid are fulfilled. At other temperatures, we assume that no significant non-uniformities arise in the carrier profile, which we find justified by the very good agreement with the data of MacFarlane *et al.*, as shown below.

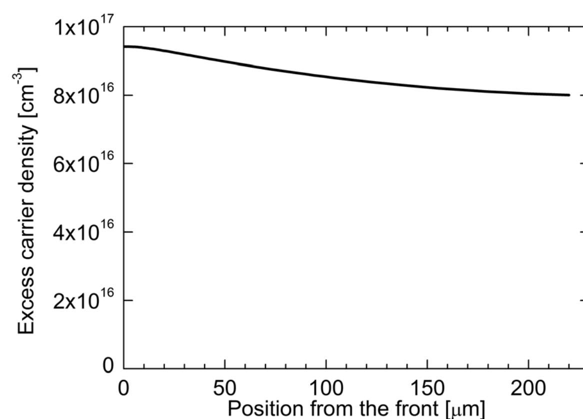

FIG. 2. Simulated excess carrier profile at the center of the illuminated spot at RT.

IV. RESULTS

A. Temperatures in the experiment of MacFarlane *et al.*

With the temperature controlled precisely (varied less than 0.5 K) by a liquid-nitrogen-cooled cryostat, PL spectra were captured at the same temperatures covered in the experiment of MacFarlane *et al.*[1] This was done in order to verify the accuracy of our data across a range of temperatures, and also to extend the data of MacFarlane *et al.* to longer wavelengths.

The resulting normalized PL spectra are shown in Figure 3. The spectra clearly show two fundamental characteristics of silicon luminescence. The first is the band-gap

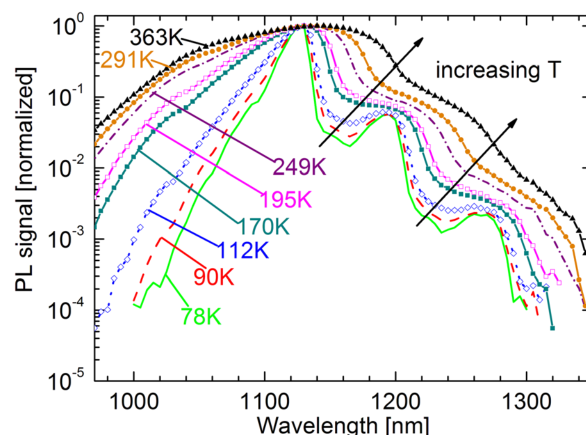

FIG. 3. PL spectra captured at temperatures covered in the experiment of MacFarlane *et al.*

[This article is copyrighted as indicated in the article. Reuse of AIP content is subject to the terms at: http://scitation.aip.org/termsconditions. Downloaded to] IP: 150.203.210.78 On: Tue, 03 Nov 2015 08:10:49

widening effect at low temperature.[24] The band-band peak at the highest point of the spectrum is shifted toward shorter wavelength side, i.e., higher energy, when the temperature decreases from 363 down to 78 K. The second feature is the evolution of the phonon edges with temperature. In figure, three shoulders in each spectrum can be observed for each temperature, and these become more distinguishable at lower temperatures. These three shoulders, starting from left to right, correspond to photon emission mediated by the concomitant emission of one-, two-, and three-phonons, respectively. Since the density of phonons is reduced and their energy distribution is narrowed at low temperatures,[25] the shoulders become sharper and more distinct as the temperature is reduced. Due to the widening of the band-gap, these shoulders also move to higher energies at lower temperatures. A shoulder corresponding to photon emission mediated by single-phonon absorption can also be observed at wavelengths around 1050 nm at high temperatures.

These spectra, along with digitized values of the absorption coefficient from MacFarlane *et al.*[1] at 1065 nm for 78 and 90 K and at 1110 nm for other temperatures, were used to extract the absorption coefficient values for wavelengths from 990–1300 nm. The first wavelength at 1065 nm was chosen to avoid the very sharp transition of the band-band peak at low temperatures, while the second wavelength at 1110 nm was selected to avoid the phonon edges where the temperature uncertainty had a larger impact at higher temperatures. Also note that Ref. 1 represented the data in terms of the square root of the product of the energy and the absorption coefficient versus the energy (see Figure 1 in Ref. 1). In this work, we have converted these values into the absorption coefficient.

Figure 4 plots our data and the data of Ref. 1. The data sets agree very well, except for a small variation at high wavelengths around 1150 nm. At these wavelengths, the values of the absorption coefficient are on the order of $1\times10^{-3}\,\mathrm{cm}^{-1}$, which is difficult to measure precisely by the conventional transmission and reflection approach. Meanwhile, the band-band peak of the PL spectrum is located around 1150 nm, where the signal-to-noise ratio in our PL measurements is larger than 10^3, as depicted in Figure 5, giving a small measurement uncertainty. In addition, given the linear axis used in the plot of MacFarlane *et al.*,[1] there is an increasing amount of digitization error when extracting data at these low values of the absorption coefficient. Finally, the very good agreement evidently validates our assumption of homogeneous carrier profiles at the various temperatures studied.

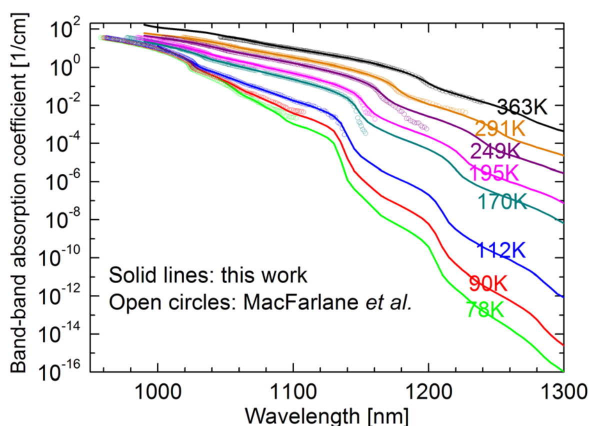

FIG. 4. Absorption coefficient in crystalline silicon obtained from PL at different temperatures 78, 90, 112, 170, 195, 249, 291, and 363 K in this work (solid lines) in comparison with MacFarlane *et al*. (open circles).

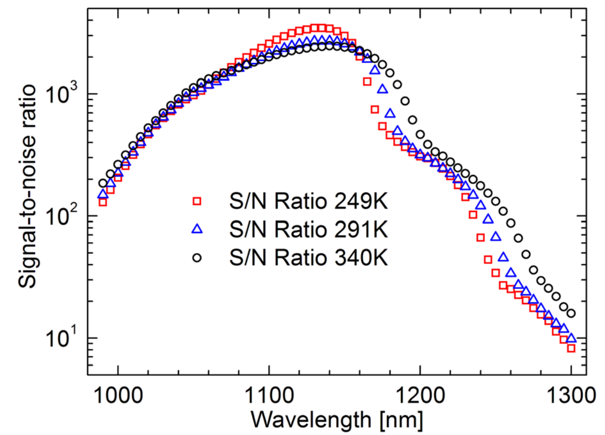

FIG. 5. Signal-to-noise ratio of PL spectra around RT. The data were obtained by subtracting the average background noise from the PL signal, then dividing the results by two standard deviations of the background noise.

B. Temperatures around RT

With the very good agreement with the data of MacFarlane *et al*., we extended our measurements to different temperatures which were not covered in their experiment. The PL spectra are plotted in Figure 6. These temperatures, from 270 to 350 K, cover a more practical operation range for silicon based devices.

In Figure 7, we have plotted values of the absorption coefficient extracted from Ref. 1 at 1110 nm (1.117 eV) versus temperature, and then fitted these points with a 6th order polynomial. From this function, we interpolated values at other temperatures near RT. These values, along with the spectra in Figure 6, were used to calculate the absorption coefficient data at temperatures between 270 and 350 K at 10 K intervals, which are presented in Figure 8. These data may be useful for modeling the operation of working devices such as solar cells. The data at 297 K are also presented here

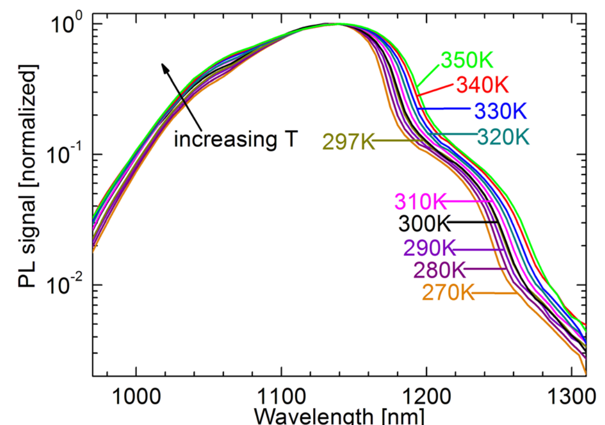

FIG. 6. PL spectra at temperatures near RT, from 270–350 K.

[This article is copyrighted as indicated in the article. Reuse of AIP content is subject to the terms at: http://scitation.aip.org/termsconditions. Downloaded to] IP: 150.203.210.78 On: Tue, 03 Nov 2015 08:10:49

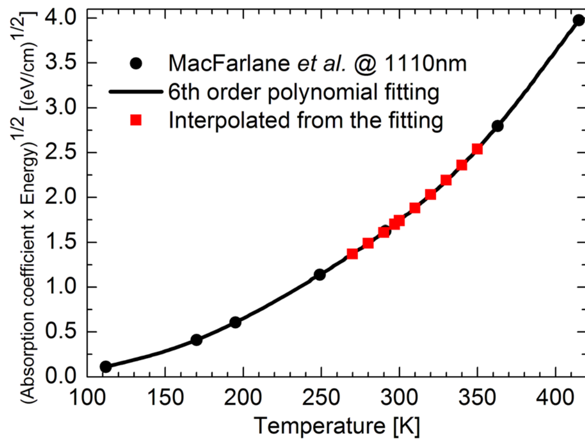

FIG. 7. 6th order polynomial fitting (solid line) for the data of MacFarlane *et al.* (black circles) of the absorption coefficient at wavelength 1110 nm, or energy 1.117 eV. From this fitting, values at temperatures between 270 and 350 K were interpolated (red squares).

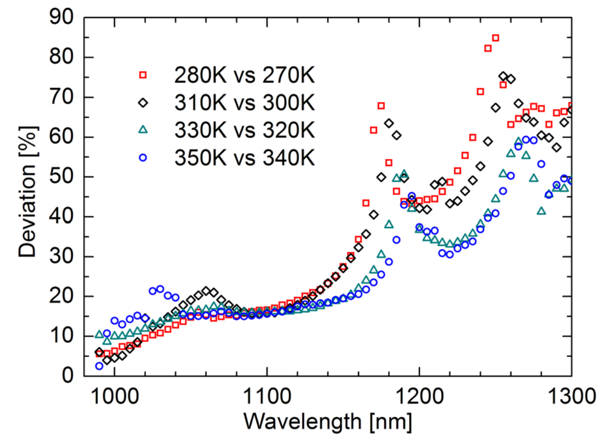

FIG. 9. Relative increment of the absorption coefficient for every 10 K increment around RT.

since this temperature is often considered to be room temperature.

Further, we have calculated the relative change of the absorption coefficient for several 10 K increments around RT. The results, plotted in Figure 9, show that the variation is mostly less than 20% for wavelengths between 990 and 1150 nm, but increases up to 50% and above for wavelengths between 1200 and 1300 nm. Therefore, we conclude that relatively small changes in temperature can significantly impact the band-band absorption coefficient in crystalline silicon.

C. Parameterization of the temperature dependence

With the dense intervals of temperatures and wavelengths in our experiments, we can establish an accurate temperature-dependent parameterization of the absorption coefficient. For each wavelength, we used the values from six different temperatures 170, 195, 249, 291, 310, and 363 K to build a 5th order polynomial fitting function, which had the form of $\sum_{i=0}^{5} a_i T^i$. The coefficients a_i of this polynomial are called the temperature coefficients in this work, from which the data at other temperatures can be interpolated. Figure 10 shows our reconstructed data using these coefficients from this fitting method compared with experimental data at some intermediate temperatures. The data sets are in excellent agreement. With these temperature-dependent parameters, one can interpolate the values of the absorption coefficient at any given temperature between 170 and 363 K for wavelengths from 990–1300 nm.

The advantage of our method is that it is based on interpolation of relatively dense data. By comparison, Green[4] obtained the temperature coefficients for wavelengths above 840 nm by extrapolating data from Ref. 26, in which the experiments were performed for wavelengths below 840 nm. Also note that this extrapolation misses the details of the temperature dependence of changes in band-gap energy, the shift of phonon edges, and the broadening of phonon distributions when the temperature increases. Our experiments allow the changes in those features with temperature to be revealed clearly in the spectra, and are accurately described by the interpolation method.

D. Comparison with independently measured spectra

As an additional verification of the accuracy of our absorption coefficient data, we reproduce the full PL spectrum fitting demonstrated in Mitchell *et al.*[9] on a 5 in. thick monocrystalline Cz-grown silicon brick (see Ref. 9 for the

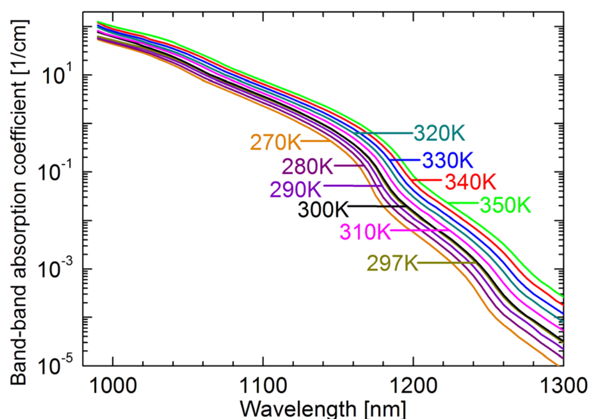

FIG. 8. Absorption coefficient of silicon obtained from PL at temperatures between 270 and 350 K. The data at 297 K and 300 K are almost overlapping.

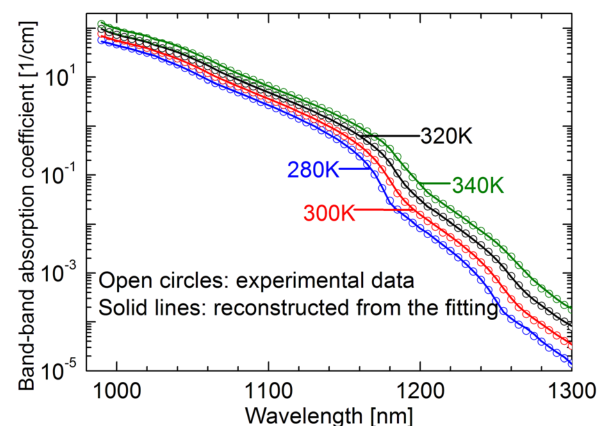

FIG. 10. Comparison of the absorption coefficient from this work between the experimental data and the reconstructed data using the 5th order polynomial fitting.

[This article is copyrighted as indicated in the article. Reuse of AIP content is subject to the terms at: http://scitation.aip.org/termsconditions. Downloaded to] IP: 150.203.210.78 On: Tue, 03 Nov 2015 08:10:49

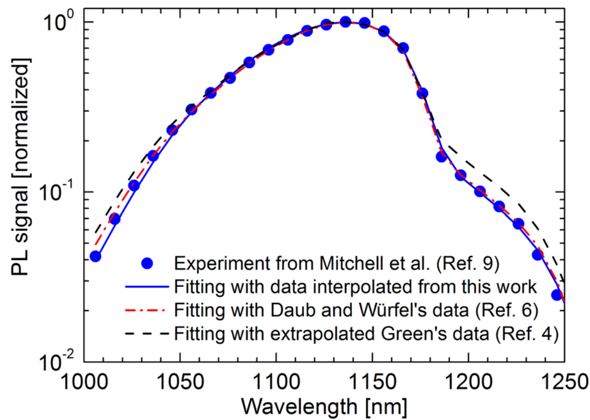

FIG. 11. Experimental PL spectrum of silicon brick from Mitchell *et al.* with theoretical fit using our interpolated absorption coefficient at 295 K as the input parameter. Fits using the data of Daub and Würfel, and Green are also shown here for comparison.

full fitting procedure). The absorption coefficient is a key input parameter in the fitting of the theoretical spectrum, as proposed by Green.[27] Mitchell *et al.* used the absorption coefficient data published by Daub and Würfel[6] and Green[4] to fit the brick measurement (see Figure 9 in Ref. 9). Here, we reproduce this graph, but also include the fit using our absorption data at 295 K as the input for Green's formula. We employed the interpolation procedure described above to obtain values at 295 K.

The spectral PL measurement carried out by Mitchell *et al.* varies from the one used in this study, for example, in the laser wavelength and power, the size of the illuminated spot, and the type of monochromator. Importantly, the sample used by Mitchell *et al.* is an unpassivated silicon brick rather than a thin and passivated silicon wafer as in our study. Despite these differences in the experimental approach, our data give excellent agreement with the measured spectrum in Mitchell *et al.*, as shown in Figure 11.

We note that in Figure 11, the fit using Green's data is 30% higher than the experimental spectrum at wavelengths around 1200 nm, while the two fits using Daub and Würfel's, and our data are almost identical to the experiment. This variation will be clarified in the Sec. IV E.

E. Comparison of RT absorption coefficient data

We compare and elucidate the inconsistencies of the absorption data at 295 K among some commonly used works. Daub and Würfel's,[6] Green's,[4] and our data are shown in Figure 12 and their relative variations in Figure 13. At 295 K Green's data were exponentially extrapolated using the temperature coefficients from Ref. 4.

In Figure 13, our data are consistently around 15% lower than Daub and Würfel's. This difference could stem from the scaling method to get the absolute absorptivity. Daub and Würfel[6] assumed that the absorptivity was saturated on the high energy side of the spectrum, i.e., $\alpha_{BB}d \gg 1$, and used the absolute value $A = 1\text{–}R$, where R is the surface reflectivity, to obtain the scaling factor. However, this is not entirely accurate, since $\alpha_{BB}d \gg 1$, with the authors' sample thickness of 262 μm, would require $\alpha_{BB} \gg 40$ cm^{-1}. However, even at the wavelength of 950 nm, α_{BB} is just 150 cm^{-1} at 295 K (extrapolated from Ref. 4), and does not fully satisfy the saturation condition. Second, the excess carrier density can be slightly reduced at the surface due to imperfect surface passivation. Since on the high energy side, more photons are emitted by a volume near the surface than from deeper inside the sample,[28] this suppressed carrier concentration near the surface may reduce the relative strength of the high energy part of the PL spectrum. Thus, scaling the high energy side to *1–R* may shift up the entire data set. By comparison, in the experiments of MacFarlane *et al.*,[1] for wavelengths close to the band-gap, such as 1110 nm (1.117 eV) as we have chosen to scale our data, one just needs to measure the reflectance and transmittance, and the sample thickness, to extract the absorption coefficient accurately. The errors in these measurements were estimated to be about 1%,[1,29] thus too small to significantly affect the absorption coefficient. Therefore, we can minimize these possible systematic errors. However, it should also be noted that the experimental uncertainties in both Daub and Würfel's, and our data could also contribute to the differences in Fig 13, in particular at longer wavelengths, where the signal-to-noise ratio for our data decreases to around 10 at 1300 nm, as shown in Figure 5. In a similar way, Daub and

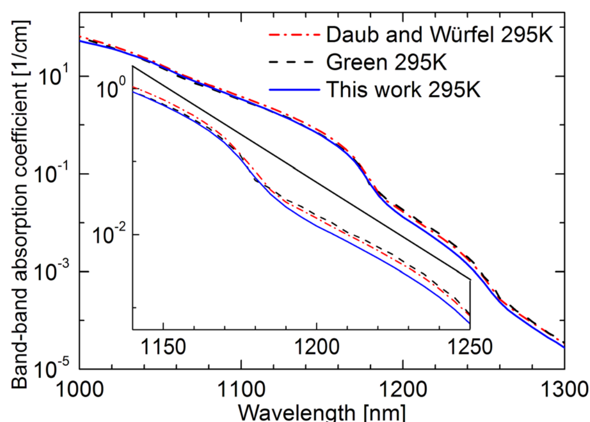

FIG. 12. Absorption data at 295 K. The insert is a zoomed-in section of wavelengths from 1140–1250 nm.

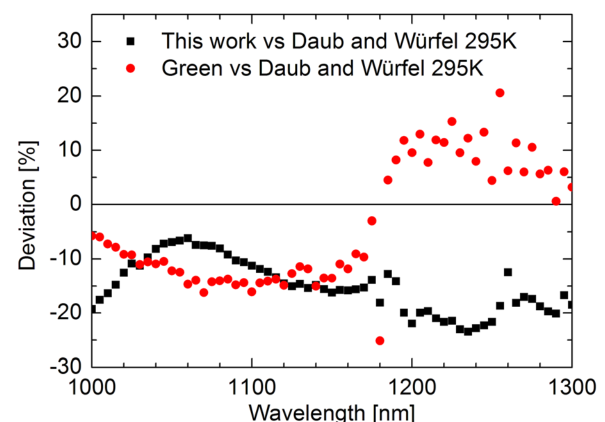

FIG. 13. Quantitative comparison of the absorption data among this work, Green, and Daub and Würfel at 295 K.

[This article is copyrighted as indicated in the article. Reuse of AIP content is subject to the terms at: http://scitation.aip.org/termsconditions. Downloaded to] IP: 150.203.210.78 On: Tue, 03 Nov 2015 08:10:49

Würfel's data must also have been subject to a decreasing signal-to-noise ratio at longer wavelengths.

In addition, Figure 13 also shows that Green's data are 15% lower than Daub and Würfel's for wavelengths below approximately 1170 nm, but increase to 10% higher than Daub and Würfel's for longer wavelengths. Since Schinke *et al.*[8] and Mitchell *et al.*[9] normalized their spectra to the band-band peak around 1150 nm, they saw up to 30% deviation using Green's data at wavelengths around 1200 nm.

Finally, Figure 14 compares the absorption data from this work, Daub and Würfel,[6] and Green[4] with MacFarlane *et al.*[1] at 295 K. The data of MacFarlane *et al.* were interpolated by a 4th order polynomial derived from data at temperatures 195, 249, 291, 363, 415 K from Ref. 1. The wavelength range is limited from 1070–1150 nm where the data used to create the polynomial fitting are available. Green's and this work's values vary less than 6% from MacFarlane *et al.*, as expected since they were scaled to the data of MacFarlane *et al.* Daub and Würfel's data set shows consistently 15% higher values possibly due to the different scaling method used in that work and the uncertainties in the measurements, as described above.

F. Extended wavelengths at 297 K

We have also extended the measurement at 297 K up to the wavelength of 1500 nm. In this experiment, we did not use the cryostat to control the temperature, since the cryostat reduced the PL signal significantly, due to absorption and reflection from the cryostat windows, leaving the signal too noisy to be captured at longer wavelengths. With the cryostat removed, we measured the spectrum in two parts: the first with wavelengths from 950–1310 nm and the second from 1255–1500 nm. Since the residual PL signal of the second half is more than an order of magnitude lower, this section was captured with the maximum gain of the lock-in amplifier, and with an increased integration time of 200 s for each wavelength. The relative spectrum was then scaled down to match the first half, and the two spectra stitched together, while other experimental conditions were kept unchanged. This scaling factor (SF) was swept through a variety of values, for each of which the weighted sum of square error (SSE) was computed for the overlapping part of the two halves by Eq. (4), and then the value giving the least SSE was chosen

$$SSE = \sum_{overlapped} \left(\frac{1st - 2nd \times SF}{1st} \right)^2. \quad (4)$$

With this stitching technique, we were able to extend the data to wavelengths up to 1500 nm. However, we observed a small peak at wavelengths between 1415–1420 nm, denoted by a dotted circle in Figure 15, in all of our measurements for numerous different samples. This unexpected peak was not caused by the laser's second harmonic since its wavelength was 785 nm. Thus, we hypothesize that this peak was a very weak, unidentified optical artifact of our system. Also note that the signal-to-noise ratio was in general improved in these measurements, due to the increased PL signal with the cryostat removed. At 1300 nm, the signal-to-noise ratio was estimated to be 40 compared to around 10 for the cryostat data. However, at 1500 nm, the signal-to-noise ratio decreased further, approaching values around 1, and therefore reaching the sensitivity limit of our experimental setup.

Using the same method as in Secs. IV A and IV B, this spectrum, along with the value of the absorption coefficient at wavelength 1110 nm from MacFarlane *et al.*,[1] was used to scale and compute our data at 297 K. Our data with and without using the cryostat, along with data from Green at 297 K (extrapolated from Ref. 4), and Daub and Würfel[6] at 295 K, are shown in Figure 16 for a qualitative comparison. In the figure, the two data sets with and without using the cryostat are almost identical. This again confirms that the cryostat did not cause any systematic errors in our previous experiments. However, it should also be noted that the data at wavelengths above 1300 nm may be more impacted by free carrier absorption than in the narrower wavelength range presented above.

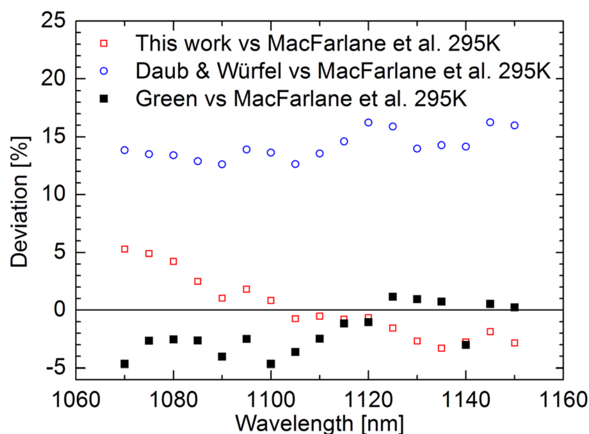

FIG. 14. Quantitative comparison of the absorption data from this work, Daub and Würfel, and Green with MacFarlane *et al.* at 295 K for wavelengths from 1070–1150 nm.

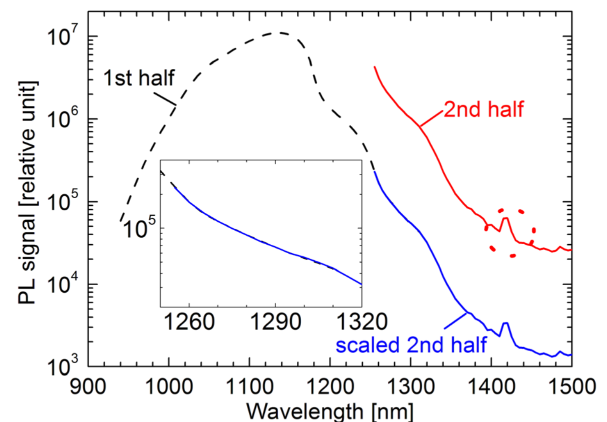

FIG. 15. PL spectrum captured by the stitching method at 297 K without using the cryostat. The second half (red solid) was captured with maximum gain of the lock-in amplifier, which was scaled down (blue solid) to match the first half (black dash). The insert is a zoomed-in section of the overlapping region.

[This article is copyrighted as indicated in the article. Reuse of AIP content is subject to the terms at: http://scitation.aip.org/termsconditions. Downloaded to] IP: 150.203.210.78 On: Tue, 03 Nov 2015 08:10:49

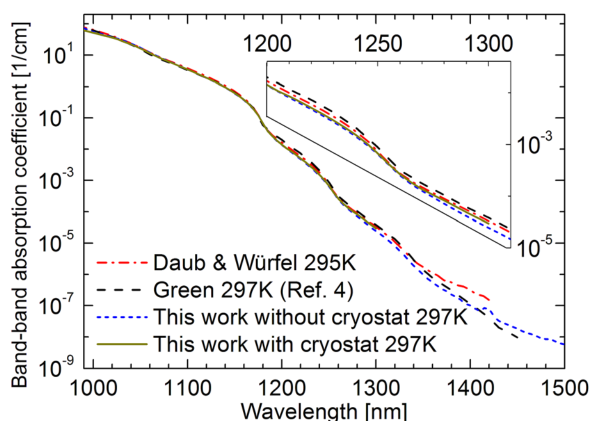

FIG. 16. Comparison of the absorption data at 297 K. Our data with and without cryostat are almost identical. The insert is a zoomed-in section for wavelengths from 1200–1310 nm.

V. CONCLUSIONS

We have presented temperature-dependent data for the band-band absorption coefficient in crystalline silicon, across a wavelength range from 990–1300 nm from spectral photoluminescence measurements, and established a parameterization of the data to allow interpolation of accurate values of the band-band absorption for any temperature between 170 and 363 K. Our data show very good agreement with the data of MacFarlane *et al*. In addition, we have demonstrated the significant impact of temperature on the band-band absorption coefficient near room temperature. Furthermore, we have discussed the possible origins of mismatches among the data sets of MacFarlane *et al*., Green, and Daub and Würfel. Finally, we have extended data up to the wavelength of 1500 nm at 297 K. All data for the absorption coefficient, the temperature-dependence parameters for each wavelength, and the normalized PL spectra are tabulated in the electronic attachment to this paper.[30]

ACKNOWLEDGMENTS

This work has been supported by the Australian Research Council (ARC) and the Australian Renewable Energy Agency (ARENA). The authors thank Di Yan for providing the silicon wafer, Teck Chong for assisting with the reflectivity measurements, Dr. Erich Daub for supplying his absorption coefficient data set, and Dr. Thorsten Trupke for very helpful discussions.

[1]G. G. MacFarlane, T. P. MacLean, J. E. Quarrington, and V. Roberts, Phys. Rev. **111**, 1245 (1958).
[2]H. A. Weakliem and D. Redfield, J. Appl. Phys. **50**, 1491 (1979).
[3]M. A. Green and M. J. Keevers, Prog. Photovoltaics **3**, 189 (1995).
[4]M. A. Green, Sol. Energy Mater. Sol. Cells **92**, 1305 (2008).
[5]M. J. Keevers and M. A. Green, Appl. Phys. Lett. **66**, 174 (1995).
[6]E. Daub and P. Würfel, Phys. Rev. Lett. **74**, 1020 (1995).
[7]T. Trupke, M. A. Green, P. Würfel, P. P. Altermatt, A. Wang, J. Zhao, and R. Corkish, J. Appl. Phys. **94**, 4930 (2003).
[8]C. Schinke, D. Hinken, J. Schmidt, K. Bothe, and R. Brendel, IEEE J. Photovoltaics **3**, 1038 (2013).
[9]B. Mitchell, M. K. Juhl, M. A. Green, and T. Trupke, IEEE J. Photovoltaics. **3**, 962 (2013).
[10]T. Trupke, E. Daub, and P. Würfel, Sol. Energy Mater. Sol. Cells **53**, 103 (1998).
[11]P. Würfel, J. Phys. C **15**, 3967 (1982).
[12]P. Würfel, S. Finkbeiner, and E. Daub, Appl. Phys. A: Mater. Sci. Process. **60**, 67 (1995).
[13]P. Würfel, T. Trupke, T. Puzzer, E. Schäffer, W. Warta, and S. W. Glunz, J. Appl. Phys. **101**, 123110 (2007).
[14]H. W. Icenogle, B. C. Platt, and W. L. Wolfe, Appl. Opt. **15**, 2348 (1976).
[15]K. R. McIntosh and S. C. Baker-Finch, in *Proceedings of the 38th IEEE Photovoltaic Specialists Conference* (2012), p. 265.
[16]S. C. Baker-Finch and K. R. McIntosh, in *Proceedings of the 35th IEEE Photovoltaic Specialists Conference* (2010), p. 2184.
[17]A. Cuevas and D. Macdonald, Sol. Energy **76**, 255 (2004).
[18]D. E. Kane and R. M. Swanson, in *Proceedings of the 18th IEEE Photovoltaic Specialists Conference* (1985), p. 578.
[19]A. Cuevas and R. Sinton, in *Proceedings of the 23rd European Photovoltaic Solar Energy Conference* (2008), p. 315.
[20]A. Cuevas, Energy Procedia **8**, 94 (2011).
[21]D. B. M. Klaassen, Solid-State Electron. **35**, 953 (1992).
[22]D. B. M. Klaassen, Solid-State Electron. **35**, 961 (1992).
[23]M. J. Kerr and A. Cuevas, J. Appl. Phys. **91**, 2473 (2002).
[24]W. Bludau, A. Onton, and W. Heinke, J. Appl. Phys. **45**, 1846 (1974).
[25]H. M. Rosenberg, *The Solid State* (Oxford University Press, New York, 1988), p. 91.
[26]G. E. Jellison, Jr. and F. A. Modine, J. Appl. Phys. **76**, 3758 (1994).
[27]M. A. Green, Appl. Phys. Lett. **99**, 131112 (2011).
[28]T. Trupke, J. Appl. Phys. **100**, 063531 (2006).
[29]G. G. MacFarlane, T. P. MacLean, J. E. Quarrington, and V. Roberts, Phys. Rev. **108**, 1377 (1957).
[30]See supplemental material at http://dx.doi.org/10.1063/1.4862912 for the full tabulated data set.

[This article is copyrighted as indicated in the article. Reuse of AIP content is subject to the terms at: http://scitation.aip.org/termsconditions. Downloaded to] IP: 150.203.210.78 On: Tue, 03 Nov 2015 08:10:49

CHAPTER 3

Temperature Dependence of Radiative Recombination Coefficient

Electrons which are excited to the conduction band of silicon have limited lifetimes. If there is no path for them to move to an external circuit, they will eventually fall back into the valence band and recombine with free holes. This process can generate photons, phonons, or both. When photons are generated, the process is known as radiative recombination. Otherwise, it is referred to as non-radiative recombination.

In a non-radiative recombination process, if the excess energy of a free electron is transferred to another hole or electron, the secondary excited carrier will be eventually thermalized back to its corresponding band edge and release the transferred energy in the form of heat. The process does not require the participation of any defects or impurities, and hence is an intrinsic property of silicon. This process is known as Auger recombination. On the other hand, if the material contains defects and impurities, these defects and impurities may occupy

different energy levels inside the silicon band gap, which can act as trapping sites for free electrons and/or holes. Because the excess energy of free carriers can be distributed into the material lattice in small portions through the emission of individual phonons, this trapping-state-assisted recombination is more likely to happen than Auger recombination in silicon wafers and solar cells. This recombination process is called Shockley-Read-Hall recombination.

On the contrary, in a radiative recombination process, some parts or all of the excess energy are released in the form of photons. If the material contains defects and impurity centers inside the band gap, the free electrons can be first trapped at these centers and loose some fractions of their excess energy via phonon emissions. After that, they recombine with the free holes in the valence band and give rise to luminescence signals. This phenomenon is classified as deep-level luminescence, and it directly reflects the properties of defect and impurity centers in silicon. Chapters 5, 7, 9, and 10 will exploit some applications of this phenomenon.

In case the free electrons fall back directly to the valence band from the conduction band and release their excess energy in the form of photons, the emitted luminescence spectrum is called the band-to-band spectrum. The global parameter characterizing this type of recombination is the radiative recombination coefficient. Since the band-to-band absorption coefficient is closely related to the emitted spectrum, the radiative recombination coefficient is, in principle, also correlated with the band-to-band absorption coefficient. In fact, by applying the generalized Planck's law, the relationship between the two parameters can be determined. Moreover, the well-established temperature data of the band-to-band absorption coefficient in Chapter 2 allow one to calculate the radiative recombination coefficient at different temperatures accurately. This chapter is, therefore, aimed to exploit the relationship between the two parameters to establish a complete temperature dataset for this very important recombination coefficient in silicon photovoltaics.

Temperature dependence of the radiative recombination coefficient in crystalline silicon from spectral photoluminescence

Hieu T. Nguyen,[1,a)] Simeon C. Baker-Finch,[1,2] and Daniel Macdonald[1]
[1]*Research School of Engineering, College of Engineering and Computer Science, The Australian National University, Canberra, ACT 0200, Australia*
[2]*PV Lighthouse, Coledale, NSW 2515, Australia*

(Received 24 February 2014; accepted 10 March 2014; published online 19 March 2014)

The radiative recombination coefficient $B(T)$ in crystalline silicon is determined for the temperature range 90–363 K, and in particular from 270 to 350 K with an interval of 10 K, where only sparse data are available at present. The band-band absorption coefficient established recently by Nguyen *et al.* [J. Appl. Phys. **115**, 043710 (2014)] via photoluminescence spectrum measurements is employed to compute the values of $B(T)$ at various temperatures. The results agree very well with literature data from Trupke *et al.* [J. Appl. Phys. **94**, 4930 (2003).] We present a polynomial parameterization describing the temperature dependence of the product of $B(T)$ and the square of the intrinsic carrier density. We also find that $B(T)$ saturates at a near constant value at room temperature and above for silicon samples with relatively low free carrier densities. © *2014 AIP Publishing LLC*. [http://dx.doi.org/10.1063/1.4869295]

Efficiencies of light emitting devices based on crystalline silicon have been improved significantly. Such devices have been demonstrated to have external efficiencies exceeding 10% at low temperature and 6% at room temperature (RT) for photoluminescence (PL).[1] Thus, a comprehensive model accurately describing the temperature dependence of the radiative recombination coefficient $B(T)$ is essential for accurate modelling and simulation of such light emitting devices, and also for silicon solar cells. There have been numerous works in which values of $B(T)$ were determined at different temperatures both theoretically and empirically.[2–6] These authors determined $B(T)$ via two different methods. The first approach[2,6] is to measure the spontaneous radiative emission rate R and the carrier densities n and p, then apply the formula $R = B \times n \times p$ to extract B. The second approach[3–6] is to determine the band-band absorption coefficient and then apply the van Roosbroech and Shockley theory[7] or the generalized Planck law.[8,9] The most recent works carried out by Trupke *et al.*[5] and Altermatt *et al.*[6] have established the values of $B(T)$ at different temperatures and free carrier densities, respectively, using the second method. However, data in Trupke *et al.* and Altermatt *et al.* are limited to only a few temperatures due to the limited temperature resolution of the band-band absorption coefficient data.

Recently, the band-band absorption coefficient in crystalline silicon has been reassessed empirically, and its temperature dependence has been formulated by Nguyen *et al.*,[10] courtesy of spectral photoluminescence measurements. In this Letter, we again employ the second approach to determine the values of $B(T)$ across the temperature range of 90–363 K, and in particular around RT with an interval of 10 K, using the experimental values of the band-band absorption coefficient from Nguyen *et al.* We also establish a parameterization of the temperature dependence to allow accurate interpolation of data in the temperature range of 90–363 K, and find that the radiative recombination coefficient saturates at a near constant value at RT and above for silicon samples with low free carrier densities.

The radiative recombination coefficient in crystalline silicon at a given temperature is determined via the formula[5,6]

$$B(T) = \frac{1}{n_i^2} \times \frac{1}{\pi^2 \hbar^3 c_o^2} \int_0^\infty \left[n^2 \times (\hbar\omega)^2 \times \alpha_{BB}(\hbar\omega, T) \times \exp\left(\frac{-\hbar\omega}{kT}\right) \times d(\hbar\omega) \right], \quad (1)$$

where c_0 is the speed of light in vacuum, k is Botlzmann's constant, T is the absolute temperature of the sample, n is the refractive index of silicon, $\alpha_{BB}(\hbar\omega, T)$ is the band-band absorption coefficient whose values are a function of energy, and temperature, and n_i is the intrinsic carrier density. The values of n_i depend on the temperature and the free carrier density, and several works have been performed to determine accurate values of this parameter.[11–15] In this work, to avoid the dependence on the choice of model for the intrinsic carrier density, instead of placing the emphasis on determining values of the radiative recombination coefficient $B(T)$, we will consider the more general parameter $B(T) \times n_i^2$. Multiplying both sides of Eq. (1) with n_i^2 yields

$$B(T) \times n_i^2 = \frac{1}{\pi^2 \hbar^3 c_o^2} \int_0^\infty \left[n^2 \times (\hbar\omega)^2 \times \alpha_{BB}(\hbar\omega, T) \times \exp\left(\frac{-\hbar\omega}{kT}\right) \times d(\hbar\omega) \right]. \quad (2)$$

From Eq. (2), to calculate $B(T) \times n_i^2$, one needs to know the refractive index n and the absorption coefficient $\alpha_{BB}(\hbar\omega, T)$. The refractive index is also a function of energy and temperature, and is extracted from Green.[16] The

a)Author to whom correspondence should be addressed. Electronic mail: hieu.nguyen@anu.edu.au

This article is copyrighted as indicated in the article. Reuse of AIP content is subject to the terms at: http://scitation.aip.org/termsconditions. Downloaded to IP: 150.203.210.78 On: Tue, 03 Nov 2015 08:11:33

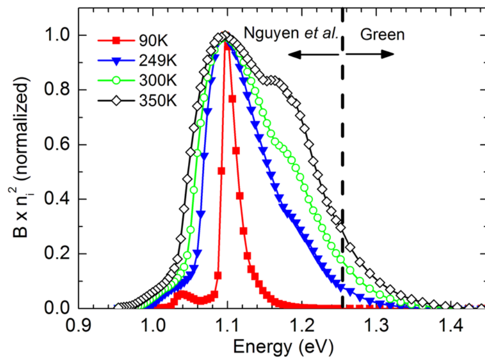

FIG. 1. Normalized $B(\hbar\omega,T) \times n_i^2$ versus energy at various temperatures. The data on the left of the vertical dashed line are calculated from the absorption coefficient in Nguyen *et al.*,[10] and the data on the right are calculated from values in Green.[16]

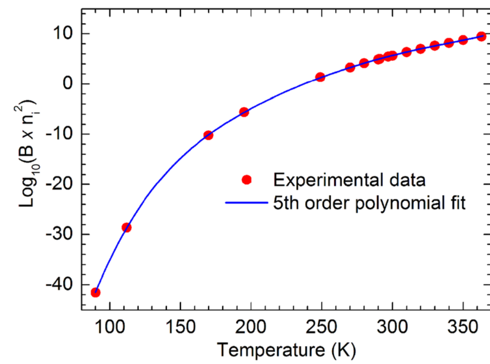

FIG. 2. $\text{Log}_{10}(B(T) \times n_i^2)$ versus temperature and the 5th order polynomial fit given by Eq. (3).

band-band absorption coefficient is obtained from our previous work.[10] The temperatures in Ref. 10 are dense around RT, and thus allow us to establish an accurate temperature parameterization for $B(T) \times n_i^2$.

Figure 1 shows the calculated values of $B(\hbar\omega, T) \times n_i^2$ versus energy at several intermediate temperatures, based on the energy-dependent absorption coefficient data of Nguyen *et al.*[10] The area under each curve is the total value of $B(T) \times n_i^2$ at a particular temperature. Note that the data in Figure 1 have been normalized to allow comparison. To calculate the absolute total value of $B(T) \times n_i^2$, we use the absolute data of $B(\hbar\omega,T) \times n_i^2$.

In the experiments in Nguyen *et al.*,[10] α_{BB} was determined for wavelengths from 990 to 1300 nm, i.e., for energies from 0.954 to 1.253 eV. Below 0.954 eV, $B(\hbar\omega,T) \times n_i^2$ contributes negligibly to the integration. Above 1.253 eV, $B(\hbar\omega,T) \times n_i^2$ still contributes a significant portion to the integration around RT, as seen in Figure 1, although at the lower temperature of 90 K it is again insignificant. To correct for this lack of high energy data from the PL spectra, we use the absorption coefficient values from Green[16] to calculate $B(\hbar\omega,T) \times n_i^2$ for energies above 1.253 eV. These values were determined from transmission and reflectance experiments, which in general are more accurate than the PL method at high energies.[5] The error in these data was estimated to be around 4% by Green.[16] Since this part of the spectrum contributes less than 8% to the area under each curve, the uncertainty due to using absorption data from two different methods is estimated to be only about 0.3%.

Figure 2 plots our data of $\text{Log}_{10}(B(T) \times n_i^2)$ across the temperature range 90–363 K, calculated as described above. We have fitted these points with a 5th order polynomial using the least squares regression method. The formula obtained is given by Eq. (3). Note that $B(T) \times n_i^2$ has the unit of $\text{cm}^{-3}\,\text{s}^{-1}$.

$$\text{Log}_{10}(B(T) \times n_i^2) = -1.7698 \times 10^2 + 2.68812 \times T - 1.8137 \times 10^{-2} \times T^2 + 6.56769 \times 10^{-5} \times T^3 - 1.21382 \times 10^{-7} \times T^4 + 8.99086 \times 10^{-11} \times T^5. \quad (3)$$

Since the values of $B(T) \times n_i^2$ do not depend on n_i and the experimental absorption data in Nguyen *et al.* are not affected by free carriers as long as their density is less than $2 \times 10^{17}\,\text{cm}^{-3}$ (Refs. 10 and 17), Eq. (3) can be used to extract data for $B(T) \times n_i^2$ at any temperature from 90 to 363 K for samples with free carrier densities below this value. Final values of $B(T)$ can be computed by choosing an appropriate model for the intrinsic carrier density, which can include the temperature and injection level dependence.

Next, to validate our data, we compare them with literature values from Trupke *et al.*[5] Since Trupke *et al.* calculated $B(T)$, we need to divide our data by n_i^2. To permit a direct comparison, we employ the same n_i model as used by those authors[5]

$$n_i(T) = 2.9135 \times 10^{15} \times T^{1.6} \times \exp\left(-\frac{E_g(T)}{2kT}\right), \quad (4)$$

with $E_g(T)$ the band-gap energy of silicon at a specific temperature in accordance with Ref. 18. Equation (4) describes the relationship between the intrinsic carrier density and the temperature, including the temperature dependence of the band-gap energy. However, this expression does not include the effect of band-gap narrowing due to free carriers.[19] Therefore, the values of $B(T)$ in Trupke *et al.*[5] reflect conditions of relatively low densities of free carriers, where the band-gap narrowing effect is insignificant. The values of n_i^2 start increasing, and therefore the values of $B(T)$ decrease, as demonstrated by Altermatt *et al.*,[6] when the free carrier densities approach approximately $10^{14}\,\text{cm}^{-3}$.

Our calculated values of $B(T)$ using the experimental data for the absorption coefficient in Nguyen *et al.*,[10] along with the values in Trupke *et al.*,[5] are plotted in Figure 3. While the data of Trupke *et al.* cover the region 90–300 K, this work extends the measurement of $B(T)$ to the higher temperature limit of 363 K, with very dense data points

This article is copyrighted as indicated in the article. Reuse of AIP content is subject to the terms at: http://scitation.aip.org/termsconditions. Downloaded to IP: 150.203.210.78 On: Tue, 03 Nov 2015 08:11:33

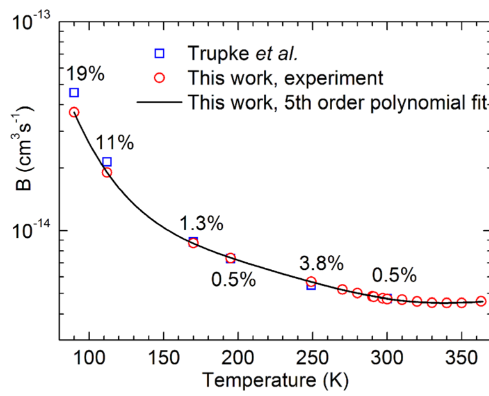

FIG. 3. Comparison of radiative recombination coefficient between this work and Trupke *et al.*[5] The inserted numbers are the relative deviation between the two works.

around room temperature. The two data sets match very well, except for the value at 90 K where the relative deviation is approximately 20%. The fact that the PL spectra are very sharp at low temperatures[10] contributes to the uncertainties in the measurements of Nguyen *et al*. This is caused by the impact of the limited wavelength resolution on the integration, which in turn affects the absorption data and the integration of $B(T) \times n_i^2$ (see curve 90 K in Figure 1 for example), and thus $B(T)$ in this study. In the same way, the data of Trupke *et al*. were likely subject to similar uncertainties in their low temperature PL measurements. This may be the reason for the 20% relative deviation at 90 K in Figure 3. We also note that the radiative recombination coefficient saturates at a near constant value at RT and above, a conclusion which could not be made on the basis of the relatively sparse data published previously.

Finally, with the same method used for $B(T) \times n_i^2$, we also establish a formula to compute $B(T)$ using the n_i model of Eq. (4) at any temperature from 90–363 K and low free carrier densities, as shown in Eq. (5). In fact, we fitted our data with different methods including the fifth order polynomial, the first and the second order exponential functions and found the best fit with this polynomial function. Note that $B(T)$ has the unit of $cm^3\ s^{-1}$, and the experimental data of both $B(T) \times n_i^2$ and $B(T)$ in this work are also given in Table I.

$$\begin{aligned}\mathrm{Log}_{10}B(T) = &-9.65614 - 8.05258 \times 10^{-2} \times T \\ &+ 6.02695 \times 10^{-4} \times T^2 - 2.29844 \times 10^{-6} \times T^3 \\ &+ 4.31934 \times 10^{-9} \times T^4 - 3.16154 \times 10^{-12} \times T^5.\end{aligned} \quad (5)$$

In summary, based on recent band-band absorption data, we have proposed and calculated a general parameter which incorporates both the radiative recombination coefficient and the intrinsic carrier density in crystalline silicon, and have established a polynomial parameterization to describe the temperature dependence for this quantity based on experimental data. This formula, along with a model for the intrinsic carrier density, can be used to extract accurate values of the radiative recombination coefficient from 90 to 363 K. Our data are shown to match very well with literature data from Trupke *et al*. Moreover, the radiative recombination coefficient is found to saturate at room temperature and above, for samples with relatively low free carrier densities.

TABLE I. Experimental values of $B(T) \times n_i^2$ and $B(T)$ in this work.

Temperature (K)	$B(T) \times n_i^2$ ($cm^{-3}\ s^{-1}$)	$B(T)$ ($cm^3\ s^{-1}$)
90	2.846×10^{-42}	3.697×10^{-14}
112	2.547×10^{-29}	1.902×10^{-14}
170	6.114×10^{-11}	8.722×10^{-15}
195	2.639×10^{-6}	7.384×10^{-15}
249	2.169×10^{1}	5.689×10^{-15}
270	1.991×10^{3}	5.220×10^{-15}
280	1.361×10^{4}	5.023×10^{-15}
290	8.203×10^{4}	4.847×10^{-15}
291	9.763×10^{4}	4.835×10^{-15}
297	2.703×10^{5}	4.750×10^{-15}
300	4.428×10^{5}	4.705×10^{-15}
310	2.205×10^{6}	4.680×10^{-15}
320	9.840×10^{6}	4.587×10^{-15}
330	4.053×10^{7}	4.526×10^{-15}
340	1.558×10^{8}	4.511×10^{-15}
350	5.592×10^{8}	4.513×10^{-15}
363	2.713×10^{9}	4.592×10^{-15}

This work has been supported by the Australian Research Council (ARC) and the Australian Renewable Energy Agency (ARENA).

[1]T. Trupke, J. Zhao, A. Wang, R. Corkish, and M. A. Green, Appl. Phys. Lett. **82**, 2996 (2003).
[2]H. Schlangenotto, H. Maeder, and W. Gerlach, Phys. Status Solidi A **21**, 357 (1974).
[3]W. Michaelis and M. H. Pilkuhn, Phys. Status Solidi **36**, 311 (1969).
[4]M. Ruff, M. Fick, R. Lindner, U. Rössler, and R. Helbig, J. Appl. Phys. **74**, 267 (1993).
[5]T. Trupke, M. A. Green, P. Würfel, P. P. Altermatt, A. Wang, J. Zhao, and R. Corkish, J. Appl. Phys. **94**, 4930 (2003).
[6]P. P. Altermatt, F. Geelhaar, T. Trupke, X. Dai, A. Neisser, and E. Daub, Appl. Phys. Lett. **88**, 261901 (2006).
[7]W. van Roosbroeck and W. Shockley, Phys. Rev. **94**, 1558 (1954).
[8]P. Würfel, J. Phys. C **15**, 3967 (1982).
[9]P. Würfel, S. Finkbeiner, and E. Daub, Appl. Phys. A: Mater. Sci. Process. **60**, 67 (1995).
[10]H. T. Nguyen, F. E. Rougieux, B. Mitchell, and D. Macdonald, J. Appl. Phys. **115**, 043710 (2014).
[11]M. A. Green, J. Appl. Phys. **67**, 2944 (1990).
[12]A. B. Sproul and M. A. Green, J. Appl. Phys. **70**, 846 (1991).
[13]A. B. Sproul and M. A. Green, J. Appl. Phys. **73**, 1214 (1993).
[14]K. Misiakos and D. Tsamakis, J. Appl. Phys. **74**, 3293 (1993).
[15]P. P. Altermatt, A. Schenk, F. Geelhaar, and G. Heiser, J. Appl. Phys. **93**, 1598 (2003).
[16]M. A. Green, Sol. Energy Mater. Sol. Cells **92**, 1305 (2008).
[17]T. Trupke, E. Daub, and P. Würfel, Sol. Energy Mater. Sol. Cells **53**, 103 (1998).
[18]W. Bludau, A. Onton, and W. Heinke, J. Appl. Phys. **45**, 1846 (1974).
[19]A. Schenk, J. Appl. Phys. **84**, 3684 (1998).

This article is copyrighted as indicated in the article. Reuse of AIP content is subject to the terms at: http://scitation.aip.org/termsconditions. Downloaded to IP: 150.203.210.78 On: Tue, 03 Nov 2015 08:11:33

CHAPTER 4

Impact of Carrier Profile and Rear Side Reflection on Photoluminescence Spectra

As discussed in Chapter 1, around room temperature, it is impossible to capture the direct spontaneous photoluminescence spectrum from a silicon wafer due to the reabsorption of the generated photons when they move towards the wafer surfaces. The final spectrum is affected by both the experimental conditions and the sample properties.

In silicon solar cell applications, the wafer surface morphology is often designed in such a way to assist the absorption of the incoming light. On the other hand, the density of defect states at the wafer surfaces is often high, causing a strong non-radiative recombination of minority carriers. In solar cell fabrication, the wafer surfaces are often coated with thin films to passivate these defect states, thus improving the minority carrier population at the surfaces. These films can also serve as antireflection coating layers to help minimize the reflection of the incoming light. All these processing steps can alter both the surface optics and the excess carrier profiles

of the wafers. Therefore, despite the same experimental conditions, different solar cell precursors at different processing steps will give different photoluminescence spectra, which reflect the variation in these properties.

In practice, changes in the optics and electronic properties of silicon solar cells often occur simultaneously. For example, random pyramid texturing is commonly used in silicon solar cell fabrication to reduce the incoming light reflection. However, the sharp vertices and the increased surface area are also known to be responsible for increased surface recombination on textured wafers. With the same principle, although light trapping structures at the rear of silicon wafers are expected to improve the photocurrent in the near-infrared region, the enhanced surface recombination due to the increased surface area is an undesirable effect. This combination, in turn, makes the interpretation of the detected photoluminescence spectra more difficult. In most cases, the effect of the optics on the spectra is assumed to be the dominating phenomenon compared to the changes in the carrier profile caused by the reduced surface passivation quality. However, it is important to evaluate these effects on the spectra separately to further understand the physical impacts of these phenomena on silicon wafers and solar cells.

The established dataset of the band-to-band absorption coefficient in Chapter 2 allows one to model the photoluminescence spectra from silicon wafers with different optics and carrier profiles at different temperatures accurately. Therefore, by examining these modeled spectra, one can study the separate effects of these phenomena on the spectra emitted from different silicon wafers and solar cell precursors as a function of temperature. However, this chapter is not aimed to discuss the applications of different light trapping structures. Rather it is dedicated to the applications of the band-to-band absorption coefficient in modeling the band-to-band luminescence spectra in order to understand the potential impacts of the optics and the carrier profiles on the spectra from a physical point of view. This work finds that, the impacts of the optics and carrier profiles on the spectral shape are more significant at higher temperatures due to the increasing values of the absorption coefficient. The results, along with the temperature dependence data of the absorption coefficient, are useful when being applied into a more general theoretical work by Green [1], where full analytical expressions to describe the spectral shape from both silicon bricks and wafers were developed for both planar and textured surfaces.

References

[1] M.A. Green, "Analytical expressions for spectral composition of band photoluminescence from silicon wafers and bricks," Appl. Phys. Lett., vol. 99, p. 131112, 2011.

Impact of Carrier Profile and Rear-Side Reflection on Photoluminescence Spectra in Planar Crystalline Silicon Wafers at Different Temperatures

Hieu T. Nguyen, Fiacre E. Rougieux, Simeon C. Baker-Finch, and Daniel Macdonald

***Abstract*—The increasing use of spectral photoluminescence as an advanced and accurate diagnostic tool motivates a comprehensive assessment of the effects of some important optical and electrical properties on the photoluminescence spectra from crystalline silicon wafers. In this paper, we present both modeling results and measurements to elucidate the effects of the internal reflectance at the planar wafer surfaces, as well as the carrier profile varying across the sample thickness due to an increased rear-surface recombination velocity, as a function of temperature. These results suggest that the accuracy of existing spectral PL techniques may be improved by using higher temperatures due to the increased effect of the carrier profile at higher temperatures. They also show that changes in the photoluminescence spectrum shape caused by the addition of a rear-side specular reflector offset those caused by changes in the carrier profile due to increased rear surface recombination, and therefore, considerable care needs to be taken when changing the rear-side optics. Finally, the possible impact of variations in the rear-side reflectance on the band–band absorption coefficient and radiative recombination coefficient, which have previously been determined using the spectral photoluminescence technique, is assessed and demonstrated to be insignificant in practice.**

***Index Terms*—Absorption, charge carrier density, photovoltaic cells, photoluminescence (PL), radiative recombination, silicon.**

I. Introduction

RECENTLY, there has been increasing interest in using spectral photoluminescence (PL) as the basis of accurate new characterization techniques for crystalline silicon photovoltaics. Würfel *et al.* [1] first developed an approach to extract the minority carrier diffusion length from PL spectra. Later works derived from this approach have been applied for both silicon wafers [2]–[4] and bricks [5]–[7] to separate the effects of bulk and surface recombination at room temperature. In addition, Schinke *et al.* [8] modeled PL spectra for different surface morphologies, and Barugkin *et al.* [9] employed spectral PL measurements to quantify the light trapping for various plasmonic structures. Besides these characterization techniques, spectral PL has also been employed to determine very precise values of fundamental parameters in silicon, such as the band–band absorption coefficient α_{BB} [10]–[12] and the radiative recombination coefficient *B* [11], [13], [14], at different temperatures. These two parameters, in turn, are very important inputs in modeling the PL spectra.

In order to ensure precision and accuracy, special care should be taken regarding the potential effects of the optical and electrical properties of a silicon sample when using spectral PL as a diagnostic tool. In particular, the internal reflectance and the shape of the excess carrier profile inside samples can play critical roles in many potential applications of spectral PL. In practice, the effects of changes in the optical properties and the carrier profiles often occur simultaneously, meaning their impacts are combined, and the resulting spectra may be misinterpreted.

In this paper, we will first examine the independent impacts of the internal reflection and the carrier profile on the PL spectrum shape, as a function of temperature, and via both modeling and measurement for planar wafers. We will demonstrate that the accuracy of spectrally resolved diagnostic PL methods [2]–[7] can potentially be enhanced at increased temperatures due to the more significant impact of the carrier profile at higher temperatures. After that, the combined effects of the reflection and the carrier profile will be demonstrated. Finally, we will reassess their potential impacts on the determination of α_{BB} and *B*, which have been reestablished recently using the spectral PL technique [12], [14].

II. Background

The spontaneous generation rate of photons per volume and energy interval due to band–band transitions in an excited nondegenerate semiconductor is described by the generalized Planck law [15], [16]:

$$dr_{sp} = C(\hbar\omega)^2 \alpha_{BB} \exp\left(\frac{-\hbar\omega}{kT}\right) \exp\left(\frac{\Delta\eta}{kT}\right) d(\hbar\omega) \quad (1)$$

with *C* a physical constant, *k* Boltzmann's constant, *T* the absolute temperature of the sample, and $\Delta\eta$ the difference between the quasi-Fermi levels of electrons and holes under illumination.

The total PL signal emitted outside a planar silicon sample, which is excited by monochromatic light, per energy interval is approximated by [17]:

$$PL = \left[\int_0^d \frac{dr_{sp}}{4n_{si}^2} \exp(-\alpha_{BB} x) dx\right] \times A \quad (2)$$

Manuscript received June 27, 2014; revised August 19, 2014; accepted September 18, 2014. Date of publication October 7, 2014; date of current version December 18, 2014. This work was supported by the Australian Government through the Australian Research Council and the Australian Renewable Energy Agency.

H. T. Nguyen, F. E. Rougieux, and D. Macdonald are with the Research School of Engineering, The Australian National University, Canberra, ACT 0200, Australia (e-mail: hieu.nguyen@anu.edu.au; fiacre.rougieux@anu.edu.au; daniel.macdonald@anu.edu.au).

S. C. Baker-Finch is with the Australian National University, Canberra, ACT 0200, Australia, and with PV Lighthouse, Coledale, NSW 2515, Australia (e-mail: simeon.bakerfinch@gmail.com).

Color versions of one or more of the figures in this paper are available online at http://ieeexplore.ieee.org.

Digital Object Identifier 10.1109/JPHOTOV.2014.2359737

2156-3381 © 2014 IEEE. Personal use is permitted, but republication/redistribution requires IEEE permission.
See http://www.ieee.org/publications_standards/publications/rights/index.html for more information.

where

$$A = \frac{[1 - R_f]\left[1 + R_b e^{-\alpha_{BB} d}\right]}{1 - R_f R_b e^{-2\alpha_{BB} d}} \tag{3}$$

and R_f and R_b are the internal reflectances at normal incident angle upon the front and back surfaces, since the spectra measured here are captured nearly perpendicularly to the sample surfaces, *d* is the sample thickness, and n_{si} is the silicon refractive index. We also have the relationship [18]

$$\exp\left(\frac{\Delta\eta}{kT}\right) = \frac{np}{n_i^2} \approx \frac{(N_{A/D} + \Delta n)\Delta n}{n_i^2} \tag{4}$$

where *n* and *p* are the electron and hole concentrations, $N_{A/D}$ is the background doping concentration, Δn is the excess carrier density, and n_i is the intrinsic carrier density.

Substituting (1) and (4) into (2), we have the following formula for the PL flux emitted outside the planar sample at a given energy:

$$PL = C(\hbar\omega)^2 \alpha_{BB} \exp\left(\frac{-\hbar\omega}{kT}\right) \times \left[\int_0^d \left[(N_{A/D} + \Delta n)\Delta n \exp(-\alpha_{BB} x)\right] dx\right] \times A \times d(\hbar\omega). \tag{5}$$

Again, *C* is a prefactor whose value is constant with photon energy.

An underlying assumption in (2), (3), and (5) is that the reabsorption of the generated photons is dominated by the band–band transitions. This assumption has been shown to be valid at room temperature when the free carrier density is less than $2 \times 10^{17}\ \mathrm{cm}^{-3}$ by Trupke *et al.* [19]. Here, we did not observe any change in the spectrum shape when we decreased the average laser intensity from 80 to 8 suns at 363 K. Thus, we conclude that the free carrier absorption does not affect the spectrum shape in the experiments reported here, in which an average intensity of 23 suns is used.

III. Experimental Details

The experimental setup to capture the PL spectra is largely the same as described in detail in [12]. In this paper, the laser employed has a wavelength of 532 nm, and on-sample average power of 160 mW. The laser spot diameter, corresponding to the width of a Gaussian intensity distribution at half maximum, is about 3 mm. The average intensity is around 23 suns. The sample temperature was controlled with a Janis VNF-100 liquid nitrogen cryostat in which the sample and sample stage were immersed in temperature-controlled nitrogen vapor. The local sample temperature under illumination was found to increase less than 0.5 K using a thermocouple attached behind the illuminated spot for 30 min.

The investigated silicon sample is a high-quality phosphorous-doped n-type float zone wafer with a resistivity of $6\ \Omega \cdot \mathrm{cm}$, corresponding to a background doping of around $8 \times 10^{14}\ \mathrm{cm}^{-3}$. Both sides were chemically polished to achieve planar surfaces, and the final thickness was 280 μm. This sample was then divided into two different samples, each of which was processed in a different way to create a different carrier profile.

The first sample was processed to achieve a homogeneous carrier profile through the entire thickness. Both surfaces of this sample were passivated with a 10-nm layer of Al_2O_3 deposited by plasma-assisted atomic layer deposition. It was then annealed at 450 °C in forming a gas consisting of argon and hydrogen for 30 min to activate the surface passivation. The effective lifetime of minority carriers was found to be around 3.3 ms at an injection level of $8 \times 10^{14}\ \mathrm{cm}^{-3}$, using the quasi-steady-state photoconductance technique [20]. The second sample was processed to achieve an inhomogeneous carrier profile, which reduces toward the rear surface. This sample went through the same passivation process as the first sample, and then its passivation layer on the rear was removed by fuming this surface with hydrofluoric acid for 3 min. The effective lifetime in this case was about 6 μs at the same injection level. The carrier profile of the first sample was considered to be uniform throughout the thickness, whereas that of the second one was estimated with the formula $\Delta n(x) = \Delta n(0) \times (1 - x/d)$, in which *x* is the distance from the front surface.

The very thin layer (10 nm) of Al_2O_3 was used for both samples in order to maintain the same optical conditions at the front and rear surfaces, since this film is thin enough to have no impact on reflection or absorption in the wavelength range of interest. Using a thicker passivation layer, or depositing a metal film on the rear to achieve a high surface recombination velocity (SRV), would create a significant difference in the optical properties between the front and rear surfaces of the second sample. This difference may have a significant impact on the spectra via rear-side internal reflection, and can mask the impact of the different carrier profiles, as shown below. The impact of the rear reflection itself and its masking effect on the carrier profile will be demonstrated in detail in Sections IV and VI, respectively.

IV. Impact of Internal Reflection on Photoluminescence Spectrum Shape

First, we examine the impact of the internal reflection on the PL spectrum shape at different temperatures. To avoid being confounded with the effect of the carrier profile, we used the first sample whose carrier profiles are symmetrical at all temperatures. We modeled the spectra from this sample for two cases. The optically symmetric case has two sides passivated with 10-nm layers of Al_2O_3; hence, the reflectances on both sides are the same. The optically asymmetric case also has two sides passivated with Al_2O_3, but a specular reflector was attached on the rear side, creating a near unity reflection on this surface. The internal reflectance of the silicon/Al_2O_3/air interface was modeled using the optical simulator OPAL developed by McIntosh and Baker-Finch [21], [22], and was approximately 30% for the wavelengths of interest. The specular reflector was a planar silicon wafer deposited with a 100-nm layer of silver. Its reflectance spectrum was both modeled and measured and was found to be around 95% for the wavelengths of interest. Here, we did not deposit silver directly on the Al_2O_3 layer to make

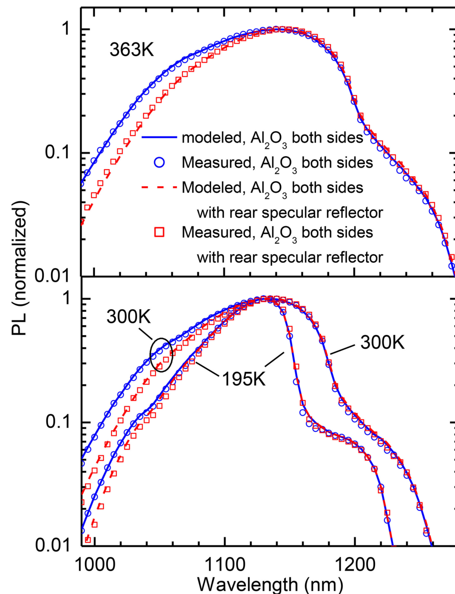

Fig. 1. Comparison of modeled (lines) and measured (symbols) normalized PL spectra between the optically symmetric (blue lines and blue circles) and optically asymmetric (red-dashed lines and red squares) cases at various temperatures. Both cases have two sides passivated with 10-nm layers of Al_2O_3, but the latter has the rear specular reflector to achieve almost unity rear reflectance. The enhanced rear reflectance increases the signal at longer wavelengths but barely affects the signal at 990 nm. This corresponds to a lowering of the normalized spectra on the shorter wavelength side.

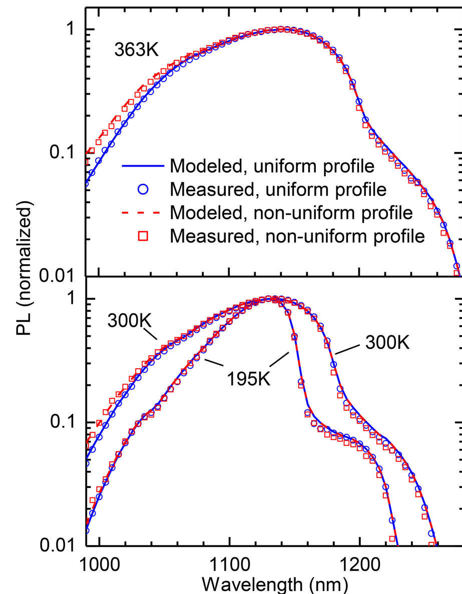

Fig. 2. Comparison of modeled (lines) and measured (symbols) normalized PL spectra between the uniform (blue lines and blue circles) and nonuniform (red-dashed lines and red squares) carrier profile cases at various temperatures.

sure that the quality of this surface passivation layer was not affected. These reflectances, the carrier profile, and the values of α_{BB} in [12] were substituted into (5) to model the spectra.

Fig. 1 compares the modeled normalized spectra between the first and second cases at various temperatures. The enhanced rear reflectance increases the intensity of the longer wavelength sides, but barely affects the signal at 990 nm. This corresponds to lowering the low wavelength sides when the spectra are normalized. In addition, this deviation between the two cases is more pronounced at higher temperatures. The reason is that α_{BB} increases at higher temperatures, and hence, the generated photons have less chance to be reflected back by the rear reflector. The experimental data were also captured and are given in Fig. 1 to validate these findings, and they agree very well with the modeling. Therefore, we conclude that the internal reflection has a significantly larger impact on the PL spectrum shapes at higher temperatures.

V. Impact of Carrier Profile on Photoluminescence Spectrum Shape

Next, we investigate the impact of the carrier profile on the PL spectrum shape at different temperatures. Fig. 2 compares the modeled and measured normalized spectra at various temperatures between the uniform (the first sample with both surfaces well passivated) and nonuniform (the second sample whose front surface was well passivated and rear surface was a bare silicon/air interface) carrier profile cases. The low-wavelength sides of the normalized spectra in the latter case are higher than those in the former case. Moreover, this deviation is more obvious at shorter wavelengths and higher temperatures. Once again, this is because α_{BB} is larger at shorter wavelengths and, hence, the generated photons are more strongly reabsorbed in transit toward the front surface. Therefore, the more carriers near the front surface (relatively speaking), the more chance to escape from the sample these high-energy photons have. As a result, the impact of the carrier profile on the emitted photons is more significant at shorter wavelengths. On the other hand, α_{BB} is small at longer wavelengths, and the generated photons are not reabsorbed when moving toward the front surface. Thus, the carrier profile plays a little role on the shapes of the spectra at longer wavelengths. In terms of the temperature dependence, once again, α_{BB} increases with temperature, and thus, the variation becomes larger and shifts to longer wavelengths at higher temperatures. The very good match between the modeling and the experimental data verifies these findings. We, therefore, conclude that the carrier profile has an increasing impact on the spectrum shapes at higher temperatures. This may provide a basis for new or improved techniques for separating bulk and surface effects in wafers and solar cell precursors [2]–[7].

VI. Combined Impact of Internal Reflection and Carrier Profile on Photoluminescence Spectrum Shape

In Sections IV and V, the internal reflection and the carrier profile have shown opposing impacts on the PL spectrum shape at different temperatures. The enhanced rear reflectance shifts down the low-wavelength side of the normalized spectra, while the inhomogeneous carrier profile shifts this side up. However,

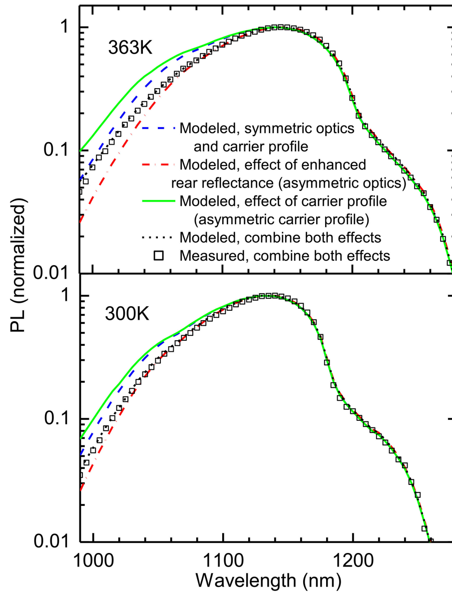

Fig. 3. Comparison of modeled normalized PL spectra between the symmetric optics and carrier profile case (blue-dashed lines) and the combined effect case (see black-dotted lines), in which the optics and the carrier profile are both asymmetric. The experimental data of the combined effect case (black squares) agree with the modeling. The normalized spectra with the effects of the enhanced rear reflectance from Section IV (red-dashed-dotted lines) and of the inhomogeneous carrier profile from Section V (green solid lines) are also plotted, again to facilitate the comparison.

in practice, these two effects often happen simultaneously, since these two properties are usually altered together during the sample processing steps. Therefore, we here inspect their combined effects on the spectrum shapes, as a function of temperature.

We deposited a 100-nm layer of silver on the rear of the second sample. This thick silver layer not only provides a very high SRV, but also makes the reflectance of the rear approach unity. Thus, this sample displays the properties of both inhomogeneous carrier profile and asymmetric optics on both surfaces. The spectra were then both captured and modeled.

Fig. 3 compares the modeled normalized spectra in this case with the symmetric optics and carrier profile case. The spectra with the effects of the enhanced rear reflectance from Section IV and of the inhomogeneous carrier profile from Section V are also plotted, again to facilitate the comparison. In this figure, the normalized spectra present a combination of both effects, the net effect of which lies in between the two cases in isolation, due to their opposing nature. At room temperature, the carrier profile has less impact on the spectrum shape, and the combined normalized spectrum shows a greater impact of the rear reflector. When the temperature increases, the impact of the carrier profile is more significant at low wavelengths, in particular near the wavelength of 1000 nm, and thus cancels out the effect of the rear reflector. However, when the wavelength increases, this impact is reduced, and the spectrum eventually displays the signature of the enhanced rear reflectance case again. Fig. 3 also shows the experimental spectra of this sample; they are identical to the modeling. This agreement has validated the combined model explained above.

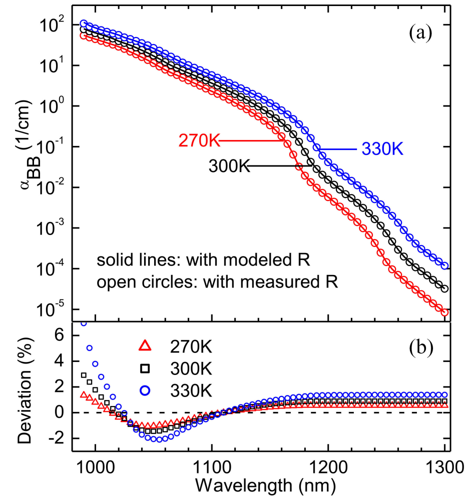

Fig. 4. (a) Comparison of α_{BB} calculated with the measured reflectance [12] and with the modeled reflectance (this paper) at different temperatures. (b) Relative deviation between the two cases at different temperatures.

VII. Impact of Internal Reflection on α_{BB} and *B*

We have confirmed that the internal reflection and the carrier profile can have significant impacts on the PL spectra at different temperatures. In addition, as can be seen from (5), the band–band absorption coefficient α_{BB} is a critical input parameter in spectral PL models. Since the values of this parameter have been reestablished recently using spectral PL measurements [12], it is supposed that the internal reflectance and the carrier profile may, in principle, have a significant impact on the measurement of α_{BB} in [12] and, hence, *B* in [14], which in turn affect our modeled spectra here. However, since the carrier profile in [12] was shown to be uniform, and the determination of *B* was based solely on the data of α_{BB} [14], here, we examine only the potential effect of the internal reflection on α_{BB}.

The long wavelength escape tail of the measured reflectance spectrum in silicon wafers is a commonly known artifact. However, in [12], we employed the measured reflectance without correcting the reflectance spectra at longer wavelengths. Thus, a question arising is whether this reflectance discrepancy significantly affects the established values of α_{BB}. To elucidate this question, using the same technique as in [12], we recalculated α_{BB} at various temperatures around room temperature using the modeled internal reflectance and compared with the data in [12], in which α_{BB} was computed using the measured external reflectance. The internal reflectance of the silicon sample used in [12] was modeled using the optical simulator OPAL [21], [22]. The results are shown in Fig. 4(a), whereas the deviation between two cases is plotted in Fig. 4(b). At longer wavelengths, α_{BB} is determined solely by the absorptivity, which has a constant deviation between the two works due to different scaling factors. Thus, the deviation in Fig. 4(b) is saturated at longer wavelengths. At shorter wavelengths, α_{BB} is a function of both the absorptivity and the surface reflectance. Thus, the deviation in Fig. 4(b) trends up or down depending on the changing relative impact of these two variables. Nevertheless, the deviation is

mostly less than 5%. Therefore, the reflectance does not affect the data of α_{BB} in [12] in the wavelength range of interest, despite the significant discrepancy between the measured and modeled reflectances.

VIII. Conclusion

We have experimentally demonstrated the separate impacts of the internal reflection and the carrier profile on the PL spectra. The enhanced rear reflectance compresses the low-wavelength sides of the normalized spectra, while the inhomogeneous carrier profile enhances them. These effects are more pronounced at shorter wavelengths and higher temperatures, giving an incentive to use higher temperatures to enhance the accuracy of some established spectral PL tools. In addition, we have shown the aggregate influence of these two properties on the spectra in which the enhanced rear reflectance has offset the impact of the inhomogeneous carrier profile caused by the increased rear-surface recombination velocity. Finally, we have demonstrated that the reflectance has little impact on the data of the band–band absorption coefficient, and hence, the radiative recombination coefficient, despite significant deviation between the measured and modeled reflectances at longer wavelengths.

Acknowledgment

The authors would like to thank Dr. S. Surve and B. Condon for assisting with the hardware setup, T. Allen and J. Bullock for assisting with the sample preparation, and H. Sio for useful discussions on the hydrofluoric fuming technique.

References

[1] P. Würfel, T. Trupke, T. Puzzer, E. Schäffer, W. Warta, and S. W. Glunz, “Diffusion lengths of silicon solar cells from luminescence images,” *J. Appl. Phys.*, vol. 101, pp. 123110-1–123110-10, 2007.

[2] J. A. Giesecke, M. Kasemann, and W. Warta, “Determination of local minority carrier diffusion lengths in crystalline silicon from luminescence images,” *J. Appl. Phys.*, vol. 106, pp. 014907-1–014907-8, 2009.

[3] J. A. Giesecke, M. Kasemann, M. C. Schubert, P. Würfel, and W. Warta, “Separation of local bulk and surface recombination in crystalline silicon from luminescence reabsorption,” *Prog. Photovoltaics: Res. Appl.*, vol. 18, pp. 10–19, 2011.

[4] M. P. Peloso, J. S. Lew, T. Trupke, M. Peters, R. Utama, and A. G. Aberle, “Evaluating the electrical properties of silicon wafer solar cells using hyperspectral imaging of luminescence,” *Appl. Phys. Lett.*, vol. 99, pp. 221915-1–221915-3, 2011.

[5] B. Mitchell, T. Trupke, J. W. Weber, and J. Nyhus, “Bulk minority carrier lifetimes and doping of silicon bricks from photoluminescence intensity ratios,” *J. Appl. Phys.*, vol. 109, pp. 083111-1–014907-12, 2011.

[6] B. Mitchell, J. W. Weber, D. Walter, D. Macdonald, and T. Trupke, “On the method of photoluminescence spectral intensity ratio imaging of silicon bricks: Advances and limitations,” *J. Appl. Phys.*, vol. 112, pp. 063116-1–063116-13, 2012.

[7] B. Mitchell, M. K. Juhl, M. A. Green, and T. Trupke, “Full spectrum photoluminescence lifetime analyses on silicon bricks,” *IEEE J. Photovoltaics*, vol. 3, no. 3, pp. 962–969, Jul. 2013.

[8] C. Schinke, D. Hinken, J. Schmidt, K. Bothe, and R. Brendel, “Modeling the spectral luminescence emission of silicon solar cells and wafers,” *IEEE J. Photovoltaics*, vol. 3, no. 3, pp. 1038–1052, Jul. 2013.

[9] C. Barugkin, Y. Wan, D. Macdonald, and K. R. Catchpole, “Evaluating plasmonic light trapping with photoluminescence,” *IEEE J. Photovoltaics*, vol. 3, no. 4, pp. 1292–1297, Oct. 2013.

[10] E. Daub and P. Würfel, “Ultralow values of the absorption coefficient of Si obtained from luminescence,” *Phys. Rev. Lett.*, vol. 74, pp. 1020–1023, 1995.

[11] T. Trupke, M. A. Green, P. Würfel, P. P. Altermatt, A. Wang, J. Zhao, and R. Corkish, “Temperature dependence of the radiative recombination coefficient of intrinsic crystalline silicon,” *J. Appl. Phys.*, vol. 94, pp. 4930–4937, 2003.

[12] H. T. Nguyen, F. E. Rougieux, B. Mitchell, and D. Macdonald, “Temperature dependence of the band-band absorption coefficient in crystalline silicon from photoluminescence,” *J. Appl. Phys.*, vol. 115, pp. 043710-1–043710-8, 2014.

[13] P. P. Altermatt, F. Geelhaar, T. Trupke, X. Dai, A. Neisser, and E. Daub, “Injection dependence of spontaneous radiative recombination in crystalline silicon: Experimental verification and theoretical analysis,” *Appl. Phys. Lett.*, vol. 88, pp. 261901-1–261901-3, 2006.

[14] H. T. Nguyen, S. C. Baker-Finch, and D. Macdonald, “Temperature dependence of the radiative recombination coefficient in crystalline silicon from spectral photoluminescence,” *Appl. Phys. Lett.*, vol. 104, pp. 112105-1–112105-3, 2014.

[15] P. Würfel, “The chemical potential of radiation,” *J. Phys. C*, vol. 15, pp. 3967–3985, 1982.

[16] P. Würfel, S. Finkbeiner, and E. Daub, “Generalized Planck’s radiation law for luminescence via indirect transitions,” *Appl. Phys. A, Mater. Sci. Process.*, vol. 60, pp. 67–70, 1995.

[17] K. Schick, E. Daub, S. Finkbeiner, and P. Würfel, “Verification of a generalized Planck law for luminescence radiation from silicon solar cells,” *Appl. Phys. A, Solids Surfaces*, vol. 54, pp. 109–114, 1992.

[18] P. Würfel, *Physics of Solar Cells: From Basic Principles to Advanced Concepts*. New York, NY, USA: Wiley-VCH, 2009.

[19] T. Trupke, E. Daub, and P. Würfel, “Absorptivity of silicon solar cells obtained from luminescence,” *Sol. Energy Mater. Sol. Cells*, vol. 53, pp. 103–114, 1998.

[20] R. A. Sinton, A. Cuevas, and M. Stuckings, “Quasi-steady-state photoconductance, a new method for solar cell material and device characterization,” in *Proc. IEEE 25th Photovoltaic Spec. Conf.*, San Jose, CA, USA, 1996, pp. 457–460.

[21] K. R. McIntosh and S. C. Baker-Finch, “OPAL 2: Rapid optical simulation of silicon solar cells,” in *Proc. IEEE 38th Photovoltaic Spec. Conf.*, Austin, TX, USA, 2012, pp. 265–271.

[22] S. C. Baker-Finch and K. R. McIntosh, “A freeware program for precise optical analysis of the front surface of a solar cell,” in *Proc. IEEE 35th Photovoltaic Spec. Conf.*, Honolulu, HI, USA, 2010, pp. 2184–2187.

Authors’ photographs and biographies not available at the time of publication.

CHAPTER 5

Deep-Level Photoluminescence Spectroscopy from Dislocations in Multicrystalline Silicon

The recombination of free electrons and holes can either take place directly via the band edges, or be assisted by defect states located inside the forbidden gap of silicon. The defect-mediated recombination is extrinsic to silicon in the sense that it requires the presence of localized defects and impurities. Many defects and impurities can be mitigated throughout solar cell fabrication steps such as phosphorus gettering, high temperature annealing, or surface passivation. However, grown-in structural defects such as dislocations are very persistent with processing steps since they are formed by the high thermal stress and strain during the ingot growth and cooling. Therefore, they are considered as one of the main efficiency limiting defects in multicrystalline silicon solar cells.

The dislocations and the secondary defects and impurities trapped by their strain field can occupy energy states inside the forbidden gap of silicon, and thus can act as effective radiative

recombination centers in silicon. At room temperature, the defect luminescence is quenched significantly since the thermal energy can excite the trapped carriers back to their corresponding band edges. Therefore, the signatures of these defects are not revealed clearly on the captured photoluminescence spectra. On the other hand, at low temperatures, the thermal energy is not sufficient to excite the trapped carriers back to the band edges. Therefore, the defect luminescence can be strong and distinct, allowing one to investigate the luminescence properties of these defect centers. However, since it is not the band-to-band luminescence, the band-to-band absorption coefficient established in Chapter 2 cannot be applied to model this type of luminescence. Also, at low temperatures, the reabsorption of the emitted photons is almost negligible, and hence the surface optics and the carrier profiles have little impact on the photoluminescence spectral shape.

In multicrystalline silicon wafers, large angle grain boundaries can act as relaxation sites for the high thermal stress and strain during the crystal growth, which can minimize the dislocation formation. On the contrary, inside the grains, the material still suffers a high level of stress and strain, causing an elastic bending of the crystal structure. The bending energy can be relaxed by the introduction of dislocations. The further the lattice is distorted, the more dislocations need to be introduced to compensate. These dislocations introduce a permanent misorientation between the two sides of the lattice, and the boundary is called a small angle grain boundary or a sub-grain boundary. Due to the forming mechanism of the sub-grain boundaries, they always contain a high density of dislocations. The stress and strain around these dislocations, in turn, can preferentially trap other defects and impurities. Therefore, the sub-grain boundaries have detrimental effects on the performance of multicrystalline silicon solar cells.

However, investigating the luminescence properties of these sub-grain boundaries and the regions surrounding them is very challenging with a conventional photoluminescence spectroscopy system due to their micron-scale sizes. Only with the advent of micro-photoluminescence spectroscopy systems equipped with confocal optics, spatial resolution has been achieved in the micron scale, allowing the investigation of the dislocations and defects distributed around the sub-grain boundaries. Therefore, this chapter utilizes the micro photoluminescence spectroscopy system to study the luminescence properties of sub-grain boundaries, revealing interesting findings on the deep-level luminescence of dislocations and decorating defects and impurities around the sub-grain boundaries after different processing steps.

Micrometer-Scale Deep-Level Spectral Photoluminescence From Dislocations in Multicrystalline Silicon

Hieu T. Nguyen, Fiacre E. Rougieux, Fan Wang, Hoe Tan, and Daniel Macdonald

Abstract—**Micrometer-scale deep-level spectral photoluminescence (PL) from dislocations is investigated around the subgrain boundaries in multicrystalline silicon. The spatial distribution of the D lines is found to be asymmetrically distributed across the subgrain boundaries, indicating that defects and impurities are decorated almost entirely on one side of the subgrain boundaries. In addition, the D1 and D2 lines are demonstrated to have different origins due to their significantly varying behaviors after processing steps. D1 is found to be enhanced when the dislocations are cleaned of metal impurities, whereas D2 remains unchanged. Finally, the D4 and D3 lines are proposed to have different origins since their energy levels are shifted differently as a function of distance from the subgrain boundaries.**

Index Terms—**Crystalline silicon, deep level, dislocations, grain boundaries, photoluminescence (PL), photovoltaic cells.**

I. Introduction

DEEP-LEVEL photoluminescence (PL) spectroscopy has been demonstrated to be a powerful characterization tool for the defects and impurities in photovoltaic silicon [1]. Distinct spectral signatures have been reported for different defects and impurities in crystalline silicon, such as Fe precipitates [2], oxygen precipitates [3], Cr-B pairs [4], and dislocations [5]. In multicrystalline silicon (mc-Si), dislocations are a major limiting factor for the cell efficiency, and often occur at small angles and other subgrain boundaries (sub-GBs) due to high thermal stresses during ingot growth and cooling [6]. Therefore, understanding the deep-level spectra of dislocations is important to improve the material quality and, thus, the final efficiency of mc-Si solar cells.

The so-called D lines, emitted from dislocations, have been studied intensively regarding their thermal behaviors [7]–[10]; spatial distributions [1], [11]–[16]; process-related changes [7]; [17]; and polarization features [1], [7], [18], [19]. The doublet D1/D2 has been hypothesized to originate from the surrounding local conditions, such as neighboring dislocations or stress by Arguirov *et al.* [8] and Lee *et al.* [15], or from decorating defects and impurities located around dislocations by Sugimoto *et al.* [13]. On the other hand, the doublet D3/D4 was believed to represent the intrinsic nature of dislocations [8], [15]. This was confirmed recently by Tajima *et al.* [1], [20], who employed micro-PL (μPL) spectroscopy with a high spatial resolution to examine the distribution of D lines around the sub-GBs, finding that D1/D2 were distributed around the sub-GBs, whereas D3/D4 were located directly at the sub-GBs.

However, various authors have reported varying behaviors of the D1 and D2 lines at cryogenic temperatures. Some reported spectra in which the D2 line was a less-significant peak embedded on the high-energy side of the intense D1 line [7], [11], [12], [14]. Others reported spectra with the D2 line present, but with D1 absent [9], [13]. Some pointed out a large change in the D1/D2 intensity ratio depending on the locations in the wafers [8], [21], [22], inconsistent thermal behaviors between D1 and D2 [8], or the difference in mapping images of D1 compared with other D lines [15]. Therefore, some uncertainty remains regarding the connection between D1 and D2.

In addition, although the intensity ratio of the doublet D3/D4 does not vary as strongly as that of D1/D2, there is still an inconsistency among reported works. Near liquid nitrogen temperature, the D4 peak was reported to be higher than the D3 peak in [7] and [11]. However, the opposite observation was presented in other works [8], [23]. Sekiguchi *et al.* [21] found the varying intensity ratio of D3/D4 along the slip lines of dislocations, and suggested that D3 is not the phonon replica of D4. Recently, employing a hyperspectral PL imaging technique at 110 K, Burud *et al.* [22] had the same findings in mc-Si wafers, and proposed that D3 and D4 could have different origins.

In this study, utilizing a μPL mapping system with spatial resolution of about 3 μm, along with well-controlled sample preparation steps, we investigate the behaviors and origins of D lines in mc-Si wafers. We first study the micrometer-scale spatial distribution of these D lines around sub-GBs at 79 K, revealing a distinctly asymmetrical distribution for D1/D2. We also compare the behavior of the D lines after different processing steps including phosphorus diffusion gettering, high-temperature annealing, and controlled contamination with Fe. From these results, we clarify some of the uncertainties about the origins and properties of the D lines.

Manuscript received January 6, 2015; revised February 11, 2015; accepted February 19, 2015. Date of publication March 13, 2015; date of current version April 17, 2015. This work was supported by the Australian Research Council and the Australian Renewable Energy Agency under research Grant RND009.

H. T. Nguyen, F. E. Rougieux, and D. Macdonald are with the Research School of Engineering, The Australian National University, Canberra, ACT 2601, Australia (e-mail: hieu.nguyen@anu.edu.au; fiacre.rougieux@anu.edu.au; daniel.macdonald@anu.edu.au).

F. Wang and H. Tan are with the Department of Electronic Materials Engineering, The Australian National University, Canberra, ACT 2601, Australia (e-mail: fan.wang@anu.edu.au; Hoe.Tan@anu.edu.au).

Color versions of one or more of the figures in this paper are available online at http://ieeexplore.ieee.org.

Digital Object Identifier 10.1109/JPHOTOV.2015.2407158

2156-3381 © 2015 IEEE. Personal use is permitted, but republication/redistribution requires IEEE permission.
See http://www.ieee.org/publications_standards/publications/rights/index.html for more information.

II. Experimental Details

The investigated samples are directionally solidified, boron-doped p-type mc-Si wafers with nominal resistivity of 1.6 Ω·cm, corresponding to a background doping of about 9×10^{15} cm^{-3}. We prepared four samples cut from four consecutive sister wafers sliced from the same ingot. These samples were first chemically etched with an etchant consisting of hydrofluoric and nitric acids to remove saw damage and to achieve optically polished surfaces. After that, the first sample was kept in the as-cut state. The second sample went through an extended phosphorous gettering process, in which it was processed at 880 °C for 60 min in a mixture of $POCl_3$ vapor, O_2, and N_2, and then was cooled down to 650 °C and left there for another 12 h in N_2 gas [24]. The sheet resistance of the resultant diffused layer was around 30 Ω/□. The third sample went through the same thermal processing step as the gettering process but with only N_2 gas, giving the same thermal budget as the second sample but without phosphorous gettering. The fourth sample was gettered in the same way as the second one, and then its diffused layer was etched off. It was then implanted with a low energy (70 keV) Fe dose of 2.4×10^{12} cm^{-2} and annealed at 900 °C for 35 min in O_2 gas to distribute the Fe uniformly across the wafer thickness. After that, this sample was cooled down to 600 °C and left for 20 h to allow Fe to precipitate along the GBs and sub-GBs [25]. All samples were chemically etched again to remove all the residual layers (diffused, implanted, and thermal oxide layers) left after the previous processing steps. Finally, they were immersed in a defect etchant consisting of acetic/nitric/hydrofluoric acids for 16 h. The purpose of this etching step is to delineate the sub-GBs, which are, otherwise, not observable under the optical microscope. The optical image of an investigated sub-GB is provided in Fig. 2(d). The investigated sub-GBs were located far away from other sub-GBs to avoid confounding effects from neighboring sub-GBs.

The μPL spectroscopy system employed in this study is a Horiba T64000 equipped with a confocal microscope. A 50× reflective objective lens was used to focus the incident laser beam into a spot of about 1 μm in diameter on the samples, and to direct the emitted PL signal into a monochromator as well. This emitted signal was then collected by a liquid-nitrogen-cooled InGaAs array detector. The monochromator gratings were set at 150 grooves/mm for PL, providing a spectral resolution of 0.25 nm. The spectral response of the entire system was calibrated with black body thermal radiation emitted from a black body cavity. The employed laser was a diode-pumped solid-state laser having a wavelength of 532 nm, and an on-sample average intensity of 6 mW. The sample stage was equipped with X and Y positioners with the smallest step size of 0.2 μm. The line scans across the sub-GBs had a step size of 2 μm, and those along the sub-GBs had a step size of 5 μm. The sample temperature was kept constant at 79 K with a liquid-nitrogen cryostat, since the spectral distribution of the D lines is resolved more clearly at these lower temperatures. The radial spatial resolution of the technique was determined by the injection level, the temperature, and the defect density and was estimated to be about 3 μm for the intragrain regions, where it is limited by the Auger-dominated diffusion length of excess carriers. This spatial resolution is better near the sub-GBs due to the reduced carrier diffusion lengths via increased Shockley–Read–Hall recombination.

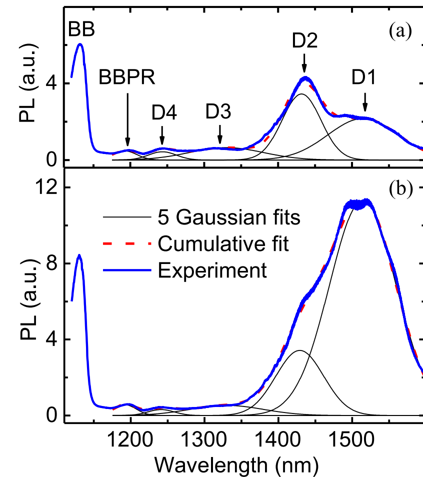

Fig. 1. Comparison of the deep-level PL spectra between the (a) as-cut and (b) gettered samples at a distance of about 20 μm from the sub-GB at 79 K.

III. Results and Analysis

Fig. 1(a) and (b) shows our spectra captured at a distance about 20 μm from the same sub-GB for the first (as-cut) and second (gettered) samples, respectively. We numerically decomposed the spectra and fitted them with five Gaussian distributions, corresponding to the first phonon replica of the band–band line (BBPR) and the D4, D3, D2, and D1 lines. The peak heights of these Gaussian functions represent the intensity of their corresponding lines. The narrow band–band (BB) line is at around 1130 nm and clearly distinguished from these five lines. Thus, we were able to accurately determine the peak height of the BB line without needing to decompose it from the other lines.

First, we consider the spatial distribution of the D1 and D2 lines around the sub-GB. Fig. 2(a) and (b) plots the amplitudes of D1 and D2 (after the total spectrum is decomposed), along with the BB peak, versus the distance away from the sub-GB for the as-cut and gettered samples, respectively. Each line scan, in fact, consists of two sections, which were started from the same location on the sub-GB and then extended in opposite directions away from the sub-GB. The two spectra measured directly on the sub-GB of the two scanning sections were found to be the same, allowing us to combine the results from these two scanning sections into one line scan. By scanning this way, we can ensure correct positioning of sub-GBs in the center of the scan, and minimize potential impacts of the imperfect alignment of the X and Y positioners on the area around sub-GBs. The distributions of D1 and D2 appear to be very asymmetric across this sub-GB. In order to ensure that this asymmetry is not a measurement artifact, we performed line scans across this sub-GB at another location, which was shifted about 40 μm compared with the previous location. Again, in Fig. 2(c) and (d), the asymmetric distributions of D1 and D2 are still present on the same side.

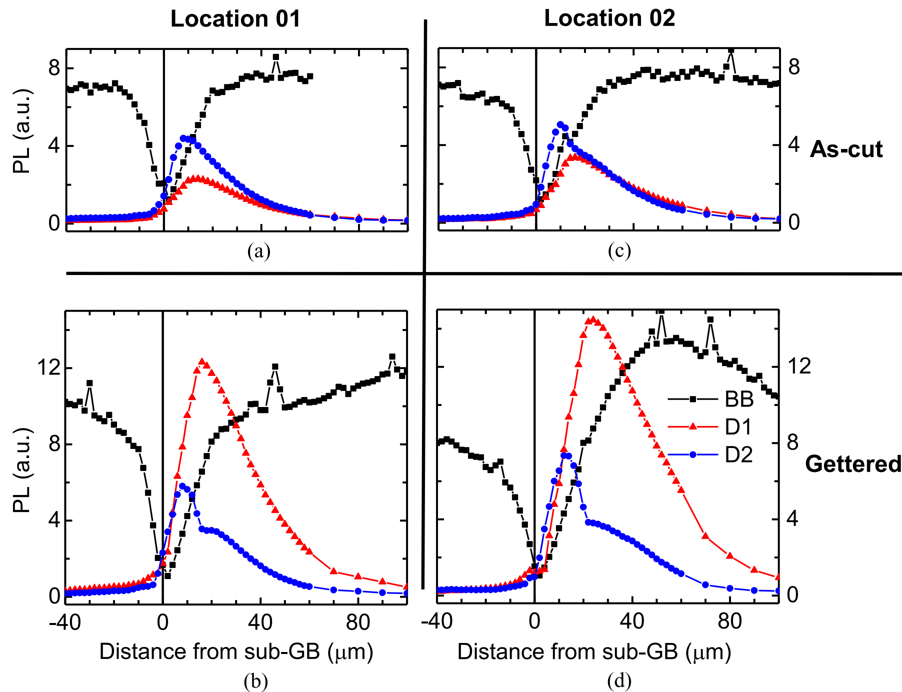

Fig. 2. [(a) and (c)] Line scans across the sub-GB of the intensities of D1, D2, and BB lines at two locations for the as-cut and gettered [(b) and (d)] samples. Location 02 [(c) and (d)] was shifted about 40 μm along the same sub-GB compared to location 01 [(a) and (b)]. The vertical line at zero distance indicates the location of the sub-GB.

Note that in Fig. 2, although the BB distribution is also asymmetric, the extent of this asymmetry is much less pronounced than those of D1 and D2 indicating that the observed asymmetry is not due to a difference in local injection levels or other optical artifacts. We found this asymmetry of D1 and D2 at all sub-GBs on the samples investigated in this paper (at approximately ten sub-GBs).

Moreover, right at the sub-GB, the intensities of both D1 and D2 are very low, and then increase when moving away from the sub-GB. This signature is consistent with the hypothesis that D1 and D2 originate from secondary defects or impurities trapped around the dislocations, as suggested by Tajima *et al.* [1], [20]. Thus, the above asymmetry suggests that these secondary defects and impurities are distributed almost entirely on one side of the sub-GBs. This asymmetry has not been observed in previous reports due to their lower spatial resolution, for example, several tens of micrometers in the case of Tajima *et al.* [20]. Note that the step size of our line-scans is only 2 μm and, thus, smaller than the estimated 3 μm spatial resolution due to carrier diffusion. Therefore, there is likely to be some degree of signal smearing in the line scans. However, the spatial extent of the observed asymmetry extends to several tens of micrometers, and thus, is much larger than the impact of any smearing caused by carrier diffusion.

Since D1 and D2 luminescence centers are originated from defects or impurities trapped by the strain field around the dislocations, the asymmetry of D1 and D2 could be due to the higher local stress on one side of the sub-GB, which was formed during the ingot cooling process. However, such stress usually extends to only a few micrometers from the dislocation sites [26], while the observed asymmetry in this study extends to several tens of micrometers. In addition, we did not observe any shift in the silicon Raman peak when performing Raman scans across this sub-GB indicating that the stress is not significantly different between two sides of this sub-GB [26]. Therefore, the hypothesis of different local stress causing the asymmetry of D1 and D2 is unlikely to be correct.

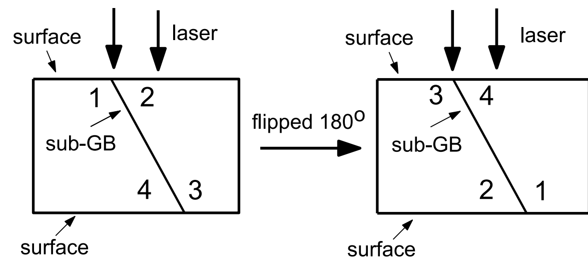

Fig. 3. Inclined sub-GB. If the asymmetry of D1 and D2 is an artifact due to the inclination, the higher intensities of D1 and D2 should be observed at side 2 before flipping and at side 4 after flipping. However, D1 and D2 were observed at side 2 and side 3 and were absent at side 1 and side 4.

Another hypothesis is that the observed asymmetry of D1 and D2 may stem from an inclination of this sub-GB compared with the surface. However, again the asymmetry extends to several tens of micrometers, whereas the investigated samples are only about 250-μm thick. Hence, the inclination angle of this sub-GB would need to be unusually large for this hypothesis to be true, considering that the sense depth of the measurements is only several micrometers. In addition, as illustrated in Fig. 3, if the observed asymmetry is an artifact caused by the inclined sub-GB, we should have higher luminescence intensities of D1 and D2 at side 2 before rotating and flipping the sample, and at

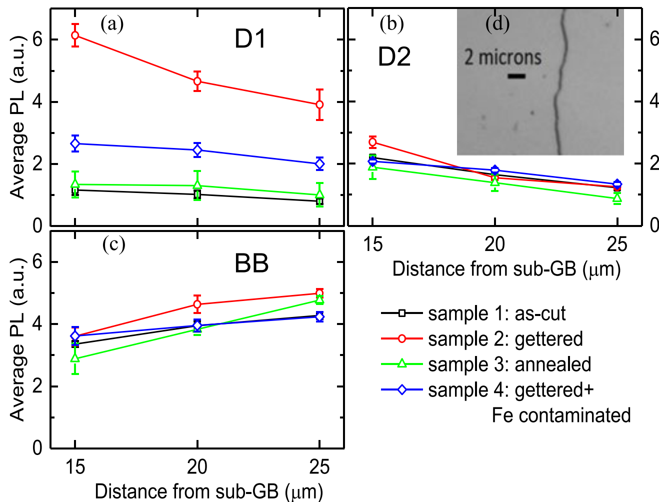

Fig. 4. Comparison of (a) D1, (b) D2, and (c) BB average intensities among the four samples at difference distances from the same sub-GB at 79 K, including one standard deviation error bars. (d) Microscope image of this sub-GB.

side 4 afterward. However, we still observed higher intensities of D1 and D2 at side 3 after flipping the sample. Thus, this second hypothesis is also incorrect. Moreover, since the higher intensities of D1 and D2 appear on the opposite side of the sub-GB (relative to the initial scan direction) after flipping the sample, the observed asymmetry is not an artifact caused by the choice of scan direction. We, therefore, propose that the notable asymmetry of D1 and D2 is due to the defects and impurities being preferentially decorated on one side of the sub-GB during the crystal growth process. More microscopic studies are needed to understand the reasons for this preferential decoration.

Furthermore, as readily seen from Figs. 1 and 2, the D1 intensity is enhanced significantly relative to the BB intensity after gettering, whereas the D2 peak is not altered significantly. In order to avoid any localized variability of the sub-GB skewing our conclusions, we performed 60-μm long line scans (13 data points per scan) parallel to this sub-GB at different distances away from it on the side of high D1 and D2 intensities. The D1 and D2 average intensities (after decomposing the spectrum) from these line scans are depicted in Fig. 4(a) and (b), respectively, for the four sister samples. D1 again shows a significant enhancement after the extended phosphorous gettering process, whereas D2 remains unchanged. Note that the BB signal is also largely unchanged among all the samples, as shown in Fig. 4(c), indicating that the enhancement of D1 after gettering is not due to an increased local injection level.

The phosphorus gettering process used here has been demonstrated to be very effective in monocrystalline silicon, in which more than 99% of dissolved Fe impurities can be removed [24]. However, our samples are mc-Si. Thus, besides this external gettering, the second sample may also experience internal gettering, in which at least some metal impurities are preferentially decorated around the GBs and sub-GBs instead of being captured in the phosphorus diffused layers [27]. Therefore, although the global concentration of metal impurities such as Fe will be reduced by the external gettering, the local concentration at GBs and sub-GBs could, in principle, actually be higher than that of the as-cut sample.

We, therefore, performed similar line scans along the same sub-GB at similar distances for the third sample. Since this sample has the same thermal budget as the phosphorus gettering process, but without phosphorous gettering, it is expected that there would be a greater extent of metal impurities decorated around the sub-GBs due to the internal gettering effects. However, from Fig. 4(a), the D1 intensity is the same as the as-cut sample, prompting us to speculate that the enhancement of D1 in the phosphorus gettered sample is due to a reduction of metal impurities near the sub-GBs after the phosphorous gettering process. To fortify this hypothesis, we performed the scanning on the fourth sample. The concentration of Fe impurities around the sub-GBs of this gettered and Fe implanted sample should be higher than that of the gettered sample. However, the D1 intensity is significantly lower than that of the gettered sample. Therefore, we conclude that D1 is enhanced when the sub-GBs are cleaned of metal impurities. This behavior may be explained by the fact that D1 and D2 are due to the secondary defects trapped around dislocation sites. When metal impurities are present, they may form complexes with the D1 centers; thus, altering their energy levels and reducing their luminescence efficiency. When the metal impurities are removed by gettering, the D1 centers become radiatively active again, and hence, the D1 intensity is increased significantly.

The above finding can be compared with the results from Tajima *et al.* [28], who reported that the D1 line was unchanged, but the D2 line was suppressed after their sample was contaminated with Fe. We also found many sub-GBs in which D1 and D2 were not altered by the gettering process, compared with the as-cut sample. Nevertheless, based on the remarkably different behaviors of D1 and D2 in our study, we also conclude that D1 is not the phonon replica of D2 and that they have different origins.

Next, we inspect the behaviors of the D3 and D4 lines. In order to avoid being confounded by the strong tails of D1 and D2, we chose another sub-GB in which D3 and D4 are strong, but D1 and D2 are completely absent. Fig. 5(a) and (b) displays the line scan intensity of D3 and D4 peaks using the Gaussian fitting method as described above. The line scanning was performed at similar locations across the same sub-GB for the first and second samples. From Fig. 5(a) and (b), the D3 and D4 intensities are flattened at the sub-GB. This signature is consistent with the fact that these two lines reflect the intrinsic nature of dislocations [1], [8], [15], [20]. However, we observed slightly asymmetric distributions of D3 and D4 across this sub-GB, although this asymmetry is certainly not as strong as that of D1 and D2. This slight asymmetry may be due to the fact that the dislocation density is slightly different between two sides of the sub-GB. In addition, the intensities of D3 and D4 still remain the same between the as-cut and gettered samples. In other words, D3 and D4 are not affected by the gettering process, which is consistent with the hypothesis that D3 and D4 are intrinsic properties of the dislocations themselves.

Furthermore, Fig. 5(c) shows the PL spectra normalized to the BB peak at different distances from the sub-GB of

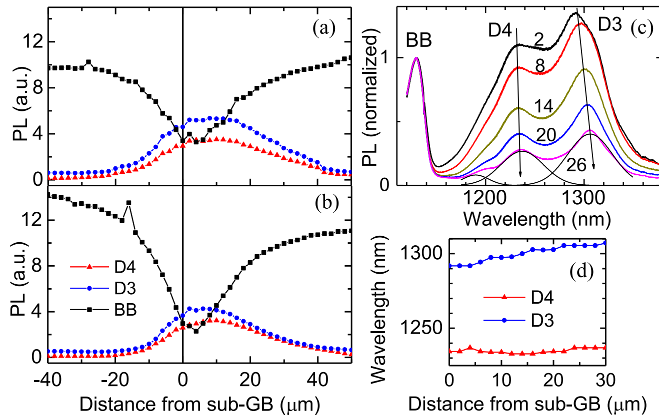

Fig. 5. Line scans of the intensities of D3, D4, and BB lines across a sub-GB of the (a) as-cut and (b) gettered samples at 79 K. The vertical line at zero distance indicates the location of this sub-GB. (c) Spectra of the as-cut sample at different distances in micrometer, indicated by the number on each spectrum, from the sub-GB was normalized to the BB peak. The Gaussian fits of the spectrum at 26 μm are also plotted (thin black lines). (d) Peak wavelengths of D3 and D4 versus the distance from the sub-GB.

the as-cut sample. The energy level of D4 is constant as a function of distance, whereas the D3 peak moves toward higher wavelengths (lower energies) at farther distances. Fig. 5(d) quantitatively shows the energy shifts for both D3 and D4. The energy level was determined by choosing the wavelength at the local maxima of PL intensity around D3 and D4. This observation contradicts the common belief from the literature that D3 is the phonon replica of D4 [8], [20]. If D3 is the transverse-optical phonon replica of D4, their peak energies should be consistently shifted by around 57 meV [29]. However, this energy difference varies from 42 to 54 meV in Fig. 5(d). We note that this finding regarding D3 and D4 could not be easily observed with a spatial resolution of several tens of micrometers or above, as was the case in most previous works in the literature. Thus, we hypothesize that D3 is not the phonon replica of D4 and that they may have different origins.

IV. Conclusion

Utilizing high spatial resolution and well-controlled processing steps, we have experimentally demonstrated the asymmetry of D lines across the sub-GBs in mc-Si wafers. In addition, we have shown the different origins of the D1 and D2 lines, and concluded that D1 is suppressed by the presence of metal impurities near the dislocations, although not via quenching caused by a reduction in the excess carrier density. Finally, we have proposed that D3 is not the phonon replica of D4 and that these two lines may have different origins due to their different energy shifts as a function of distance from the sub-GBs.

Acknowledgment

The authors would like to thank R. Elliman for access to the ion implant facility, and K. Belay, S. Surve, C. Samundsett, T. Ratcliff, J. Bullock, and A. Y. Liu for assisting with the sample preparation, as well as The Australian National Fabrication Facility for providing access to some of the facilities used in this paper.

References

[1] M. Tajima, "Spectroscopy and topography of deep-level luminescence in photovoltaic silicon," *IEEE J. Photovoltaics*, vol. 4, no. 6, pp. 1452–1458, Nov. 2014.

[2] P. Gundel, M. C. Schubert, W. Kwapil, J. Schön, M. Reiche, H. Savin, M. Yli-Koski, J. A. Sans, G. Martinez-Criado, W. Seifert, W. Warta, and E. R. Weber, "Micro-photoluminescence spectroscopy on metal precipitates in silicon," *Physica Status Solidi, Rapid Res. Lett.*, vol. 3, pp. 230–232, 2009.

[3] S. Binetti, S. Pizzini, E. Leoni, R. Somaschini, A. Castaldini, and A. Cavallini, "Optical properties of oxygen precipitates and dislocations in silicon," *J. Appl. Phys.*, vol. 92, pp. 2437–2445, 2002.

[4] H. Conzelmann and J. Weber, "Photoluminescence from chromium-boron pair in silicon," *Physica B+C*, vol. 116, pp. 291–296, 1983.

[5] R. Sauer, J. Weber, J. Stolz, E. R. Weber, K.-H. Küsters, and H. Alexander, "Dislocation-related photoluminescence in silicon," *Appl. Phys. A*, vol. 36, pp. 1–13, 1985.

[6] B. Sopori, P. Rupnowski, V. Mehta, V. Budhraja, S. Johnston, N. Call, H. Mountinho, M. Al-Jassim, A. Shaikh, M. Seacrist, and D. Carlson, "Performance limitations of mc-si solar cells caused by defect clusters," *ECS Trans.*, vol. 18, no. 1, pp. 1049–1058, 2009.

[7] S. Ostapenko, I. Tarasov, J. P. Kalejs, C. Haessler, and E.-U. Reisner, "Defect monitoring using scanning photoluminescence spectroscopy in multicrystalline silicon wafers," *Semicond. Sci. Technol.*, vol. 15, pp. 840–848, 2000.

[8] T. Arguirov, W. Seifert, M. Kittler, and J. Reif, "Temperature behaviour of extended defects in solar grade silicon investigated by photoluminescence and EBIC," *Mater. Sci. Eng. B*, vol. 102, pp. 251–256, 2003.

[9] M. C. Schubert, P. Gundel, M. The, W. Warta, M. Romero, S. Ostapenko, and T. Arguirov, "Spatially resolved luminescence spectroscopy on multicrystalline silicon," in *Proc. 23rd Eur. Photovoltaic Sol. Energy Conf.*, Valencia, Spain, 2008, pp. 17–23.

[10] F. Dreckschmidt and H.-J. Möller, "Defect luminescence at grain boundaries in multicrystalline silicon," *Phys. Status Solidi C*, vol. 8, pp. 1356–1360, 2011.

[11] I. Tarasov, S. Ostapenko, W. Seifert, M. Kittler, and J. P. Kaleis, "Defect diagnostics in multicrystalline silicon using scanning techniques," *Physica, Condensed Matter*, vol. 308–310, pp. 1133–1136, 2001.

[12] M. Kittler, W. Seifert, T. Arguirov, I. Tarasov, and S. Ostapenko, "Room-temperature luminescence and electron-beam-induced current (EBIC) recombination behaviour of crystal defects in multicrystalline silicon," *Sol. Energy Mater. Sol. Cells*, vol. 72, pp. 465–472, 2002.

[13] H. Sugimoto, M. Inoue, M. Tajima, A. Ogura, and Y. Ohshita, "Analysis of intra-grain defects in multicrystalline silicon wafers by photoluminescence mapping and spectroscopy," *Jpn. J. Appl. Phys.*, vol. 45, pp. L641–L643, 2006.

[14] M. Inoue, H. Sugimoto, M. Tajima, Y. Ohshita, and A. Ogura, "Microscopic and spectroscopic mapping of dislocation-related photoluminescence in multicrystalline silicon wafers," *J. Mater. Sci. Mater. Electron.*, vol. 19, pp. S132–S134, 2008.

[15] W. Lee, J. Chen, B. Chen, J. Chang, and T. Sekiguchi, "Cathodoluminescence study of dislocation-related luminescence from small-angle grain boundaries in multicrystalline silicon," *Appl. Phys. Lett.*, vol. 94, pp. 112103-1–112103-3, 2009.

[16] R. P. Schmid, D. Mankovics, T. Arguirov, M. Ratzke, T. Mchedlidze, and M. Kittler, "Rapid dislocation-related D1-photoluminescence imaging of multicrystalline Si wafers at room temperature," *Physica Status Solidi A*, vol. 208, pp. 888–892, 2011.

[17] S. Binetti, A. Le Donne, and M. Acciarri, "Processing step-related upgrading of silicon-based solar cells detected by photoluminescence spectroscopy," *Sol. Energy Mater. Sol. Cells*, vol. 86, pp. 11–18, 2005.

[18] M. P. Peloso, J. S. Lew, P. Chaturvedi, B. Hoex, and A. G. Aberle, "Polarisation analysis of luminescence for the characterisation of defects in silicon wafer solar cells," *Prog. Photovoltaics, Res. Appl.*, vol. 20, pp. 661–669, 2011.

[19] G. Kato, M. Tajima, H. Toyota, and A. Ogura, "Polarized photoluminescence imaging analysis around small-angle grain boundaries in multicrystalline silicon wafers for solar cells," *Jap. J. Appl. Phys.*, vol. 53, pp. 080303-1–080303-3, 2014.

[20] M. Tajima, Y. Iwata, F. Okayama, H. Toyota, H. Onodera, and T. Sekiguchi, “Deep-level photoluminescence due to dislocations and oxygen precipitates in multicrystalline Si,” *J. Appl. Phys.*, vol. 111, pp. 113523-1–113523-6, 2012.

[21] T. Sekiguchi and K. Sumino, “Cathodoluminescence study on dislocations in silicon,” *J. Appl. Phys.*, vol. 79, pp. 3253–3260, 1996.

[22] I. Burud, A. S. Flø, and E. Olsen, “On the origin of inter band gap radiative emission in crystalline silicon,” *AIP Advances*, vol. 2, pp. 042135-1–042135-7, 2012.

[23] C. Krause, D. Mankovics, H.-M. Krause, Tz. Arguirov, and M. Kittler, “On the origin of intense luminescence at 0.93 eV from multi-crystalline silicon,” *J. Appl. Phys.*, vol. 114, pp. 034902-1–034902-6, 2013.

[24] S. P. Phang and D. Macdonald, “Direct comparison of boron, phosphorus, and aluminum gettering of iron in crystalline silicon,” *J. Appl. Phys.*, vol. 109, pp. 073521–1–073521-6, 2011.

[25] A. Y. Liu and D. Macdonald, “Precipitation of iron in multicrystalline silicon during annealing,” *J. Appl. Phys.*, vol. 115, pp. 114901-1–114901-10, 2014.

[26] P. Gundel, M. C. Schubert, and W. Warta, “Simultaneous stress and defect luminescence study on silicon,” *Physica Status Solidi A*, vol. 207, pp. 436–441, 2010.

[27] D. Macdonald, A. Y. Liu, and S. P. Phang, “External and internal gettering of interstitial iron in silicon for solar cells,” *Solid State Phenom.*, vol. 205, pp. 26–33, 2013.

[28] M. Tajima, M. Ikebe, Y. Ohshita, and A. Ogura, “Photoluminescence analysis of iron contamination effect in multicrystalline silicon wafers for solar cells,” *J. Electron. Mater.*, vol. 39, pp. 747–750, 2010.

[29] K. L. Shaklee and R. E. Nahory, “Valley-orbit splitting of free excitons? The absorption edge of Si,” *Phys. Rev. Lett.*, vol. 24, pp. 942–945, 1970.

Authors’ photographs and biographies not available at the time of publication.

CHAPTER 6

Characterization of Heavily-Doped Layers in Solar Cells by Photoluminescence Spectroscopy

Heavily-doped layers are critical components of crystalline silicon solar cells. They form the required p-n junctions which allow separation of free electrons and holes. Metal contacts are then placed directly on these heavily-doped layers to extract the photo-induced current. However, due to their high dopant densities and direct contacts with metal, the heavily-doped layers are often very recombination active, and hence can reduce the cell performance significantly. Therefore, there is often a requirement to minimize the surface area of the heavily-doped layers in order to achieve high efficiency solar cells. In practice, the localized heavily-doped regions can be formed through different doping techniques, such as thermal diffusion followed by an etch-back step, ion implantation, or laser doping. However, unlike the conventional thermal diffusion process which covers the entire wafer surface and is rather laterally homogeneous, these localized doping techniques often generate lateral non-

uniformities of the dopant density across the doped regions. As a result, it is more challenging to assess the dopant density variation of these micron-scale heavily-doped regions contactlessly and non-destructively. Conventional techniques to characterize the dopant concentration such as Electro-chemical Capacitance-Voltage (ECV), four-point probe, or Secondary-Ion Mass-Spectroscopy (SIMS) have limitations due to either their spatial resolutions or their destructive natures.

In heavily-doped silicon, the band gap is narrowed. Therefore, the band-to-band photoluminescence spectrum is shifted to longer wavelengths or lower energies. In principle, both the luminescence spectral shape and the luminescence intensity should reflect the dopant density of the silicon wafers. However, in practical applications of spectrally-resolved photoluminescence, in order to minimize the surface recombination and to have a uniform carrier distribution across the wafer thickness, the excitation wavelength employed to excite the samples is often within the red to near-infrared region. Therefore, the luminescence signal emitted from the thin heavily-doped layer near the wafer surface is usually negligible compared to the signal emitted from the underlying silicon substrate.

As discussed in Chapter 1, if an appropriate excitation wavelength is employed, the excitation light will be absorbed in both the heavily-doped layer and the underlying substrate, giving rise to two band-to-band spectra. However, at room temperature, the two band-to-band peaks are very broad, and thus they significantly overlap together, making it difficult to observe them individually. On the other hand, at low temperatures, the band-to-band peaks are very sharp, and the two spectra can be unambiguously distinguished. Therefore, by examining the relative positions and intensities of these two band-to-band luminescence peaks at low temperatures, one, in principle, can assess the dopant density of the heavily-doped layer qualitatively.

Therefore, combining the advantages of the micro photoluminescence spectroscopy system and the luminescence phenomena at low temperatures described above, this chapter reports and explains a new method which allows the qualitative assessment of the dopant density of micron-scale structures in silicon wafers and solar cell precursors. The technique is then applied to various localized diffused and laser-doped regions, highlighting the significance of this micron-scale technique in silicon photovoltaics.

The work has been published. However, there is an important point that needs to be clarified in this publication. The two main luminescence peaks at 1130 nm and 1160 nm, denoted as "Si BB" and "diffused BB" peaks in the publication, are the band-to-band emission assisted by a Transverse-Optical (TO) phonon from the Si substrate and the heavily-doped layer, respectively. The two shoulders at 1195 nm and 1225 nm, denoted as "Si BBTO" and "diffused BBTO", are therefore the band-to-band emission involving both a TO phonon plus an optical zone center phonon.

Phys. Status Solidi RRL **9**, No. 4, 230–235 (2015) / **DOI** 10.1002/pssr.201510049

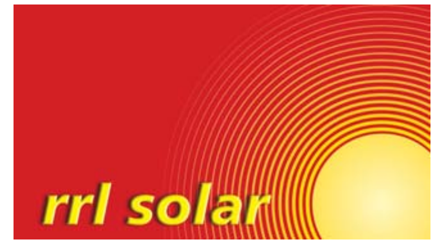

Micro-photoluminescence spectroscopy on heavily-doped layers of silicon solar cells

Hieu T. Nguyen[*,1], **Di Yan**[1], **Fan Wang**[2], **Peiting Zheng**[1], **Young Han**[1], **and Daniel Macdonald**[1]

[1] Research School of Engineering, College of Engineering and Computer Science, The Australian National University, Canberra, ACT 2601, Australia
[2] Department of Electronic Materials Engineering, Research School of Physics and Engineering, The Australian National University, Canberra, ACT 2601, Australia

Received 12 February 2015, revised 3 March 2015, accepted 3 March 2015
Published online 6 March 2015

Keywords band gaps, crystals, silicon, doping, photoluminescence, solar cells

[*] Corresponding author: e-mail hieu.nguyen@anu.edu.au

We report and explain the photoluminescence spectra emitted from silicon solar cells with heavily-doped layers at the surface. A micro-photoluminescence spectroscopy system is employed to investigate the total spectrum emitted from both the heavily-doped layer and the silicon substrate with micron-scale spatial resolution. The two regions of the device give rise to separate photoluminescence peaks, due to band-gap narrowing effects in the highly-doped layer. Two key parameters, the absorption depth of the excitation wavelength, and the sample temperature, are shown to be critical to reveal the separate signatures from the two regions. Finally, this technique is applied to locally diffused and laser-doped regions on silicon solar cell pre-cursors, demonstrating the potential value of this micron-scale technique in studying and optimizing locally doped regions.

© 2015 WILEY-VCH Verlag GmbH & Co. KGaA, Weinheim

1 Introduction Spectral photoluminescence (PL) has been demonstrated to be a promising and powerful characterization technique in crystalline silicon. By capturing the band-to-band (BB) photoluminescence signal, fundamental parameters of silicon such as the band-to-band absorption coefficient [1–3], radiative recombination coefficient [2, 4, 5], and temperature [6] and doping dependencies [7, 8] of the silicon band gap have been determined. In addition, spectral PL methods have also been employed as a characterization tool in photovoltaics, for example to extract the diffusion length of minority carriers in silicon wafers [9, 10] and bricks [11], to quantify the light trapping capability of plasmonic structures [12], to examine the impacts of surface reflectance [13, 14] and different carrier profiles [14] on PL spectra, or to evaluate the laser-doped layers of silicon solar cells by applying the band-gap-narrowing effect in heavily-doped silicon [15, 16].

Heavily-doped layers, typically formed by dopant diffusion or laser doping, are critical components of a silicon solar cell, as they form the required p–n junction, and allow electrical contact to be made to the device. However, these heavily doped layers are also often a source of significant carrier recombination in solar cells. Thus there is usually a requirement to minimize the surface area of these layers in order to achieve high efficiency solar cells [17]. Therefore, an insightful understanding of the PL spectra emitted from the heavily-doped layers of silicon solar cells with high spatial resolution will facilitate the development of precise characterization tools for silicon photovoltaics.

Micro-photoluminescence spectroscopy has been applied previously on carefully cross-sectioned and polished solar cell pre-cursors [15, 16] to reveal the depth profile of highly-doped regions, based on the shift of the PL peak caused by band-gap narrowing. This method is restricted to relatively thick doped layers (tens of microns), such as aluminum-alloyed regions. In this study, we demonstrate a method based on PL spectra measured from above the sample surface, which contain luminescence emitted from both the diffused layer and the underlying silicon substrate. We show that these two regions give rise to distinct PL

© 2015 WILEY-VCH Verlag GmbH & Co. KGaA, Weinheim

peaks, due to band-gap narrowing effects in the heavily-doped layer. The method can be applied to detect heavily-diffused regions with thicknesses below 1 μm, which is more typical for phosphorus and boron-diffused layers in high efficiency silicon solar cells. We then examine two critical parameters allowing an unambiguous identification of the individual components of the combined spectrum emitted by the two layers, the sample temperature and the excitation wavelength. Finally, we demonstrate this method of detecting heavily doped layers on a passivated-emitter rear locally-diffused (PERL) solar cell pre-cursor in which the locally diffused region is a few tens of microns wide. We also apply the method to laser-doped wafers, revealing interesting effects at the edges of the laser doped regions with lateral spatial resolution in the micron range.

2 Background In heavily doped silicon, the intrinsic band gap is reduced [18]. Thus, the PL spectrum emitted from heavily doped silicon is shifted to longer wavelengths, i.e. lower energies. Wagner [7, 8] utilized this phenomenon to determine the extent of band-gap narrowing in silicon, using epitaxially grown silicon layers whose doping densities were homogeneous depthwise.

For solar cells, heavily-doped sub-surface layers are typically formed by thermal diffusion or laser doping, which give rise to relatively shallow (typically less than 1 μm), and inhomogeneously doped layers depthwise. In these cases, if an appropriate excitation wavelength is employed, this excitation light will be absorbed in both the diffused layer and the underlying silicon substrate. These two layers will then both emit PL spectra. The total detected PL spectrum is a superposition of the spectra from the two layers, with the spectrum from the heavily-doped layer being energy-shifted by varying degrees via band-gap narrowing.

However, at room temperature, the BB PL spectrum from silicon is relatively broad [2, 3]. Thus, when the PL spectra from the two regions are combined, the contributions of the individual components from each layer are difficult to distinguish. On the other hand, at cryogenic temperatures, the BB peaks are much sharper due to reduced lattice vibrations [2, 3]. Therefore, the BB peaks from the two layers may be resolved clearly from each other, allowing us to unambiguously detect the presence of the diffused layers.

3 Experimental details The investigated samples were phosphorus-doped n-type float zone silicon wafers whose surfaces were mechanically polished and chemically etched to remove saw damage. Their resistivities were between 1 Ω cm and 10 Ω cm, corresponding to background doping levels between 6×10^{15} cm^{-3} and 6×10^{14} cm^{-3}. These samples were heavily doped with boron from a BBr_3 vapor source (for forming the p+ layer) or phosphorous from a $POCl_3$ vapor source (for the n+ layer) in a quartz tube furnace at high temperatures between 900–1000 °C with various drive-in times to achieve different doping profiles in the diffused layers. The samples were then immersed in HF solution to remove the borosilicate or phosphosilicate glass layers. The doping profiles of the p+ and n+ layers were measured using the electrochemical capacitance–voltage (ECV) technique, and are plotted in Fig. 1b for four representative p+ boron diffused samples. The sample size is about 1 × 1 cm^2, with a thickness of about 400 μm.

The diffused solar cell pre-cursor and laser-doped sample were phosphorus-doped n-type float zone silicon wafers with background doping levels of 2×10^{15} cm^{-3} and 7×10^{14} cm^{-3}, respectively. The diffused pre-cursor went through the standard fabrication steps for PERL n-type cells, which achieve efficiencies above 20%, as described in more detail elsewhere [19]. The rear locally phosphorus-diffused regions were 75 μm in diameter on 300 μm spacing. The dopant source used for the laser-doped sample was a commercial boron spin-on-dopant solution. The laser doping was achieved using a HeCd laser (325 nm wavelength, 4.05 Jcm^{-2} fluence, 25 ns pulse duration, and 320 μm square beam diameter).

The micro-PL spectroscopy system employed in this study is a Horiba T64000 equipped with a confocal microscope. The incident laser beam was focused into a spot of about 1 μm in diameter on the samples using a 50× objective reflective lens. The emitted PL signal was collected by a liquid-nitrogen-cooled InGaAs array detector. The spectral response of the entire system was calibrated with black body thermal radiation. The employed lasers were a continuous wave diode-pumped solid-state (DPSS) laser and a diode laser. The DPSS laser wavelength was 532 nm, corresponding to an absorption depth of about 3.3 μm at 79 K (calculated from Ref. [20]), and on-sample average intensity was 6 mW. The diode laser wavelength was 830 nm, corresponding to an absorption depth of about 45 μm at 79 K, and its power was adjusted to be the same as that of the DPSS laser. The sample temperature was controlled with a liquid-nitrogen cryostat. More details on the setup can be found in Ref. [21]. We simulated the heating effect of the excitation laser on the samples using the *LCPSim* software [22, 23], and found that the local temperature at the center of the illuminated spot was increased less than 6°. In addition, we varied the excitation power from 0.7 mW to 8.5 mW and captured the spectra at 300 K; and then varied the temperature from 300 K to 305 K and captured the spectra with 8.5 mW excitation power. We found that the change in the BB spectrum shape of the former case was very much less than that of the latter, and thus conclude that the degree of local heating due to the excitation laser is insignificant. We note that the samples had no surface passivation layers present during the measurements.

4 Results and analysis First, we examine the combined spectra emitted from the diffused samples at 79 K. Figure 1a shows the normalized PL spectra from four p+ diffused samples, corresponding to two categories: heavy

© 2015 WILEY-VCH Verlag GmbH & Co. KGaA, Weinheim

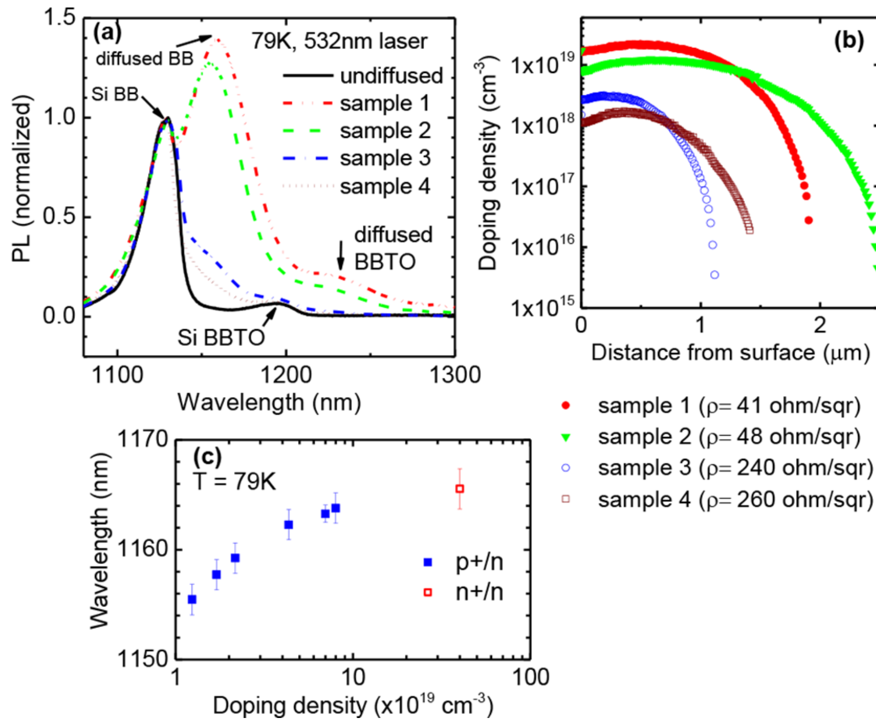

Figure 1 (a) Normalized PL spectra of the four samples with different boron diffusion profiles, measured with the 532 nm laser at 79 K. The spectrum of an undiffused sample is also given for comparison. (b) The corresponding diffusion profiles with the sheet resistances indicated in brackets. (c) Wavelength of the diffused BB peak, along with one standard deviation error bars, versus peak doping density in n+ and p+ layers on n-type substrates.

and deep profiles (samples 1 and 2), and light and shallow profiles (samples 3 and 4). The spectrum from an undiffused sample is also given for comparison. The dopant profiles of the diffused layers are plotted in Fig. 1b. For the case of heavy and deep profiles (samples 1 and 2) in Fig. 1a, two distinct peaks at around 1130 nm and 1160 nm correspond to the BB peak of the silicon substrate (Si BB) and the BB peak of the diffused layer (diffused BB), respectively. The wavelength of the diffused BB peak moves towards longer wavelengths when the doping concentration at the surface is higher (sample 1). In addition, we can observe the transverse-optical phonon replica (shifted by ~60 meV) of the diffused BB peak (diffused BBTO) at around 1225 nm. This phonon replica is the analogue of the transverse-optical phonon replica of the Si BB peak (Si BBTO) at around 1195 nm, which is also depicted in Fig. 1a for the case of light and shallow profiles (samples 3 and 4), and for the undiffused case. For the lighter diffusions, the signal of the diffused BB peak is not strong enough to mask the phonon replica of the Si BB peak.

Note that the energy difference between the two BB peaks is around ~30 meV, which is smaller than the expected energy shift of ~60 meV for the doping concentrations ~1×10^{19} cm^{-3} [24] in comparison to intrinsic silicon. The reason is that the silicon substrate itself is under high injection, thus its BB peak is also partly affected by band-gap narrowing. The average injection level in the silicon substrate was estimated to be between 1×10^{17} cm^{-3} and 1×10^{18} cm^{-3}, for which the silicon band gap is reduced by ~30–40 meV [25, 26]. We note that this band-gap narrowing effect should not be confused with the donor-acceptor pair (DAP) luminescence in compensated silicon [27], since the DAP peak is detected at lower temperatures, and is shifted towards higher energies as the net doping concentration increases [28], whereas the diffused BB peak here is shifted towards lower energies (longer wave

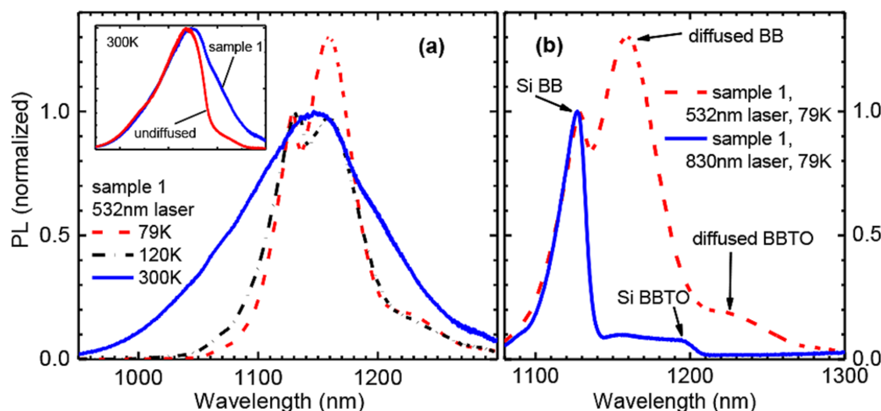

Figure 2 Normalized PL spectra of sample 1, (a) at different temperatures excited with 532 nm laser, and (b) excited with 532 nm and 830 nm lasers at 79 K. The insert compares the normalized spectra of sample 1 and the undiffused sample at 300 K.

© 2015 WILEY-VCH Verlag GmbH & Co. KGaA, Weinheim

lengths). Figure 1c plots the wavelength of the diffused BB peak versus the peak doping concentration in the diffused layer. Since the diffused BB peak is broad, the peak wavelength was determined by taking the average of all points having PL intensities larger than 99% of the maximum value. The peak wavelength clearly increases as the peak doping concentration increases, supporting the suggestion that the peak is due to the band-gap narrowing effect.

Next, we demonstrate the importance of temperature and excitation wavelength on detecting the diffused layers on silicon substrates. Figure 2a shows the normalized spectra of sample 1 at different temperatures. As the temperature increases, the two BB peaks are thermally broadened, and eventually combine together into a very broad peak having a maximum in between the two low temperature BB peaks. Also, the insert compares the spectra of sample 1 and the undiffused sample at 300 K, which have maxima at 1146 nm and 1135 nm, respectively. This wavelength shifting is due to the aggregation of the diffused and Si BB peaks in sample 1. These two spectra are indistinguishable on the lower wavelength side. However, on the higher wavelength side, the heavily doped region gives rise to a clear shoulder, although not a distinct peak. The spectra from the light and shallow profiles (samples 3 and 4) are closer to that of the undiffused sample, and thus the presence of their diffused layer is much more difficult to observe at room temperature. Note that this signature is opposite to the effects caused by non-uniform excess carrier profile and surface reflectivity, in which the higher wavelength side of the normalized spectrum is not affected due to the very long absorption depth of photons in this wavelength region, whereas the low wavelength side is affected more significantly at higher temperatures [14].

In addition, Fig. 2b shows the spectra of sample 1 excited with both 532 nm and 830 nm lasers. Since the absorption depth of the 830 nm laser is about 45 μm at 79 K [20], the laser light is mostly absorbed in the silicon substrate, and thus the signature of the diffused layer is suppressed significantly. This suggests that only the diffused BB peak may be observed if the sample is illuminated with an ultraviolet laser, for example with a 325 nm HeCd laser having an absorption depth of less than 0.01 μm at 79 K. The results from this figure confirm that the peak at around 1160 nm is emitted from the layer close to the surface, and is associated with the diffused layer in this study. Therefore, employing an appropriate excitation wavelength and performing the measurements at low temperatures are essential to observe the two separate BB peaks.

We also captured the spectra at numerous different locations for several samples, and found that despite a small change in the relative PL intensity, the spectrum shape from each sample is consistently unchanged regardless of the locations, indicating a high degree of spatial homogeneity of the diffused layers. This property could be potentially applied to directly characterize the spatial homogeneity of the diffused layers on silicon solar cells and cell precursors, which could be particularly useful for studying locally-diffused or laser-doped regions.

Furthermore, we examine the effect of excitation power on the spectrum shape. Unlike the undiffused silicon sample whose spectrum shape does not change with a small variation of excitation power, the spectrum shape of the diffused sample displays a notable dependence on excitation power. Figure 3 shows the normalized spectra of sample 1 with different excitation powers from the 532 nm laser at 79 K. The normalized Si BB peak is saturated whereas the normalized diffused BB peak is reduced with increasing excitation power. The reason is that the average injection level was estimated to be between 1×10^{17} cm^{-3} and 1×10^{18} cm^{-3}, whereas the doping density in the diffused layer near the surface is around 2×10^{19} cm^{-3}, while that in the silicon substrate is around 1×10^{15} cm^{-3}. Thus, the silicon substrate is under high injection level whereas the diffused layer is still in the low injection regime. Therefore, the dependence of the BB peak intensities on the excitation power is different for the two layers. Since the PL intensity $\sim(N_D + \Delta n) \times \Delta n$ where N_D is the doping density and Δn is the excess carrier density [14], the PL signal is expected to be approximately linearly proportional to Δn in the diffused layer, but should be a quadratic function of Δn in the silicon substrate. When the excitation power is increased, the PL signal of the diffused layer increases more slowly than that of the substrate, and thus the normalized diffused BB peak is less pronounced. When the dopant concentration of the diffused region is reduced, this effect is reduced.

Finally, we demonstrate this method on a locally n+ diffused region of a PERL n-type silicon solar cell precursor, and on an edge of the p+ region of a laser-doped sample. The profile of the localized n+ region on the rear is given in Fig. 4a. This profile was measured using the ECV technique on a control wafer undergoing the same diffusion process. The 3D optical surface image of the edge of the laser-doped p+ region is given in Fig. 4d. The raised

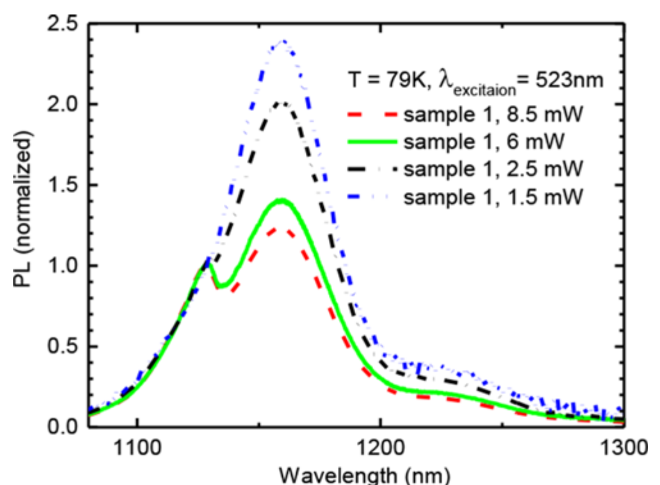

Figure 3 Excitation power dependence of normalized PL spectra of sample 1, measured with the 532 nm laser at 79 K.

© 2015 WILEY-VCH Verlag GmbH & Co. KGaA, Weinheim

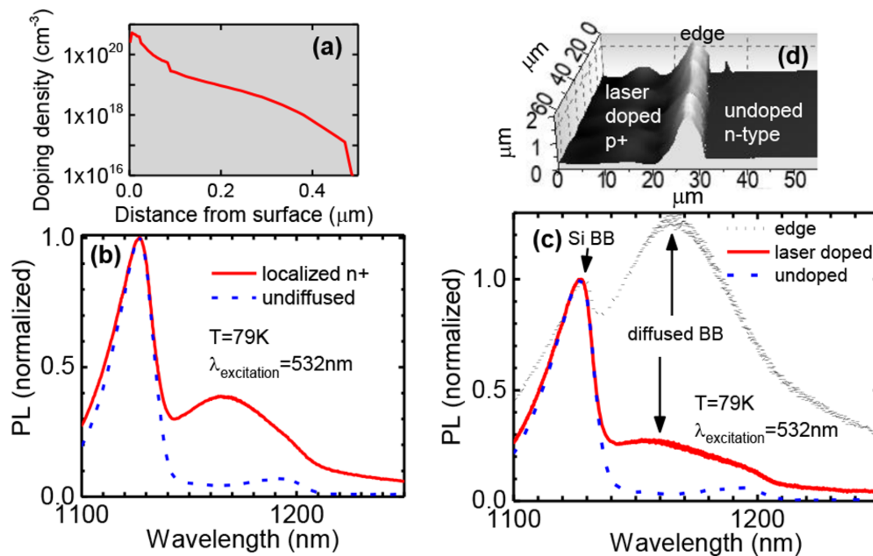

Figure 4 Normalized PL spectra (b) of the localized n+ and undiffused regions of the PERL solar cell precursor and (c) of the p+, undoped, and edge regions of the laser-doped sample, excited with the 532 nm laser at 79 K. (a) Diffusion profile of the localized n+ region of the precursor. (d) 3D optical surface image of the edge of the laser-doped p+ region.

edge region is about 5 μm wide and 2 μm higher than the surface of the p+ and undoped regions. Figure 4b and c show the normalized spectra captured from the n+ and undiffused regions of the precursor, and from the three regions (p+, undoped, and edge) of the laser-doped sample. For the diffused precursor, in Fig. 4a and b, the diffused profile (heavy but shallow) lies between the two categories examined above, so the diffused BB peak in this case is somewhere between the two cases in Fig. 1a. For the laser-doped sample, in Fig. 4c, the diffused BB peak of the edge is notably higher than that of the p+ region, and its peak energy is shifted slightly to longer wavelengths compared to that of the p+ region. These features indicate that the edge is doped more heavily than the p+ region. In our experimental setup, this technique is effective for diffused layers having doping concentrations as low as 1×10^{18} cm^{-3} (sample 4 in Fig. 1a). In practice, the doping levels of the n+ and p+ regions in solar cell applications are generally higher than this concentration. Therefore, this technique can provide a measure of the lateral extent of heavily-doped layers with micron-scale resolution, and may be extended to allow quantitative estimates of the dopant concentrations in such heavily-doped regions.

5 Conclusions Utilizing the doping dependence of the band gap in silicon, we have demonstrated a contactless and non-destructive spectral photoluminescence technique to detect thin heavily-doped layers on silicon substrates with micron-scale spatial resolution. In addition, we have empirically shown the importance of appropriate excitation wavelengths and sample temperature in order to separate the signatures of the two layers. Finally, we have demonstrated this technique on a silicon solar cell pre-cursor whose diffused regions are several tens of microns wide, and on a laser-doped damaged edge whose width is only several microns.

Acknowledgements This work has been supported by the Australian Research Council (ARC) and the Australian Renewable Energy Agency (ARENA) through research grant RND009. The Australian National Fabrication Facility is acknowledged for providing access to some of the facilities used in this work. The authors are in debt to Prof. H. Tan for providing access to the spectroscopic equipment and for commenting on the manuscript, Dr. A. Fell for assisting with the LCPSim simulation, and Dr. S. P. Phang and Dr. F. E. Rougieux for assisting with some measurements.

References

[1] E. Daub and P. Würfel, Phys. Rev. Lett. **74**, 1020 (1995).
[2] T. Trupke, M. A. Green, P. Würfel, P. P. Altermatt, A. Wang, J. Zhao, and R. Corkish, J. Appl. Phys. **94**, 4930 (2003).
[3] H. T. Nguyen, F. E. Rougieux, B. Mitchell, and D. Macdonald, J. Appl. Phys. **115**, 043710 (2014).
[4] P. P. Altermatt, F. Geelhaar, T. Trupke, X. Dai, A. Neisser, and E. Daub, Appl. Phys. Lett. **88**, 261901 (2006).
[5] H. T. Nguyen, S. C. Baker-Finch, and D. Macdonald, Appl. Phys. Lett. **104**, 112105 (2014).
[6] W. Bludau, A. Onton, and W. Heinke, J. Appl. Phys. **45**, 1846 (1974).
[7] J. Wagner, Phys. Rev. B **29**, 2002 (1984).
[8] J. Wagner, Phys. Rev. B **32**, 1323 (1985).
[9] P. Würfel, T. Trupke, T. Puzzer, E. Schäffer, W. Warta, and S. W. Glunz, J. Appl. Phys. **101**, 123110 (2007).
[10] J. A. Giesecke, M. Kasemann, M. C. Schubert, P. Würfel, and W. Warta, Prog. Photovolt.: Res. Appl. **18**, 10 (2011).
[11] B. Mitchell, M. K. Juhl, M. A. Green, and T. Trupke, IEEE J. Photovolt. **3**, 962 (2013).
[12] C. Barugkin, Y. Wan, D. Macdonald, and K. R. Catchpole, IEEE J. Photovolt. **3**, 1292 (2013).
[13] C. Schinke, D. Hinken, J. Schmidt, K. Bothe, and R. Brendel, IEEE J. Photovolt. **3**, 1038 (2013).
[14] H. T. Nguyen, F. E. Rougieux, S. C. Baker-Finch, and D. Macdonald, IEEE J. Photovolt. **5**, 77 (2015).

© 2015 WILEY-VCH Verlag GmbH & Co. KGaA, Weinheim

[15] R. Woehl, P. Gundel, J. Krause, K. Rühle, F. D. Heinz, M. Rauer, C. Schmiga, M. C. Schubert, W. Warta, and D. Biro, IEEE Trans. Electron Devices **58**, 441 (2011).
[16] P. Gundel, D. Suwito, U. Jäger, F. D. Heinz, W. Warta, and M. C. Schubert, IEEE Trans. Electron Devices **58**, 2874 (2011).
[17] A. Wang, J. Zhao, and M. A. Green, Appl. Phys. Lett. **57**, 602 (1990).
[18] R. A. Abram, G. J. Rees, and B. L. H. Wilson, Adv. Phys. **27**, 799 (1978).
[19] Y. Wan, C. Samundsett, T. Kho, J. McKeon, L. Black, D. Macdonald, A. Cuevas, J. Sheng, Y. Sheng, S. Yuan, C. Zhang, Z Feng, and P. J. Verlinden, in: Proc. IEEE, 40th Photovoltaic Spec. Conf., Denver, Colorado (2014).
[20] M. A. Green, Sol. Energy Mater. Sol. Cells **92**, 1305 (2008).
[21] H. T. Nguyen, F. E. Rougieux, F. Wang, H. Tan, and D. Macdonald, Micron-scale deep-level spectral photoluminescence from dislocations in multicrystalline silicon, IEEE J. Photovolt., accepted for publication (2015).
[22] A. Fell and G. P. Willeke, Appl. Phys. A **98**, 435 (2010).
[23] A. Fell, Modelling and simulation of laser chemical processing (LCP) for the manufacturing of silicon solar cells, Ph.D. dissertation, Fraunhofer Institute for Solar Energy Systems (2010).
[24] J. Wagner and J. A. del Alamo, J. Appl. Phys. **63**, 425 (1988).
[25] J. W. Slotboom and H. C. de Graaff, Solid-State Electron. **19**, 857 (1976).
[26] M. Y. Ghannam and R. P. Mertens, Microelectron. Eng. **19**, 691 (1992).
[27] M. Tajima, T. Iwai, H. Toyota, S. Binetti, and D. Macdonald, J. Appl. Phys. **110**, 043506 (2011).
[28] B. D. Rezgui, J. Veirman, S. Dubois, and O. Palais, Phys. Status Solidi A **209**, 1917 (2012).

© 2015 WILEY-VCH Verlag GmbH & Co. KGaA, Weinheim

CHAPTER 7

Characterization of Dislocations in Laser-Doped Silicon by Photoluminescence Spectroscopy

In order to reduce the surface recombination induced by the heavily-doped layers, their surface area should be minimized. Although thermal diffusion is still a common doping technique in silicon solar cell research, photolithography-based wet chemical processing is required to create the localized doped regions. The process complexity of this technique prevents it from being widely used for industrial scales. On the other hand, laser doping is considered as a potentially attractive doping technique in industry due to its high throughput and process simplicity. The advantages of the laser doping technique are that it melts only a few micrometers of the material near the wafer surface without disturbing the bulk, due to the very short duration and penetration depth of the laser pulse; and the laser beam diameter and position can be controlled precisely. Therefore, micron-scale localized doped regions can be fabricated with high lateral precisions.

However, the laser doping process is also known to frequently introduce high levels of crystal damage. The damage can, in turn, degrade electrical properties of finished devices. Microscopic pictures of the damage can be investigated by different methods including Transmission Electron Microscopy (TEM) and Scanning Electron Microscopy (SEM). However, these methods are destructive and require complicated sample preparation steps. Common electrical and optical characterization methods such as Electron Beam Induced Current (EBIC) or photoluminescence imaging cannot differentiate the effects of the dopant and the damage since both of them simultaneously affect the recombination activity in the heavily-doped regions.

As discussed in Chapter 5, defects and impurities can occupy energy levels inside the silicon band gap, and emit deep-level photoluminescence spectra. However, unlike the structural defects formed during the ingot growth and cooling, which are distributed uniformly depth-wise in the wafers, the laser-induced crystal damage is confined to the thin heavily-doped layers below the surface. Therefore, in order to excite sufficient luminescence from the laser-induced damage, the excitation wavelength needs to be in an appropriate range. If it is too short, the excitation light will be absorbed in sub-nanometer layers at the surface, in which case the surface recombination is the dominant phenomenon. If it is too long, the excitation light will be absorbed mostly in the underlying substrate, and thus the band-to-band luminescence from the silicon substrate will dominate the total spectrum. When an appropriate excitation wavelength is used, the laser is absorbed in both layers, and the detected spectrum contains three components: the band-to-band luminescence from the underlying substrate, the band-to-band luminescence from the heavily-doped layer, and the deep-level luminescence from the laser-induced damage. They are different physical mechanisms, and in principle, they should have different dependences on the excitation power and the temperature.

This chapter continues utilizing the micro-photoluminescence spectroscopy system and low temperature measurements to evaluate the damage induced by the laser doping process. By comparing with the photoluminescence properties of dislocations, the laser-induced damage is confirmed to be related to dislocations, and the edges of the laser-doped regions are found to contain much more damage than inside the laser-doped regions.

The work has been published. However, there is an important point that needs to be clarified in this publication. The two luminescence peaks at 1130 nm and 1160 nm, denoted as "SiBB" and "HDBB" peaks in the publication, are the band-to-band emission assisted by a Transverse-Optical (TO) phonon from the Si substrate and the heavily-doped layer, respectively.

APPLIED PHYSICS LETTERS **107**, 022101 (2015)

Dislocations in laser-doped silicon detected by micro-photoluminescence spectroscopy

Hieu T. Nguyen,[a] Young Han, Marco Ernst, Andreas Fell, Evan Franklin, and Daniel Macdonald
Research School of Engineering, College of Engineering and Computer Science, The Australian National University, Canberra ACT 2601, Australia

(Received 14 May 2015; accepted 8 June 2015; published online 13 July 2015)

We report the detection of laser-induced damage in laser-doped layers at the surface of crystalline silicon wafers, via micron-scale photoluminescence spectroscopy. The properties of the sub-band-gap emission from the induced defects are found to match the emission characteristics of dislocations. Courtesy of the high spatial resolution of the micro-photoluminescence spectroscopy technique, micron-scale variations in the extent of damage at the edge of the laser-doped region can be detected, providing a powerful tool to study and optimize laser-doping processes for silicon photovoltaics. © *2015 AIP Publishing LLC*. [http://dx.doi.org/10.1063/1.4926360]

Recently, there has been growing interest in employing micro-photoluminescence spectroscopy (μPLS) as a non-destructive and precise characterization tool in silicon photovoltaics (PV). With the advantages of high spatial and spectral resolution, μPLS techniques have been utilized to pinpoint micron-scale features of defects and impurities in crystalline silicon (c-Si), such as Fe precipitates,[1] dislocations,[2–6] or internal stress.[7] Besides that, μPLS has been also employed to extract minority carrier lifetimes around grain boundaries in multicrystalline silicon (mc-Si) wafers,[8] to quantify doping densities in laser-doped regions,[9–12] and to detect very thin localized diffusion layers.[13] On the other hand, laser doping has been demonstrated to be an effective method to create heavily doped regions required for junction and contact formation in high efficiency silicon solar cells.[14–17] Despite the precision and simplicity of laser doping compared to doping techniques such as thermal diffusion or ion implantation, laser doping has been known to induce dislocations in the heavily doped layers, which in turn can have detrimental effects on final cell performance.[18–20] Moreover, a challenge in the characterization of laser-doped regions is the strong spatial non-uniformity on the micron scale, in particular, at potentially highly defective edge regions.[21–23]

In this study, we demonstrate the micron-scale detection of laser-induced dislocations embedded in the highly doped layers using μPLS. We first compare and explain the PL spectra emitted from different regions of laser-doped silicon wafers, including at the edges of the doped regions. We then demonstrate that the observed sub-band-gap PL signal is due to dislocations by comparing its energy position and temperature dependence with those of the well-known dislocation-related "D-lines" from mc-Si wafers. Finally, we also report and explain the observed excitation power dependence of the dislocation PL intensity.

First, we describe the underlying principles of this approach. When illuminated by appropriate excitation wavelengths, silicon wafers with thin heavily doped layers at the surface give rise to two separate peaks in their photoluminescence spectra at low temperatures,[13] courtesy of band-gap narrowing effects in the heavily doped layer.[24,25] On the other hand, dislocations in c-Si are known to emit distinct sub-band-gap PL lines besides the band-to-band (BB) line at low temperatures.[2–6] The laser-doping process can induce structural defects, in particular, dislocations, during the solidification phase of molten silicon.[18–20] Therefore, at low temperatures, PL spectra from laser-doped silicon wafers could be expected to contain three different components originating from three different mechanisms. The first component is emitted by the radiative recombination of free carriers between the two band edges from the underlying silicon substrate, referred to here as SiBB (Silicon Band-to Band). The second component is also band-to-band radiation, but emitted from the thin laser-doped layer, and therefore, subject to a shift to longer wavelengths due to band-gap narrowing effects in this heavily doped layer, referred to as HDBB (heavily doped band-to-band). The third component is due to laser damage caused by the laser-doping process, referred to as LD (laser damage). These three components cannot be distinguished from each other at room temperature, since the SiBB and HDBB lines merge into a very broad peak due to thermal broadening; and the luminescence from dislocations is almost absent since most of the carriers trapped at the defect levels are thermally excited back to their corresponding band edges.[26–29]

A description of the experimental setup of our μPLS system can be found in Refs. 6 and 13. This μPLS system has a spectral resolution of 0.25 nm. The employed excitation sources were a continuous wave 532-nm diode-pumped solid-state (DPSS) laser and an 830-nm laser diode. For both lasers, the on-sample laser spot size was about 1 μm in diameter, and the on-sample excitation power was about 6 mW. The spectral response of the entire system was determined with a calibrated halogen-tungsten light source. The investigated sample was a phosphorus-doped n-type float zone silicon wafer with a background doping level of $7 \times 10^{14}\,\mathrm{cm}^{-3}$. It was chemically etched with tetramethylammonium hydroxide (TMAH) solution for 10 min to remove saw damage.

[a]Author to whom correspondence should be addressed. Electronic mail: hieu.nguyen@anu.edu.au

This article is copyrighted as indicated in the article. Reuse of AIP content is subject to the terms at: http://scitation.aip.org/termsconditions. Downloaded to IP: 150.203.210.78 On: Tue, 03 Nov 2015 08:13:07

The dopant source used for the laser-doping process was a commercial boron spin-on-dopant solution. The laser doping was achieved using a KrF laser having 248-nm wavelength, 3.9-J.cm^{-2} fluence, 25-ns pulse duration, and 320-μm square laser spot size.[17,30] Note that these laser parameters, with a relatively high fluence and a homogenous spot instead of the more typical Gaussian beam shape, are different from those commonly used in silicon solar cell applications. They were used in this case to achieve a moderately high level of damage and a narrow, distinctive edge region, which best illustrates the capabilities of the presented characterization method. A 3D optical surface image of the edge of the investigated laser-doped region is given in Figure 1(a). Due to the high laser fluence, the edge is heavily damaged, giving a very inhomogeneous surface structure. This damaged edge is several microns higher than the wafer surface and about 10-μm wide.

Figure 1(b) plots the normalized PL spectra captured at different locations including the doped, undoped, and the edge (interface between doped and undoped) regions, excited by the 532-nm laser at 79 K. Compared to the undoped region, both the edge and doped regions give rise to a very strong PL peak located around 1270 nm. This peak is due to the damage caused by the laser-doping process. Moreover, at the edge region, this LD peak is so intense that the SiBB peak is completely quenched. Thus, we normalized the spectrum from the edge region to the LD peak, instead of to the SiBB peak. The results suggest that the edge region is much more heavily damaged by the laser doping than the doped region itself, which can have a significant impact on device performance. Figure 1(a) also includes the spectrum from the same location in the doped region, but excited by the 830-nm laser. Since the absorption depth of the 830-nm excitation wavelength is about 45 μm at 79 K, compared to 3 μm for the 532-nm laser (calculated from Ref. 31), most of the 830-nm laser light is absorbed in the silicon substrate. Therefore, the LD peak is nearly absent in the PL spectrum from the doped region when illuminated by the 830-nm laser. This result confirms that the LD peak located around 1270 nm comes from the near-surface region.

As discussed above, at low temperatures, the spectra from the edge and doped regions should contain the HDBB peak associated with the heavily doped layer, due to bandgap narrowing effects in this layer. This HDBB peak is absent in Figure 1(b), since it has been completely masked by the very intense and broad LD peak. However, defect luminescence usually displays a very strong thermal quenching rate, since more carriers trapped at defect levels in the forbidden gap can be thermally activated and return to their nearest band edges with increasing temperatures.[26–29] Hence, as the temperature increases, the LD peak should be suppressed and the HDBB peak may appear. Figure 1(c) shows the change of the spectrum shape from the laser-doped region as the temperature increases, excited by the 532-nm laser. The HDBB peak is clearly revealed at 150 K due to the suppression of the LD peak. At room temperature, the LD peak almost disappears and only a very broad peak located around 1140 nm is present. This broad peak at room temperature is the aggregate PL signal of both the SiBB and HDBB lines.[13] Note that there is also a very sharp peak located at 1064 nm on all spectra. This is not the entirely suppressed 1064-nm component from the 532-nm DPSS laser.

Now, we verify that the LD line is due to dislocations, which are known to be induced by the laser-doping process.[18–20] Dislocations are known to be the underlying cause for four distinct deep-level PL lines, namely, D1, D2, D3, and D4 at low temperatures.[2–6] The D3 and D4 lines have been confirmed to reflect the intrinsic properties of dislocations whereas the D1 and D2 lines have been demonstrated to be emitted by other defects and impurities trapped around dislocation sites.[4–6] Thus, we may expect the LD line to match the D3 and D4 lines.

Figure 2(a) plots the deep-level PL spectrum of dislocations captured at a sub-grain boundary in the mc-Si wafer from Ref. 6 at 79 K. The D4 and D3 lines have their peak locations around 1230 and 1300 nm, respectively. The D4 line's peak location has been shifted by ~100 nm compared to that of the SiBB line. This shift is similar to the shift between the LD and HDBB lines observed here. Note that this particular sub-grain boundary was chosen for comparison as it yielded strong D3 and D4, but very low D1 and D2 emissions (see Ref. 6 for more details on the properties of these D lines). In addition, Figure 2(b) plots the intensities of the D3, D4, and LD lines versus temperature. Each individual line was decomposed from their corresponding spectra using Gaussian functions.[6] The amplitude of each resultant Gaussian function is the peak intensity of its corresponding line. In Figure 2(b), the thermal dependence of the LD line is very similar to that of both D3 and D4 lines. Thus, all three lines should have a similar activation energy E_A, which can

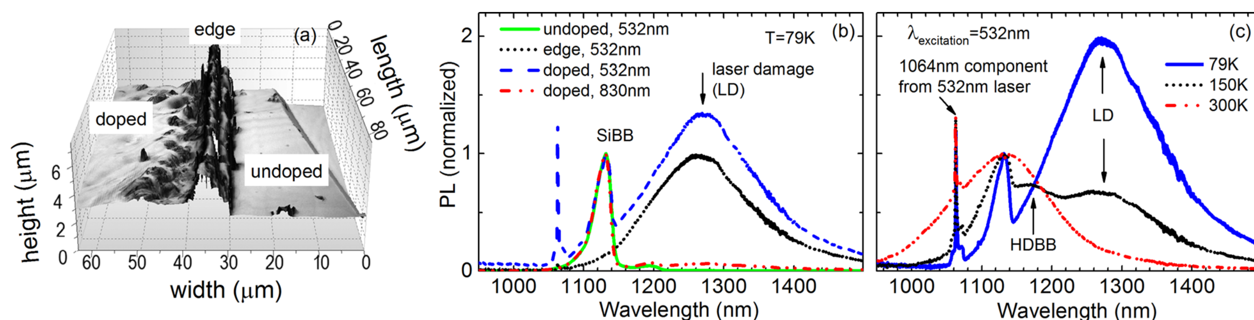

FIG. 1. (a) 3D optical surface image at the edge of the laser-doped region. (b) Normalized PL spectra of the undoped, edge, and doped regions, excited by the 532-nm and 830-nm lasers at 79 K. The spectrum of the edge was normalized to the LD peak, whereas those of the doped and undoped regions were normalized to the SiBB peak. (c) Temperature dependence of normalized PL spectra from the doped region, excited by the 532-nm laser.

This article is copyrighted as indicated in the article. Reuse of AIP content is subject to the terms at: http://scitation.aip.org/termsconditions. Downloaded to IP: 150.203.210.78 On: Tue, 03 Nov 2015 08:13:07

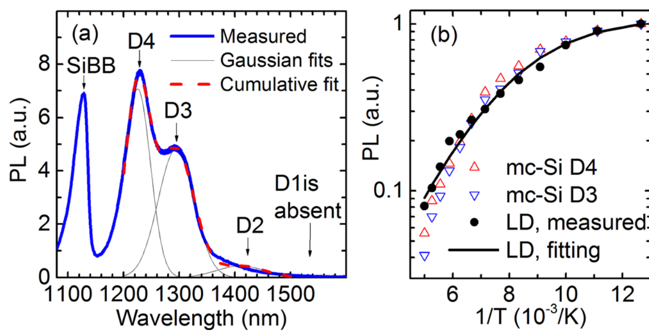

FIG. 2. (a) PL spectrum from dislocations at a sub-grain boundary of a mc-Si wafer, excited by the 532-nm laser at 79 K. (b) Temperature dependence of peak intensities of the LD, D3, and D4 lines, excited by the 532-nm laser.

be extracted by fitting the equation below with the experimental data[26–29]

$$I(T) = \frac{I_0}{1 + CT^{3/2}\exp\left(-\frac{E_A}{kT}\right)}, \quad (1)$$

where $I(T)$ is the PL intensity at a certain absolute temperature T, I_0 is a constant, C is a fitting parameter, and k is Boltzmann's constant. The factor $T^{3/2}$ accounts for the effective density of states in the band edge. The derivation and meaning of these parameters are explained in detail in Ref. 26. Fitting the data in Figure 2(b) gives E_A of 38, 43, and 46 meV for the LD, D4, and D3 lines, respectively, which are within experimental uncertainty. The fitting of Eq. (1) for the LD line is also plotted in Figure 2(b). Note that above 150 K, the slope of the LD line is somewhat lower than that of the D3 and D4 lines. This discrepancy may be explained by the fact that the damage is in the near-surface region whose thickness is only about 1 μm, and the absorption depth of the laser is shorter at higher temperatures. Therefore, more 532-nm laser light is absorbed in the laser-doped region at higher temperatures, contributing more to the relative LD intensity. Meanwhile, for the mc-Si wafer, the dislocation density is expected to be uniform depthwise, and thus, the changing absorption depth is not expected to affect the slopes of D3 and D4 for that sample.

Since the energy difference between LD and HDBB is similar to that between D4 and SiBB, and the activation energy E_A of LD is also similar to that of D4 from dislocations, we conclude that this LD line is emitted by dislocation sites formed during the laser-doping process. The large difference in the full-width at half-maximum (FWHM) between LD and D4 may be explained by two reasons. The first is caused by the fact that the doping profile of the heavily doped layer is not homogeneous depthwise. Therefore, LD is in fact the combined emission from layers of different doping densities, which are shifted by varying amounts due to changing band-gap narrowing, thus leading to a broader peak than D4 emitted from a sample with a homogenous doping density depthwise. Another possibility is that LD may contain components of both D3 and D4, and these two lines are also broadened due to the inhomogeneous doping profile. However, decomposing these two lines from the broad LD line is difficult since the peaks of D3 and D4 in this case are very broad and not well-defined compared to those of the mc-Si wafer.

Next, we investigate the dependence of the LD line on the excitation power. Figure 3(a) plots the normalized PL spectra from the doped region with various 532-nm excitation powers at 79 K. Similar to the case of diffused silicon wafers,[13] the spectra from the damaged laser-doped region show a strong dependence on the excitation power due to different injection dependencies of the PL signals from the two different layers—the heavily doped layer and the underlying silicon substrate. However, within the heavily doped layer, the HDBB and LD lines also show different injection dependencies from each other due to different recombination mechanisms. The D3 and D4, and thus LD, lines were demonstrated to be emitted by the recombination of trapped carriers between a deep level (E_D) and a shallow level (E_S),[26–29] as illustrated in Figure 3(b). This two-level model is implied from the very strong temperature dependence of D3 and D4, which suggests the participation of shallow levels; and also from the relatively large energy difference between these two lines and the BB line, which suggests the presence of deeper levels. Here, we assume that E_D and E_S are closer to the conduction band (E_C) and the valance band (E_V), respectively. Hence, the energy difference between E_S and E_V is the activation energy E_A in Eq. (1). In case E_D and E_S swap their positions, the following explanation is still valid by simply swapping the roles of electrons and holes.

The radiative recombination rate between the two levels E_D and E_S depends on the product of the number of electrons trapped at E_D and the number of holes trapped at E_S. The occupational probability of electrons at E_D is given by[26,32]

$$f_e(E_D) = \frac{1}{1 + \exp\left(\frac{E_D - E_{FC}}{kT}\right)}, \quad (2)$$

with E_{FC} being the quasi-Fermi level of electrons under illumination.

The number of free electrons located around the defect centers is determined by[32]

$$n_e = N_C \exp\left(\frac{E_{FC} - E_C}{kT}\right), \quad (3)$$

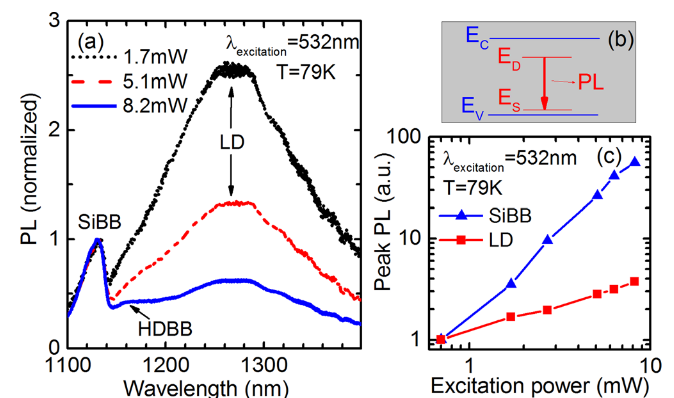

FIG. 3. (a) Excitation power dependence of normalized PL spectra from the laser-doped region, excited by the 532-nm laser at 79 K. (b) Illustration for the recombination scheme of deep-level PL. (c) Peak intensities of the LD and SiBB lines versus 532-nm excitation power at 79 K.

This article is copyrighted as indicated in the article. Reuse of AIP content is subject to the terms at: http://scitation.aip.org/termsconditions. Downloaded to IP: 150.203.210.78 On: Tue, 03 Nov 2015 08:13:07

where N_C is the effective density of states in the conduction band.

Combining Eqs. (2) and (3) yields

$$f_e(E_D) = \frac{1}{1 + \frac{N_C}{n_e}\exp\left(\frac{E_D - E_C}{kT}\right)}. \quad (4)$$

N_C and kT are $\sim 4 \times 10^{18}\,\mathrm{cm}^{-3}$ and $\sim 7\,\mathrm{meV}$ at 79 K, respectively. Under high injection, $n_e \approx \Delta n$, which is the excess carrier density and is estimated to be about 10^{17}–$10^{18}\,\mathrm{cm}^{-3}$. Since $E_C - E_D$ is much higher than kT at 79 K, the second term in the denominator of Eq. (4) is much less than 1. Therefore, the occupational probability of electrons at E_D is independent of Δn under high injection at low temperatures.[26] With the same derivation for holes, the occupational probability of holes at E_S still slightly depends on Δn. The boundary occurs when E_S approaches E_V, in which case the occupational probability linearly depends on Δn. As a result, the radiative recombination rate via the defect centers does not increase as fast as Δn.

Meanwhile, the BB recombination rate is determined by $\Delta n \times (\Delta n + N_D)$.[33] Hence, the SiBB peak intensity is a quadratic function of Δn in high injection, but the HDBB peak intensity is still between a linear and quadratic function of Δn. Therefore, the LD line is reduced most quickly with increasing excitation power when the spectra are normalized relative to the BB peak, as in Figure 3(a). Note that the HDBB line is eventually revealed with increasing excitation power in Figure 3(a) due to its intermediate dependence on Δn.

In order to fortify the explanation above, Figure 3(c) plots the peak intensities of the SiBB and LD lines versus the excitation power in logarithmic scale. In order to avoid overlapping the two lines, the data of the LD line were captured at the edge of the laser-doped region (the SiBB line was absent), and those of the SiBB line were captured at the undoped region (only the SiBB line was present). The slope of the SiBB curve is close to 2 since the SiBB PL signal is proportional to Δn^2 under high injection, but that of the LD curve is significantly less than 1. The results from this figure are, therefore, consistent with the explanation of different recombination mechanisms between the SiBB and LD lines above. We note that, in general, different laser-doping techniques or conditions may give rise to different types of defect luminescence.

In summary, micro-photoluminescence spectroscopy has been applied to detect laser-induced damage in heavily doped layers of laser-doped crystalline silicon wafers for solar cell applications. The high spatial resolution of this method can be of particular use to identify defective edge regions which impact device performance. The detected laser-induced damage is demonstrated to be caused by dislocations, due to the similar properties of its PL spectrum compared to those of dislocations. This method is effective for probing micron-scale features of laser-doped regions and could be employed as a characterization tool for studying and optimizing laser-doping processes for silicon photovoltaics.

This work has been supported by the Australian Research Council (ARC) and the Australian Renewable Energy Agency (ARENA) through Research Grant No. RND009. The Australian National Fabrication Facility is acknowledged for providing access to some of the facilities used in this work. The authors are in debt to Professor H. Tan for providing access to the spectroscopic equipment, Dr. F. Wang and Dr. S. Mokkapati for assisting with some of the experimental setups, and Dr. F. E. Rougieux for helpful discussions.

[1] P. Gundel, M. C. Schubert, W. Kwapil, J. Schön, M. Reiche, H. Savin, M. Yli-Koski, J. A. Sans, G. Martinez-Criado, W. Seifert, W. Warta, and E. R. Weber, Phys. Status. Solidi RRL **3**, 230 (2009).
[2] T. Sekiguchi and K. Sumino, J. Appl. Phys. **79**, 3253 (1996).
[3] W. Lee, J. Chen, B. Chen, J. Chang, and T. Sekiguchi, Appl. Phys. Lett. **94**, 112103 (2009).
[4] M. Tajima, Y. Iwata, F. Okayama, H. Toyota, H. Onodera, and T. Sekiguchi, J. Appl. Phys. **111**, 113523 (2012).
[5] M. Tajima, IEEE J. Photovoltaics **4**, 1452 (2014).
[6] H. T. Nguyen, F. E. Rougieux, F. Wang, H. Tan, and D. Macdonald, IEEE J. Photovoltaics **5**, 799 (2015).
[7] P. Gundel, M. C. Schubert, and W. Warta, Phys. Status Solidi A **207**, 436 (2010).
[8] P. Gundel, F. D. Heinz, M. C. Schubert, J. A. Giesecke, and W. Warta, J. Appl. Phys. **108**, 033705 (2010).
[9] R. Woehl, P. Gundel, J. Krause, K. Rühle, F. D. Heinz, M. Rauer, C. Schmiga, M. C. Schubert, W. Warta, and D. Biro, IEEE Trans. Electron Devices **58**, 441 (2011).
[10] P. Gundel, D. Suwito, U. Jäger, F. D. Heinz, W. Warta, and M. C. Schubert, IEEE Trans. Electron Devices **58**, 2874 (2011).
[11] F. D. Heinz, P. Gundel, W. Warta, and M. C. Schubert, IEEE J. Photovoltaics **3**, 341 (2013).
[12] A. Roige, J. Alvarez, J.-P. Kleider, I. Martin, R. Alcubilla, and L. F. Vega, IEEE J. Photovoltaics **5**, 545 (2015).
[13] H. T. Nguyen, D. Yan, F. Wang, P. Zheng, Y. Han, and D. Macdonald, Phys. Status Solidi RRL **9**, 230 (2015).
[14] E. Schneiderlöchner, R. Preu, R. Lüdemann, and S. W. Glunz, Prog. Photovoltaics Res. Appl. **10**, 29 (2002).
[15] D. Kray, A. Fell, S. Hopman, K. Mayer, G. P. Willeke, and S. W. Glunz, Appl. Phys. A **93**, 99 (2008).
[16] E. Franklin, K. Fong, K. McIntosh, A. Fell, A. Blakers, T. Kho, D. Walter, D. Wang, N. Zin, M. Stocks, E. C. Wang, N. Grant, Y. Wan, Y. Yang, X. Zhang, Z. Feng, and P. J. Verlinden, "Design, fabrication and characterisation of a 24.4% efficient interdigitated back contact solar cell," Prog. Photovoltaics Res. Appl. (published online).
[17] M. Dahlinger, B. Bazer-Bachi, T. C. Röder, J. R. Köhler, R. Zapf-Gottwick, and J. H. Werner, IEEE J. Photovoltaics **5**, 812 (2015).
[18] A. Sugianto, B. S. Tjahjono, J. H. Guo, and S. R. Wenham, "Impact of laser induced defects on the performance of solar cells using localised laser doped regions beneath the metal contacts," in 22nd European Photovoltaic Solar Energy Conference, Milan, Italy (2007).
[19] S. Hopman, A. Fell, K. Mayer, C. Fleischmann, K. Drew, D. Kray, and F. Granek, "Study on laser parameters for silicon solar cells with LCP selective emitters," in *24th European Photovoltaic Solar Energy Conference and Exhibition, Hamburg, Germany* (2009).
[20] Z. Hameiri, T. Puzzer, L. Mai, A. B. Sproul, and S. R. Wenham, Prog. Photovoltaics Res. Appl. **19**, 391 (2011).
[21] X. Lujia, K. Weber, A. Fell, Z. Hameiri, P. Sieu Pheng, Y. Xinbo, and E. Franklin, IEEE J. Photovoltaics **4**, 594 (2014).
[22] A. Fell, S. Surve, E. Franklin, and K. J. Weber, IEEE Trans. Electron Devices **61**, 1943 (2014).
[23] C. Geisler, W. Hördt, S. Kluska, A. Mondon, S. Hopman, and M. Glatthaar, Sol. Energy Mater. Sol. Cells **133**, 48 (2015).
[24] J. Wagner, Phys. Rev. B **29**, 2002 (1984).
[25] J. Wagner, Phys. Rev. B **32**, 1323 (1985).
[26] M. Suezawa, Y. Sasaki, and K. Sumino, Phys. Status Solidi A **79**, 173 (1983).
[27] R. Sauer, J. Weber, J. Stolz, E. R. Weber, K.-H. Küsters, and H. Alexander, Appl. Phys. A **36**, 1 (1985).
[28] V. V. Kveder, E. A. Steinman, S. A. Shevchenko, and H. G. Grimmeiss, Phys. Rev. B **51**, 10520 (1995).

This article is copyrighted as indicated in the article. Reuse of AIP content is subject to the terms at: http://scitation.aip.org/termsconditions. Downloaded to IP: 150.203.210.78 On: Tue, 03 Nov 2015 08:13:07

[29]M. C. Schubert, P. Gundel, M. The, W. Warta, M. Romero, S. Ostapenko, and Tz. Arguirov, "Spatially resolved luminescence spectroscopy on multicrystalline silicon," in *Proceedings of 23rd EU-PVSEC, Valencia* (2008), p. 17.
[30]D. Walter, A. Fell, E. Franklin, D. Wang, K. Fong, T. Kho, K. Weber, and A. W. Blakers, Sol. Energy Mater. Sol. Cells **136**, 1 (2015).
[31]M. A. Green, Sol. Energy Mater. Sol. Cells **92**, 1305 (2008).
[32]P. Würfel, *Physics of Solar Cells: From Basic Principles to Advanced Concepts* (Wiley-VCH, 2009), p. 81.
[33]H. T. Nguyen, F. E. Rougieux, S. C. Baker-Finch, and D. Macdonald, IEEE J. Photovoltaics **5**, 77 (2015).

This article is copyrighted as indicated in the article. Reuse of AIP content is subject to the terms at: http://scitation.aip.org/termsconditions. Downloaded to IP: 150.203.210.78 On: Tue, 03 Nov 2015 08:13:07

CHAPTER 8

Characterization of Amorphous Silicon, Silicon Nitride, and Heavily-Doped Layers in Solar Cells

Recombination in silicon solar cells can happen either in the bulk or at the surface. Minimizing the bulk recombination is achievable, but eliminating it entirely is impossible since radiative and Auger recombination are fundamental properties of silicon. On the other hand, surface recombination is due to dangling bonds and defects at the surface, which can trap photo-generated carriers. Therefore, it is possible to passivate these dangling bonds to avoid this type of recombination. To date, hydrogenated amorphous silicon nitride (SiN_x:H) is the most commonly used technique for surface passivation as it can not only provide excellent surface passivation qualities, but also act as an anti-reflection coating layer, which helps minimize the reflection of incoming lights. Alternatively, hydrogenated amorphous silicon (a-Si:H) is also employed as passivation layers for heterojunction silicon solar cells. The a-Si:H films not only feature high quality and stable electronic properties, but also can be fabricated at low

temperatures (typically < 200 °C). However, solar cells passivated with a-Si:H films can suffer considerable parasitic loss due to the strong optical absorption of a-Si:H films from ultra-violet to visible wavelengths. Therefore, in practice, it is desirable to keep the a-Si:H films as thin as possible while still maintaining a good passivation quality.

Unlike crystalline silicon whose luminescence signal is emitted by free carriers located at the two band edges, the luminescence of a-Si:H originates from carriers trapped at the two band tail states. Therefore, luminescence spectra of a-Si:H are very broad even at low temperatures. Moreover, at room temperature, the carriers trapped at the band tail states can be thermally excited back to their corresponding band edge, and freely move inside the material until they are trapped by other non-radiative recombination centers. This effect results in a strong suppression of the a-Si:H luminescence intensity at room temperature. Therefore, luminescence experiments on a-Si:H need to be carried out at low temperatures.

In SiN_x:H depositions, silane and ammonia are commonly used as two main gas precursors, and as such they determine the concentrations of silicon, nitrogen, and hydrogen in the passivation films. When the percentage of silane in the gas precursors is increased, the silicon component in the passivation films is also increased, and eventually the SiN_x:H films should become similar to a-Si:H films. These silicon-rich SiN_x:H films, in principle, should have similar luminescence properties to a-Si:H, and should be optically absorptive. Therefore, by observing the luminescence signals from the SiN_x:H films, one may be able to evaluate the structures and optical properties of these films.

This chapter is devoted to the application of spectrally-resolved photoluminescence in characterizing a-Si:H and SiN_x:H passivation films on silicon solar cells. Furthermore, combined with the ability to detect the luminescence signal from heavily-doped layers as reported in Chapters 6 and 7; and the micron-scale spatial resolution of the micro-photoluminescence spectroscopy system, this technique is applied to evaluate the parasitic absorption of the passivation films, and the dopant density of the heavily-doped regions, on various complete silicon solar cells.

The work has been published. However, there is an important point that needs to be clarified in this publication. The main luminescence peak at 1130 nm, denoted as “c-Si” in the publication, is the band-to-band emission assisted by a Transverse-Optical (TO) phonon from the Si substrate. Therefore, the shoulder at 1195 nm, denoted as “phonon replica of c-Si peak”, is the band-to-band emission involving both a TO phonon plus an optical zone center phonon.

Solar Energy Materials & Solar Cells 145 (2016) 403–411

Contents lists available at ScienceDirect

Solar Energy Materials & Solar Cells

journal homepage: www.elsevier.com/locate/solmat

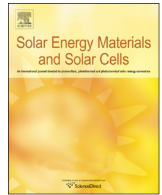

Characterizing amorphous silicon, silicon nitride, and diffused layers in crystalline silicon solar cells using micro-photoluminescence spectroscopy

Hieu T. Nguyen [a,*], Fiacre E. Rougieux [a], Di Yan [a], Yimao Wan [a], Sudha Mokkapati [b], Silvia Martin de Nicolas [c], Johannes Peter Seif [c], Stefaan De Wolf [c], Daniel Macdonald [a]

[a] Research School of Engineering, College of Engineering and Computer Science, The Australian National University, Canberra, ACT 2601, Australia
[b] Department of Electronic Materials Engineering, Research School of Physics and Engineering, The Australian National University, Canberra, ACT 2601, Australia
[c] Photovoltaics and Thin-Film Electronics Laboratory, Institute of Microengineering (IMT), École Polytechnique Fédérale de Lausanne (EPFL), 2000 Neuchâtel, Switzerland

ARTICLE INFO

Article history:
Received 25 August 2015
Received in revised form
28 October 2015
Accepted 2 November 2015
Available online 18 November 2015

Keywords:
Photoluminescence
Amorphous silicon
Crystalline silicon
Diffused silicon
Silicon nitride
Silicon photovoltaics

ABSTRACT

We report and explain the photoluminescence (PL) spectra from crystalline silicon (c-Si) wafers passivated by hydrogenated amorphous silicon (a-Si:H) films under various measurement conditions, utilizing the different absorption coefficients and radiative recombination mechanisms in c-Si and a-Si:H. By comparison with the luminescence properties of a-Si:H, we also demonstrate that SiN_x films deposited under certain silicon-rich conditions yield luminescence spectra similar to those of a-Si:H, indicating the presence of an a-Si:H-like phase in the SiN_x films. This causes a reduction in the blue response of the solar cells via parasitic absorption. In addition, with the ability to detect the specific emission from heavily-doped silicon via band-gap narrowing effects, we can unambiguously separate individual spectral PL signatures of three different layers in a single substrate: the SiN_x passivation films, the diffused layers, and the underlying c-Si substrate. Finally, we apply this technique to evaluate parasitic absorption in the passivation films, and the doping density of the diffused layers on different finished solar cells, highlighting the value of this nondestructive contactless, micron-scale technique for photovoltaic applications.

© 2015 Elsevier B.V. All rights reserved.

1. Introduction

There has been a growing interest in employing micro-pho`toluminescence spectroscopy (μPLS) as a precise and non-destructive characterization tool in silicon photovoltaics (PV). Utilizing the high spatial and spectral resolutions of the μPLS technique, the microscopic properties of micron-scale features on crystalline silicon (c-Si) wafers and cell pre-cursors have been investigated, such as dislocations [1–4], iron precipitates [5], internal stress [6], laser-doped regions [7–11], or locally diffused layers [12]. Besides that, luminescence of hydrogenated amorphous silicon (a-Si:H) films has also been intensively studied for many decades, and is well known as an effective tool to study fundamental properties of this material.

Over the past decades, a-Si:H/c-Si heterojunctions have come to play an important role in silicon PV, since they not only feature high quality and stable electronic properties, but also utilize low temperature deposition processes (typically < 200 °C). These junctions are the key building blocks of record efficiency silicon heterojunction solar cells [13–15]. Furthermore, a-Si:H has been demonstrated as an excellent passivation layer in silicon homojunction solar cells, which can achieve very good majority carrier conduction [16]. On the other hand, diffused junctions and SiN_x passivation layers are two very important components in today's standard industrial silicon solar cells. Therefore, an insightful understanding of the combined PL spectra from c-Si wafers containing these layers (diffused layers, a-Si:H, and SiN_x films) may prove useful in the development of precise characterization tools for PV applications.

Although the electronic and optical qualities of these layers can be evaluated directly after they are formed, using commonly-known techniques such as electrochemical capacitance–voltage (for diffused layers) [17] or spectroscopic ellipsometry and infrared spectroscopy (for a-Si:H and SiN_x) [18–22], their properties can be affected by successive fabrication steps. However, it is difficult to nondestructively assess the properties of these layers in finished solar cells since they are often buried underneath other materials or layers. Furthermore, as the complexity of device structures increases, it is more difficult to probe micron-scale features on

* Corresponding author.
E-mail address: hieu.nguyen@anu.edu.au (H.T. Nguyen).

http://dx.doi.org/10.1016/j.solmat.2015.11.006
0927-0248/© 2015 Elsevier B.V. All rights reserved.

finished solar cells and cell pre-cursors such as locally-doped regions.

In this study, we first report and explain the combined PL spectra emitted from a-Si:H films and the underlying c-Si substrate, including the effects of different measurement and sample preparation conditions. We then demonstrate that SiN_x films deposited under silicon-rich conditions yield PL spectra similar to those of a-Si:H films, suggesting the presence of an a-Si:H-like phase, and indicating that the SiN_x films can reduce the blue response of the solar cells via parasitic absorption. In addition, combining this method with our recently established technique for detecting heavily-doped layers in silicon wafers [12], we can unambiguously separate individual spectral PL signatures of three different layers in a single substrate: the SiN_x passivation films, the diffused layers, and the underlying c-Si substrate, all with micron-scale spatial resolution. Finally, we apply this technique to evaluate unwanted absorption in the passivation films and the doping density of the diffused layers on different solar cell designs, in which some investigated features are only a few tens of microns wide. These applications highlight the value of this contactless and nondestructive technique, which can be applied directly both on finished cells and cell pre-cursors, to study and optimize the fabrication process. A critical aspect of this technique is the use of low temperatures (78 K and above), since the individual spectral PL signatures from different layers are not discernible at room temperature, due to both thermal broadening of band-to-band luminescence, and thermal quenching of defect luminescence [11,12].

2. Experimental details

The experimental set up of our μPLS system is described in detail elsewhere [4,12]. The spectral resolution of this system is 0.25 nm. Two different excitation lasers were employed in this work, a 532 nm continuous-wave diode-pump solid-state (CW-DPSS) laser and an 830-nm CW laser diode. For both lasers, the beam diameter on the sample surface is about 1 μm, and the excitation power is about 6 mW. The spectral response of the entire system was determined with a calibrated halogen–tungsten light source. The sample temperature was controlled by a liquid-nitrogen cryostat.

The investigated wafers are p-type boron-doped c-Si wafers with resistivities ≥ 100 Ω cm. They were chemically etched in an HF/HNO_3 solution to remove saw damage and to achieve planar surfaces. Their final thickness is about 300 μm. Some were passivated by thin a-Si:H films, whose thicknesses vary from 10 to 100 nm, by plasma-enhanced chemical-vapor deposition (PECVD). Some were passivated by thin PECVD SiN_x films with various SiH_4:NH_3 gas flow ratios in order to achieve different optical properties. Some were heavily doped with phosphorus from a $POCl_3$ vapor source to form n+ layers on the surfaces, and then immersed in diluted HF to remove the phosphosilicate glass layers. The resultant sheet resistance is about 45 Ω /□. These n+ diffused wafers were then passivated by PECVD SiN_x films with various SiH_4:NH_3 gas flow ratios. The thicknesses of these thin SiN_x films were determined by an ellipsometer. The investigated c-Si solar cell structures are the passivated-emitter rear locally-diffused (PERL) cell [23], interdigitated back contact cell with a diffused front surface field (FSF-IBC) [24,25], and interdigitated back contact cell without a front surface field (IBC) [26]. All devices have efficiencies above 20%.

The investigated a-Si:H and SiN_x films were prepared at three different laboratories including The Australian National University (ANU), Australian National Fabrication Facility (ANFF), and École Polytechnique Fédérale de Lausanne (EPFL) in Switzerland. Table 1 gives a summary of substrate temperatures and frequency modes of the PECVD reactors employed in this study.

Table 1
Substrate temperatures and frequency modes of PECVD reactors employed in this study.

Film	Substrate temperature (°C)	Frequency mode
ANU a-Si:H	300	Microwave/radio frequency dual-mode
ANFF a-Si:H	400	Capacitive-coupled plasma
EPFL a-Si:H	200	Capacitive-coupled plasma
ANU SiN_x	300	Microwave/radio frequency dual-mode
ANFF SiN_x	400	Capacitive-coupled plasma

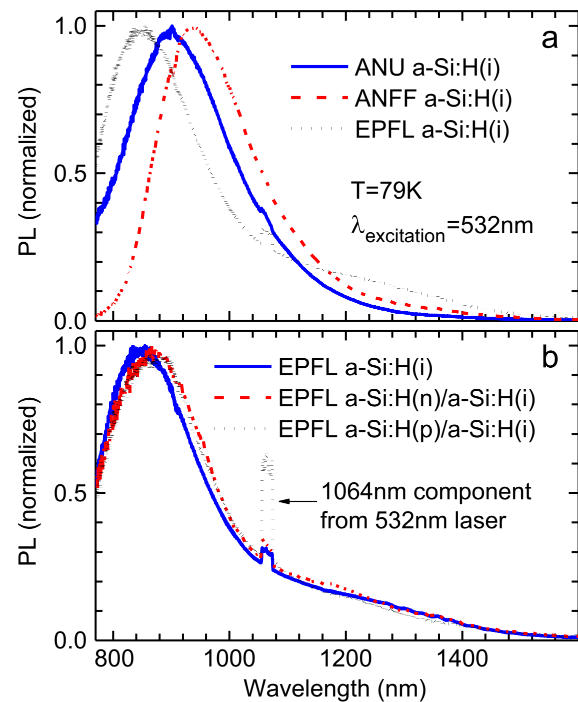

Fig. 1. Comparison of normalized PL spectra (a) from a-Si:H deposited at different laboratories and (b) between intrinsic a-Si:H and doped/intrinsic a-Si:H stacks. The a-Si:H films were deposited directly on glass substrates. The excitation wavelength is 532 nm and the measurement temperature is 79 K. The spurious peak at 1064 nm is due to the not-entirely-suppressed 1064-nm component from the 532-nm DPSS laser.

3. Luminescence of a-Si:H deposited on glass substrates

For many decades, luminescence spectra from a-Si:H have been studied intensively regarding their spectral shapes, peak locations, and relative intensities under different measurement conditions and with various preparation conditions and techniques. Therefore, in this first section, we aim to review only the basic PL spectra captured from a-Si:H deposited directly on glass substrates, which will serve as a basis for our later discussions on the combined PL signal from different layers stacked together.

Fig. 1a shows the normalized PL spectra from intrinsic a-Si:H films deposited on glass substrates, excited by the 532-nm laser at 79 K, prepared at ANU (~70 nm), ANFF (~30 nm), and EPFL (~10 nm). The first notable feature is that, at 79 K the spectra of a-Si:H are much broader than those of c-Si. The full width at half maximum (FWHM) of the a-Si:H peak is ~300 meV, whereas that

of c-Si is only ~25 meV at 79 K [27]. This broadening stems from the fact that the PL spectra from a-Si:H are emitted by the carriers trapped at band-tail states at the band edges [28–33], resulting in a relatively broad range of energies, rather than being emitted from the two sharp band edges, as is the case for c-Si. Furthermore, even for perfect crystalline materials, the Urbach energy, which is basically the slope of the absorption edge, is a non-zero value, and this value scales with temperature. Amorphous and disordered materials will have additional Urbach energy broadening due to the additional band edge roughness caused by the disorder [34]. As such, low Urbach energies usually imply high mobilities, and thus the broadening of PL spectra likely indirectly implies a lowering of the carrier mobility in the amorphous films. In addition, in Fig. 1a, different deposition conditions (see Table 1) yield different peak locations of the a-Si:H spectra. The peak energy varies between ~1.3 and 1.45 eV (~850 to 950 nm), consistent with the results reported in the literature [28–33]. The reason is that the optical band gap of a-Si:H depends strongly on the deposition conditions [35–38], and hence the luminescence energy is affected correspondingly. Note that the varying peak energies observed are not due to the difference in the film thickness among the three samples, since the shape and peak location of the PL spectra did not change when we varied the film thickness between 10 and 100 nm under the same deposition conditions.

Furthermore, Fig. 1b compares the normalized spectra among the boron-doped (p) and phosphorus-doped (n) a-Si:H (deposited on the intrinsic a-Si:H layer) and the intrinsic a-Si:H itself. These layer stacks were prepared with EPFL's standard recipes for heterojunction silicon solar cells, which achieve efficiencies higher than 21% [39,40]. The doped (n- and p- types) and intrinsic layers are ~10 nm thick. The absorption depth of the 532-nm excitation light in a-Si:H is ~160 nm at 79 K (calculated from Ref. [41]). Therefore, the 532 nm excitation light is absorbed by both the intrinsic and doped layers. In the case of c-Si, if the laser light is absorbed by both the diffused layer and the underlying c-Si substrate, one can observe two separate band-to-band PL peaks from the two layers due to the band-gap narrowing in heavily-doped c-Si [12]. However, we did not observe two separate peaks from the doped/intrinsic a-Si:H stacks in Fig. 1b. Again, this result is explained by the fact that, the luminescence signal from a-Si:H is emitted from the band-tail states, not from the band edges, and these band-tail states are distributed over a wide energy range, rather than a well-defined value as for the band edges. The doping leads to even wider band tails due to the increased disorder in the material [42]. Therefore, any small change in the band gap due to the doping is very likely to be masked by the broad luminescence peak.

Note that, although the shape of the PL spectra from the doped/intrinsic a-Si:H stacks are similar to that from the intrinsic a-Si:H itself, the relative PL intensity of the former is five-fold smaller than that of the latter, due to increased non-radiative recombination introduced by doping [42–45]. Such undesired doping-induced recombination explains why doped layers at the front of silicon heterojunction solar cells should be kept as thin as possible [46]. When the doping level is high enough, another peak at around 0.9 eV (1380 nm) in the luminescence spectrum has been reported, attributed to the radiative transition of electrons and holes through the defect band in the band gap [42–45]. We did not observe such an additional peak in this study.

4. Luminescence of c-Si wafers passivated by a-Si:H

4.1. Dependence of luminescence on excitation wavelength and measurement temperature

Next, we examine the spectra emitted from a-Si:H passivated c-Si wafers. Since the a-Si:H passivation layer is ~30 nm thick, the 532 nm excitation light (absorption depth in a-Si:H is 160 nm at 79 K) is absorbed in both the a-Si:H and c-Si layers. In Fig. 2, the spectrum at 79 K from this passivated wafer displays two separate peaks: (1) a very broad peak at ~940 nm attributed to the a-Si:H passivation layer, and (2) a sharp peak at ~1125 nm attributed to the underlying c-Si substrate. Note that the a-Si:H layer was deposited at ANFF and hence the a-Si:H peak position (~940 nm) is comparable to that shown in Fig. 1a. The spectrum from an uncoated c-Si wafer was also included for comparison. The small peak at ~1200 nm in all spectra is the phonon replica of the c-Si peak. Also shown is the spectrum from the a-Si:H passivated c-Si wafer, but with the 830-nm excitation laser. Due to the increasing absorption depth of this excitation light, most of this laser light is absorbed in the underlying c-Si substrate, and thus the emission from the a-Si:H layer is suppressed in relative terms and the spectrum is very similar to that from an uncoated c-Si wafer (see Fig. 2). This shows the importance of using an appropriate illumination wavelength to identify the presence of an a-Si:H passivating layer [47].

Furthermore, the luminescence from a-Si:H is known to display a very strong thermal quenching and is usually entirely suppressed at room temperature [42–44,48], since the carriers trapped at the tail states can be thermally excited back to their corresponding band edges and freely move in the material until they are trapped by other non-radiative recombination centers. Fig. 3 shows the evolution of the normalized spectra from the a-Si:H passivated c-Si wafer versus the temperature, excited by the 532 nm laser. The a-Si:H peak from the passivated wafer is significantly reduced with increasing temperatures. At room temperature, the normalized spectrum from this passivated sample is overlapped with that from the uncoated c-Si wafer, although the relative PL intensity of the former sample is one order of magnitude higher than that of the latter due to the passivation effects of the a-Si:H film on the c-Si substrate [49,50]. Therefore, performing measurements at cryogenic temperatures with an appropriate excitation wavelength is critical to detect the presence of a-Si:H layers on the c-Si substrate. Note that there is a very sharp peak at 1064 nm in all spectra. This is an artifact due to the not-entirely-suppressed 1064 nm component from the 532 nm DPSS laser.

4.2. Dependence of luminescence on excitation power

When the PL spectrum contains multiple components from various layers on the substrate, its spectral shape is very sensitive to the excitation power due to the different dependencies of each individual component on the excess carrier density, which is related to the excitation power [11,12]. Fig. 4a plots the PL spectra, normalized to the c-Si peak, from the a-Si:H passivated c-Si wafer

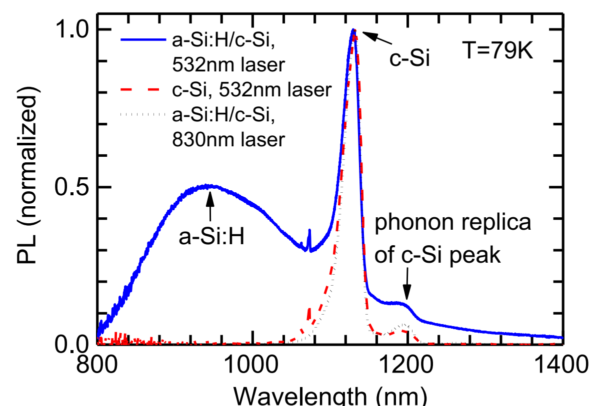

Fig. 2. Comparison of normalized PL spectra between the a-Si:H passivated c-Si wafer and the uncoated c-Si wafer, excited by the 532- and 830 nm lasers at 79 K.

at various 532-nm excitation powers at 79 K. The higher the excitation power, the less pronounced the a-Si:H peak compared to the c-Si peak. This dependence stems from the different radiative recombination mechanisms between the a-Si:H layer and the underlying c-Si substrate. The c-Si PL signal originates from carriers at the two band edges, and thus is a quadratic function of the excess carrier density Δn under high injection [51]. Meanwhile, the a-Si:H PL signal, in principle, has a similar recombination mechanism compared to that of the deep-level PL signal from dislocations in c-Si [11] since both are emitted from defect states in the band gap. Therefore, the same as the deep-level PL signal from dislocations [11], the a-Si:H PL signal shows a much weaker dependence on the excitation power than the band-to-band PL signal from c-Si.

In order to support the above explanation, we measured the peak intensities of a-Si:H and c-Si versus the excitation power at 79 K, and plotted the results in Fig. 4b. The data of c-Si was captured on the uncoated c-Si wafer in order to avoid overlapping with the low energy tail of the broad a-Si:H peak, whereas the data of a-Si:H was captured directly on the a-Si:H passivated c-Si wafer since the PL peak intensity of a-Si:H is not affected by the very sharp PL peak of c-Si. As can been seen in Fig. 4b, the c-Si PL intensity shows a very strong dependence on the excitation power, whereas that of a-Si:H has a very weak dependence.

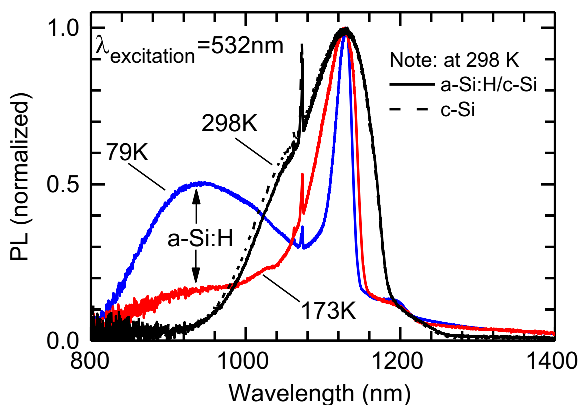

Fig. 3. Temperature dependence of normalized PL spectra from the a-Si:H passivated c-Si wafer, excited by the 532 nm laser. The spectrum at 298 K from the uncoated c-Si wafer was also included for comparison.

The PL intensities from the uncoated c-Si sample and the a-Si:H layer can be simply fitted by Eqs. (1) and (2), respectively:

$$PL_{c-Si} \propto P_0^x \tag{1}$$

$$PL_{a-Si:H} \propto \left[P_0\left(1-e^{-\alpha d}\right)\right]^y \tag{2}$$

P_0 is the excitation power, which is directly related to the excess carrier density. α is the absorption coefficient of a-Si:H, and d is the thickness of the a-Si:H film. x and y are the fitting parameters. The term $P_0(1-e^{-\alpha d})$, instead of P_0, in Eq. (2) accounts for the fraction of P_0 absorbed in the a-Si:H layer since this layer is thinner than the absorption depth of the 532 nm laser at 79 K. Fitting the data in Fig. 4b yields x and y of 1.64 and 0.23, respectively. In fact, x is expected to be close to 2 since $PL_{c\text{-}Si} \sim \Delta n^2$. However, the wafers are under high injection, and thus Auger recombination plays a role. Therefore, Δn does not increase as quickly as P_0.

5. Luminescence of c-Si wafers passivated by SiN_x films

5.1. Detection of a-Si:H PL signature in SiN_x films

Fig. 5a plots the normalized PL spectra from SiN_x passivated c-Si wafers, deposited by PECVD with various SiH_4:NH_3 gas flow ratios. Similar to the a-Si:H passivated c-Si wafers, besides the c-Si peak at ~1125 nm, we can observe another peak between 850 and 900 nm, similar in shape to that of the a-Si:H passivated c-Si wafers, and hence denoted as a-Si:H in Fig. 5a. The intensity of this a-Si:H peak increases with increasing SiH_4:NH_3 gas flow ratios. Interestingly, this is not simply due to the increasing silicon component in the SiN_x films, but it suggests that the excess Si atoms are clustered in a form that replicates the bond structure of a-Si:H, because the PL spectra are akin to that of this amorphous semiconductor. We also observed the same trend in the n+ diffused c-Si wafers passivated by the PECVD SiN_x films with different SiH_4:NH_3 gas ratios, as shown in Fig. 5b. In this case, besides the a-Si:H and c-Si peaks, we observe another peak at ~1160 nm due to the band-to-band emission from the n+ diffused c-Si layer, which is shifted to longer wavelengths compared to the c-Si peak due to band-gap narrowing effects in the heavily-doped layer [12]. We have labeled this peak HDBB (heavily-doped band-to-band) in Fig. 5b.

As an additional test, we removed the SiN_x film (SiH_4:NH_3=30:10) from one wafer using a dilute HF solution. The a-Si:H

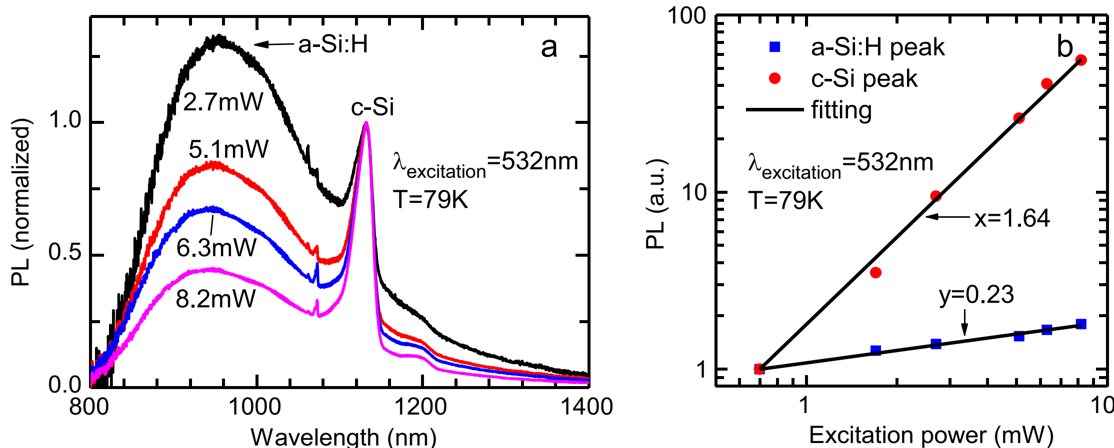

Fig. 4. (a) Excitation power dependence of PL spectra, normalized to the c-Si peak, from the a-Si:H passivated c-Si wafer. (b) Peak PL intensity of a-Si:H and c-Si versus the excitation power. The excitation wavelength is 532 nm and the measurement temperature is 79 K.

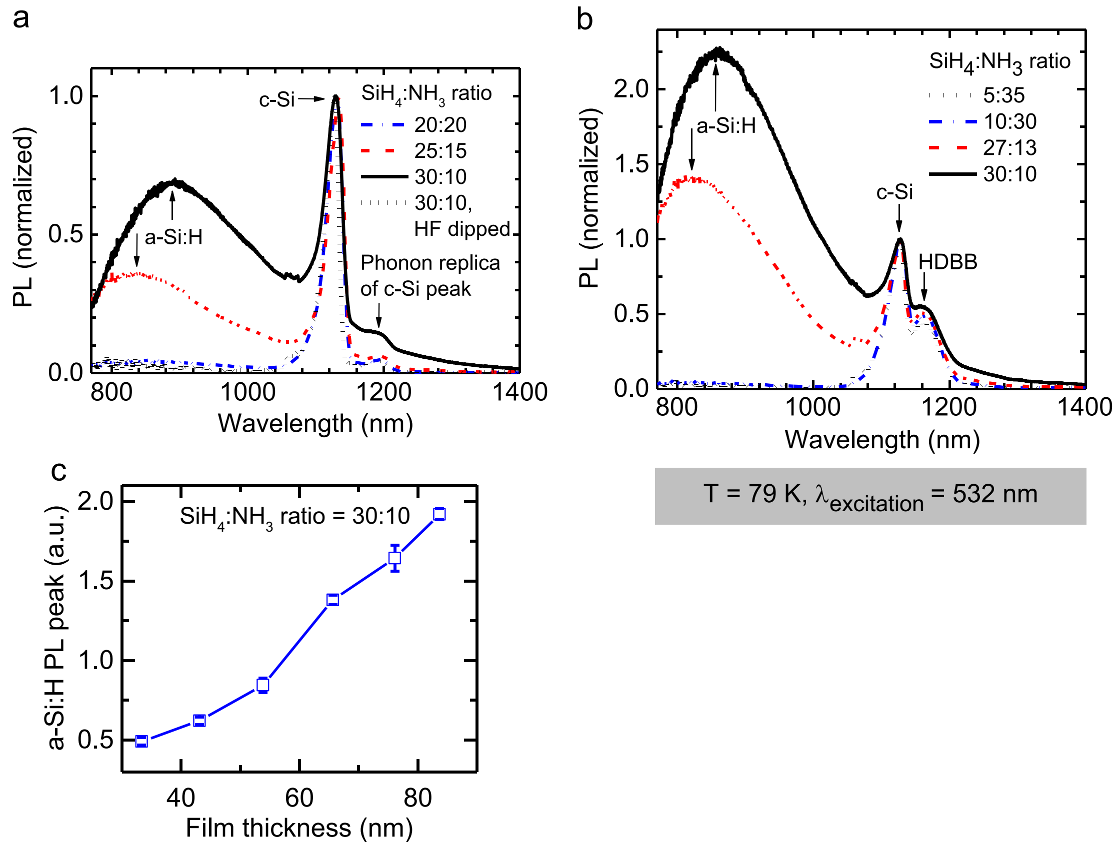

Fig. 5. Comparison of PL spectra, normalized to the c-Si peak, among different SiH_4:NH_3 gas ratios from (a) SiN_x passivated c-Si wafers, and (b) n+ diffused, SiN_x passivated c-Si wafers. (c) a-Si:H PL peak intensity, along with one standard deviation error bars, of the SiN_x passivated c-Si wafer (SiH_4:NH_3=30:10) versus the passivation film thickness. The excitation wavelength is 532 nm and the measurement temperature is 79 K. The spectrum, after the SiN_x film (SiH_4:NH_3=30:10) was removed by HF, was also included in Fig. 5a.

PL peak disappeared, as shown in Fig. 5a. Since neither a-Si:H nor c-Si can be dissolved in HF, the a-Si:H peak observed before etching cannot originate from an a-Si:H layer which may be present at the interface between the SiN_x film and the c-Si wafer, but must be emitted from within the SiN_x film itself. To further investigate if the source for this a-Si:H PL peak is distributed across the entire thickness of the SiN_x film, we changed the PECVD deposition time, but kept other parameters the same, in order to achieve various thicknesses of the SiN_x film (SiH_4:NH_3=30:10). Fig. 5c shows that the relative PL intensity of the a-Si:H peak increases with the SiN_x film thickness. Therefore, we conclude that the observed a-Si:H PL peak is emitted from the bulk of the SiN_x film, not from just an interfacial layer.

5.2. Correlation of a-Si:H PL and SiN_x optical properties

Fig. 6a and b shows the a-Si:H peak intensity of the SiN_x passivated c-Si wafers versus the refractive index n at 632 nm and the absorption coefficient α at 400 nm of the SiN_x film, respectively. The results in these two figures confirm that the film with higher n, and thus higher α, yields a stronger a-Si:H PL peak. This finding is consistent with the fact that the more silicon-rich film has higher n and α [21,52]. In addition, Fig. 6c compares the absorptance spectra between the SiN_x (SiH_4:NH_3=30:10) and a-Si:H films, deposited directly on the glass substrates with the same thickness of ~75 nm. The absorptance spectrum of the glass substrate was also included to facilitate the comparison. Since we were interested in the percentage of the entering light absorbed in the material, we applied the following formula to determine the weighted absorptance in Fig. 6c:

$$A = \frac{1-T-R}{1-R} \tag{3}$$

T and R are the total transmittance and reflectance, respectively, and are measured with a spectrophotometer. The denominator accounts for the light fraction entering the material, and the numerator accounts for the total absorbed light. In Fig. 6c, the glass substrate hardly absorbs any light above 360 nm. Therefore, the absorption from 360 to 600 nm of both thin films (SiN_x and a-Si:H) deposited on the glass substrate must be due to the two films themselves. Therefore, the passivation layers, although reducing the surface recombination, could detrimentally impact the performance of c-Si solar cells via unwanted absorption. Note that the SiN_x recipe (SiH_4:NH_3=30:10), giving a very high refractive index n, was chosen to best illustrate the capabilities of the presented method. In practice, the recipe should be optimized to achieve both low surface recombination and low absorption in the passivation films.

Furthermore, we verify that there is a-Si:H embedded in the SiN_x film. We performed Raman spectroscopy on the n+ diffused, SiN_x passivated c-Si wafer (SiH_4:NH_3=30:10), and plotted the results in Fig. 7. The setup for Raman measurements is the same as that for PL measurements [4,12], except that a silicon detector and a 900 grooves/mm grating monochromator were employed (compared to an InGaAs detector and 150 grooves/mm grating monochromator for PL measurements). Compared to the spectrum of the undiffused, uncoated c-Si wafer, besides the c-Si peak at ~520.9 cm^{-1}, there is another peak at ~480 cm^{-1} associated with a-Si:H [53]. These results confirm that the PL peaks between

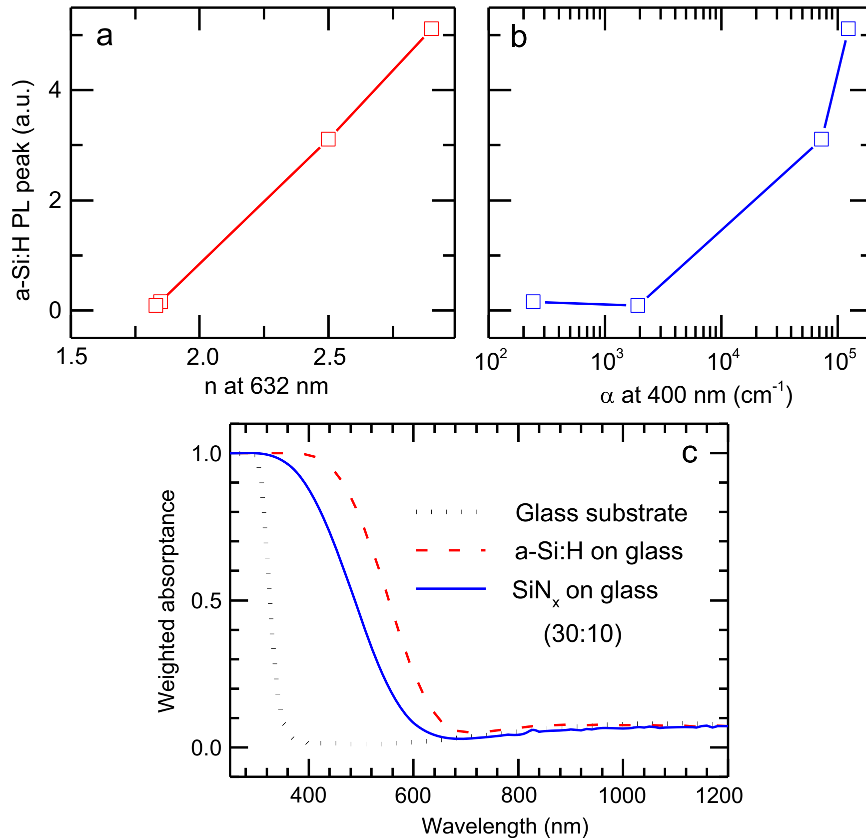

Fig. 6. a-Si:H peak intensity versus (a) the refractive index n and (b) the absorption coefficient α in the SiN_x film, excited by the 532-nm laser at 79 K. (c) Comparison of room temperature weighted absorptance spectra between a-Si:H and SiN_x films, deposited on the same glass substrate with the same film thickness.

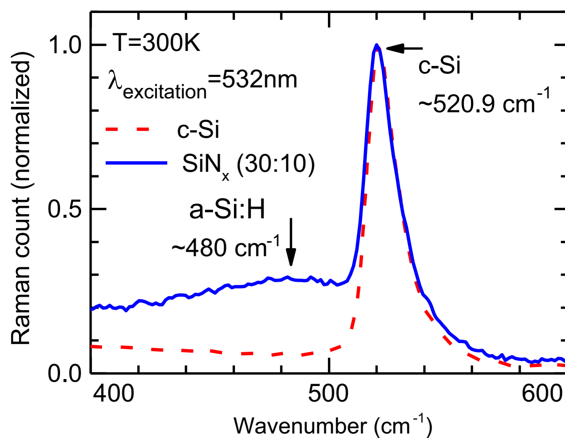

Fig. 7. Comparison of the normalized Raman spectra between the n+ diffused, SiN_x passivated c-Si wafer and the undiffused, uncoated c-Si wafer, excited by the 532 nm laser at 300 K.

850 and 900 nm in Fig. 5a and b are emitted by the a-Si:H clusters embedded in the SiN_x film.

The Raman and PL signals have different emission mechanisms: the Raman photons are emitted from the excited electrons which are still bound to their host atoms or molecules, whereas the PL photons are emitted from the excited carriers which move freely in the material. Therefore the Raman measurement can be considered as an independent comparison with the PL measurement, thus verifying the presence of a certain material detected by the luminescence technique. Compared with PL, the Raman technique itself has some advantages. (1) The Raman signal is not affected by the carrier diffusion since the excited electrons are confined within their host atoms or molecules, thus increasing the lateral resolution. (2) The Raman signal from different materials can be readily resolved at room temperature. (3) One can employ shorter excitation wavelengths, for example ultra-violet (UV), to probe much thinner layers of different materials since the detection wavelengths are close to the excitation wavelengths, while being able to increase the spatial resolution. Detecting the PL signal in the near-infrared (NIR) wavelength region, excited by a UV laser using the confocal system, usually requires special optics which can cover a broad range of wavelengths (from UV to NIR). These advantages of a micro-Raman system have been exploited by Heinz et al. [54] to characterize very thin a-Si:H layers on textured c-Si wafers with a spatial resolution of ~200 nm. However, many microscopic properties of defects and impurities in silicon are not revealed on the Raman spectra, but are more easily detected by the micro-PLS technique, such as the energy levels of iron precipitates [5], oxygen precipitates [2], dislocations [1–4], localized heavily-doped regions [11,12], or the distribution of defects and impurities along sub-grain boundaries in multicrystalline silicon wafers after different solar cell processing steps [55]. Therefore, the two techniques can complement each other, as exploited by Heinz et al. [54].

We note that the a-Si:H PL spectra captured from our SiN_x films are different from the commonly reported spectra from SiN_x films in the literature [56–60]. The spectra reported in the literature were in the visible wavelength range and are still present at room temperature, and required lower excitation wavelengths (< 460 nm) to be observed. On the other hand, our a-Si:H spectra from the SiN_x films are in the infrared wavelength range and completely disappear at room temperature, and these properties are similar to

those of the spectra from the pure a-Si:H films. They can be stimulated by 532 nm laser excitation with energy below the bandgap of SiN_x.

6. Characterization of SiN_x films and diffused layers in complete solar cells

Finally, we demonstrate the application of the techniques presented above on various finished solar cells. Fig. 8a shows the layouts of three different n-type c-Si solar cell structures fabricated at ANU, including the so-called PERL [23], FSF-IBC [24,25], and IBC cells [26]. The notable differences among these three cells are the surface passivation and diffused layers. The passivation layer on the FSF-IBC cell was deposited by low-pressure chemical-vapor-deposition (LPCVD) Si_3N_4, and hence is stoichiometric, whereas the SiN_x layers on the IBC (ANU SiN_x) and PERL (ANFF SiN_x) cells were deposited by PECVD (see Table 1). The diffused layers of these cells also have different sheet resistances. For the FSF-IBC cell, since we still have 40-µm gaps between two metal lines, we were also able to measure at the rear without interference from the metal layer.

Fig. 8b compares the normalized PL spectra measured on the front of the three solar cells. Only the PERL cell has the a-Si:H signal in its PL spectrum, whereas the other two have no signature of a-Si:H. This indicates parasitic absorption occurring in the SiN_x film of the PERL cell, leading to a lower blue response compared to the other two cells. Moreover, comparing the shoulders at around 1160 nm in the spectra in Fig. 8b, we can observe that the IBC cell does not have a front diffused layer underneath the passivation layer, whereas the FSF-IBC and PERL cells do. In order to compare the doping levels among different diffused regions, we captured the normalized spectra from different diffused regions and plotted them in Fig. 8c and d for n+ and p+ regions, respectively. Their sheet resistances are given in the brackets. In Fig. 8c and d, the lower the sheet resistance, corresponding to a heavier diffusion, the higher the HDBB peak. Therefore, this technique could be employed directly on finished solar cells as a nondestructive contactless characterization tool to study and optimize both the diffused and passivation layers.

7. Conclusion

Utilizing the different luminescence mechanisms from amorphous silicon films and crystalline silicon wafers, we have presented and explained the combined photoluminescence spectra from crystalline silicon wafers passivated by thin amorphous silicon films, including the dependencies on both the measurement and preparation conditions. Based on these findings, we have demonstrated that silicon nitride films can give rise to the amorphous silicon luminescence, suggesting the presence of amorphous silicon clusters in silicon-rich silicon nitride films. This luminescence was found to correspond to the onset of unwanted parasitic absorption of visible light in the nitride layer. Adding the ability to detect distinct emission from heavily-doped silicon layers courtesy of band-gap narrowing effects, we have demonstrated that spectral PL measurements can be useful to evaluate both the passivating and diffused layers of finished solar cells, with micron-scale spatial resolution.

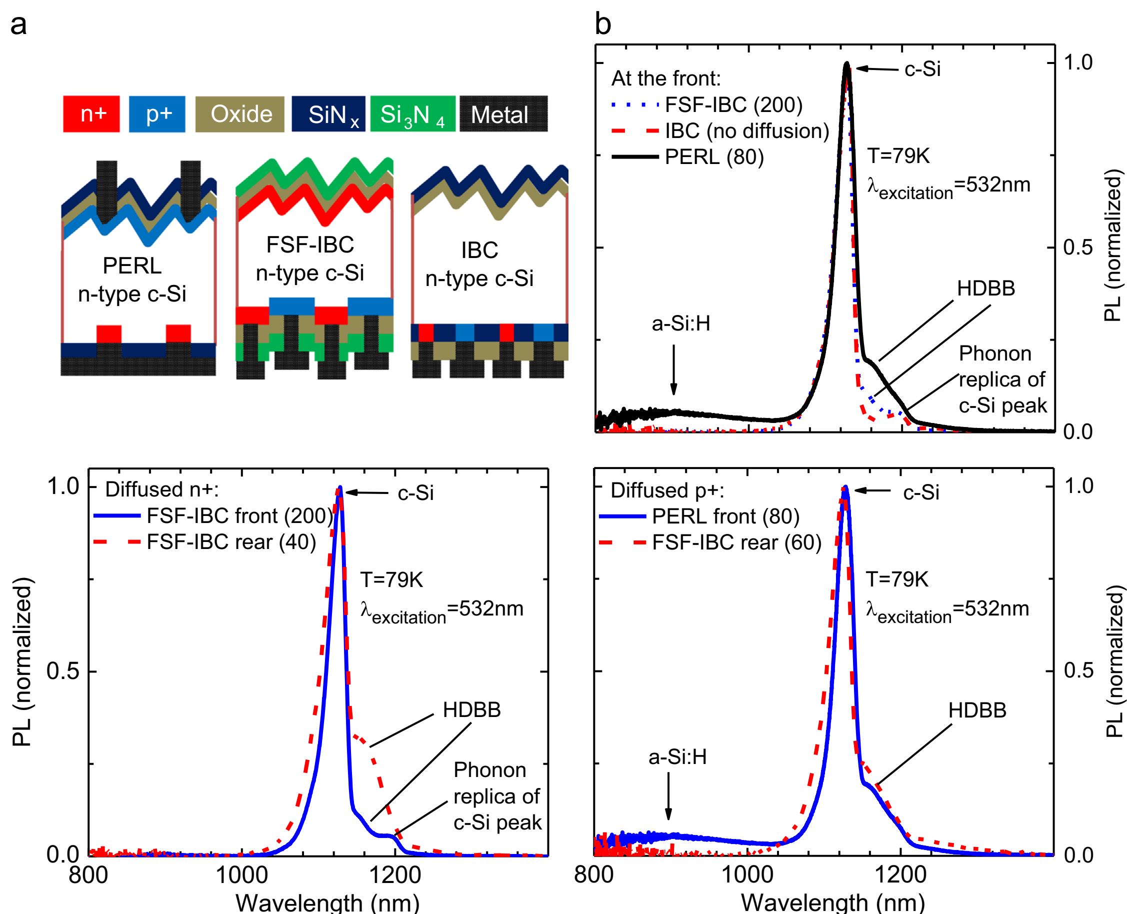

Fig. 8. (a) Layouts of the investigated PERL, FSF-IBC, and IBC solar cells. (b) Comparison of the normalized spectra (b) at the front, (c) at the n+ diffused regions, and (d) at the p+ diffused regions of these three solar cells, excited by the 532 nm laser at 79 K. The numbers in brackets are the sheet resistances of the diffused layers.

Acknowledgments

This work has been supported by the Australian Research Council (ARC), the Australian Renewable Energy Agency (ARENA) through research Grant RND009, the Swiss Federal Office of Energy (SI/501253-01), and the EuroTech University Alliance in the framework of the Interface Sciences for Photovoltaics initiative. The Australian National Fabrication Facility (ANFF) is acknowledged for providing access to some of the facilities used in this work. The authors are in debt to Prof. H. Tan for providing access to the spectroscopic equipment, B. Luther-Davies for assisting with the hardware set up, A. Cuevas for stimulating discussions and proof reading, and Dr. N. Zin and Mr. P. Zheng for providing the finished solar cells.

References

[1] W. Lee, J. Chen, B. Chen, J. Chang, T. Sekiguchi, Cathodoluminescence study of dislocation-related luminescence from small-angle grain boundaries in multicrystalline silicon, Appl. Phys. Lett. 94 (2009) 112103.
[2] M. Tajima, Y. Iwata, F. Okayama, H. Toyota, H. Onodera, T. Sekiguchi, Deep-level photoluminescence due to dislocations and oxygen precipitates in multicrystalline Si, J. Appl. Phys. 111 (2012) 113523.
[3] M. Tajima, Spectroscopy and topography of deep-level luminescence in photovoltaic silicon, IEEE J. Photovolt. 4 (2014) 1452.
[4] H.T. Nguyen, F.E. Rougieux, F. Wang, H. Tan, D. Macdonald, Micrometer-scale deep-level spectral photoluminescence from dislocations in multicrystalline silicon, IEEE J. Photovolt. 5 (2015) 799.
[5] P. Gundel, M.C. Schubert, W. Kwapil, J. Schön, M. Reiche, H. Savin, M. Yli-Koski, J.A. Sans, G. Martinez-Criado, W. Seifert, W. Warta, E.R. Weber, Micro-photoluminescence spectroscopy on metal precipitates in silicon, Phys. Status Solidi RRL 3 (2009) 230.
[6] P. Gundel, M.C. Schubert, W. Warta, Simultaneous stress and defect luminescence study on silicon, Phys. Status Solidi A 207 (2010) 436.
[7] R. Woehl, P. Gundel, J. Krause, K. Rühle, F.D. Heinz, M. Rauer, C. Schmiga, M. C. Schubert, W. Warta, D. Biro, Evaluating the aluminum-alloyed p+-layer of silicon solar cells by emitter saturation current density and optical microspectroscopy measurements, IEEE Trans. Electron Devices 58 (2011) 441.
[8] P. Gundel, D. Suwito, U. Jäger, F.D. Heinz, W. Warta, M.C. Schubert, Comprehensive microscopic analysis of laser-induced high doping regions in silicon, IEEE Trans. Electron Devices 58 (2011) 2874.
[9] F.D. Heinz, P. Gundel, W. Warta, M.C. Schubert, Doping density in silicon and solar cells analyzed with micrometer resolution, IEEE, J. Photovolt. 3 (2013) 341.
[10] A. Roigé, J. Alvarez, J.-P. Kleider, I. Martin, R. Alcubilla, L.F. Vega, Microscale spatially resolved characterization of highly doped regions in laser-fired contacts for high-efficiency crystalline Si solar cells, IEEE J. Photovolt. 5 (2015) 545.
[11] H.T. Nguyen, Y. Han, M. Ernst, A. Fell, E. Franklin, D. Macdonald, Dislocations in laser-doped silicon detected by micro-photoluminescence spectroscopy, Appl. Phys. Lett. 107 (2015) 022101.
[12] H.T. Nguyen, D. Yan, F. Wang, P. Zheng, Y. Han, D. Macdonald, Micro-photoluminescence spectroscopy on heavily-doped layers of silicon solar cells, Phys. Status Solidi RRL 9 (2015) 230.
[13] M. Taguchi, A. Yano, S. Tohoda, K. Matsuyama, Y. Nakamura, T. Nishiwaki, K. Fujita, E. Maruyama, 24.7% record efficiency HIT solar cell on thin silicon wafer, IEEE J. Photovolt. 4 (2014) 96.
[14] K. Masuko, M. Shigematsu, T. Hashiguchi, D. Fujishima, M. Kai, N. Yoshimura, T. Yamaguchi, Y. Ichihashi, T. Mishima, N. Matsubara, T. Yamanishi, T. Takahama, M. Taguchi, E. Maruyama, S. Okamoto, Achievement of more than 25% conversion efficiency with crystalline silicon heterojunction solar cell, IEEE J. Photovolt. 4 (2014) 1433.
[15] J. Nakamura, N. Asano, T. Hieda, C. Okamoto, H. Katayama, K. Nakamura, Development of heterojunction back contact Si solar cells, IEEE J. Photovolt. 4 (2014) 1491.
[16] J. Bullock, D. Yan, Y. Wan, A. Cuevas, B. Demaurex, A. Hessler-Wyser, S. De Wolf, Amorphous silicon passivated contacts for diffused junction silicon solar cells, J. Appl. Phys. 115 (2014) 163703.
[17] F. Huster, G. Schubert, ECV doping measurements of aluminium alloyed back surface fields, in: Proceedings of the 20th European Photovoltaic Solar Energy Conference and Exhibition 2005, p. 1462.
[18] F. Giorgis, F. Giuliani, C.F. Pirri, E. Tresso, C. Summonte, R. Rizzoli, R. Galloni, A. Desalvo, P. Rava, Optical, structural and electrical properties of device-quality hydrogenated amorphous silicon nitrogen films deposited by plasma enhanced chemical vapour deposition, Philos. Mag. B 77 (1998) 925.
[19] H. Fujiwara, M. Kondo, Real-time monitoring and process control in amorphous–crystalline silicon heterojunction solar cells by spectroscopic ellipsometry and infrared spectroscopy, Appl. Phys. Lett. 86 (2005) 032112.
[20] P.J. van den Oever, M.C.M. van de Sanden, W.M.M. Kessels, Real time spectroscopic ellipsometry on ultrathin (< 50 Å) hydrogenated amorphous silicon films on Si(100) and GaAs(100), J. Appl. Phys. 101 (2007) 123529.
[21] Y. Wan, K.R. McIntosh, A.F. Thomson, Characterisation and optimisation of PECVD SiN_x as an antireflection coating and passivation layer for silicon solar cells, AIP Adv. 3 (2013) 032113.
[22] J. Holovský, S. De Wolf, P. Jiříček, C. Ballif, Attenuated total reflectance Fourier-transform infrared spectroscopic investigation of silicon heterojunction solar cells, Rev. Sci. Instrum. 86 (2015) 073108.
[23] Y. Wan, C. Samundsett, T. Kho, J. McKeon, L. Black, D. Macdonald, A. Cuevas, J. Sheng, Y. Sheng, S. Yuan, C. Zhang, Z. Feng, P.J. Verlinden, Towards industrial advanced front-junction n-type silicon solar cells, in: Proceedings of the IEEE 40th Photovoltaic Specialist Conference 2014, Denver, Colorado.
[24] N. Zin, A. Blakers, E. Franklin, T. Kho, K.R. McIntosh, J. Wong, T. Mueller, A. G. Aberle, Y. Yang, X. Zhang, Z. Feng, Q. Huang, Progress in the development of all-back-contacted silicon solar cells, Energy Procedia 25 (2012) 1.
[25] N. Zin, A. Blakers, K.R. McIntosh, E. Franklin, T. Kho, K. Chern, J. Wong, T. Mueller, A.G. Aberle, Y. Yang, X. Zhang, Z. Feng, Q. Huang, P.J. Verlinden, Continued development of all-back-contact silicon wafer solar cells at ANU, Energy Procedia 33 (2013) 50.
[26] E. Franklin, K. Fong, K. McIntosh, A. Fell, A. Blakers, T. Kho, D. Walter, D. Wang, N. Zin, M. Stocks, E.C. Wang, N. Grant, Y. Wan, Y. Yang, X. Zhang, Z. Feng, P.J. Verlinden, Design, fabrication and characterisation of a 24.4% efficient interdigitated back contact solar cell, in: Proceedings of Progress in Photovoltaics: Research and Applications, 2014, doi: 10.1002/pip.2556.
[27] H.T. Nguyen, F.E. Rougieux, B. Mitchell, D. Macdonald, Temperature dependence of the band–band absorption coefficient in crystalline silicon from photoluminescence, J. Appl. Phys. 115 (2014) 043710.
[28] J.I. Pankove, D.E. Carlson, Electroluminescence in amorphous silicon, Appl. Phys. Lett. 29 (1976) 620.
[29] D. Engemann, R. Fischer, Photoluminescence in amorphous silicon, Phys. Status Solidi B 79 (1977) 195.
[30] F. Alvarez, F. Williams, Photoluminescence of hydrogenated amorphous silicon, J. Non-Cryst. Solids 50 (1982) 139.
[31] S. Rauscher, H. Pfleiderer, B. Bullemer, Tail–tail luminescence in amorphous silicon, Phys. Status Solidi A 78 (1983) 623.
[32] W. Fuhs, Recombination and transport through localized states in hydrogenated amorphous and microcrystalline silicon, J. Non-Cryst. Solids 354 (2008) 2067.
[33] K. Murayama, R. Sagawa, K. Monji, K. Tsushima, H. Deki, Luminescence gap in hydrogenated amorphous silicon, J. Non-Cryst. Solids 358 (2012) 2027.
[34] V. Sa-Yakanit, H.R. Glyde, Urbach tails and disorder, Comments Cond. Matter Phys. 13 (1987) 35.
[35] M. Janai, D.D. Allred, D.C. Booth, B.O. Seraphin, Optical properties and structure of amorphous silicon films prepared by CVD, Sol. Energy Mater. 1 (1979) 11.
[36] C.C. Tsai, H. Fritzsche, Effect of annealing on the optical properties of plasma deposited amorphous hydrogenated silicon, Sol. Energy Mater. 1 (1979) 29.
[37] M.L. Theye, Optical absorption in amorphous semiconductors, Phys. Scr. T29 (1989) 157.
[38] I. Umezu, T. Murota, M. Kawata, Y. Takashima, K. Yoshida, M. Inada, A. Sugimura, Correlation between photoluminescence intensity and microstructure in amorphous silicon films prepared by reactive RF sputtering, Jpn. J. Appl. Phys. 39 (2000) L844.
[39] A. Descoeudres, Z.C. Holman, L. Barraud, S. Morel, S. De Wolf, C. Ballif, > 21% efficient silicon heterojunction solar cells on n- and p-type wafers compared, IEEE J. Photovolt. 3 (2013) 83.
[40] A. Tomasi, B. Paviet-Salomon, D. Lachenal, S.M. de Nicolas, A. Descoeudres, J. Geissbühler, S. De Wolf, C. Ballif, Back-contacted silicon heterojunction solar cells with efficiency > 21%, IEEE J. Photovolt. 4 (2014) 1046.
[41] G.D. Cody, T. Tiedje, B. Abeles, B. Brooks, Y. Goldstein, Disorder and the optical-absorption edge of hydrogenated amorphous silicon, Phys. Rev. Lett. 47 (1981) 1480.
[42] R.A. Street, D.K. Biegelsen, J.C. Knights, Defect states in doped and compensated a-Si:H, Phys. Rev. B 24 (1981) 969.
[43] I.G. Austin, T.S. Nashashibi, T.M. Searle, P.G. Le Comber, W.E. Spear, Photoluminescence and lifetime studies on plasma discharge a-Si, J. Non-Cryst. Solids 32 (1978) 373.
[44] R. Fischer, W. Rehm, J. Stuke, U. Voget-Grote, Thermalization and recombination of excess carriers in a-Si:H, J. Non-Cryst. Solids 35–36 (1980) 687.
[45] M. Tajima, S. Yamasaki, H. Okushi, K. Tanaka, Direct evidence for strong electron-phonon interaction on deep trapping process in P-doped a-Si:H, J. Non-Cryst. Solids 77–78 (1985) 603.
[46] Z.C. Holman, A. Descoeudres, L. Barraud, F.Z. Fernandez, J.P. Seif, S. De Wolf, C. Ballif, Current losses at the front of silicon heterojunction solar cells, IEEE J. Photovolt. 2 (2012) 7.
[47] A. Tomasi, B. Paviet-Salomon, D. Lachenal, S.M. de Nicolas, M. Ledinsky, A. Descoeudres, S. Nicolay, S. De Wolf, C. Ballif, Photolithography-free interdigitated back-contacted silicon heterojunction solar cells with efficiency > 21%, in: Proceedings of the IEEE 40th Photovoltaic Specialist Conference, 2014.
[48] R.W. Collins, M.A. Paesler, W. Paul, The temperature dependence of photoluminescence in a-Si:H alloys, Solid State Commun. 34 (1980) 833.
[49] J.I. Pankove, M.L. Tarng, Amorphous silicon as a passivant for crystalline silicon, Appl. Phys. Lett. 34 (1979) 156.

[50] S. Olibet, E. Vallat-Sauvain, C. Ballif, Model for a-Si:H/c-Si interface recombination based on the amphoteric nature of silicon dangling bonds, Phys. Rev. B 76 (2007) 035326.

[51] H.T. Nguyen, F.E. Rougieux, S.C. Baker-Finch, D. Macdonald, Impact of carrier profile and rear-side reflection on photoluminescence spectra in planar crystalline silicon wafers at different temperatures, IEEE J. Photovolt. 5 (2015) 77.

[52] S. Jung, D. Gong, J. Yi, The effects of the band gap and defects in silicon nitride on the carrier lifetime and the transmittance in c-Si solar cells, Sol. Energy Mater. Sol. Cells 95 (2010) 546.

[53] D. Bermejo, M. Cardona, Raman-scattering in pure and hydrogenated amorphous-germanium and silicon, J. Non-Cryst. Solids 32 (1979) 405.

[54] F.D. Heinz, W. Warta, M.C. Schubert, Optimizing micro raman and PL spectroscopy for solar cell technological assessment, Energy Procedia 27 (2012) 208.

[55] H.T. Nguyen, F.E. Rougieux, F. Wang, D. Macdonald, Effects of solar cell processing steps on dislocation luminescence in multicrystalline silicon, Energy Procedia 77 (2015) 619.

[56] S.V. Deshpande, E. Gulari, S.W. Brown, S.C. Rand, Optical properties of silicon nitride films deposited by hot filament chemical vapor deposition, J. Appl. Phys. 77 (1995) 6534.

[57] H.L. Hao, L.K. Wu, W.Z. Shen, H.F.W. Dekkers, Origin of visible luminescence in hydrogenated amorphous silicon nitride, Appl. Phys. Lett. 91 (2007) 201922.

[58] M. Anutgan, T. Anutgan, I. Atilgan, B. Katircioglu, Photoluminescence analyses of hydrogenated amorphous silicon nitride thin films, J. Lumin. 131 (2011) 1305.

[59] O. Debieu, R.P. Nalini, J. Cardin, X. Portier, J. Perrière, F. Gourbilleau, Structural and optical characterization of pure Si-rich nitride thin films, Nanoscale Res. Lett. 8 (2013) 31.

[60] S. Mohammed, M.T. Nimmo, A.V. Malko, C.L. Hinkle, Chemical bonding and defect states of LPCVD grown silicon-rich Si_3N_4 for quantum dot applications, J. Vacuum & Technology – > Sci. Technol. 32 (2014) 021507.

CHAPTER 9

Spectrally-Resolved Micro-Photoluminescence Excitation Spectroscopy

So far, this thesis has reported various applications of spectrally-resolved photoluminescence (PLS) in silicon photovoltaics. In these PLS-based techniques, the entire spectrum from the silicon wafer is captured using a single excitation energy. Due to the different radiative recombination mechanisms of different structures in a single silicon wafer, different spectral components of the total spectrum captured have different dependences on the excitation intensity and the sample temperature. Thus, by varying the sample temperature or the excitation power, the shapes of the spectra containing various components are changed remarkably (see Chapters 6, 7, and 8), allowing one to tailor the experimental conditions in order to observe the signature of a particular component on the spectra (Chapter 7).

Photoluminescence excitation spectroscopy (PLE) is, on the other hand, a method in which the luminescence intensity from the wafer at certain wavelengths is monitored while the

excitation energy is varied. In general, if the excitation power is kept constant, the luminescence intensity from a certain radiative recombination mechanism will be suppressed with reducing excitation energies. Eventually, once the excitation energy passes a threshold level, the luminescence will completely disappear. Each radiative recombination mechanism has its own threshold energy. Therefore, this PLE-based method is also applied to investigate the electronic and optical properties of materials.

As the complexity of devices increases, there is a requirement of reducing the size of various structures and stacking different layers together. Therefore, investigating the properties of these structures is more challenging. However, both lateral and vertical spatial information is important for understanding and characterizing the devices. In principle, by varying the excitation energy, the absorption depth of the excitation light in the material is changed, and as such the fraction of the excitation light absorbed in each layer or structure is also varied. This phenomenon results in changes in the luminescence intensity of each component on the total spectrum detected.

This chapter takes advantages of both PLS- and PLE-based techniques to report a new photoluminescence-based method for characterizing silicon solar cells. In particular, the entire spectrum from a silicon wafer or solar cell is captured while the excitation energy is varied. Therefore, the evolution of the luminescence components, emitted from different recombination centers at different depths below the wafer surface, can be observed. Furthermore, adding the high spatial resolution of the micro-photoluminescence spectroscopy system, this combined PLS-PLE technique is proven to be a powerful tool for characterizing materials and devices both in spectral and spatial (lateral and vertical) dimensions.

The work has been published. However, there are two important points that need to be clarified in this publication. First, the two luminescence peaks at 1130 nm and ~1160 nm, denoted as “c-Si” and “HDBB” peaks in the publication, are the band-to-band emission assisted by a Transverse-Optical (TO) phonon from the Si substrate and the heavily-doped layer, respectively. Second, the broad wavy features in the TEM image are bending contours due to the elastic bending of the thin TEM specimen, not thickness fringes.

Photoluminescence Excitation Spectroscopy of Diffused Layers on Crystalline Silicon Wafers

Hieu T. Nguyen, Sieu Pheng Phang, Jennifer Wong-Leung, and Daniel Macdonald

***Abstract*—Photoluminescence (PL) excitation spectroscopy is applied to observe the evolution of the luminescence spectra from dopant-diffused crystalline silicon wafers with varying excitation wavelength. Utilizing the micrometer-scale spatial resolution achievable with confocal optics in a micro-photoluminescence spectroscopy system, along with the well-resolved luminescence peaks at cryogenic temperatures from various defects and structures in a single-silicon substrate, we are able to examine the doping densities and junction depths of various boron-diffused wafers, as well as the distribution of defects induced underneath the wafer surface by the post-diffusion thermal treatment. Our conclusions are validated by photoluminescence scans and transmission electron microscopy applied to vertical cross sections, which confirm the presence of dislocations below the diffused regions.**

***Index Terms*—Crystalline silicon, diffusion process, excitation spectroscopy, photoluminescence (PL), photovoltaic cells.**

I. Introduction

PHOTOLUMINESCENCE spectroscopy (PLS) is a powerful technique to assess fundamental properties of crystalline silicon (c-Si), such as the temperature [1] and doping [2], [3] dependences of the band gap, the band-to-band absorption [4]–[6], radiative recombination [5], [7], [8], and donor–acceptor pair luminescence [9], [10]. Besides that, PLS-based methods have also been employed for precise and nondestructive characterization in silicon photovoltaics (PV), for example, to extract minority carrier diffusion lengths in c-Si wafers [11], [12] and bricks [13], to quantify the light-trapping capability of various plasmonic structures [14], or to examine the impacts of surface reflectance [15], [16] and different carrier profiles [16] on photoluminescence (PL) spectra. Recently, utilizing a micro-PLS (μPLS) system with micrometer-scale spatial resolution courtesy of confocal optics, spectroscopic properties of various microscopic defects and structures in c-Si wafers and solar cells have been studied, such as dislocations [17]–[19], iron precipitates [20], laser-doped regions [21]–[24], and locally diffused regions [25].

On the other hand, photoluminescence excitation (PLE) spectroscopy, in which the luminescence intensity at certain wavelengths is monitored with varying excitation wavelengths, has also been employed to study many fundamental properties of c-Si, such as the optical band gap in degenerate silicon [2], [26], oxygen-related deep defects in irradiated silicon [27], and isoelectronic bound excitons in beryllium-doped silicon [28]. Recently, Juhl *et al.* [29] applied a PLE-type method to capture the total PL emission from c-Si wafers in imaging mode, under two different excitation wavelengths, from which they were able to extract high-resolution images of the absolute absorptance of solar cell precursors.

In this work, we combine the two PL techniques mentioned above (PLS and PLE) and capture the entire band-to-band luminescence spectrum, while varying the excitation wavelength, with the measurements performed at cryogenic temperatures and with micrometer-scale spatial resolution. This spectrally resolved PLE technique is founded on the fact that the radiative recombination mechanism is generally different for each layer or defect type in a c-Si wafer, leading to distinct peaks in PL spectra at cryogenic temperatures. Furthermore, these components of the aggregate luminescence spectrum from a wafer composed of multiple layers are expected to have different dependences on the excitation wavelength, since the fraction of the excitation light absorbed in each layer varies with excitation wavelength. Therefore, by varying the excitation wavelengths, we can probe the layers and defects at different depths below the wafer surface, providing useful information about the spatial distribution of dopants and defects. First, we demonstrate this method on boron-diffused c-Si samples with various doping densities and junction depths. After that, we apply the method to detect and characterize specific defects induced underneath the wafer surface by the post-diffusion thermal treatment, highlighting some potential applications of the technique for silicon PV. The results are confirmed by μPLS measurements and transmission electron microscopy (TEM) performed on vertical cross sections of relevant samples.

II. Experimental Details

The samples studied in Section III are float-zone phosphorus-doped c-Si wafers with a resistivity of 100 $\Omega\cdot$cm. They were first chemically etched in a solution consisting of HF and HNO_3 to remove saw damage. After that, they were heavily doped with boron from a BBr_3 gas source between 900 and 1000 °C in a quartz tube furnace with various drive-in times in a pure oxygen environment to achieve different doping profiles in the diffused layers. More details about this diffusion process can be found in [30].

The samples studied in Sections IV and V are $\langle 1\ 0\ 0\rangle$-oriented float-zone boron-doped c-Si wafers with a resistivity of

Manuscript received November 15, 2015; revised January 12, 2016; accepted February 11, 2016. Date of publication March 3, 2016; date of current version April 19, 2016. This work was supported by the Australian Research Council and the Australian Renewable Energy Agency through Research Grant RND009.

H. T. Nguyen, S. P. Phang, and D. Macdonald are with the Research School of Engineering, The Australian National University, Canberra, A.C.T. 2601, Australia (e-mail: hieu.nguyen@anu.edu.au; pheng.phang@anu.edu.au; daniel.macdonald@anu.edu.au).

J. Wong-Leung is with the Department of Electronic Materials Engineering, The Australian National University, Canberra, A.C.T. 2601, Australia (e-mail: jenny.wongleung@anu.edu.au).

Color versions of one or more of the figures in this paper are available online at http://ieeexplore.ieee.org.

Digital Object Identifier 10.1109/JPHOTOV.2016.2532460

2156-3381 © 2016 IEEE. Personal use is permitted, but republication/redistribution requires IEEE permission.
See http://www.ieee.org/publications_standards/publications/rights/index.html for more information.

TABLE I
PROCESSING STEPS FOR THE SAMPLES INVESTIGATED IN SECTIONS IV AND V

Processes (in sequence)	Sample names					
	N1	N2	N3	O1	O2	O3
1. Boron-diffused at 1050 °C, 60 min	Yes	Yes	Yes	Yes	Yes	Yes
2. BSG layer was removed by diluted HF	Yes	Yes	No	Yes	Yes	No
3. BRL layer was removed by boiling HNO_3	Yes	No	No	Yes	No	No
4. Annealed at 1090 °C for 5 h	Yes, in N_2	Yes, in N_2	Yes, in N_2	Yes, in O_2	Yes, in O_2	Yes, in O_2
5. Both BSG and BRL layers were removed	Yes	Yes	Yes	Yes	Yes	Yes

"N" indicates the samples annealed in nitrogen and "O" indicates samples annealed in oxygen.

about 0.3 Ω·cm, corresponding to a background doping of 6×10^{16} cm^{-3}. They were first chemically etched in HF/HNO_3 to remove saw damage and then went through the thermal diffusion process in a BBr_3 gas source at 1050 °C for 60 min. The resultant borosilicate glass (BSG) and boron-rich layer (BRL) on the surface were either kept or removed by diluted HF (for removing the BSG layer) and boiling HNO_3 (for removing the BRL layer). After that, these samples were annealed in either pure nitrogen or oxygen gases at 1090 °C for 5 h. Any residual BSG and BRL layers were finally removed prior to performing the PL measurements. Table I summarizes the process steps for these samples. These process steps are, in general, impractical for solar cell applications. They are aimed to generate different types of defects separated at different depths below the wafer surface, which best illustrate the capabilities of the technique presented here.

The experimental setup of our μ-PLS system is described in detail elsewhere [31]. A supercontinuum excitation light source (NKT SuperK Extreme EXR-20) with a tunable wavelength range between 490 nm and 2 μm was employed. In this work, excitation wavelengths between 510 and 810 nm were used with a bandwidth of 10 nm for the chosen wavelengths, and the on-sample power was kept constant at 6 mW for all excitation wavelengths. The wavelength selection was achieved using a SuperK VARIA attachment allowing the tuning of both the center wavelength and the bandwidth of the filtered light. The diameter of the illuminated spot on the samples varied between ~1 μm (for 510-nm excitation wavelength) and ~2 μm (for 810-nm excitation wavelength). The spectral response of the entire system was determined with a calibrated halogen–tungsten light source. The measurement temperature was kept at 79 K using a liquid-nitrogen-cooled cryostat. The cross-sectional specimens for μPLS measurements were prepared by a conventional mechanical polishing technique, whereas the cross-sectional specimens for TEM were prepared by focused ion beam. TEM analysis was carried out in a Phillips CM300 instrument operated at 300 keV. The doping profiles of the diffused layers were measured using the electrochemical capacitance–voltage (ECV) technique.

III. SPECTRALLY RESOLVED PHOTOLUMINESCENCE EXCITATION ON DIFFUSED SILICON WAFERS

Fig. 1(a) shows doping profiles of two different boron-diffused samples measured by ECV. The doping profile of sample 1 is shallower but higher in concentration, compared with sample 2. Fig. 1(b) plots the absorption depth versus excitation wavelength in c-Si at 79 K. The data were calculated from [32] and the effects of heavy doping were neglected. Fig. 1(c) and (d) shows the evolution of normalized PL spectra of samples 1 and 2, respectively, with increasing excitation wavelengths from 510 to 810 nm at 79 K. Two distinct peaks can be observed in each spectrum. The peak located at ~1130 nm is the band-to-band emission from the underlying c-Si substrate (denoted as c-Si peak) and was used for normalizing the spectra for different excitation wavelengths. The second peak at ~1165 nm (sample 1) and ~1157 nm (sample 2) is the band-to-band emission attributed to the heavily doped layer near the surface (denoted as HDBB peak) [24], [25]. Compared with the c-Si peak, this HDBB peak is shifted to longer wavelengths due to band-gap narrowing (BGN) effects in heavily doped silicon [2], [3]. At the shortest excitation wavelength (510 nm), a large fraction of the laser light is absorbed in the diffused layer near the surface. Therefore, the HDBB peak is intense compared with the c-Si peak. However, when the excitation wavelength increases, i.e., the absorption depth increases, the laser light is absorbed more in the silicon substrate but less in the diffused layer. Therefore, the relative intensity of the HDBB peak is suppressed, compared with the c-Si peak.

Fig. 2(a) compares the normalized spectra between the two samples at two excitation wavelengths: 510 and 810 nm. The first notable feature is the difference in the energy and width of the HDBB peak between the two samples. The HDBB peak of sample 1 is lower in energy (i.e., longer wavelength) and broader compared with that of sample 2, indicating that the diffused layer of sample 1 is more heavily doped than that of sample 2. The difference is explained by the illustration in Fig. 2(b). There are two distinct points for the heavily doped silicon: 1) the luminescence gap E_{g2} is smaller than that of the low-doped silicon E_{g1} due to BGN effects [2], [3]; and 2) the Fermi energy level E_F is shifted into the valence band E_V (for p-type doping), and thus, all energy states between E_F and E_V are occupied by free holes [26], [33]. Meanwhile, the free holes in low-doped silicon are very close to the valence band edge due to rapid carrier thermalization. Thus, the radiative recombination between the two band edges has a wider energy distribution in heavily doped silicon compared with lowly doped silicon [26], [33], [34]. Therefore, the higher the doping density in the diffused layer, the lower the energy and the broader the width of the HDBB peak. Note that the nonhomogeneous doping profile throughout the thickness of the diffused layer also contributes to the broadening of the HDBB peak, compared with the c-Si peak, which is emitted from the homogeneously doped substrate.

The second notable feature is the difference in the HDBB peak intensity between the two samples. The normalized HDBB peak of sample 1 is reduced more quickly than that of sample 2 when the laser light penetrates deeper into the substrate. This feature demonstrates that the junction depth of sample 2 is deeper than that of sample 1. Therefore, by employing this spectrally resolved PLE technique, one can qualitatively assess both the doping level and the junction depth of the heavily doped layers in c-Si wafers and solar cells. The technique is, in principle, only

Fig. 1. (a) Doping profiles of the two boron-diffused samples. The numbers in brackets are the measured sheet resistance (using the four-point probe technique) and emitter saturation current density (see [30] for the measurement technique), respectively. (a) Absorption depth versus excitation wavelength in c-Si at 79 K. The data were calculated from [32], and the effects of heavy doping were neglected. PL spectra of (c) sample 1 and (d) sample 2, captured at 79 K with varying excitation wavelengths. All spectra were normalized to the c-Si peak. The spurious peaks marked by broken-line arrows are harmonic artifacts due to the not-entirely-suppressed sidebands of the supercontinuum laser.

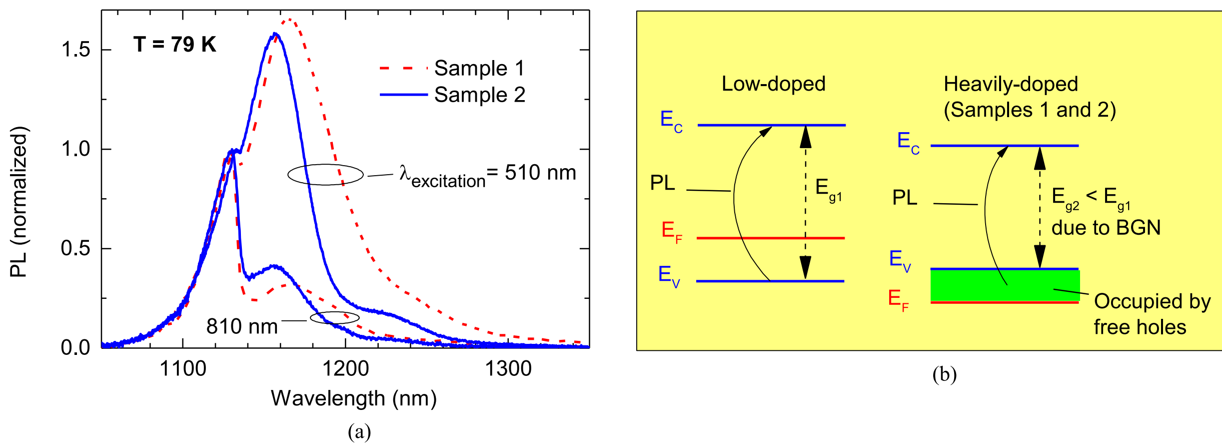

Fig. 2. (a) Comparison of normalized PL spectra between sample 1 and sample 2, excited with the 510- and 810-nm wavelengths at 79 K. All spectra were normalized to the c-Si peak. (b) Radiative recombination scheme in low-doped and heavily doped p-type c-Si wafers.

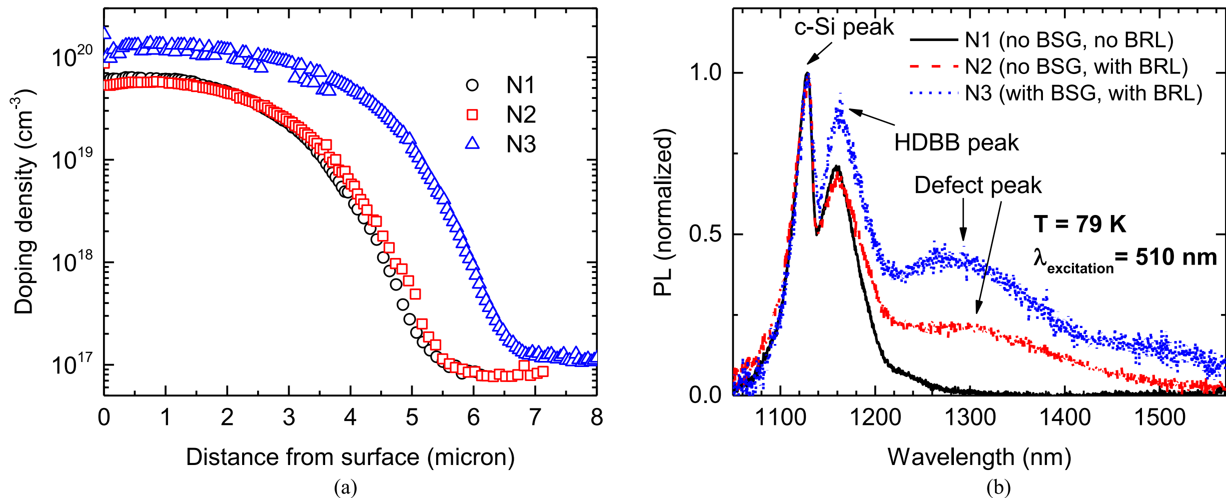

Fig. 3. (a) Doping profiles of three samples N1, N2, and N3. (b) Comparison of normalized PL spectra among the three samples, excited with the 510-nm wavelength at 79 K.

sensitive to active dopants since only active dopants contribute to the BGN effects, causing the HDBB peak. However, the absorption depth of the excitation light is expected to be smaller than the values presented in Fig. 1(b) due to the smaller effective band gap in heavily doped silicon. In addition, this parameter varies throughout the thickness of the diffused layer. Hence, we do not place an emphasis on calculating the exact junction depth from this technique at the current stage. Note that there is also a weak shoulder around 1230 nm, which is mostly visible in sample 2. This is the phonon replica of the HDBB peak.

IV. Spectrally Resolved Photoluminescence Excitation on Defects Induced by Post-Diffusion Thermal Treatment

In this section, we examine the impact of the post-diffusion thermal treatment on the formation of defects underneath the wafer surface, applying the spectrally resolved PLE technique. Fig. 3(a) plots the doping profiles of the three samples N1, N2, and N3 (see Table I for a description of these samples). As can be seen from this figure, sample N3 (retaining both BSG and BRL layers before annealing) is more heavily doped than the other two, since the BSG layer acts as a further source of boron doping, which diffuses into the silicon wafer during annealing at high temperatures [35]. Fig. 3(b) shows the normalized spectra from the three samples, excited with the 510-nm wavelength at 79 K. Besides the c-Si (from the silicon substrate) and HDBB (from the heavily doped region) peaks, samples N2 and N3 also show a strong deep-level luminescence peak at ~1300 nm. However, sample N1 (for which both the BRL and BSG layers were removed before being annealed) does not show any defect luminescence, despite having a similar doping profile with sample N2. The BSG layer was removed by diluted HF, in which silicon is not dissolved. The BRL layer was removed by oxidizing the wafers in boiling HNO_3 with 20-min intervals and was considered to be removed completely if the wafer surface was hydrophobic after HF dip. The boiling HNO_3 was demonstrated to oxidize less than 5 nm of silicon in 10 min [36], and thus, the 20-min interval oxidation causes no significant changes to the boron diffusion profiles across all samples. This suggests that the heavily doped layer itself, annealed at high temperatures, does not cause the observed deep-level luminescence.

Furthermore, we did not observe any defect luminescence from the three samples annealed in an oxygen environment O1, O2, and O3. Since the oxidation process converts the BRL layer into a BSG layer [35], the absence of defect luminescence from these samples suggests that annealing the BSG layer by itself does not cause deep-level defects inside the silicon wafers. These findings are consistent with the results reported by Cousins and Cotter [37] and Kessler *et al.* [38]. Cousins and Cotter found that their boron-diffused wafers were heavily dislocated when driving them in with an inert gas directly after the diffusion process (thus, the BRL layer was still present) but found minimal dislocations in the wafers driven in with an oxygen environment [37]. Kessler *et al.* reported that a thick BRL layer caused a bulk lifetime degradation of silicon wafers during the annealing and cooling process, and this degradation could be avoided by a drive-in step in oxygen gas to reverse the BRL formation [38]. Therefore, we propose that annealing the BRL layer causes a mechanical stress between this layer and the silicon wafer, creating dislocations that can glide into the silicon wafer and cause the deep-level luminescence. The type and origin of the deep-level luminescence, as well as the presence of dislocations, will be clarified in Section V.

Next, we demonstrate the application of the spectrally resolved PLE method on the defects induced by the post-diffusion thermal treatment mentioned above, giving us useful information about the depth distribution of different types of defects below the wafer surface. Fig. 4(a) and (b) shows the normalized spectra of samples N2 and N3 with varying excitation wavelengths at 79 K. As in Fig. 1(b) and (c), the longer the excitation wavelengths, the less pronounced the HDBB peak, compared with the c-Si peak. However, we can also observe a suppression of the defect peak with increasing excitation wavelengths,

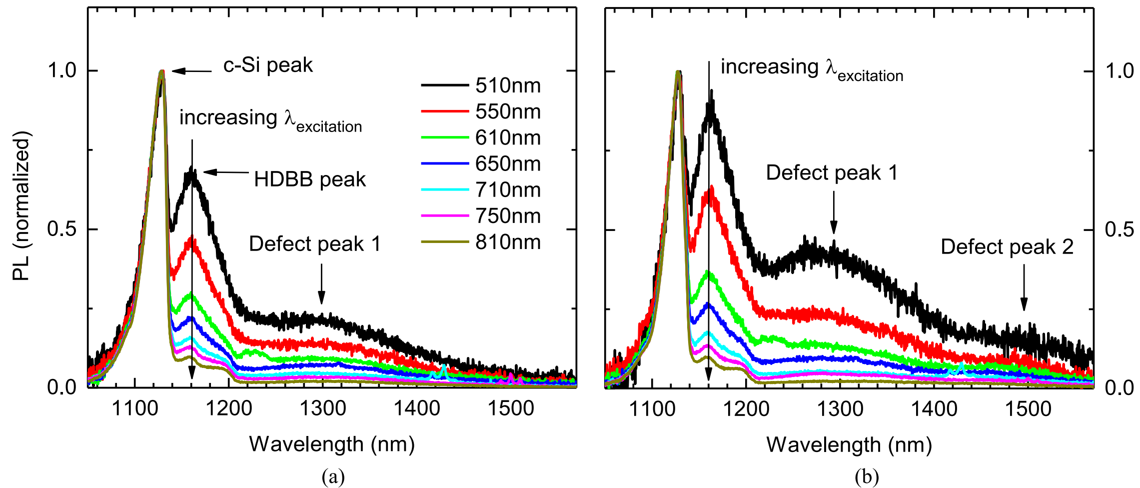

Fig. 4. PL spectra of (a) sample N2 and (b) sample N3, captured at 79 K with varying excitation wavelengths. All spectra were normalized to the c-Si peak.

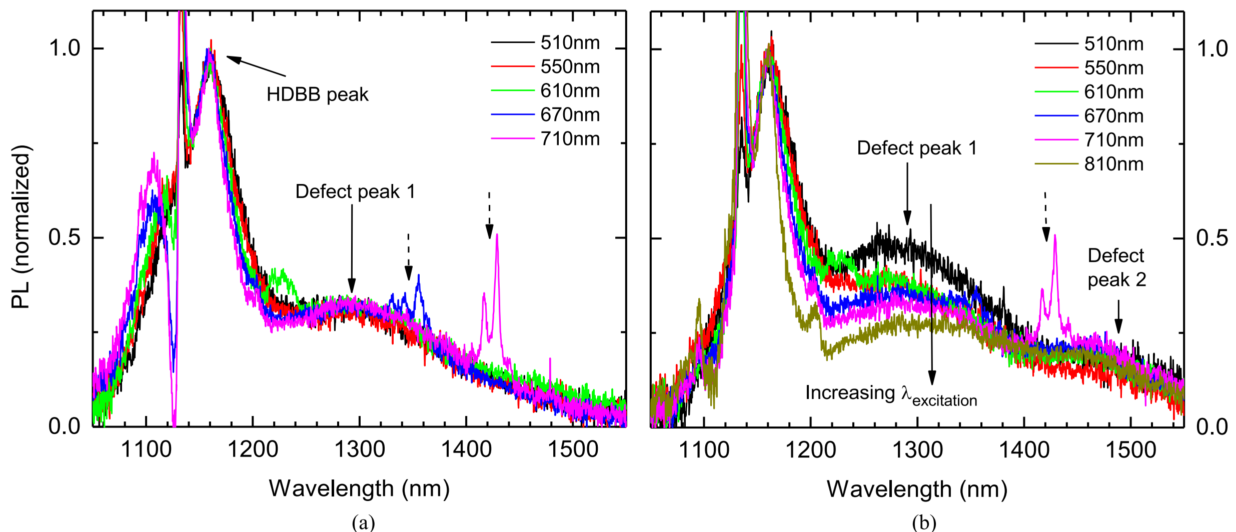

Fig. 5. PL spectra of (a) sample N2 and (b) sample N3, captured at 79 K with varying excitation wavelengths. The c-Si component was subtracted from all spectra, and the resultant spectra were normalized to the HDBB peak. The spurious peaks marked by broken-line arrows are harmonic artifacts due to the not-entirely-suppressed sidebands of the supercontinuum laser. The spectrum at 810-nm excitation wavelength was not shown in (a) since the HDBB peak was not well resolved after subtracting the c-Si component.

compared with the c-Si peak. Therefore, we conclude that the observed defect luminescence originates from the region near the wafer surface. Moreover, a detailed inspection of the defect luminescence reveals a difference between the two samples. Sample N2 has only one defect peak located at ~1300 nm, whereas sample N3 seems to have another weak defect peak at ~1480 nm. Therefore, we denoted the two peaks at ~1300 and ~1480 nm as "defect peak 1" and "defect peak 2," respectively, in Fig. 4(a) and (b).

Furthermore, Fig. 5(a) and (b) plots the spectra, normalized to the HDBB peak, of samples N2 and N3. The c-Si peak has been subtracted from all spectra in order to avoid the impact of this peak on the spectral components from the near surface region. In Fig. 5(a), the shape of the defect luminescence is very consistent, and there is only one peak for all excitation wavelengths. However, in Fig. 5(b), there are two different defect peaks at ~1300 and ~1480 nm, and their relative intensity is different from each other with increasing excitation wavelengths. Compared with defect peak 2, defect peak 1 is less pronounced when the laser light penetrates more deeply into the c-Si substrate. Therefore, these results suggest that although both defects are distributed near the surface region, defect peak 2 is distributed more deeply into the substrate than defect peak 1. Note that all spectra presented so far were measured from above the wafer surface, i.e., this method is nondestructive.

V. Verification of Defect Luminescence Using Cross-Sectional μPhotoluminescence Spectroscopy and Transmission Electron Microscopy

Now, we verify the findings regarding the spatial distribution of defect peaks 1 and 2 mentioned above, using the PL spectra captured from a vertical cross-sectional slice of the investigated boron-diffused c-Si wafers. The cross section was

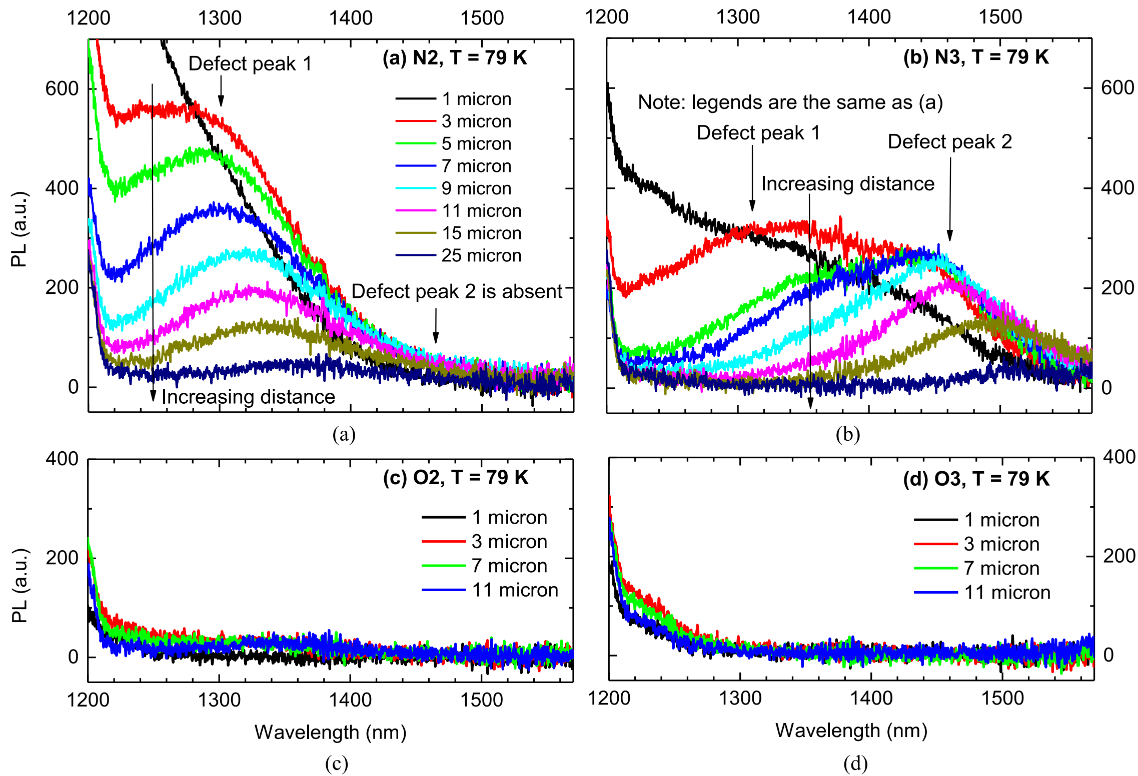

Fig. 6. PL spectra on the cross sections of samples (a) N2, (b) N3, (c) O2, and (d) O3, captured at 79 K with 810-nm excitation wavelength. The lengths indicate the distance from the original wafer surface on the cross section.

excited with the 810-nm wavelength to allow the laser light to penetrate deeply into the samples (from the cross-sectional view), thus reducing the nonradiative recombination caused by the damaged layer resulting from the mechanical polishing on the cross-sectional surface. Fig. 6(a) and (b) shows the relative PL spectra from samples N2 and N3, captured at different distances from the edge of the cross section (which is the original sample surface). As can be readily seen from Fig. 6(a), defect peak 2 is absent from all spectra, whereas the intensity of defect peak 1 reduces with increasing distances from the edge. However, in Fig. 6(b), we can observe unambiguously both defect peaks. The intensity of defect peak 1 reduces quickly, whereas that of defect peak 2 still remains strong up to a certain distance from the edge. Meanwhile, no defect luminescence is observed in the spectra from the samples annealed in an oxygen environment, as depicted in Fig. 6(c) and (d). The results from these four figures are consistent with our conclusions above.

In addition, comparing the two defect peaks with the so-called D lines emitted from dislocations, their spatial distributions are consistent with those of the doublets D3/D4 and D1/D2, respectively [18], [19], [31], [38]. The doublet D1/D2 was demonstrated to be emitted from the secondary defects and impurities trapped around dislocation sites, and thus, their spatial distribution is usually extended over a broader region around the dislocation sites [18], [19], [31], [38]. Meanwhile, the doublet D3/D4 was found to reflect the intrinsic properties of dislocations themselves, since the luminescence was confined to very near the dislocation sites [18], [19], [31], [39]. Therefore, we propose that defect peak 1 represents the doublet D3/D4, whereas defect peak 2 is expected to be the doublet D1/D2. Decomposing defect peaks 1 and 2 into their individual D lines is difficult, since these two peaks are emitted from the regions in which the doping profile is nonuniform, thus broadening the two peaks due to varying amount of BGN in heavily doped silicon. However, once the distance from the edge of the cross section is far enough [e.g., the 15-μm curve in Fig. 6(b)], the contribution from the uniform- and low-doped region dominates the spectrum and the position of defect peak 2 is similar to the reported D1 line [31], [39].

Finally, a TEM two-beam [–1 –1 1] bright-field image of the (0 1 1) cross section of the boron-diffused silicon wafer N3 is shown in Fig. 7(a) and (b) for low and high magnifications, respectively. The micrograph in Fig. 7(a) reveals a dislocation band located about 3 μm below the wafer surface. Between this dislocation band and the surface is a dislocation-free zone. This distribution of dislocations is similar to the results reported by Ning [40] and was explained by the movement of dislocations formed at the wafer surface during the annealing and cooling process. Therefore, the observed deep-level luminescence is likely to be related to the dislocations.

Since defect peak 2 was not present on samples N1 (annealed in nitrogen gas) and N2 (annealed in nitrogen gas with the BRL layer present), this defect peak is not likely to be due to either nitrogen diffused into the wafers or nitrogen–oxygen complexes [41]. Another possibility is that this defect peak could originate from oxygen precipitates, since its energy level is similar to

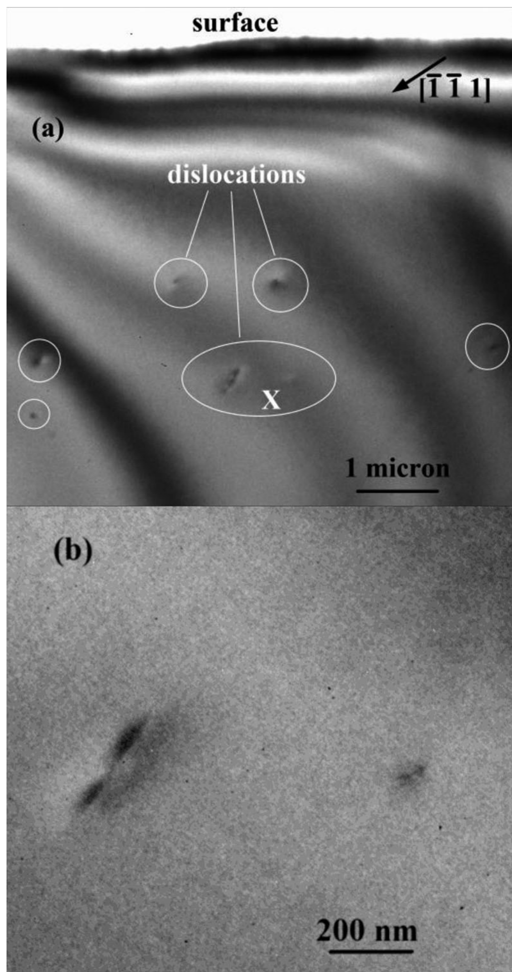

Fig. 7. (a) TEM two-beam [–1 –1 1] bright-field image of the (0 1 1) cross section of the (1 0 0) boron-diffused silicon wafer N3. The [0 1 1] zone-axis is along the beam direction. The dislocations are marked with the white circles, and they form a band parallel to the wafer surface. The broad wavy features are thickness fringes due to the nonuniformity of the thickness of the TEM specimen. (b) Image with higher magnification of the area marked with "X" in (a).

the luminescence from oxygen precipitates, reported by Tajima *et al.* [18] and Bothe *et al.* [42]. However, oxygen precipitates and dislocations often appear together [43] due to the local stress and strain around the precipitates. In addition, Tajima *et al.* [18] reported that oxygen precipitate luminescence was confined around small-angle grain boundaries, which were known to have high dislocation densities, and the luminescence only appeared at 100 K or above. Meanwhile, our defect peak 2 can be observed at 79 K and extends well below the wafer surface compared with the dislocation band. Therefore, the observed luminescence peak is unlikely due to oxygen precipitates, although oxygen precipitates could possibly decorate around the dislocations near the surface.

In fact, defect peak 2 can be compared with the results reported by Charnvanichborikarn *et al.* [44], [45]. These authors found a broad PL band beyond 1400 nm from irradiated c-Si wafers annealed at high temperatures and proposed that this PL band arose from the localized strain in the early stages of extended defect formation or interstitial clusters. In addition, in Fig. 6(a), there is a shifting toward longer wavelengths of defect peak 1 with increasing distances from the edge, which is similar to that of D3 when moving away from the subgrain boundaries in mc-Si [31]. We note that, although the spectrally resolved PLE technique was demonstrated here on boron-diffused layers and dislocations in c-Si wafers, it could, in principle, be applied for others structures and defects separated at different depths within a wafer.

VI. Conclusion

Combining spectrally resolved PL and PLE spectroscopy techniques, we have captured full luminescence spectra with varying excitation wavelengths, allowing us to examine the properties of different layers and defect types at various depths inside boron-diffused silicon wafers. We have demonstrated that this method can be used to qualitatively assess doping concentrations and junction depths. In addition, we have applied this method to detect dislocations induced by the post-diffusion thermal treatment process, giving insightful information about the spatial distribution of both dislocations and secondary defects located below the wafer surfaces.

Acknowledgment

The authors would like to thank Prof. H. Tan for providing access to the spectroscopic equipment; Prof. B. Luther-Davies, Dr. S. Mokkapati, and D. Llewellyn for assisting with the hardware setup; and D. Yan for providing the boron-diffused n-type silicon wafers. The Australian National Fabrication Facility, the Center for Advanced Microscopy, and the Australian Microscopy and Microanalysis Research Facility ACT node are greatly acknowledged for providing access to some of the facilities used in this work.

References

[1] W. Bludau, A. Onton, and W. Heinke, "Temperature dependence of the band gap of silicon," *J. Appl. Phys.*, vol. 45, pp. 1846–1848, 1974.

[2] J. Wagner, "Photoluminescence and excitation spectroscopy in heavily doped n- and p-type silicon," *Phys. Rev. B*, vol. 29, pp. 2002–2009, 1984.

[3] J. Wagner, "Band-gap narrowing in heavily doped silicon at 20 and 300 K studied by photoluminescence," *Phys. Rev. B*, vol. 32, pp. 1323–1325, 1985.

[4] E. Daub and P. Würfel, "Ultralow values of the absorption coefficient of Si obtained from luminescence," *Phys. Rev. Lett.*, vol. 74, pp. 1020–1023, 1995.

[5] T. Trupke *et al.*, "Temperature dependence of the radiative recombination coefficient of intrinsic crystalline silicon," *J. Appl. Phys.*, vol. 94, pp. 4930–4937, 2003.

[6] H. T. Nguyen, F. E. Rougieux, B. Mitchell, and D. Macdonald, "Temperature dependence of the band-band absorption coefficient in crystalline silicon from photoluminescence," *J. Appl. Phys.*, vol. 115, pp. 043710-1–043710-8, 2014.

[7] P. P. Altermatt *et al.*, "Injection dependence of spontaneous radiative recombination in crystalline silicon: Experimental verification and theoretical analysis," *Appl. Phys. Lett.*, vol. 88, pp. 261901-1–261901-3, 2006.

[8] H. T. Nguyen, S. C. Baker-Finch, and D. Macdonald, "Temperature dependence of the radiative recombination coefficient in crystalline silicon from spectral photoluminescence," *Appl. Phys. Lett.*, vol. 104, pp. 112105-1–112105-3, 2014.

[9] M. Tajima, T. Iwai, H. Toyota, S. Binetti, and D. Macdonald, "Donor-acceptor pair luminescence in compensated Si for solar cells," *J. Appl. Phys.,* vol. 110, pp. 043506-1–043506-5, 2011.

[10] B. D. Rezgui, J. Veirman, S. Dubois, and O. Palais, “Study of donor–acceptor pair luminescence in highly doped and compensated Cz silicon,” *Phys. Status Solidi A*, vol. 209, pp. 1917–1920, 2012.

[11] P. Würfel *et al.*, “Diffusion lengths of silicon solar cells from luminescence images,” *J. Appl. Phys.*, vol. 101, pp. 123110-1–123110-10, 2007.

[12] J. A. Giesecke, M. Kasemann, M. C. Schubert, P. Würfel, and W. Warta, “Separation of local bulk and surface recombination in crystalline silicon from luminescence reabsorption,” *Prog. Photovoltaics, Res. Appl.*, vol. 18, pp. 10–19, 2011.

[13] B. Mitchell, M. K. Juhl, M. A. Green, and T. Trupke, “Full spectrum photoluminescence lifetime analyses on silicon bricks,” *IEEE J. Photovoltaics*, vol. 3, no. 3, pp. 962–969, Jul. 2013.

[14] C. Barugkin, Y. Wan, D. Macdonald, and K. R. Catchpole, “Evaluating plasmonic light trapping with photoluminescence,” *IEEE J. Photovoltaics*, vol. 3, no. 4, pp. 1292–1297, Oct. 2013.

[15] C. Schinke, D. Hinken, J. Schmidt, K. Bothe, and R. Brendel, “Modeling the spectral luminescence emission of silicon solar cells and wafers,” *IEEE J. Photovoltaics*, vol. 3, no. 3, pp. 1038–1052, Jul. 2013.

[16] H. T. Nguyen, F. E. Rougieux, S. C. Baker-Finch, and D. Macdonald, “Impact of carrier profile and rear-side reflection on photoluminescence spectra in planar crystalline silicon wafers at different temperatures,” *IEEE J. Photovoltaics*, vol. 5, no. 1, pp. 77–81, Jan. 2015.

[17] W. Lee, J. Chen, B. Chen, J. Chang, and T. Sekiguchi, “Cathodoluminescence study of dislocation-related luminescence from small-angle grain boundaries in multicrystalline silicon,” *Appl. Phys. Lett.*, vol. 94, pp. 112103-1–112103-1, 2009.

[18] M. Tajima *et al.*, “Deep-level photoluminescence due to dislocations and oxygen precipitates in multicrystalline Si,” *J. Appl. Phys.*, vol. 111, pp. 113523-1–113523-6, 2012.

[19] M. Tajima, “Spectroscopy and topography of deep-level luminescence in photovoltaic silicon,” *IEEE J. Photovoltatics*, vol. 4, no. 6, pp. 1452–1458, Nov. 2014.

[20] P. Gundel *et al.*, “Micro-photoluminescence spectroscopy on metal precipitates in silicon,” *Phys. Status Solidi RRL*, vol. 3, pp. 230–232, 2009.

[21] R. Woehl *et al.*, “Evaluating the aluminum-alloyed p+-layer of silicon solar cells by emitter saturation current density and optical microspectroscopy measurements,” *IEEE Trans. Electron Devices*, vol. 58, no. 2, pp. 441–447, Feb. 2011.

[22] P. Gundel *et al.*, “Comprehensive microscopic analysis of laser-induced high doping regions in silicon,” *IEEE Trans. Electron Devices*, vol. 58, no. 9, pp. 2874–2877, Sep. 2011.

[23] A. Roigé *et al.*, “Microscale spatially resolved characterization of highly doped regions in laser-fired contacts for high-efficiency crystalline Si solar cells,” *IEEE J. Photovoltatics*, vol. 5, no. 2, pp. 545–551, Mar. 2015.

[24] H. T. Nguyen *et al.*, “Dislocations in laser-doped silicon detected by micro-photoluminescence spectroscopy,” *Appl. Phys. Lett.*, vol. 107, pp. 022101-1–022101-5, 2015.

[25] H. T. Nguyen *et al.*, “Micro-photoluminescence spectroscopy on heavily-doped layers of silicon solar cells,” *Phys. Status Solidi RRL*, vol. 9, pp. 230–235, 2015.

[26] J. Wagner, “Heavily doped silicon studied by luminescence and selective absorption,” *Solid-State Electron.*, vol. 28, pp. 25–30, 1985.

[27] J. Wagner, K. Thonke, and R. Sauer, “Excitation spectroscopy on the 0.79-eV (C) line defect in irradiated silicon,” *Phys. Rev. B*, vol. 29, pp. 7051–7053, 1984.

[28] M. L. W. Thewalt, S. P. Watkins, U. O. Zlemelis, E. C. Lightowlers, and M. O. Henry, “Photoluminescence lifetime, absorption and excitation spectroscopy measurements on isoelectronic bound excitons in beryllium-doped silicon,” *Solid State Commun.*, vol. 44, pp. 573–577, 1982.

[29] M. K. Juhl, T. Trupke, M. Abbott, and B. Mitchell, “Spatially resolved absorptance of silicon wafers from photoluminescence imaging,” *IEEE J. Photovoltaics*, vol. 5, no. 6, pp. 1840–1843, Nov. 2015.

[30] D. Yan and A. Cuevas, “Empirical determination of the energy band gap narrowing in p+ silicon heavily doped with boron,” *J. Appl. Phys.*, vol. 116, pp. 194505-1–194505-7, 2014.

[31] H. T. Nguyen, F. E. Rougieux, F. Wang, H. Tan, and D. Macdonald, “Micrometer-scale deep-level spectral photoluminescence from dislocations in multicrystalline silicon,” *IEEE J. Photovoltaics*, vol. 5, no. 3, pp. 799–804, May 2015.

[32] C. Schinke *et al.*, “Uncertainty analysis for the coefficient of band-to-band absorption of crystalline silicon,” *AIP Advances*, vol. 5, pp. 067168-1–067168-22, 2015.

[33] W. P. Dumke, “Comparison of band-gap shrinkage observed in luminescence from n+-Si with that from transport and optical absorption measurements,” *Appl. Phys. Lett.*, vol. 42, pp. 196–198, 1983.

[34] P. E. Schmid, M. L. W. Thewalt, and W. P. Dumke, “Photoluminescence in heavily doped Si:B and Si:As,” *Solid State Commun.*, vol. 38, pp. 1091–1093, 1981.

[35] E. Arai, H. Nakamura, and Y. Terunuma, “Interface reactions of B2O3-Si system and boron diffusion into silicon,” *J. Electrochem. Soc. Solid State Sci. Technol.*, vol. 120, pp. 980–987, 1973.

[36] N. E. Grant and K. R. McIntosh, “Passivation of a (100) silicon surface by silicon dioxide grown in nitric acid,” *IEEE Electron Device Lett.*, vol. 30, no. 9, pp. 922–924, Sep. 2009.

[37] P. J. Cousins and J. E. Cotter, “The influence of diffusion-induced dislocations on high efficiency silicon solar cells,” *IEEE Trans. Electron Devices*, vol. 53, no. 3, pp. 457–464, Mar. 2006.

[38] M. A. Kessler, T. Ohrdes, B. Wolpensinger, and N.-P. Harder, “Charge carrier lifetime degradation in Cz silicon through the formation of a boron-rich layer during BBr3 diffusion processes,” *Semicond. Sci. Technol.*, vol. 25, pp. 055001-1–055001-9, 2010.

[39] H. T. Nguyen, F. E. Rougieux, F. Wang, and D. Macdonald, “Effects of solar cell processing steps on dislocation luminescence in multicrystalline silicon,” *Energy Procedia*, vol. 77, pp. 619–625, 2015.

[40] X. J. Ning, “Dislocations induced by boron diffusion in silicon: A transmission electron microscopy study,” *Philosoph. Mag. A*, vol. 75, pp. 115–135, 1997.

[41] A. Hara, T. Fukuda, T. Miyabo, and I. Hirai, “Oxygen-nitrogen complexes in silicon formed by annealing in nitrogen,” *Appl. Phys. Lett.*, vol. 54, pp. 626–628, 1989.

[42] K. Bothe, R. J. Falster, and J. D. Murphy, “Room temperature sub-bandgap photoluminescence from silicon containing oxide precipitates,” *Appl. Phys. Lett.*, vol. 101, pp. 032107-1–032107-4, 2012.

[43] S. Binetti *et al.*, “Optical properties of oxygen precipitates and dislocations in silicon,” *J. Appl. Phys.*, vol. 92, pp. 2437–2445, 2002.

[44] S. Charnvanichborikarn *et al.*, “Effect of boron on interstitial-related luminescence centers in silicon,” *Appl. Phys. Lett.*, vol. 96, pp. 051906-1–051906-3, 2010.

[45] S. Charnvanichborikarn, J. Wong-Leung, C. Jagadish, and J. S. Williams, “Direct correlation of R-line luminescence with rod-like defect evolution in ion-implanted and annealed silicon,” *MRS Commun.*, vol. 2, pp. 101–105, 2012.

Authors’ photographs and biographies not available at the time of publication.

CHAPTER 10

Investigation of Enhanced Diffusion at Grain Boundaries in Multicrystalline Silicon Wafers

In this chapter, employing micro-photoluminescence spectroscopy at low temperatures, we are able to detect dopant diffusion enhancement along various grain boundaries and sub-grain boundaries in multicrystalline silicon wafers. We find an enhancement of phosphorus diffusion not only at all investigated grain boundary types, including Σ3, Σ5, Σ9, Σ11, Σ27a, and random large angle grain boundaries, but also at small-angle or sub-grain boundaries. In addition, the sub-grain boundaries are demonstrated to contain a relatively high density of defects and impurities, suggesting that their presence does not hinder the preferential diffusion of dopant atoms along the sub-grain boundaries. The results are validated with secondary electron dopant contrast images, which confirm the higher dopant concentration along the grain boundaries and sub-grain boundaries. This manuscript was submitted to IEEE Journal of Photovoltaics on 31st May 2016 and is under review.

10.1 Introduction

Homogenous diffused junctions are important for high efficiency multicrystalline silicon (mc-Si) solar cells. However, the diffusivities of dopant atoms along certain grain boundaries (GBs) have been reported to be higher than in the intra-grain regions, thus creating deeper p-n junctions at these GBs [1,2]. This diffusion enhancement has previously been studied empirically using electron beam induced current (EBIC) [1] and light beam induced current (LBIC) [3] techniques. However, these techniques require not only contact formation to extract the induced current, but also an angle-lapping [1] or cross-sectioning [3] of the GBs to expose the junctions. Furthermore, there has been no experimental assessment of the diffusion enhancement along so-called small-angle or sub-grain boundaries (sub-GBs). Since sub-GBs often contain high densities of defects and impurities, they are very recombination active. Therefore, investigating the diffusion enhancement along the sub-GBs using EBIC and LBIC is limited because the defects/impurities and diffused dopants have opposing impacts on the induced current.

Recently, employing a micro photoluminescence spectroscopy (μ-PLS) system, we demonstrated the separation of luminescence peaks from diffused layers and the underlying silicon substrate at low temperatures [4,5], courtesy of band gap narrowing effects in heavily-doped silicon [6,7]. Furthermore, by varying the excitation wavelength, the penetration depth of the laser light inside silicon wafers can be controlled, and thus the depth distributions of different structures underneath the wafer surface can be assessed qualitatively [8]. In this work, we apply the technique to study the diffusion enhancement of dopant atoms along large angle GBs and sub-GBs. First, we demonstrate that the diffusion is enhanced for numerous types of large angle GBs, rather than only at some specific GBs as reported in the literature [3,9]. After that, we show that sub-GBs also enhance the dopant diffusion, even though they are decorated with a high density of defects and impurities. Our conclusions are supported by secondary electron (SE) images, which confirm the enhanced diffusion along both large angle GBs and sub-GBs. These results highlight the value of this nondestructive, contactless characterization technique in silicon photovoltaics.

10.2 Experimental details

The two investigated samples are standard boron-doped p-type mc-Si wafers with a boron doping of about 9×10^{15} cm^{-3}. They were cut from the two consecutive sister wafers from the same ingot. Both of them were chemically etched in HF/HNO_3 solution to remove saw damage and to achieve polished surfaces, and were then immersed in a defect etchant consisting of HF/HNO_3/acetic acid for 16 hours to delineate the sub-grain boundaries [10,11]. One sample

was kept in the as-cut state (after the defect etching step). The other sample went through a $POCl_3$ diffusion process at 850 ^oC for 1 hour, and then annealed in N_2 gas at 850 ^oC for another 1 hour. The resultant sheet resistance was measured on a control float-zone p-type wafer, and was found to be 10.5 Ω/□. The diffused sample was then immersed in HF to remove the phosphosilicate glass.

The setup of the μ-PLS system used here is described in detail in Ref. 6. An excitation light source with a tunable wavelength range from 490 nm to 2 μm was employed and focused onto the sample surface through confocal optics. In this work, a wavelength range of 510 – 810 nm with a bandwidth of 10 nm was used. Therefore, the on-sample illuminated spot size varied from 1 μm (for 510-nm excitation wavelength) to ~2 μm (for 810-nm excitation wavelength). The on-sample excitation power was kept constant at 6 mW for all excitation wavelengths. The spectral response of the entire system was determined with a calibrated halogen-tungsten lamp. The cross-sectional surfaces for scanning electron microscope (SEM) analysis were prepared with the focused ion beam (FIB) technique. GB types were determined from electron backscatter diffraction (EBSD) measurements.

10.3 Enhanced diffusion at large angle GBs

First, we demonstrate that there are more dopant atoms diffused along GBs than within the intra-grain regions. Figure 10.1a compares the normalized PL spectrum captured at 79K at a random large angle GB (black curve) with that captured 15 μm away from the same GB (dashed-red curve) of the diffused mc-Si wafer, excited with a 510-nm wavelength source. The spectrum at the same GB but from the undiffused as-cut wafer is also shown for comparison (dotted-blue curve). The main peak located at ~1130 nm is the band-to-band (BB) emission from the underlying Si substrate. The shoulder located at ~1160 nm is the band-to-band emission from the heavily-doped layer [4], denoted as HDBB peak (Heavily-Doped Band-to-Band). The HDBB peak captured at the GB is higher than that captured 15 μm away, suggesting that the GB is more heavily doped than the surrounding regions. The peak around 1200 nm in the spectrum from the as-cut wafer is the phonon-replica of the BB peak, denoted as PRBB (Phonon-Replica of Band-to-Band).

Figure 10.1b shows an SEM image of the vertical cross-section of the investigated GB. We can observe clearly the contrast difference between the n+ diffused layer and the p-type substrate. Compared to the common SEM contrast between n- and p-type Si (brighter for p-type and darker for n-type), the contrast in Figure 10.1b is inverted (brighter for n+ layer and darker for p-substrate) since the cross-sectional surface was contaminated with Ga atoms (whose work function is smaller than that of Si) during the FIB preparation. The mechanism of this contrast inversion was explained in detail in Ref. 12. The contrast profile scan in Figure 10.1c shows

that, at the line scan position (about 1 µm below the surface) there are still considerable phosphorus atoms at the GB, i.e. the p-n junction extends much more deeply into the substrate at the GB than in the adjacent regions.

Moreover, Figure 10.2 (a-d) compares the absolute PL spectra captured at the GB with those captured 15 µm away from it for the diffused mc-Si wafer, with different excitation wavelengths at 79 K. In Figure 10.2a, the HDBB intensity is clearly higher at the GB than 15 µm away from it, although the BB intensity is the same. When the excitation wavelength increases (Figures 10.2b-d), both the BB peaks increase significantly in magnitude, as the impact of the surface recombination in the diffused layer is reduced and a larger fraction of the excitation light is absorbed in the bulk. The difference between the two HDBB shoulders is also reduced, consistent with the reduced absorption in the heavily-doped layer. Note that, in the spectrum from the as-cut wafer at 79 K (dotted-blue line in Figure 10.1a), the PL intensity around 1160 nm is only about 6% of the BB intensity. Therefore, the difference between the two HDBB peaks in Figure 10.2 is not due to the small difference between the two BB peaks.

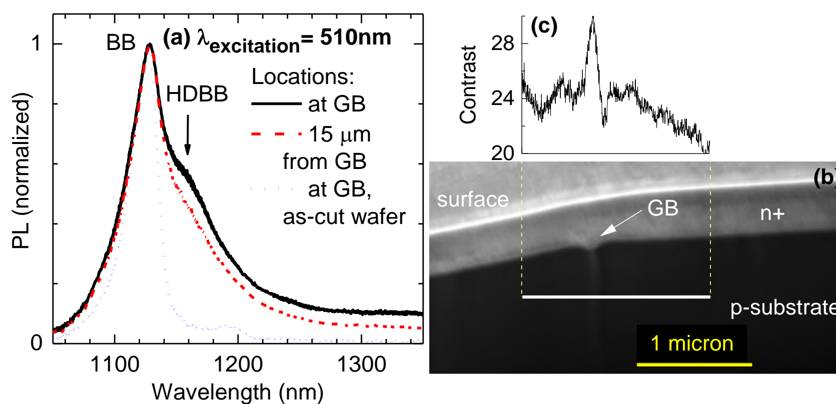

Figure 10.1: *(a) Normalized PL spectra at a random large angle GB (black line) and 15 microns (dashed-red line) away from it of the diffused mc-Si wafer, excited with a 510-nm source at 79 K. The grain misorientation is 53.40 around the [0 1 1] axis. The spectrum at the same GB from the as-cut mc-Si wafer (dotted-blue line) is also included for comparison. (b) Vertical cross-sectional SEM image of the investigated GB of the diffused mc-Si wafer. (c) SE contrast profile of the line scan marked with the white line in Figure 10.1b.*

We captured the spectra from numerous large angle GBs including Σ3, Σ5, Σ9, Σ11, Σ27a, and random angle GBs, and always found an enhanced diffusion along these GBs. The results are in contrast with the findings reported in Ref. 3, in which the diffusion was shown to be enhanced along Σ3 GBs, but no enhanced diffusion was observed along Σ27a and random large angle GBs. Therefore, a detailed study on the diffusion mechanism of dopant atoms along different types of GBs under various conditions is required to clarify these uncertainties, and

this contactless and non-destructive PLS-based method could be a powerful tool to study this diffusion mechanism without complex sample preparation.

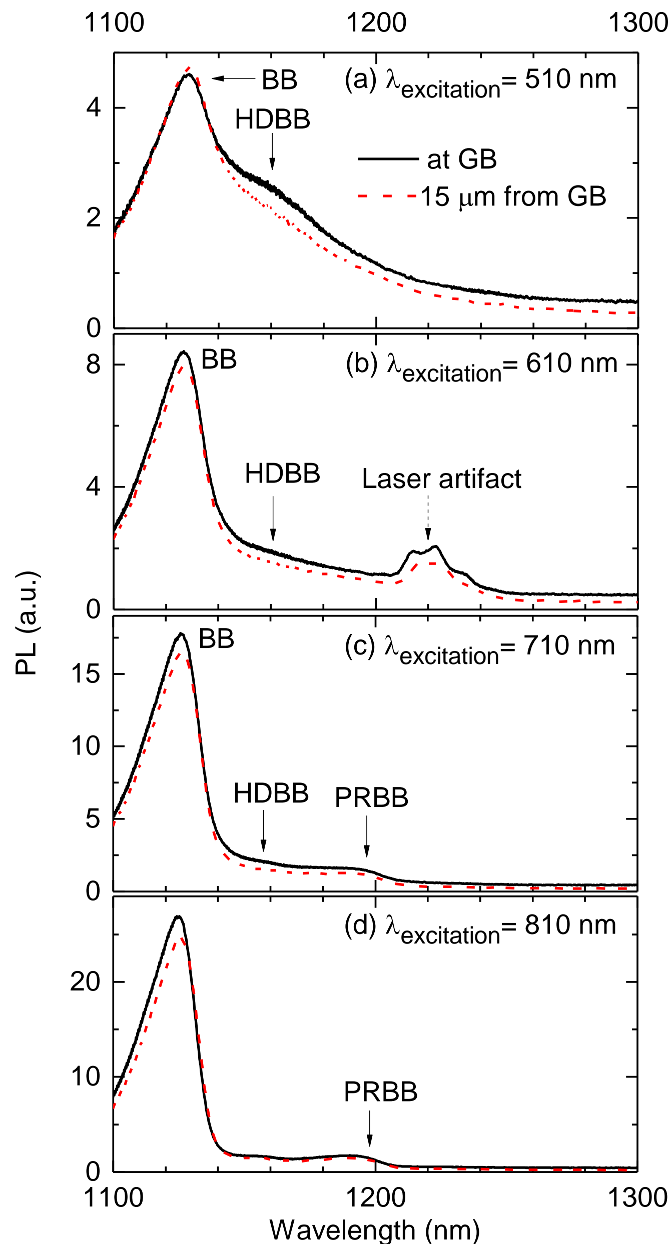

Figure 10.2: *Comparison of absolute PL spectra at a random large angle GB (black line) and 15 microns (dashed-red line) away from it for the diffused mc-Si wafer, excited with different excitation wavelengths at 79 K. The spurious peak marked by the broken arrow in Figure 10.2b is an artifact from the laser. Its center wavelength is always twice of the excitation wavelength.*

10.4 Enhanced diffusion at sub-GBs

Now, we investigate the distribution of dopant atoms around sub-GBs in mc-Si wafers after the phosphorus diffusion step. Sub-GBs contain a high density of dislocations due to the high

thermal stress and strain during the ingot growing and cooling. Also, they are often decorated with secondary defects and impurities trapped by the dislocation networks. The dislocations themselves are known to emit two distinct deep-level PL peaks (the so-called D3 and D4 lines), whereas the surrounding secondary defects and impurities emit another two deep-level peaks (D1 and D2 lines) [13-16]. First, we examine sub-GBs at which the density of decorating defects and impurities is high. A typical PL spectrum at this kind of sub-GBs from the as-cut mc-Si wafer is given in Figure 10.3a (dotted-blue curve). Besides the D3 and D4 peaks emitted from dislocations, the sub-GB also emits the D1 and D2 peaks due to decorating defects and impurities. Figures 10.3a and 10.3b compare the normalized and absolute PL spectra, respectively, of the diffused mc-Si wafer at 79 K, captured at the same sub-GB (black line) and the intra-grain region (dashed-red line). The intensity (both in normalized and absolute scales) of the HDBB peak at the sub-GB is higher than that at the intra-grain region, although the absolute BB intensity at the sub-GB is lower than that at the intra-grain region. The results suggest that there are more active dopant atoms along the sub-GB than the intra-grain regions. The dopant atoms are still preferentially diffused into the sub-GB even though there is a high density of defects and impurities around it. We note that although the D4 luminescence peak does partly overlap with the HDBB shoulder, making the comparison with the spectra measured away from the sub-GB more difficult, in this case the magnitude of the D4 luminescence is small enough to still conclude that there is an increased dopant concentration at the sub-GB. To fortify this conclusion, an SEM dopant contrast image was captured on a vertical cross-section of this sub-GB of the diffused wafer and is displayed as an insert in Figure 10.3b. The p-n junction clearly extends more deeply into the substrate at the sub-GB than the surrounding regions.

In addition, Figures 10.3c and 10.3d (a zoom-in of Figure 10.3c) show the evolution of normalized PL spectra with increasing excitation wavelengths, captured at the sub-GB of the diffused wafer at 79 K. In Figure 10.3c, the longer the excitation wavelength, the higher the intensities of the D lines. The results confirm that the defects (both intrinsic dislocations and secondary defects) and impurities are distributed deeply across the wafer thickness, rather than being limited to the near-surface region. In contrast, in Figure 10.3d, the shoulder around 1160 nm, attributed to the HDBB peak, is reduced significantly with increasing excitation wavelengths. This is because the HDBB peak is emitted from the diffused layer located near the surface.

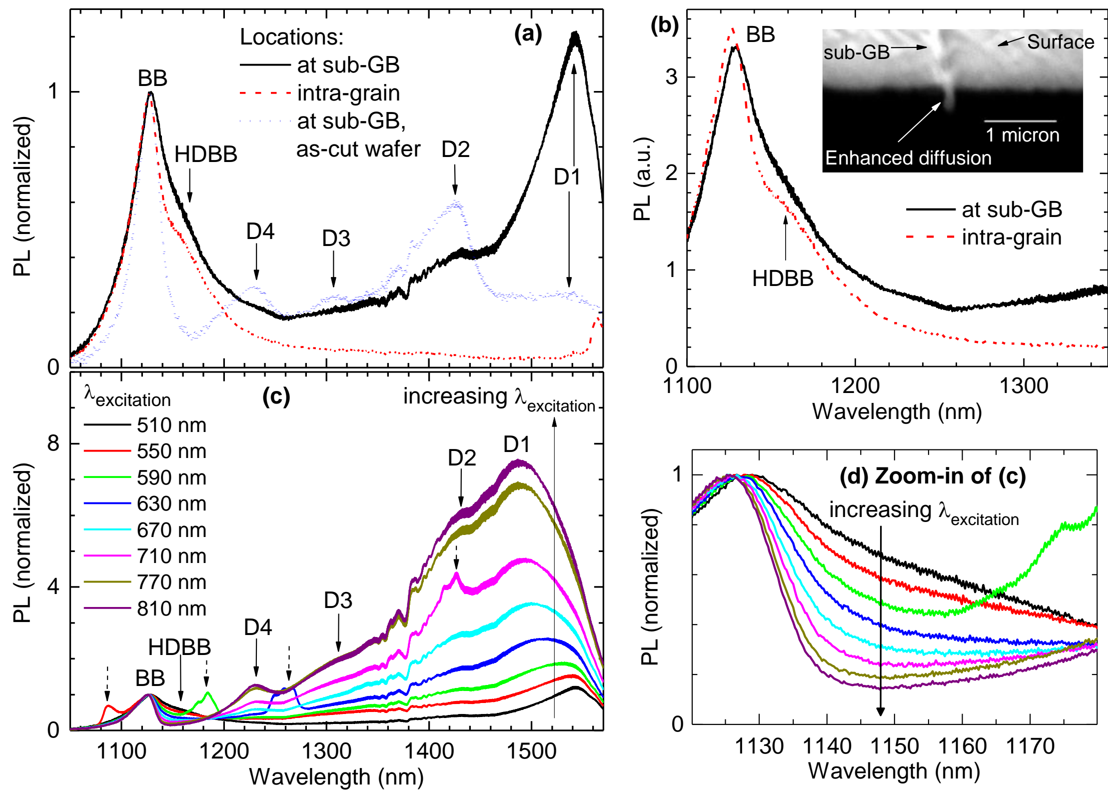

Figure 10.3: *(a) Normalized and (b) absolute PL spectra at the sub-GB (black line) and the intra-grain region (dashed-red line) of the diffused mc-Si wafer, excited with a 510-nm source. The spectrum at the same sub-GB from the as-cut mc-Si wafer (dotted-blue line) is also included for comparison. The insert in Figure 10.3b is a vertical cross-sectional SEM image of this sub-GB of the diffused mc-Si wafer. (c) Normalized PL spectra at the sub-GB of the diffused mc-Si wafer with different excitation wavelengths. (d) A zoom-in between 1120 and 1180 nm of Figure 10.3c. All measurements were done at 79 K. The normalized spectra were normalized to the band-to-band peak. The spurious peaks marked by broken arrows in Figure 10.3c are artifacts from the laser light.*

Furthermore, we continue investigating sub-GBs which contain dislocations but a relatively low density of secondary defects and impurities, and thus emit strong D3 and D4 but minimal D1 and D2 lines [15]. Figures 10.4a and 10.4b compare the normalized PL spectra captured at a sub-GB (black curve) and 15 μm away from it (dashed-red curve) of the diffused mc-Si wafer at 79 and 300 K, respectively. The spectra at the same sub-GB but from the as-cut wafer are also presented for comparison. In Figure 10.4a, due to the intense D4 line, it is not possible to observe the HDBB shoulder at low temperatures. However, since the D3 and D4 lines display a strong thermal quenching rate [17], at room temperature these two lines are quenched significantly and the contribution of the HDBB peak into the total spectra is more obvious, as depicted in Figure 10.4b. As can be clearly seen from Figure 10.4b, around 1170 nm, the

spectra from the as-cut wafer at and away from the sub-GB are not affected by the deep-level peaks. Nevertheless, the shoulder around 1170 nm (due to the HDBB peak) of the spectrum captured at the sub-GB (of the diffused wafer) is still broader than that captured at the intra-grain region. The results suggest that more dopants have diffused into this sub-GB than the surrounding regions. Note that, the carrier profile and surface reflectivity have a negligible impact on the PL spectral shape at the long wavelength side since reabsorption of the generated photons is negligible at these wavelengths, as demonstrated in Ref. 18.

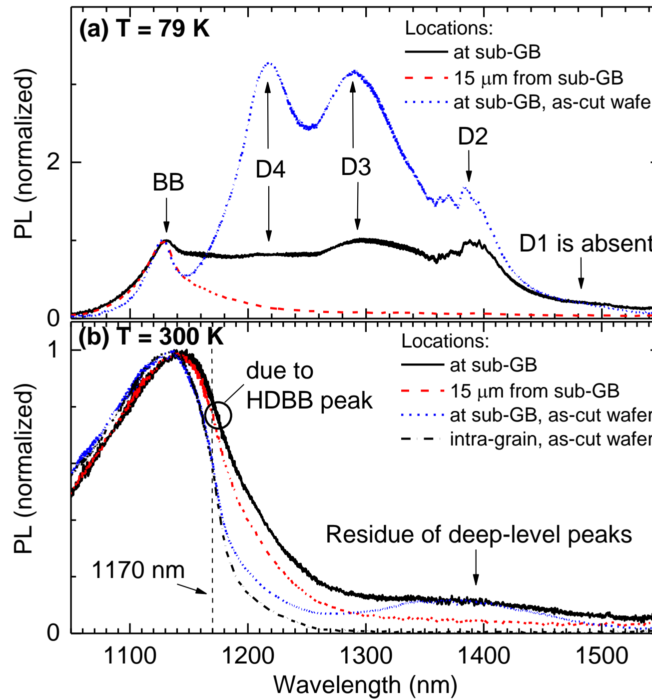

Figure 10.4: *Normalized PL spectra at another sub-GB (black line) and 15 microns (dashed-red line) away from it of the diffused mc-Si wafer at (a) 79 K and (b) 300 K, excited with the 510-nm wavelength. The spectra at the same sub-GB (dotted-blue lines) and the intra-grain region (dashed-dotted black line) from the as-cut mc-Si wafer were also included for comparisons. The dashed-vertical line in Figure 10.4b is the location from which the intensity mapping in Figure 10.5b is extracted. The normalized spectra were normalized to the band-to-band peak.*

Finally, Figures 10.5a shows a mapping of the total absolute PL intensity integrated between 1000 and 1250 nm (the impact of the deep-level peaks is minimal in this range), whereas Figure 10.5b shows a mapping of the normalized PL intensity at 1170 nm, at room temperature around a sub-GB of the diffused mc-Si wafer. The dark line in Figure 10.5a indicates an increased recombination activity along the sub-GB due to the defects and impurities, whereas the bright line in Figure 10.5b indicates more dopant atoms diffused along this sub-GB since the broader long-wavelength shoulder is caused by the HDBB peak (see

Figure 10.4b). The results from these two images confirm that, although the recombination activity is increased along the sub-GBs, more dopant atoms are also diffused into the sub-GBs. This conclusion is more difficult to make based on EBIC or LBIC measurements since the total induced current is determined by both the defect/impurity and dopant concentrations. The defects and impurities reduce the current whereas the dopants act to increase it.

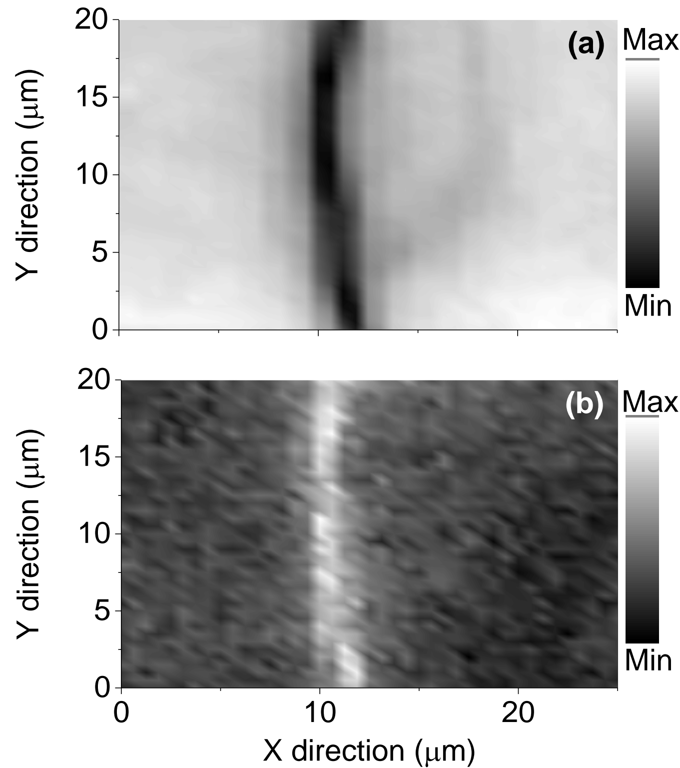

Figure 10.5: *(a) Mapping of integrated PL intensity around a sub-GB of the diffused mc-Si wafer at 300 K. The intensity is the sum of the PL signal from 1000 to 1250 nm. (b) Mapping of normalized PL intensity at 1170-nm wavelength of the same area as Figure 10.5a at 300 K. The scanning step sizes are 0.5 μm in both x and y directions. The excitation wavelength is 532 nm.*

10.5 Summary

In conclusion, applying micro-photoluminescence spectroscopy techniques, we have detected dopant diffusion enhancement along grain boundaries and sub-grain boundaries in multicrystalline silicon wafers. We have demonstrated that this enhancement occurs at numerous types of grain boundaries, rather than only at some specific grain boundaries. In addition, we have shown that the presence of defects and impurities around sub-grain boundaries does not hinder the preferential diffusion of dopant atoms. These findings help demonstrate the value of such spectrally-resolved PL techniques in silicon photovoltaics.

Acknowledgement

This work has been supported by the Australian Research Council (ARC) and the Australian Renewable Energy Agency (ARENA) through research grant RND009. The Australian National Fabrication Facility is acknowledged for providing access to some of the facilities used in this work. The authors are in debt to Prof. H. Tan for providing access to the spectroscopic equipment, T. Duong and Dr. S. P. Phang for assisting with the sample preparation, and Dr. H. C. Sio for helping with the EBSD measurements.

References

[1] A.D. Buonaquisti, W. Carter, and P.H. Holloway, “Diffusion characteristics of boron and phosphorus in polycrystalline silicon,” Thin Solid Films 100, 235 (1983)

[2] Y. Mishin and Chr. Herzig, “Grain boundary diffusion: recent progress and future research,” Materials Science and Engineering A 260, 55 (1999).

[3] M. Breitwieser, F. D. Heinz, A. Büchler, M. Kasemann, J. Schön, W. Warta, and M. C. Schubert, “Analysis of solar cell cross sections with micro-light beam induced current (μLBIC),” Solar Energy Materials & Solar Cells 131, 124 (2014).

[4] H. T. Nguyen, D. Yan, F. Wang, P. Zheng, Y. Han, and D. Macdonald, “Micro-photoluminescence spectroscopy on heavily-doped layers of silicon solar cells,” Physica Status Solidi RRL 9, 230 (2015).

[5] H. T. Nguyen, F. E. Rougieux, D. Yan, Y. Wan, S. Mokkapati, S. M. de Nicolas, J. P. Seif, S. De Wolf, and D. Macdonald, “Characterizing amorphous silicon, silicon nitride, and diffused layers in crystalline silicon solar cells using micro-photoluminescence spectroscopy,” Solar Energy Materials & Solar Cells 145, 403 (2016).

[6] J. Wagner, “Photoluminescence and excitation spectroscopy in heavily doped n- and p-type silicon,” Phys. Rev. B, vol. 29, pp. 2002-2009, 1984.

[7] J. Wagner, “Band-gap narrowing in heavily doped silicon at 20 and 300 K studied by photoluminescence,” Phys. Rev. B, vol. 32, pp. 1323-1325, 1985.

[8] H. T. Nguyen, S. P. Phang, J. Wong-Leung, and D. Macdonald, “Photoluminescence excitation spectroscopy of diffused layers on crystalline silicon wafers,” IEEE Journal of Photovoltaics 6, 746 (2016).

[9] H. J. Möller, Semiconductors for Solar Cells, Artech House, Boston, 1993.

[10] W.C. Dash, “Copper precipitation on dislocations in silicon,” J. Appl. Phys 27, 1193 (1956).

[11] Y. Kashigawa, R. Shimokawa, and M. Yamanaka, "Highly sensitive etchants for delineation of defects in single- and polycrystalline silicon materials," J. Electrochem. Soc. 143, 4079 (1996).

[12] M. El-Gomati, F. Zaggout, H. Jayacody, S. Tear, and K. Wilson, "Why is it possible to detect doped regions of semiconductors in low voltage SEM: a review and update," Surface and Interface Analysis 37, 901 (2005).

[13] M. Tajima, Y. Iwata, F. Okayama, H. Toyota, H. Onodera, and T. Sekiguchi, "Deep-level photoluminescence due to dislocations and oxygen precipitates in multicrystalline Si," J. Appl. Phys., vol. 111, pp. 113523-1 - 113523-6, 2012.

[14] M. Tajima, "Spectroscopy and topography of deep-level luminescence in photovoltaic silicon," IEEE Journal of Photovoltatics, vol. 4, pp. 1452-1458, 2014.

[15] H. T. Nguyen, F. E. Rougieux, F. Wang, H. Tan, and D. Macdonald, "Micrometer-scale deep-level spectral photoluminescence from dislocations in multicrystalline silicon," IEEE Journal of Photovoltaics, vol. 5, pp. 799-804, 2015.

[16] H. T. Nguyen, F. E. Rougieux, F. Wang, and D. Macdonald, "Effects of solar cell processing steps on dislocation luminescence in multicrystalline silicon," Energy Procedia, vol. 77, pp. 619 – 625, 2015.

[17] H. T. Nguyen, Y. Han, M. Ernst, A. Fell, E. Franklin, and D. Macdonald, "Dislocations in laser-doped silicon detected by micro-photoluminescence spectroscopy," Appl. Phys. Lett., vol. 107, pp. 022101-1 - 022101-5, 2015.

[18] H. T. Nguyen, F. E. Rougieux, S. C. Baker-Finch, and D. Macdonald, "Impact of carrier profile and rear-side reflection on photoluminescence spectra in planar crystalline silicon wafers at different temperatures," IEEE Journal of Photovoltaics, vol. 5, pp. 77-81, 2015.

CHAPTER 11

Composition of Luminescence Spectra from Heavily-Doped p-Type Silicon under Low and High Excitation

In this chapter, we present a systematic investigation of the effects of doping on the luminescence spectra from p-type crystalline silicon wafers. First, we explain the difference in the approaches between the line shape analysis and the generalized Planck's law in modeling the spectral shape, and connect the two methods together. After that, we elucidate the separate impacts of individual phenomena including band gap narrowing, band tails and dopant bands, Fermi level shifting, and hot carriers on the luminescence spectra in heavily-doped silicon. Finally, employing appropriate excitation levels, we can unambiguously observe the growing of the band tails and the broadening of the dopant band, as well as the merging of the valence and dopant bands together, on measured luminescence spectra. This manuscript has been accepted by Journal of Luminescence on 17th August 2016, and published online on 17th September 2016.

11.1 Introduction

Due to rich features contained in photoluminescence (PL) spectra from crystalline silicon (c-Si) wafers, photoluminescence spectroscopy (PLS) has been employed to study many fundamental properties of c-Si, such as the band gap at different temperatures [1] and doping levels [2,3], absorption coefficients [4-7], doping concentrations [8], or radiative recombination rates [6,9,10]. Recently, with the advent of micro-PLS tools equipped with confocal optics, it is feasible to pinpoint to micron-scale features in c-Si wafers and solar cells to study the luminescence properties of the material and defects [11-15], or to characterize devices [16-19]. Recently, we have employed micro-PLS to qualitatively assess doping levels of localized heavily-doped regions in c-Si wafers and solar cells [20,21], since these regions emit a distinct luminescence peak courtesy of the band-gap narrowing effects in heavily-doped silicon at temperatures around 80 K [2,3]. In principle, such distinct peaks could allow quantitative micron-scale PL methods for measuring doping concentrations and junction depths. However, the detailed analysis of such spectra is complicated by the fact that there are numerous physical phenomena occurring in parallel inside the heavily-doped c-Si, rather than just a simple narrowing of the band gap caused by a single effect. These phenomena can be understood by a systematic investigation of the PL spectra.

When the doping density increases, there are at least four phenomena occurring simultaneously which impact PL spectra from c-Si. Firstly, the conduction band and valance band rigidly shift towards one another, causing a reduction in the band gap. Secondly, the two band edges are perturbed and band tails are formed, yielding not only an effectively-smaller band gap but also a wider distribution of free carriers at the two band edges [22-25]. Thirdly, the dopant band, located slightly above the valence band (for p-type silicon), broadens due to an increasing interaction among the dopant atoms. When the doping density approaches the Mott transition (~3×10^{18} cm^{-3}), this dopant band slowly overlaps the valence band tail, and eventually the two bands (dopant and valence) merge together at a doping density higher than the Mott transition, forming a deeper and continuous band tail [24,26]. Fourthly, the Fermi level shifts towards the valence band (for p-type silicon) and eventually moves into the valence band (i.e. the semiconductor becomes degenerate) at a doping density much higher than the Mott transition [27]. However, although changes in luminescence spectra at heavy doping reflect complex combinations of these four phenomena, the PL spectra are often characterized by two simple properties of the spectra: the energy shift of the peak, and the broadening of the width [28-30]; and thus the individual effects of each phenomenon are confounded.

In addition, although Schmid *et al.* [29] and Wagner [2] reported the PL spectra at different doping densities for p+ silicon, the effects of the band tails and dopant band, as well as their evolutions with doping densities, could not be observed in the spectra from these works. These features were either masked by the deep-level emission at low excitation levels due to

unintended impurities [29], or smeared out due to the broadening of the band-to-band spectra and the relative suppression of the dopant peak under high excitation levels [2,29]. Therefore, there is still a lack of empirical luminescence data, in which the effects of these phenomena are unambiguously revealed. Furthermore, although the so-called line shape analysis is commonly used to study the properties of luminescence spectra at different doping densities [2,3,30,31], the formula describing the spectral shape in this method is very different from that of the generalized Planck's law [32,33], which has also been widely used to model the PL spectra [4-7,9,34,35].

In this study, we present a systematic experimental and modeling study to give a more insightful understanding of the PL spectra at both low and high excitation levels, obtained from heavily-doped p-type c-Si wafers. When the dopant and valence bands have not merged together, the use of a low excitation level (in this case around 4 W/cm^2) helps avoid the overlapping of the dopant and band-to-band luminescence peaks. Once the two bands merge into one, the use of a high excitation level (250 kW/cm^2) can suppress the influence of unintentional impurities on the PL spectra, which are evident in the low excitation spectra. First, we resolve the differences in the formulas between the line shape analysis and the generalized Planck's law, and connect the two methods together. We then elucidate the separate impacts of individual parameters, including the band gap, Fermi level, hot carriers, and band tails on the PL spectra from heavily-doped p-type c-Si wafers using both modeling and empirical results. Finally, we show the impacts of the band tails as well as the dopant band on the PL spectra, and clarify the difference in the spectra between the high excitation (HE) and low excitation (LE) measurements. These understandings of the luminescence spectra in heavily-doped c-Si, at both low and high excitation levels, are likely to aid the further development of powerful new techniques for silicon photovoltaics based on spectral luminescence.

11.2 Experimental details

The samples investigated are float-zone boron-doped crystalline silicon (c-Si) wafers having different doping concentrations from 5.7×10^{16} to 1.1×10^{20} cm^{-3}. Their doping densities were measured using the electrochemical capacitance–voltage (ECV) technique. In preparation for PL measurements, the wafers were chemically etched in an HF/HNO_3 solution to remove residual saw damage. After that, they were passivated with an 18-nm layer of Al_2O_3 deposited on both surfaces by plasma assisted atomic layer deposition (PA-ALD). They were then annealed at 450 ^{0}C in forming gas consisting of argon and hydrogen for thirty minutes to activate the surface passivation [36]. The presence of the surface passivation layers increases the excess carrier density under illumination, leading to a stronger PL signal, even for the high excitation cases.

The experimental setups of our low excitation (LE) and high excitation (HE) systems are described in detail in Ref. 7 and Ref. 14, respectively. Both systems utilize an excitation wavelength of 785 nm in this work. In the LE experiments, the on-sample laser spot size, on-sample excitation power, and spectral resolution are 2.2 mm in diameter, 150 mW (corresponding to an excitation intensity of ~4 W/cm^2), and 5 nm, respectively. These parameters in the HE experiments, in which the laser is coupled through a confocal microscope, are 1.7 μm in diameter, 6 mW (corresponding to an excitation intensity of ~250 kW/cm^2), and 0.25 nm, respectively. The injection level is estimated to be in the range of 1×10^{16} and 1×10^{18} cm^{-3} in the LE and HE experiments, respectively. The spectral responses of both systems were determined with the same calibrated tungsten-halogen light source. The sample temperature was controlled by a liquid-nitrogen-cooled cryostat.

11.3 Connections between line shape formula and generalized Planck's law

The so-called line shape analysis has been used to describe the band-to-band luminescence spectra from a semiconductor by many authors [2,3,30,31]. In n-type semiconductors, the line shape formula is given by:

$$\int_0^\infty f_e(E_e)D_e(E_e)f_h(E_h)D_h(E_h)dE_e, \tag{1}$$

where f_e, D_e, and E_e (f_h, D_h, and E_h), respectively, are the distribution function, density of states DOS, and energy above the conduction band edge E_C (below the valence band edge E_V) of free electrons (holes).

There are several assumptions which need to be noted in this approach. First, the above formula only describes the ability of the material to generate photons. The emitted photon flux also depends on the capability of the surrounding environment to accept these generated photons (i.e. c-Si in this study). This capability is described by the energy distribution of photons, which is a product of the distribution function (f_γ) and DOS (D_γ) of photons, and is given by [37]:

$$f_\lambda(\hbar\omega)\times D_\lambda(\hbar\omega)\propto\frac{(\hbar\omega)^2}{\exp\left(\frac{\hbar\omega}{kT}\right)-1}\approx(\hbar\omega)^2\times\exp\left(-\frac{\hbar\omega}{kT}\right), \tag{2}$$

where $\hbar\omega$ and kT are the energy of emitted photons and thermal energy, respectively. Therefore, the spectral shape from n-type semiconductors (without illumination) should be determined by the following relationship:

$$I(\hbar\omega) \propto \left[\int_0^\infty f_e(E_e)D_e(E_e)f_h(E_h)D_h(E_h)dE_e\right] \times \left[(\hbar\omega)^2 \times \exp\left(-\frac{\hbar\omega}{kT}\right)\right]. \quad (3)$$

However, under illumination, the Fermi level E_F is split into two separate levels $E_{FC}=E_F+\Delta E_{FC}$ and $E_{FV}=E_F-\Delta E_{FV}$ for electrons and holes, respectively. Therefore, the distribution functions of electrons and holes under illumination ($f_{e,illum}$ and $f_{h,illum}$) should be written as:

$$f_{e,illum}(E_e) = \frac{1}{1+\exp\left(\frac{E_e-(E_F+\Delta E_{FC})}{kT}\right)} \text{ and } f_{h,illum}(E_h) = \frac{1}{1+\exp\left(\frac{(E_F-\Delta E_{FV})-E_h}{kT}\right)}.$$

In non-degenerate semiconductors, under low excitation levels in which the quasi-Fermi levels are far enough from the band edges, i.e. $E_e-(E_F+\Delta E_{FC})$ and $(E_F-\Delta E_{FV})-E_h$ are several times larger than kT, we can rewrite $f_{e,illum}$ and $f_{h,illum}$ as:

$$f_{e,illum}(E_e) \approx f_e(E_e) \times \exp\left(\frac{\Delta E_{FC}}{kT}\right) \text{ and } f_{h,illum}(E_h) \approx f_h(E_h) \times \exp\left(\frac{\Delta E_{FV}}{kT}\right).$$

Therefore Eq. (3) should become:

$$I(\hbar\omega) \propto \left[\int_0^\infty f_e(E_e)D_e(E_e)f_h(E_h)D_h(E_h)dE_e\right] \times \left[(\hbar\omega)^2 \times \exp\left(-\frac{\hbar\omega-(\Delta E_{FC}+\Delta E_{FV})}{kT}\right)\right]. \quad (4)$$

Eq. (4) is of similar form to the generalized Planck's law for non-degenerate semiconductors [32,33]. The first square bracket in Eq. (4) is, in principle, related to the band-to-band absorption coefficient, which is solely determined by the distribution functions and DOS of electrons and holes in the material. Some studies did not consider the energy distribution of photons $f_\gamma \times D_\gamma$, and did not account for the separation of the Fermi level under illumination, and as such their line shape formulas were different from the generalized Planck's law [2,3,30,31]. This difference has been noticed by Daub and Würfel [5].

However, at low temperatures, there is negligible reabsorption of the generated photons, and thus the carrier distributions do not affect the spectral shape and we can neglect the term $\Delta E_{FC}+\Delta E_{FV}$ in Eq. (4). Also, when the silicon wafers become degenerate, the excitation levels have little impact on the band-to-band PL spectral shapes, as empirically verified in Section

11.5 (see Figures 11.6e and 11.6f). Therefore, in principle, we can use Eq. (3) to describe the spectral shape of the band-to-band luminescence from both non-degenerate and degenerate silicon at low temperatures. For p-type silicon in this study, we simply swap the roles of electrons and holes in Eq. (3) together, and thus the Fermi level E_F will be negative if it is higher than the valence band edge E_V, and positive if it moves into the valence band.

11.4 Effects of different parameters on the band-to-band PL spectra

In this section, we elucidate the separate impacts of individual parameters, including the band gap, Fermi level, and band tails on the band-to-band PL spectra from heavily-doped silicon wafers. At relatively low doping densities, for which the dopant band has a negligible impact on the PL spectra, and the DOS in both conduction and valence bands is still a parabolic function, the spectral shape at 79 K from silicon can be determined by Eq. (3). In addition, from Figure 11.1, we also have the relationship:

$$\hbar\omega \pm E_P = E_e + E_h + E_G, \tag{5}$$

where E_P and E_G are the phonon energy and silicon band gap, respectively. '+/-' denotes the emission/absorption of phonons.

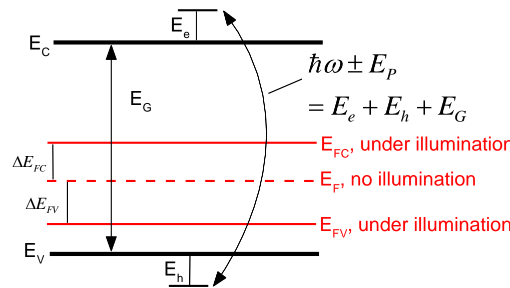

Figure 11.1: *Illustration of the energy relationship among emitted photons ħω, phonons E_P ('+' denotes a phonon emission event, whereas '-' denotes a phonon absorption event), free holes E_h, and free electrons E_e in p-type silicon under illumination. See the text for descriptions of the symbols.*

Figure 11.2a compares the modeled spectrum including three components - Transverse-Acoustic (TA) phonons, Transverse-Optical (TO) phonons, and both TO and zone-center optical (O^Γ) phonons - with the measured LE spectrum from a lightly-doped c-Si wafer having a doping density N_A of 5.7×10^{16} cm^{-3} at 79 K. The general shape of the modeled spectrum, in particular the TO component, follows the empirical spectrum closely, except for a mismatch around 1.07 eV. The peak around 1.07 eV occurs due to free carriers recombining through neutral dopant atoms, and was reported and denoted as B_3^{TO} by Dean *et al.* [38]. However, in

Figure 11.2b, the high energy side of the HE spectrum remarkably deviates from the modeling although their low energy sides match very well. The difference can be explained by the incomplete thermalization of hot carriers in the HE measurements. Under very high injection levels, more free carriers are distributed further from the band edges, and the energy distribution of the luminescence is broadened [26]. Meanwhile, this incomplete thermalization of free carriers does not change the band gap, and thus the lower energy side of the PL spectrum does not change.

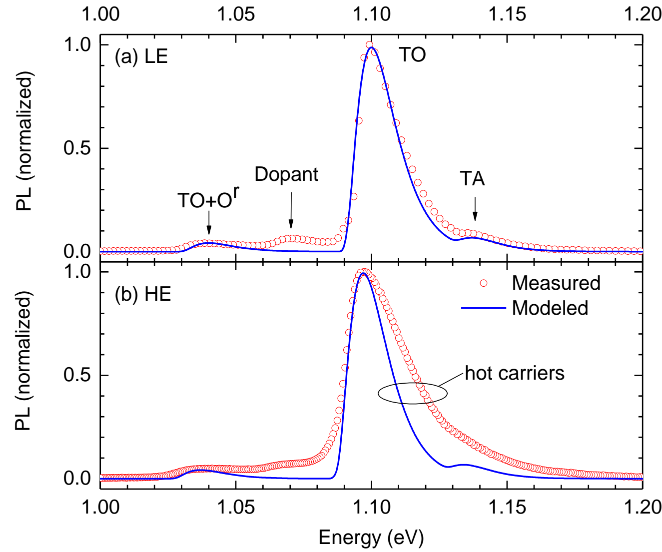

Figure 11.2: *Comparison between measured and modeled (band-to-band, without broadening effects) PL spectra at 79 K under (a) LE and (b) HE levels.* $N_A = 5.7\times10^{16}\ cm^{-3}$

Near the Mott transition, there is a significant overlap between the dopant and the TO components, and thus Eq. (3) does not reproduce the spectral shape well any more. When the doping density increases further, the dopant band merges with the valence band and Eq. (3) becomes valid again. However, since a new deep and continuous band tail is formed due to the merging of the two bands, the spectrum is broadened significantly which is not accounted for in Eq. (3). To account for the band tails, the merging of dopant band, and the incomplete ionization of free carriers, a broadening term E_S is introduced into Eq. (3) via the relationship [2,3,30]:

$$I_{Broadening}(\hbar\omega) \propto \int_0^\infty I(\hbar\omega')\exp\left[-\frac{(\hbar\omega'-\hbar\omega)^2}{E_S^2}\right]d(\hbar\omega'), \tag{6}$$

In fact, the broadening model employed in Eq. (6) is a simple way to account for the band tailing effects. Above the Mott transition, the DOS in the valence band is no longer a parabolic function, but has a complex structure due to the combination of the dopant band and valence

band tail [24]. However, we found that Eqs. (3) and (6) are sufficient to qualitatively explain the effects of the band gap, Fermi level, and band tails on our measured PL spectra, as discussed below.

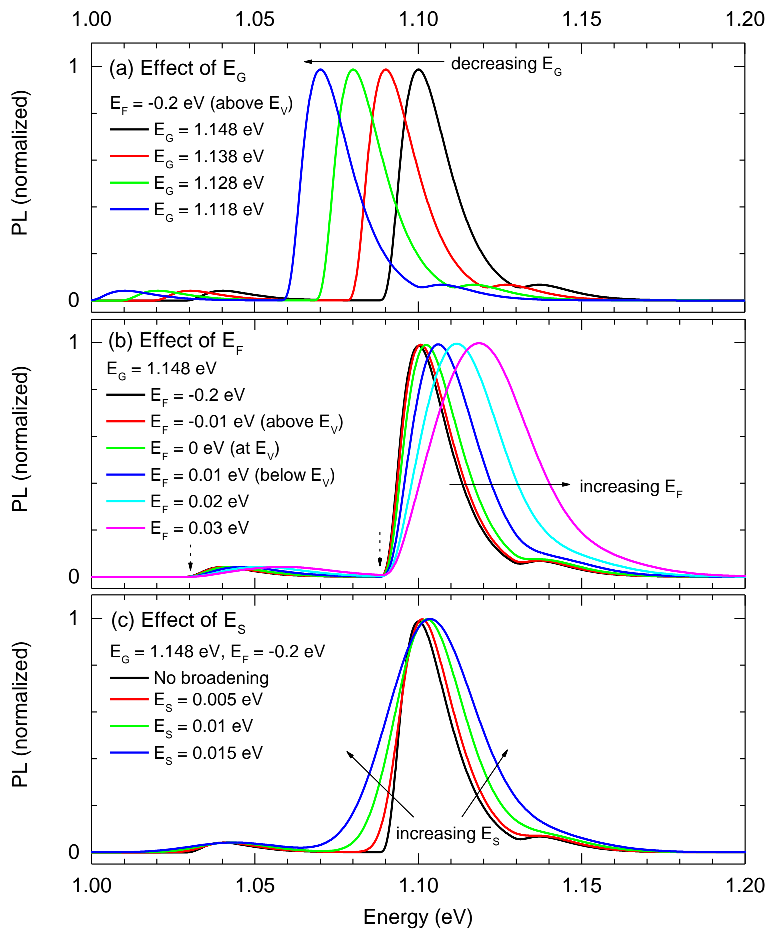

Figure 11.3: *Modeling of individual effects of E_G, E_F, and E_S on band-to-band PL spectra at 79 K.*

Now, we investigate the separate effects of individual parameters (E_G, E_F, and E_S) on the PL spectra when the doping density increases. Figures 11.3a-c plot the modeled PL spectra when one parameter is changed while the other two are kept the same. In Figure 11.3a, the narrowing of E_G only shifts the spectra towards lower energies without altering their shapes. In Figure 11.3b, E_F does not affect the spectral shape until it reaches E_V and moves beyond E_V. The increasing E_F (when situated in the valence band) not only shifts the spectra to higher energies, but also broadens all their components due to the band filling effects. Nevertheless, the low energy thresholds of all components (marked by broken arrows in Figure 11.3b) are still the same since the E_F shifting does not change the band edge positions. In Figure 11.3c, the broadening factor E_S simply broadens the spectra, causing different components to overlap together. As a result, E_G and E_F have opposing effects on the spectra peak location, whereas E_F and E_S have similar effects on the broadening width of the PL spectra.

Based on the modeling results above, one would expect that, in degenerate p-type silicon (i.e. when E_F moves into the valence band), there is more than one single combination of $\{E_G, E_F, E_S\}$ giving a good fit with the measured spectra. Indeed, Figure 11.4 compares the HE spectra to the modeled PL spectra with various combinations of $\{E_G, E_F, E_S\}$. The fitted spectra, excluding the broadening parameter E_S, are also included for comparisons. The results from Figures 11.4a and 11.4b clearly show that the choice of $\{E_G, E_F, E_S\}$ is arbitrary due to the complementary effects of these parameters together. These results are consistent with the results reported by Daub and Würfel [5]. By comparing the absorption curves between heavily-doped and lightly-doped silicon wafers, these authors found various amounts of apparent band-gap narrowing in the heavily-doped silicon wafers, depending on which energy range they chose to compare. Note that, the excitation level has little impact on the band-to-band spectral shape in degenerate silicon, as demonstrated in Section 11.5.

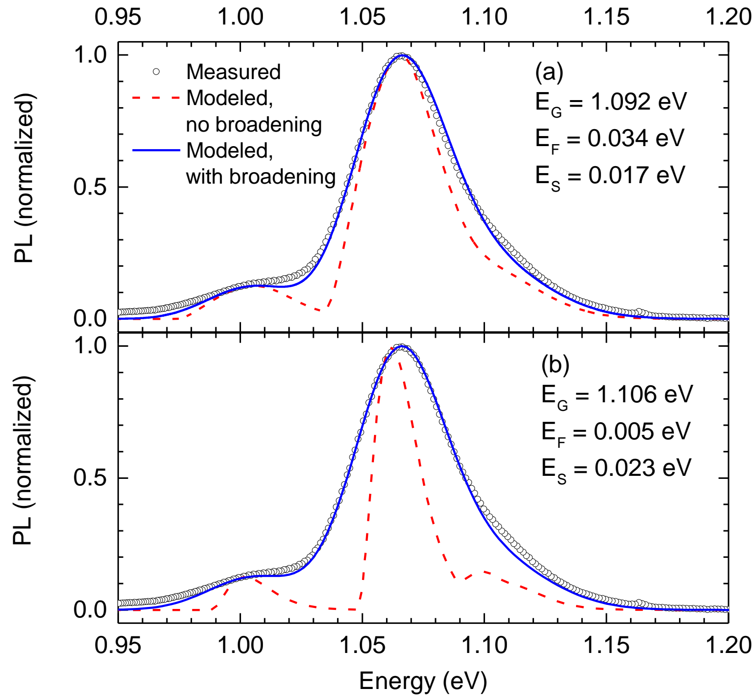

Figure 11.4: *Measured (under HE levels) and modeled (band-to-band) PL spectra for different combinations of E_G, E_F, and E_S at 79 K in a degenerate silicon wafer. $N_A = 2.7\times10^{19}$ cm^{-3}*

However, although determining the exact values of E_G and E_F in degenerate silicon using Eqs. (3) and (6) has a large uncertainty, the modeling is still useful to explain the properties of the PL spectra at high doping densities. Combining the effects of E_G and E_F, one would expect that the shifting of the spectrum peak location is smaller than the amount of band-gap narrowing in heavily-doped silicon. In addition, the spectral width should be broadened more quickly when the doping level is above the Mott transition than below the Mott transition, since both E_F and the band tails contribute to the broadening in the former case, whereas only the band tails

contribute to the broadening in the latter case. In order to fortify these predictions, we plot the HE spectra with increasing doping densities at 79 K in Figure 11.5. When the doping density increases from 1.4×10^{19} cm^{-3} to 1.1×10^{20} cm^{-3}, the spectrum peak energy is reduced only about 10 meV, whereas the amount of band-gap narrowing was reported to be between 40 – 60 meV by different authors [39-41]. In addition, the full-width at half-maximum (FWHM) of the spectra increases 24 meV when the doping density increases from 1.4×10^{19} cm^{-3} (FWHM = 42 meV) to 1.1×10^{20} cm^{-3} (FWHM = 66 meV), but increases only 12 meV from 5.7×10^{16} cm^{-3} (FWHM = 27 meV) to 1.2×10^{18} cm^{-3} (FWHM = 39 meV).

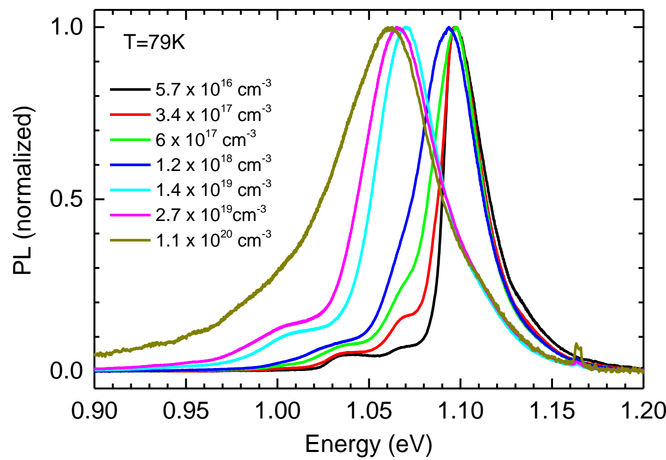

Figure 11.5: *Evolution of measured PL spectra with doping density, under HE level at 79 K.*

11.5 Evolution of PL spectra with doping densities under low and high excitations

In this section, we examine the evolution of the PL spectra with increasing doping densities, and elucidate the difference in the spectra between the LE and HE measurements. Figure 11.6 shows the normalized PL spectra, under LE and HE levels at 79 K, at different doping densities. At LE level, in Figure 11.6a we can observe unambiguously four peaks. Respectively, the three peaks located at 1.14, 1.1, and 1.04 eV are the band-to-band luminescence assisted by the emissions of Transverse-Acoustic (TA) phonons, Transverse-Optical (TO) phonons, and both TO and zone-center optical (O^{Γ}) phonons [2,38]. The peak located at ~1.07 eV is attributed to the free carriers recombining through neutral dopant atoms [4,38,42]. When the dopant density increases, both the dopant (1.07 eV) and main TO (1.1 eV) peaks broaden due to the broadening of the dopant band and the extension of the band tails, and the dopant peak also becomes more and more pronounced (Figures 11.6b-d). Above the Mott transition (Figures 11.6e and 11.6f), the dopant and original TO peaks merge together and form a new TO peak due to the merging of the dopant and valence bands. Nevertheless, the new main peak still continues broadening

and moves towards lower energies with increasing doping densities. Note that, in Figure 11.6b, there is another small shoulder marked by a broken arrow at ~1.09 eV. This shoulder was reported and denoted as B^{TO} by Dean *et al.* [38] at lower temperatures, and was attributed to the recombination of excitons bound to the neutral dopant atoms.

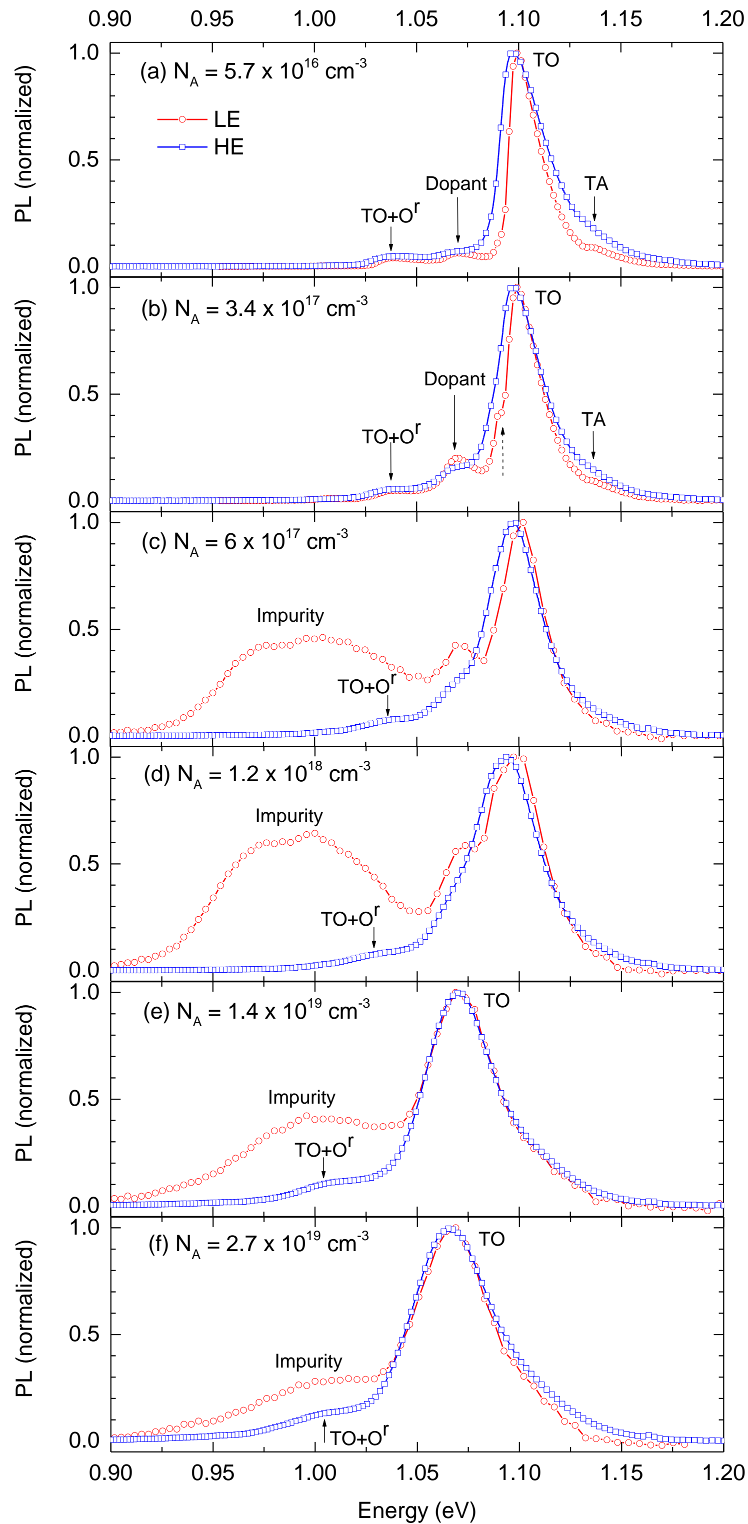

Figure 11.6: *Comparison of normalized measured PL spectra between LE and HE measurements with different doping densities at 79 K.*

Below the Mott transition (Figures 11.6a-d), the spectra captured under the HE level are significantly different from those captured under the LE level. Compared to the LE spectra, the TO component of the HE spectra is broader, and their dopant peak is less pronounced. The broader TO peak of the HE spectra is due to the much higher excess carrier density in the band edges, widening the energy distribution of the free carriers [26]. Meanwhile, the compression of the dopant component in the HE spectra, compared to the TO component, can be explained by the weaker dependence on the excitation intensity of the dopant peak. Since the dopant band is located inside the forbidden gap, it can be considered as a defect band. Therefore, this dopant peak does not increase with the excitation level as quickly as the TO peak [19]. However, when the valence and dopant bands merge together, the main TO peaks of the spectra between the LE and HE measurements are similar (Figures 11.6e and 11.6f). Here, we did not try to model the PL spectra because, near the Mott transition, the band-to-band spectrum is significantly affected by the dopant peak (Figures 11.6b-d), and as such the band-to-band spectral shape cannot be reproduced well using Eq. (3). When silicon becomes degenerate (Figures 11.6e and 11.6f), as discussed in Section 11.4, there is no unique solution of $\{E_G, E_F, E_S\}$ to describe the band-to-band spectral shape.

Surprisingly, there is another very broad peak located at ~1 eV on the LE spectra in Figures 11.6c-f. This peak is not present in Figure 11.6b (boron concentration $N_A = 3.4\times10^{17}$ cm^{-3}), but then appears in Figure 11.6c ($N_A = 6\times10^{17}$ cm^{-3}) even though the doping density increases only slightly. Therefore, this broad peak is unlikely to be related to the boron dopants themselves. In addition, since the shape and intensity of this peak are consistent among different locations within the same wafer, it cannot be due to extended defects such as dislocations or oxygen/metal precipitates. Therefore, it is likely to be related to impurities introduced unintentionally but homogeneously in the wafers. Therefore, we denoted it as “impurity” peak in Figures 11.6c-f. However, this “impurity” peak completely disappears in all HE spectra. In order to verify that this “impurity” peak is not an artifact from the LE measurements, we performed the HE measurements on the c-Si wafer having $N_A = 1.2\times10^{18}$ cm^{-3} with different excitation intensities. When the excitation intensity is reduced more than one order of magnitude, we start observing the “impurity” peak on the normalized spectra (Figure 11.7). The results demonstrate that the “impurity” peak is, in fact, still present on the HE spectra, but is masked by the strong luminescence signals from both the dopant band and the two band edges. Furthermore, Figure 11.8 continues by showing the evolution of PL spectra of this silicon wafer ($N_A = 1.2\times10^{18}$ cm^{-3}) when the temperature increases. The “impurity” peak is completely suppressed at 150 K whereas the dopant peak is still present, although the intensity of the former is stronger than the latter at 79 K.

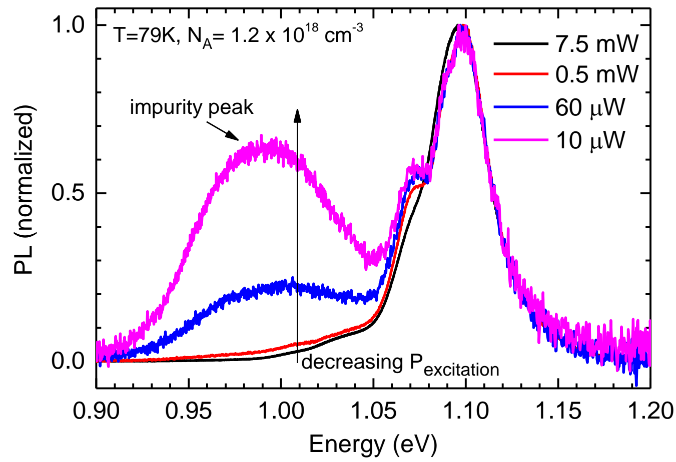

Figure 11.7: *Normalized PL spectra, measured with the HE system at 79 K, at different excitation powers.*

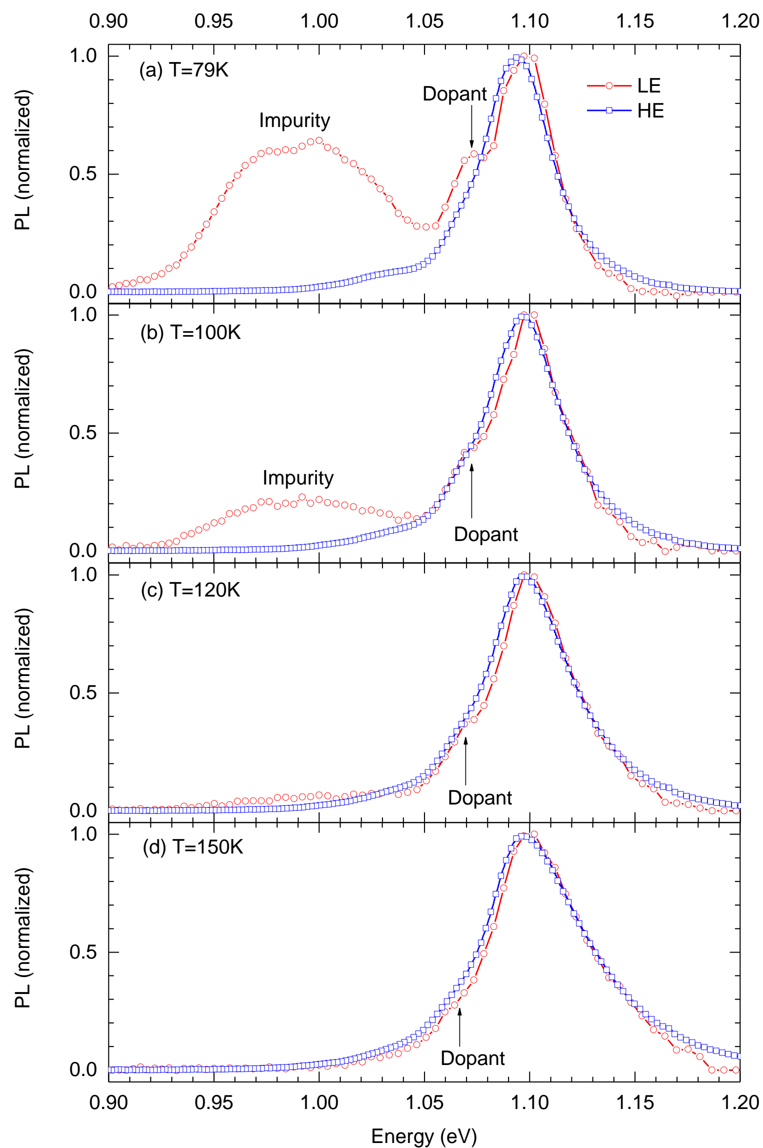

Figure 11.8: *Comparison of normalized PL spectra between LE and HE measurements at different temperatures.* $N_A=1.2\times10^{18}\ cm^{-3}$.

In fact, the properties of this "impurity" peak are similar to the findings reported by Parsons [31] and Schmid *et al.* [29]. These authors found a deep-level luminescence peak which was present in their lightly-excited heavily-doped silicon wafers at low temperatures, but disappeared at either higher temperatures or high excitation levels. They attributed this deep-level peak to the recombination of the majority carriers in the dopant band with the minority carriers, trapped by the compensating impurities introduced unintentionally into the wafers during the ingot growth. Employing the HE system, we can avoid the influence of this unexpected peak on the luminescence spectra.

Next, we examine the impacts of temperatures on the PL spectra of the heavily-doped silicon wafers. The LE (Figures 11.9a and 11.9b) and HE (Figure 11.9c) spectra show a remarkably different trend from each other. In Figure 11.9a, the band-to-band PL intensity increases with temperatures, contradicting the thermal quenching property of the luminescence from c-Si [6]. At low temperatures and low excitation levels, excess carriers are trapped at the impurity centers, and thus the band-to-band luminescence is suppressed. However, when the temperature increases, the impurity luminescence is quenched as the trapped carriers are thermally excited back to their corresponding band edges. Therefore, the excess carriers in the band edges effectively increase, leading to the increment of the band-to-band PL intensity. This increment is more than the expected thermal quenching rate of the band-to-band luminescence up to a certain temperature. However, when the temperature is high enough (400 K in this case), the thermal quenching becomes more dominant again, causing a reduction in the PL intensity as depicted in Figure 11.9b.

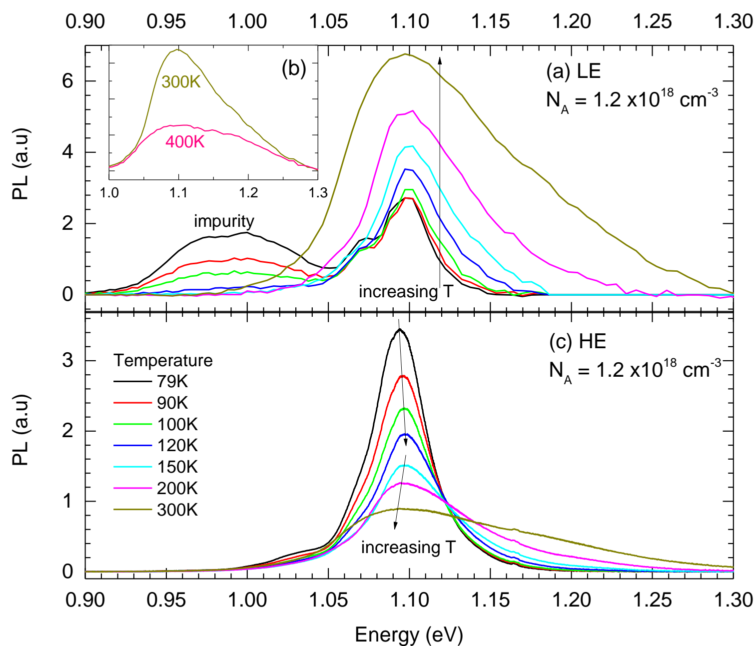

Figure 11.9: *Temperature dependence of PL spectra, measured with both LE (a and b) and HE (c) systems. The two arrows in Figure 11.9c show the shifting of the peak location.*

In the HE measurements (Figure 11.5c), since the impurity luminescence has little impact on the total spectra, the PL signal displays the expected thermal quenching property due to the known temperature dependence of the radiative recombination coefficient [10]. However, one can observe two distinct trends in the peak location of the spectra. The peak energy increases when the temperature increases from 79 to 120 K, contradicting the expected temperature-induced band-gap narrowing in c-Si [1]. Nevertheless, with further increasing temperatures, the peak energy displays the expected reduction due to the band-gap narrowing effects. This property is observed in all heavily-doped wafers investigated in this study. One possible explanation of this behavior is that, the excess carriers in the band tails are thermally excited to higher energy levels, and thus the luminescence peak is first shifted to higher energies with increasing temperatures. However, up to a certain temperature, the amount of band-gap narrowing due to the rising temperature dominates the spectra again, and thus the PL peak shifts back to lower energies.

11.6 Conclusion

We have investigated the effects of doping on the photoluminescence spectra from boron-doped crystalline silicon wafers. Utilizing a low excitation level, we can avoid the overlapping of the dopant and band-to-band luminescence components. Utilizing a high excitation level from the micro-photoluminescence spectroscopy system, we can suppress the influence of the unexpected impurities on the spectra. Therefore, we can perform a systematic study on the effects of different phenomena on the luminescence spectra. We have also explained the difference between the two common approaches in studying the luminescence spectra, including the line shape analysis and generalized Planck's law.

Acknowledgement

This work has been supported by the Australian Research Council (ARC) and the Australian Renewable Energy Agency (ARENA) through research grant RND009. The Australian National Fabrication Facility is acknowledged for providing access to some of the facilities used in this work. The authors are in debt to Prof. H. Tan for providing access to the spectroscopic equipment, and Dr. S. Mokkapati for assisting with some of the experimental setups.

References

[1] W. Bludau, A. Onton, and W. Heinke, “Temperature dependence of the band gap of silicon,” J. Appl. Phys., vol. 45, pp. 1846-1848, 1974.

[2] J. Wagner, “Photoluminescence and excitation spectroscopy in heavily doped n- and p-type silicon,” Phys. Rev. B, vol. 29, pp. 2002-2009, 1984.

[3] J. Wagner, “Band-gap narrowing in heavily doped silicon at 20 and 300 K studied by photoluminescence,” Phys. Rev. B, vol. 32, pp. 1323-1325, 1985.

[4] E. Daub and P. Würfel, “Ultralow values of the absorption coefficient of Si obtained from luminescence,” Phys. Rev. Lett., vol. 74, pp. 1020-1023, 1995.

[5] E. Daub and P. Würfel, “Ultralow values of the absorption coefficient for band–band transitions in moderately doped Si obtained from luminescence,” J. Appl. Phys., vol. 80, pp. 5325-5331, 1996.

[6] T. Trupke, M. A. Green, P. Würfel, P. P. Altermatt, A. Wang, J. Zhao, and R. Corkish, “Temperature dependence of the radiative recombination coefficient of intrinsic crystalline silicon,” J. Appl. Phys., vol. 94, pp. 4930-4937, 2003.

[7] H. T. Nguyen, F. E. Rougieux, B. Mitchell, and D. Macdonald, “Temperature dependence of the band-band absorption coefficient in crystalline silicon from photoluminescence,” J. Appl. Phys., vol. 115, pp. 043710-1 -043710-8, 2014.

[8] M. Tajima, “Determination of boron and phosphorus concentration in silicon by photoluminescence analysis,” Appl. Phys. Lett., vol 32, pp. 719-721, 1978.

[9] P. P. Altermatt, F. Geelhaar, T. Trupke, X. Dai, A. Neisser, and E. Daub, “Injection dependence of spontaneous radiative recombination in crystalline silicon: Experimental verification and theoretical analysis,” Appl. Phys. Lett., vol. 88, pp. 261901-1 -261901-3, 2006.

[10] H. T. Nguyen, S. C. Baker-Finch, and D. Macdonald, “Temperature dependence of the radiative recombination coefficient in crystalline silicon from spectral photoluminescence,” Appl. Phys. Lett., vol. 104, pp. 112105-1 -112105-3, 2014.

[11] M. Tajima, Y. Iwata, F. Okayama, H. Toyota, H. Onodera, and T. Sekiguchi, “Deep-level photoluminescence due to dislocations and oxygen precipitates in multicrystalline Si,” J. Appl. Phys., vol. 111, pp. 113523-1 - 113523-6, 2012.

[12] M. Tajima, “Spectroscopy and topography of deep-level luminescence in photovoltaic silicon,” IEEE Journal of Photovoltatics, vol. 4, pp. 1452-1458, 2014.

[13] P. Gundel, M. C. Schubert, W. Kwapil, J. Schön, M. Reiche, H. Savin, M. Yli-Koski, J. A. Sans, G. Martinez-Criado, W. Seifert, W. Warta, and E. R. Weber, “Micro-photoluminescence spectroscopy on metal precipitates in silicon,” Physica Status Solidi RRL, vol. 3, pp. 230-232, 2009.

[14] H. T. Nguyen, F. E. Rougieux, F. Wang, H. Tan, and D. Macdonald, “Micrometer-scale deep-level spectral photoluminescence from dislocations in multicrystalline silicon,” IEEE Journal of Photovoltaics, vol. 5, pp. 799-804, 2015.

[15] H. T. Nguyen, F. E. Rougieux, F. Wang, and D. Macdonald, "Effects of solar cell processing steps on dislocation luminescence in multicrystalline silicon," Energy Procedia, vol. 77, pp. 619 – 625, 2015.

[16] R. Woehl, P. Gundel, J. Krause, K. Rühle, F. D. Heinz, M. Rauer, C. Schmiga, M. C. Schubert, W. Warta, and D. Biro, "Evaluating the aluminum-alloyed p+-layer of silicon solar cells by emitter saturation current density and optical microspectroscopy measurements," IEEE Trans. Elec. Devices, vol. 58, pp. 441-447, 2011.

[17] P. Gundel, D. Suwito, U. Jäger, F. D. Heinz, W. Warta, and M. C. Schubert, "Comprehensive microscopic analysis of laser-induced high doping regions in silicon," IEEE Trans. Elec. Devices, vol. 58, pp. 2874-2877, 2011.

[18] A. Roigé, J. Alvarez, J.-P. Kleider, I. Martin, R. Alcubilla, and L. F. Vega, "Microscale spatially resolved characterization of highly doped regions in laser-fired contacts for high-efficiency crystalline Si solar cells," IEEE Journal of Photovoltaics, vol. 5, pp. 545-551, 2015.

[19] H. T. Nguyen, Y. Han, M. Ernst, A. Fell, E. Franklin, and D. Macdonald, "Dislocations in laser-doped silicon detected by micro-photoluminescence spectroscopy," Appl. Phys. Lett., vol. 107, pp. 022101-1 - 022101-5, 2015.

[20] H. T. Nguyen, D. Yan, F. Wang, P. Zheng, Y. Han, and D. Macdonald, "Micro-photoluminescence spectroscopy on heavily-doped layers of silicon solar cells," Physica Status Solidi RRL, vol. 9, pp. 230 – 235, 2015.

[21] H. T. Nguyen, S. P. Phang, J. Wong-Leung, and D. Macdonald, "Photoluminescence excitation spectroscopy of diffused layers on crystalline silicon wafers," IEEE Journal of Photovoltaics, vol. 6, pp. 746 – 753, 2016.

[22] M. Eswaran, B. Bergersen, J.A. Rostworowski, and R. R. Parsons, "Impurity band states in Si(P)," Solid State Communications, vol. 20, pp. 811-813, 1976.

[23] R. R. Parsons, "Photoluminescence in heavily-doped Si(P)," Can. J. Phys., vol. 56, pp. 814-826, 1978.

[24] J. R. Lowney, "Impurity bands and band tailing in moderately doped silicon," J. Appl. Phys., vol. 59, pp. 2048-2053, 1986.

[25] P. V. Mieghem, "Theory of band tails in heavily doped semiconductors," Rev. Mod. Phys., vol. 64, pp. 755-793, 1992.

[26] P. P. Altermatt, A. Schenk, and G. Heiser, "A simulation model for the density of states and for incomplete ionization in crystalline silicon. I. Establishing the model in Si:P," J. Appl. Phys., vol. 100, pp. 113714-1 -113714-10, 2006.

[27] K. Morigaki and F. Yonezawa, "Metal-nonmetal transition in doped semiconductors," Supplement of the Progress of Theoretical Physics, No. 57, pp. 146-155, 1975.

[28] R. E. Halliwell and R. R. Parsons, "Photoluminescent studies of the condensed phase in phosphorus-doped silicon," Solid State Communications, vol. 13, pp. 1245-1248, 1973.

[29] P. E. Schmid, M. L. W. Thewalt, and W. P. Dumke, "Photoluminescence in heavily doped Si:B and Si:As," Solid State Communications, vol. 38, pp. 1091-1093, 1981.

[30] W. P. Dumke, "Comparison of band-gap shrinkage observed in luminescence from n+-si with that from transport and optical absorption measurements," Appl. Phys. Lett., vol. 42, pp. 196-198, 1983.

[31] R. R. Parsons, "On the origin of photoluminescence in heavily-doped silicon," Solid State Communications, vol. 29, pp. 763-766, 1979.

[32] P. Würfel , "The chemical potential of radiation," J. Phys. C: Solid State Phys., vol. 15, pp. 3967-3985, 1982.

[33] P. Würfel, S. Finkbeiner, and E. Daub, "Generalized Planck's radiation law for luminescence via indirect transitions," Appl. Phys. A, vol. 60, pp. 67-70, 1995.

[34] T. Trupke, E. Daub, and P. Würfel, "Absorptivity of silicon solar cells obtained from luminescence," Solar Energy Materials and Solar Cells, vol. 53, pp. 103-114, 1998.

[35] T. Trupke, "Influence of photon reabsorption on quasi-steady-state photoluminescence measurements on crystalline silicon," J. Appl. Phys., vol. 100, pp. 063531-1 -063531-8, 2006.

[36] W. Liang, K. J. Weber, D. Suh, S. P. Phang, J. Yu, A. K. McAuley, and B. R. Legg, "Surface passivation of boron-diffused p-type silicon surfaces with (1 0 0) and (1 1 1) orientations by ALD Al_2O_3 layers," IEEE Journal of Photovoltaics, vol. 3, pp. 678 – 683, 2013.

[37] P. Würfel, Physics of Solar Cells: From Basic Principles to Advanced Concepts, p. 14, Wiley-VCH, 2009.

[38] P. J. Dean, J. R. Haynes, and W. F. Flood, "New radiative recombination processes involving neutral donors and acceptors in silicon and germanium," Physical Review, vol. 161, pp. 711-729, 1967.

[39] W. P. Dumke, "Band-gap narrowing from luminescence in p-type Si," J. Appl. Phys., vol. 54, pp. 3200-3202, 1983.

[40] J. Wagner and J. A. del Alamo, "Band-gap narrowing in heavily doped silicon: A comparison of optical and electrical data," J. Appl. Phys., vol. 63, pp. 425-429, 1988.

[41] D. Yan and A. Cuevas, "Empirical determination of the energy band gap narrowing in p+ silicon heavily doped with boron," J. Appl. Phys., vol. 116, pp. 194505-1 - 194505-7, 2014.

[42] B. Bergersen, J. A. Rostworowski, M. Eswaran, and R. R. Parsons, "Electron-hole droplets and impurity band states in heavily doped Si(P): Photoluminescence experiments and theory," Phys. Rev. B, vol. 14, pp. 1633-1648, 1976.

CHAPTER 12

Summary and Future Work

In summary, photoluminescence spectra captured from crystalline silicon wafers and solar cells contain rich information about the intrinsic properties of the material, the defects and impurities, the surface optics, the carrier profiles, the cell structures, and the fabrication processes. Interpreting the total spectra emitted from the silicon solar cells is extremely challenging. However, by systematically controlling these properties, we can observe and study the individual impacts of each phenomenon on the luminescence spectra. This thesis has utilized the rich information on the photoluminescence spectra to develop a variety of new spectrally-resolved photoluminescence-based characterization methods for studying the properties of different structures in silicon solar cells. Although the focus of all techniques presented in this thesis is on silicon, these techniques in principle can be extended to other materials in photovoltaic applications.

Band-to-band photoluminescence spectroscopy

Band-to-band photoluminescence spectra are emitted from the two band edges of silicon, and thus reflect the intrinsic properties of the material. However, due to the reabsorption of the generated photons, the spectra detected outside the silicon wafers are affected by the surface morphologies and the excess carrier profiles. By controlling the experimental conditions and the geometrical properties of the wafers systematically, the values of the band-to-band absorption and radiative recombination coefficients, two of the most important parameters in silicon, have been established as a function of temperature. The temperature data showed that, around room temperature, the values of the band-to-band absorption coefficient varied significantly even though the temperature was changed only a few degrees. Therefore, the exact value of the temperature at room condition should be used for precise device modeling and characterization. Furthermore, we found a saturation of the radiative recombination coefficient at temperatures around room temperature and above.

The established temperature dependence of the band-to-band absorption coefficient in this thesis allows us to model photoluminescence spectra from silicon wafers with different surface morphologies under various experimental conditions as a function of temperature. We have applied the modeled results to elucidate the individual impacts of the excess carrier profiles and the surface reflectivities on the total luminescence spectra captured. We also suggested that, the sensitivity of many photoluminescence-based techniques, which have been established mainly at room temperature in the literature, could be improved by carrying out the measurements at higher temperatures. The reason is that, the impacts of the carrier profiles and the surface reflectivities on the spectra were found to be more pronounced at higher temperatures due to the increasing reabsorption of the generated photons in silicon wafers.

Besides the applications established in this thesis, band-to-band photoluminescence spectroscopy still has many potential applications in silicon photovoltaics. One possible extension could be to investigate photoluminescence spectra from complete silicon solar cells under different bias conditions. When a voltage is applied on solar cells, the excess carrier profiles in the solar cells are altered and thus the spectra emitted from them should also be changed. Therefore, we could potentially study the electrical and optical properties of finished solar cells under different working conditions using the detected spectra.

Deep-level micro-photoluminescence spectroscopy

Dislocations, along with other defects and impurities trapped around them, are important efficiency limiting defects in silicon solar cells. These defect centers were demonstrated to emit deep-level luminescence peaks besides the band-to-band peak from silicon. This thesis has

utilized this phenomenon to investigate the spatial distributions of dislocations, and secondary defects and impurities, around sub-grain boundaries in multicrystalline silicon wafers. We found an asymmetrical distribution of the secondary defects and impurities across the sub-grain boundaries investigated, suggesting that the defects and impurities were preferentially trapped at one side of the sub-grain boundaries.

Furthermore, the behaviors of individual D lines after different processing steps were studied. We found that, although the D1 and D2 lines were known to originate from the defects and impurities trapped around dislocations, the D1 intensity was enhanced significantly after the phosphorus gettering step whereas the D2 intensity was consistent after various processing steps. The experimental results suggested that the enhancement of D1 was because the sub-grain boundaries were cleaned of metal impurities after the gettering process. This finding may open paths to apply this micro-photoluminescence-based technique to monitor the effectiveness of the gettering process in solar cell fabrications, or to study the distribution of metal impurities around dislocation sites.

Nevertheless, there are still some uncertainties about the origins of the D lines. Although D1 and D2 are known to originate from the secondary defects and impurities trapped around dislocations, and D3 and D4 are confirmed to reflect the intrinsic properties of the dislocations, this thesis has demonstrated that, not only D1 and D2, but also D3 and D4 have different origins from each other due to their different luminescence properties. However, an arising question is which type of dislocations causes D3 and D4, and which type of defects and impurities causes D1 and D2. Further breaking down the origins of these deep-level luminescence peaks is of importance for understanding the physics of these recombination centers, as well as for developing techniques to mitigate their detrimental impacts on finished silicon solar cells.

Separation of photoluminescence fingerprints from different layers

When different materials are stacked on a single silicon wafer and an appropriate excitation wavelength is employed, the total spectrum detected contains luminescence signatures from all layers. However, at room temperature, the luminescence peaks are either too broad due to thermal broadening, or reduced in intensity due to thermal quenching. Therefore, the individual signatures from each layer cannot be observed. This thesis has utilized the distinct luminescence peaks at low temperatures to investigate the electronic and optical properties of different micron-scale features on silicon solar cells.

First, the aggregate luminescence spectra from various diffused silicon wafers were reported. Band-gap narrowing effects in heavily-doped silicon cause the band-to-band luminescence peak to be shifted to longer wavelengths. Therefore, both the band-to-band luminescence peaks from the heavily-doped layer and the underlying substrate could be

observed. The relative intensity of the band-to-band peak emitted from the heavily-doped layer, compared to that emitted from the underlying substrate, was found to correlate with the dopant density of the heavily-doped layer. Based on these results, the technique was applied to characterize the dopant levels of localized diffused and laser-doped regions on crystalline silicon wafers. The results showed that, the interfaces between the laser-doped and un-doped regions were more heavily doped than the laser-doped regions themselves.

Second, the damage induced by the laser-doping process was demonstrated to emit a deep-level photoluminescence peak. The damage was found to be located near the wafer surface. Moreover, the laser-doped wafers were found to emit three separate luminescence peaks originating from the heavily-doped silicon in the laser-doped layer, the damage induced by the laser-doping process, and the underlying substrate at low temperatures. Due to the different radiative recombination mechanisms among these three components, the three luminescence peaks were demonstrated to have different dependences on the excitation power and the temperature. In addition, the laser damage peak was found to have similar luminescence properties to those of dislocations in multicrystalline silicon wafers, suggesting that the damage observed was related to dislocations, and the interfaces between the doped and un-doped regions contained more dislocations than the laser-doped regions.

Finally, the aggregate luminescence spectra from the silicon wafers passivated with hydrogenated amorphous silicon and hydrogenated silicon nitride films were also reported and explained. Their dependences on the experimental and deposition conditions were investigated. Silicon-rich silicon nitride films were found to emit photoluminescence spectra whose properties are similar to those of hydrogenated amorphous silicon, thus suggesting the presence of amorphous silicon clusters inside the silicon nitride films. The thesis also showed a correlation between the refractive index, as well as the optical absorption, of the silicon nitride films and the luminescence intensity from these films. In addition, adding the capability to detect heavily-doped layers in silicon wafers, the technique was then applied to evaluate parasitic absorption in different passivation films, and dopant levels of heavily-doped regions on various finished silicon solar cells.

Spectrally-resolved micro-photoluminescence excitation spectroscopy

As device complexity increases, there is a trend to utilize both lateral and vertical spatial dimensions in silicon wafers. Therefore, many structures in silicon solar cells are not only reduced in size but also stacked together on a single substrate. This tendency makes the characterization of silicon solar cells more challenging. This thesis reported a novel contactless, non-destructive technique, which combined the advantages of both spectrally-resolved photoluminescence and photoluminescence excitation spectroscopy techniques, to characterize small features distributed at different depths below wafer surfaces. The principle of this

technique is to observe the evolution of the entire luminescence spectrum from a silicon wafer or solar cell at low temperatures while the excitation wavelength is varied.

This technique was applied to evaluate both the junction depth and the doping level of various diffused silicon wafers. It was also used to detect and differentiate different deep-level luminescence peaks emitted from defects and impurities induced by the post-diffusion thermal treatment. In addition, this newly-developed method was applied to detect the enhanced diffusion of dopant atoms along grain boundaries in multicrystalline silicon wafers. The results showed that, the enhanced diffusion occurred at numerous types of large angle grain boundaries investigated in this thesis, rather than some specific large angle grain boundaries as reported in the literature. Furthermore, sub-grain boundaries were found to act as preferential diffusion sites for dopant atoms during the thermal diffusion process. These sub-grain boundaries were demonstrated to contain a high level of defects and impurities trapped around them, and these defects and impurities were distributed homogeneously throughout the wafer thickness. The results indicated that, the presence of the defects and impurities around the sub-grain boundaries did not hinder the preferential diffusion of the dopant atoms.

However, at the current stage, this spectrally-resolved photoluminescence excitation spectroscopy has not been demonstrated to detect photoluminescence signatures from sub-nanometer layers at the wafer surface due to the lower limit of the excitation wavelength of the light source employed in this thesis. The lowest achievable excitation wavelength was 500 nm. A possible extension of this method is to employ shorter excitation wavelengths, for example 325-nm wavelength at which the absorption depth in crystalline silicon at 79 K is only about 10 nanometers. In this case, the luminescence signal detected should be emitted mostly from a few nanometers at the silicon wafer surface. Also, the shorter excitation wavelengths can be used to excite electrons and holes in different passivation films such as silicon nitride, amorphous silicon, or titanium oxide, which in turn can emit luminescence spectra. By increasing the excitation wavelength starting from the ultra-violet range, and observing changes in the spectrum, one may be able to quantitatively evaluate the depth distributions of numerous materials and features in finished silicon solar cells. Combining with the micro-photoluminescence spectroscopy system, one could develop a very powerful contactless, nondestructive characterization tool in both spectral and spatial dimensions for silicon photovoltaics.

List of Other Publications

Oral presentations

[1] Hieu T. Nguyen, Fiacre E. Rougieux, Simeon C. Baker-Finch, and Daniel Macdonald, "Temperature dependence of band-band absorption and radiative recombination in c-Si," 40th IEEE Photovoltaics Specialists Conference, Denver, 2014.

[2] Hieu T. Nguyen and Daniel Macdonald, "Applications of photoluminescence spectroscopy in silicon photovoltaics," 3rd Australian Center for Advanced Photovoltaics (ACAP) Conference, Brisbane, 2015.

[3] Hieu T. Nguyen, Sieu Pheng Phang, and Daniel Macdonald, "Applications of photoluminescence excitation spectroscopy in silicon photovoltaics," 6th International Conference on Silicon Photovoltaics, Chambéry, 2016.

Refereed journal papers

[1] Chog Barugkin, Jinjin Cong, The Duong, Shakir Rahman, Hieu T. Nguyen, Daniel Macdonald, Thomas P. White, and Kylie R. Catchpole, "Ultralow absorption coefficient and temperature dependence of radiative recombination of $CH_3NH_3PbI_3$ Perovskite from photoluminescence," The Journal of Physical Chemistry Letters, volume 6, 767, 2015.

[2] Carsten Schinke, P. Christian Peest, Jan Schmidt, Rolf Brendel, Karsten Bothe, Malte R. Vogt, Ingo Kröger, Stefan Winter, Alfred Schirmacher, Siew Lim, Hieu T. Nguyen, and Daniel MacDonald, "Uncertainty analysis for the coefficient of band-to-band absorption of crystalline silicon," AIP Advances, volume 5, 067168, 2015.

[3] Young-Joon Han, Evan Franklin, Andreas Fell, Marco Ernst, Hieu T. Nguyen, Daniel Macdonald, "Low-temperature micro-photoluminescence spectroscopy on laser-doped silicon with different surface conditions," Applied Physics A, volume 122, 1, 2016.

[4] AnYao Liu, Hieu T. Nguyen, and Daniel Macdonald, "Quantifying boron and phosphorous dopant concentrations in silicon from photoluminescence spectroscopy at 79 K," Physica Status Solidi A: Applications and Materials Science, 2016. DOI: 10.1002/pssa.201600335

Other contributions to international conferences

[1] Carsten Schinke, P. Christian Peest, Karsten Bothe, Jan Schmidt, Rolf Brendel, Malte R. Vogt, Ingo Kröger, Stefan Winter, Alfred Schirmacher, Siew Lim, Hieu T. Nguyen, and

Daniel Macdonald, "Experimental determination of the uncertainty of the absorption coefficient of crystalline silicon," Energy Procedia, volume 77, 170, 2015.

[2] Daniel Macdonald, AnYao Liu, Hieu T. Nguyen, Siew Yee Lim, and Fiacre E. Rougieux, "Physical Modelling of Luminescence Spectra from Crystalline Silicon," 31st European Photovoltaic Solar Energy Conference and Exhibition, Hamburg, 2015

[3] Hang C. Sio, Sieu P. Phang, Hieu T. Nguyen, Di Yan, Thorsten Trupke, and Daniel Macdonald, "Comparison of recombination activity of grain boundaries in various multicrystalline silicon materials," 31st European Photovoltaic Solar Energy Conference and Exhibition, Hamburg, 2015.

[4] Chang Sun, Hieu T. Nguyen, Fiacre E. Rougieux, and Daniel Macdonald, "Characterization of Cu and Ni precipitates in n- and p-type Czochralski-grown silicon by photoluminescence," 6th International Conference on Silicon Photovoltaics, Chambéry, 2016.

[5] AnYao Liu, Hieu T. Nguyen, and Daniel Macdonald, "Silicon luminescence spectra modelling and the impact of dopants," 6th International Conference on Silicon Photovoltaics, Chambéry, 2016.

[6] Di Yan, Andres Cuevas, Peiting Zheng, Hieu T. Nguyen, Yimao Wan, and James Bullock, "Silicon nitride/silicon oxide interlayer for solar cell passivating contacts based on PECVD amorphous silicon," 43rd IEEE Photovoltaics Specialists Conference, Portland, 2016.

Appendix

This appendix consists of two conference papers, each of which was presented at The 5th and 6th International Conferences on Silicon Photovoltaics in 2015 and 2016, respectively. The first conference paper is an extension of the work presented in Chapter 5. In this chapter, we demonstrated that in multicrystalline silicon wafers the dislocations themselves emitted the deep-level photoluminescence lines D3 and D4, whereas the defects and impurities trapped around the dislocations emitted the deep-level lines D1 and D2. After phosphorus gettering, the D2, D3, and D4 lines were not altered, but the D1 line was increased significantly. Moreover, we suggested that D3 had a different origin from D4 even though they were both emitted from dislocations. This first conference paper continues to investigate the luminescence properties of these D lines after phosphorus gettering and hydrogenation steps. The results show that while the gettering process changes the D1 line intensity, the hydrogenation process does not alter the intensities of the D lines. Moreover, the effectiveness of the phosphorus gettering is found to be varied along the sub-grain boundaries due to the different intensity increment of D1. Finally, the work presents further experimental evidences to support the hypothesis that D3 and D4 have different origins.

The second conference paper is an extension of the work presented in Chapter 9. In this chapter, we demonstrated the proof of concept of combining spectrally-resolved photoluminescence and photoluminescence excitation spectroscopy to characterize silicon wafers and solar cells. By capturing the luminescence spectrum emitted from silicon wafers under varying excitation wavelengths at low temperatures, we were able to qualitatively examine the depth distribution of different layers in silicon wafers. This conference paper continues to apply this technique to investigate the depth distribution of dislocations formed in silicon wafers during two different processes: the ingot growth and cooling, and the post-diffusion thermal treatment. The results show that, the dislocations formed during the former process are distributed uniformly depth-wise throughout the wafer thickness, whereas those formed during the latter process are confined to the near surface region.

Available online at www.sciencedirect.com

ScienceDirect

Energy Procedia 77 (2015) 619 – 625

Energy Procedia

5th International Conference on Silicon Photovoltaics, SiliconPV 2015

Effects of solar cell processing steps on dislocation luminescence in multicrystalline silicon

Hieu T. Nguyen[a,]*, Fiacre E. Rougieux[a], Fan Wang[b], and Daniel Macdonald[a]

[a]*Research School of Engineering, College of Engineering and Computer Science, The Australian National University, Canberra, ACT 2601, Australia*
[b]*Department of Electronic Materials Engineering, Research School of Physics and Engineering, The Australian National University, Canberra, ACT 2601, Australia*

Abstract

We examine the impacts of hydrogenation and phosphorus gettering steps on the deep-level photoluminescence spectra of dislocations and the surrounding regions in multicrystalline silicon wafers, using micro-photoluminescence spectroscopy with micron-scale spatial resolution. We found that the D1 line, originating from secondary defects around dislocation sites, was enhanced significantly after gettering but remained unchanged after hydrogenation, suggesting that the former process reduced the concentration of metal impurities around the dislocations while the latter process did not alter the relevant properties of defects and impurities. In addition, the D3 and D4 intensities were found to be unchanged after different processing steps, indicating that the intrinsic structure of the dislocations was not affected by the investigated processes. Finally, we report empirical evidence supporting the hypothesis that D3 is not the phonon replica of D4 due to their different intensity ratio at different locations in the wafers.

© 2015 The Authors. Published by Elsevier Ltd. This is an open access article under the CC BY-NC-ND license
(http://creativecommons.org/licenses/by-nc-nd/4.0/).
Peer review by the scientific conference committee of SiliconPV 2015 under responsibility of PSE AG

Keywords: Crystalline silicon; deep level; dislocations; grain boundaries; photoluminescence (PL); photovoltaic cells

* Corresponding author.
E-mail address: hieu.nguyen@anu.edu.au

1876-6102 © 2015 The Authors. Published by Elsevier Ltd. This is an open access article under the CC BY-NC-ND license
(http://creativecommons.org/licenses/by-nc-nd/4.0/).
Peer review by the scientific conference committee of SiliconPV 2015 under responsibility of PSE AG
doi:10.1016/j.egypro.2015.07.089

1. Introduction

Recently, there has been an increasing interest in employing spectrally-resolved photoluminescence (PL) as an accurate and non-destructive characterization tool in silicon photovoltaics. By capturing the luminescence signal emitted from transitions of free carriers between the two band edges of crystalline silicon, fundamental properties of this material have been determined such as the band-to-band (BB) absorption coefficient [1-3], radiative recombination coefficient [2,4,5], temperature dependence of the band gap [6], and the extent of band-gap narrowing in heavily-doped silicon [7,8]. Also, BB spectral PL has been employed to extract the minority carrier diffusion length in silicon wafers [9,10] and bricks [11], to quantify light trapping in plasmonic structures [12], to investigate the effects of different surface morphologies [13,14] as well as carrier profiles [14] on the spectrum shapes, and recently to study properties of thin heavily-doped layers of cell pre-cursors [15]. On the other hand, defects and impurities occupying energy states within the forbidden gap of crystalline silicon can give rise to deep-level luminescence spectra, with the peak energies lower than that of the BB peak. These deep-level spectra contain distinct signatures for different kinds of defects and impurities such as Cr-B pairs [16], oxygen precipitates [17], Fe precipitates [18], and dislocations [19,20] in crystalline silicon.

In multicrystalline silicon (mc-Si), dislocation networks are one of the key factors limiting the final cell efficiency [21], and usually occur at small angle grain boundaries (SAGBs) and other sub-grain boundaries (sub-GBs). These dislocation sites have been reported to emit four distinct deep-level lines, known as D1, D2, D3, and D4. The doublet D1/D2 originates from secondary defects and impurities decorated around dislocations [22,23], whereas the doublet D3/D4 reflects the intrinsic properties of dislocations [22-26]. These results have been confirmed recently by Tajima *et al.* [23], in which D1 and D2 were found to occur around SAGBs, and D3 and D4 were present directly on SAGBs. Recently, utilizing the micron-scale spatial resolution of a confocal microscope PL spectroscopy system, we have shown that the D1 intensity was enhanced when the dislocations were cleaned of metal impurities after gettering, whereas the D2 intensity still remained the same, and confirmed that D1 and D2 had different origins [27]. Also, we proposed that D3 was not the phonon replica of D4 due to their different energy shifting when moving away from the sub-GBs.

Since the D lines reflect the properties of dislocations and the surrounding local conditions, they can be employed as a tool to monitor the behavior of defects and impurities around dislocations and the dislocations themselves during cell fabrication processes. Moreover, phosphorous gettering and hydrogenation are two essential steps which are naturally incorporated during the formation of diffused layers, and of antireflection coating (ARC) layers by chemical vapor deposition (CVD) and their subsequent firing. Thus, an insightful understanding of the behaviors of the D lines after these two processing steps may provide more information about the impact of gettering and hydrogenation on dislocations. Therefore, in this work, utilizing the high spatial resolution of a micro-PL (μPL) spectroscopy system, we report findings regarding the various effectiveness of the gettering process along the sub-GBs based on the D line emissions, and also investigate the behaviors of the D lines after the hydrogenation process. In addition, we also report further experimental findings to support the hypothesis that D3 is not the phonon replica of D4 [27].

2. Experimental details

The experimental setup in this study is described in detail elsewhere [27]. The μPL spectroscopy system has a spatial resolution of about 3 microns and a spectral resolution of about 0.25 nm. The sample temperature was kept constant at 79 K using a liquid-nitrogen-cooled cryostat. The samples studied here are directionally solidified, boron-doped p-type mc-Si wafers having a background doping of about 9×10^{15} cm^{-3}. Three samples were cut from three consecutive wafers in the same ingot, and chemically etched with an etchant of HF and HNO_3 to remove saw damage and to achieve optically polished surfaces. After that, the first sample was kept in the as-cut state. The second sample was passivated with a layer of SiN_x:H deposited by plasma-enhanced chemical vapor deposition (PECVD) using ammonia and silane as precursor gases. It was then annealed at 700 ^oC for 30 minutes in a N_2 gas environment in a quartz tube furnace to distribute hydrogen throughout the sample thickness. The third sample went through an extended phosphorous gettering process [28], which is described in greater details in Ref. 27. The sheet resistance of the resultant diffused layer was about 30 Ω/□. All samples were chemically etched again to remove

residual layers left after the previous processing steps, leaving bare silicon surfaces. Finally, they were immersed in a defect etchant consisting of acetic/nitric/hydrofluoric acids for 16 hours [29,30]. The purpose of this etching step is to delineate the sub-GBs, which are otherwise not observable under the optical microscope. The final thickness of these samples is around 250 microns.

3. Results and analysis

First, we examine the behaviors of D1 and D2 after the hydrogenation and gettering steps. In order to ensure that the presence of the D3 and D4 lines does not affect our analysis on the D1 and D2 lines, the investigated sub-GB was chosen to have strong D1 and D2 emissions, but low D3 and D4 emissions. We captured the PL spectra at a location about 10 microns away from the same sub-GB for the three samples. Each individual spectrum was then decomposed with 5 Gaussian peaks representing the four lines D1, D2, D3, D4, and the first phonon replica of the band-to-band line (BBPR). The amplitudes of these Gaussian peaks are the intensities of their corresponding PL lines. Here we did not fit the band-to-band (BB) peak with the Gaussian function since this BB peak was distinctly sharp at 79 K [2,3], allowing us to isolate the BB peak. We note that decomposing the spectrum in this way is necessary to accurately estimate the intensities of the individual D lines, since there is significant overlap between them. By contrast, a common way to investigate their spatial distributions, in particular D1 and D2, is to apply band-pass filters to collect individual components of the spectra. However, the detected PL signal using band-pass filters is, in principle, still the aggregate signal of multiple components. For example, in Fig. 1c, the apparent intensity of D2 is almost as twice the intensity of the decomposed D2 peak, since the D2 line in this case occurs on the tail of the more intense D1 peak. This effect may give a misleading conclusion regarding the change of the D2 line if applying band-pass filters.

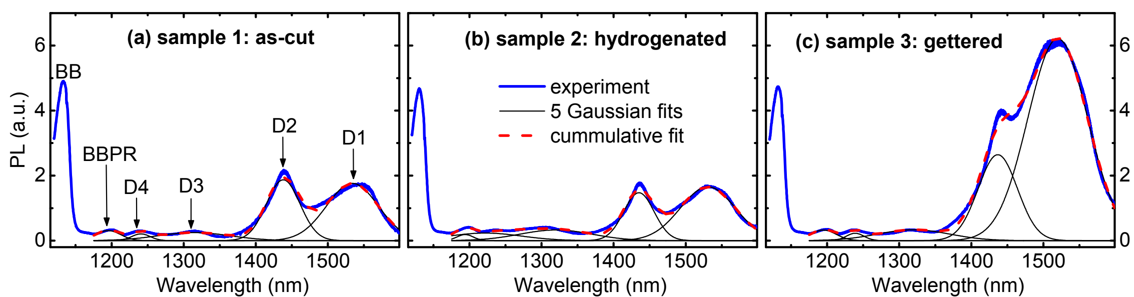

Fig. 1. Comparison of PL spectra among (a) as-cut, (b) hydrogenated, and (c) gettered samples at a location about 10 microns away from the same sub-GB at 79 K.

In Fig. 1, the spectrum of the hydrogenated sample is similar to that of the as-cut sample, whereas the spectrum of the gettered sample changes significantly. Since the D1 and D2 lines are emitted by the secondary defects or impurities trapped by the strain field around the dislocation sites, the consistency of the D1 and D2 intensities indicates that the hydrogenation process performed in this study is not effective in altering or passivating these defects and impurities around the dislocations. However, after gettering, D1 is enhanced notably whereas D2 does not change significantly. This behavior of D1 has been reported by our group recently, and was suggested as being due to a reduction in the concentration of metal impurities, in particular Fe, around the sub-GBs after gettering [27]. This finding can be compared with the results from Johnston *et al.* [31], in which the authors found an enhancement of the sub-band gap luminescence from defect clusters in mc-Si wafers after the phosphorus diffusion, although via the imaging technique employing a long-pass filter (> 1350 nm). Due to this behavior of D1, we therefore hypothesize that the D1 line originates from only the secondary defects, and the metal impurities may form complexes with the D1 centers, thus alternating their energy levels and suppressing their luminescence efficiency. Moreover, as we performed line scans parallel to this sub-GB at a distance about 10 microns away from the sub-GB, the spectra of the as-cut sample are almost the same, whereas those of the gettered sample are altered significantly, as plotted in Fig. 2. The D1 intensity increases from the starting point to the final point of the line scan on the

gettered sample. We continued performing the line scans again but in the opposite direction, and observed the opposite trend of the D1 intensities, indicating that the observed increment of D1 is not due to scanning artifacts. Therefore, the results in Fig. 2 suggest that the gettering extent of metal impurities varies along the length of the sub-GB itself. The more effective the gettering process is, the higher the D1 intensity is.

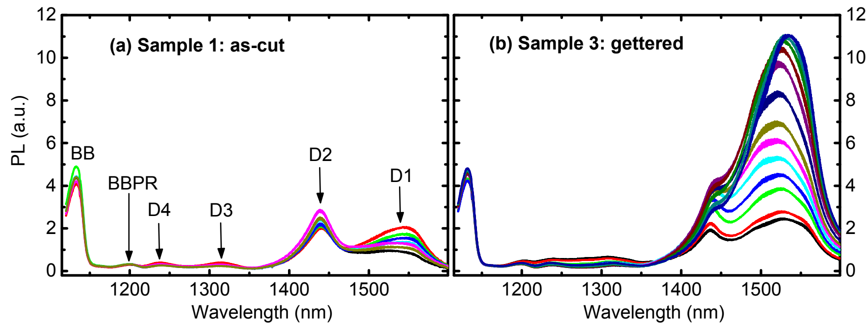

Fig. 2. PL spectra from line scans parallel to the sub-GB of (a) as-cut and (b) gettered samples. The line scans were performed at a distance about 10 microns away from the sub-GB, and each spectrum in the figure corresponds to one position along the line scans.

In order to avoid the differences in local conditions, as shown above, from affecting our general conclusions, we performed 80-micron line scans parallel to this sub-GB in 5-micron step sizes, at different distances (5, 10, and 15 microns) away from this sub-GB. Fig. 3 shows the average intensities of the D1, D2, and BB peaks (after the total spectrum was decomposed), along with one standard deviation error bars. As can be readily seen in Figs. 3a and 3b, the D1 intensity of the gettered sample is notably higher than that of the other two samples, although the BB intensity in Fig. 3c is the same among the three samples. Also, the extent of the D1 error bars of the gettered sample is consistently much larger than that of the other two samples at different distances. Therefore, we conclude that the hydrogenation process used in our study does not affect the D1 and D2 luminescence efficiencies, whereas the gettering process enhances the deep-level luminescence of D1 due to the reduction of metal impurities, and this effect varies along the sub-GB itself.

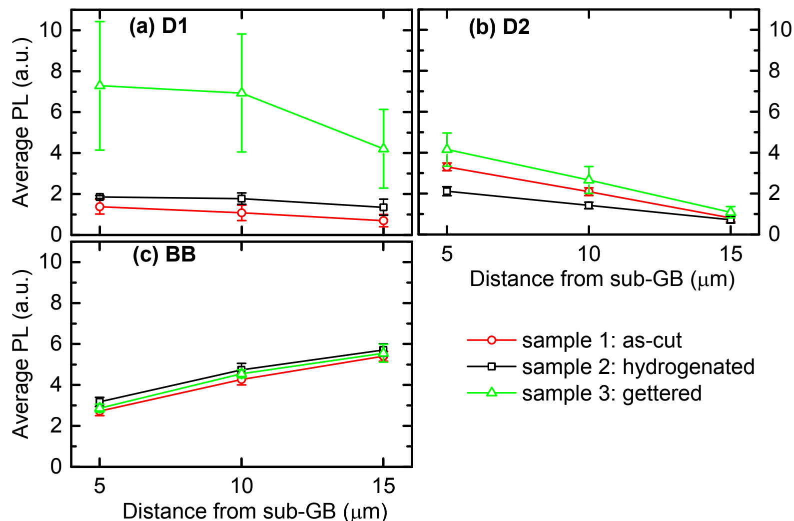

Fig. 3. Average PL intensities, along with one standard deviation error bars, of (a) D1, (b) D2, and (c) BB peaks among the three samples at 79 K.

Next, we investigated the behaviors of D3 and D4 after the two processing steps. For this we chose sub-GBs having strong D3 and D4 emissions. The D3 and D4 intensities are consistent among the as-cut, hydrogenated, and gettered samples for the investigated sub-GBs as shown in Fig. 4. Since D3 and D4 are thought to reflect the intrinsic properties of the dislocation sites [22-27], this consistency suggests that the structure of dislocations is very stable and not altered after different processing steps including hydrogenation, gettering, and the high thermal treatment incorporated during the gettering process. This behavior of D3 and D4 is similar to the results in Ref. 27, in which the D3 and D4 lines were found to be unchanged after gettering, high temperature annealing, and Fe implantation steps. Note that the D1 intensity after gettering (Fig. 4c) is increased as twice that of the as-cut sample (Fig. 4a), whereas the D2 intensity remains the same.

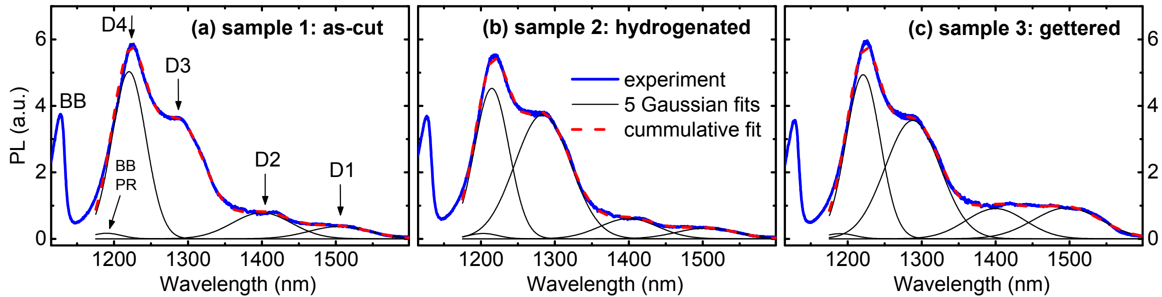

Fig. 4. Comparison of PL spectra among (a) as-cut, (b) hydrogenated, and (c) gettered samples on the same sub-GB at 79 K.

Finally, as can be qualitatively seen from Fig. 5a, the intensity ratio between D3 and D4 varies significantly from location to location. Note that although the D1 and D2 intensities are very strong at location 01, the high energy side of the D2 Gaussian peak is not overlapping with the center of the D3 peak when decomposing the spectrum as shown in Fig. 5b, and hence the D3 peak intensity is not affected by the high energy side of the D2 distribution. Therefore, the intensity ratio between D3 and D4 is not affected by D1 and D2 emissions in Fig. 4a. This different behavior between D3 and D4 contradicts the common belief that D3 is the phonon replica of D4 [23,25], but is similar to what was reported in Ref. 27, in which the peak energy was shifted differently between D3 and D4. If D3 is a phonon replica of D4, their intensity ratio should be the same at a certain temperature regardless of the locations. Therefore, we conclude that D3 is not the phonon replica of D4.

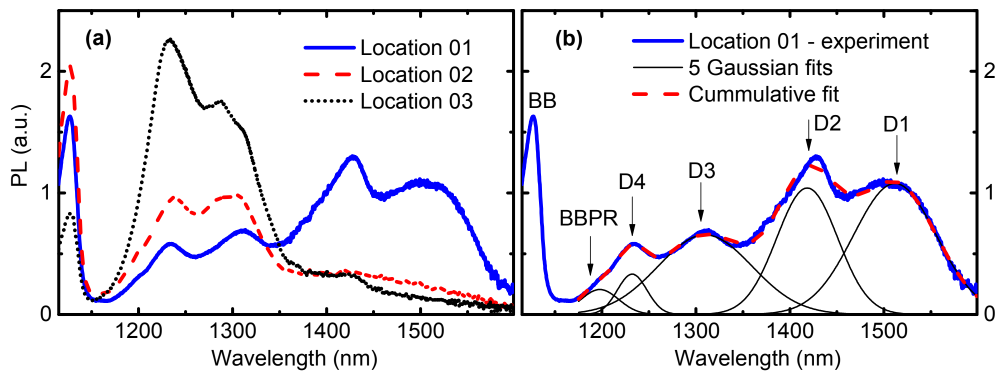

Fig. 5. (a) PL spectra of the as-cut sample at different locations at 79 K. (b) Gaussian fits of PL spectrum at location 01 on the as-cut sample at 79 K.

4. Conclusion

We have empirically examined the impacts of hydrogenation and gettering steps on the deep-level photoluminescence spectra from dislocations. Our results suggest that the reduced concentration of metal impurities trapped around the dislocation sites after gettering enhances the luminescence of D1, while hydrogenation has no effect on the intensity of D1. The effectiveness of the gettering is found to vary along the sub-grain boundaries due to the different enhancement of the D1 intensity. In addition, the structure of the dislocations is found not to be affected by the two processes due to the consistency of the D3 and D4 intensities. Finally, we have reported the difference in intensity ratio between D3 and D4, suggesting that D3 is not the phonon replica of D4.

Acknowledgements

This work has been supported by the Australian Research Council (ARC) and the Australian Renewable Energy Agency (ARENA) through research grant RND009. The Australian National Fabrication Facility is acknowledged for providing access to some of the facilities used in this work. The authors are in debt to Prof. H. Tan for providing access to the spectroscopic equipment.

References

[1] E. Daub and P. Würfel, Ultralow values of the absorption coefficient of Si obtained from luminescence, Phys. Rev. Lett. 74, 1020 (1995).
[2] T. Trupke, M. A. Green, P. Würfel, P. P. Altermatt, A. Wang, J. Zhao, and R. Corkish, Temperature dependence of the radiative recombination coefficient of intrinsic crystalline silicon, J. Appl. Phys. 94, 4930 (2003).
[3] H. T. Nguyen, F. E. Rougieux, B. Mitchell, and D. Macdonald, Temperature dependence of the band-band absorption coefficient in crystalline silicon from photoluminescence, J. Appl. Phys. 115, 043710 (2014).
[4] P. P. Altermatt, F. Geelhaar, T. Trupke, X. Dai, A. Neisser, and E. Daub, Injection dependence of spontaneous radiative recombination in crystalline silicon: Experimental verification and theoretical analysis, Appl. Phys. Lett. 88, 261901 (2006).
[5] H. T. Nguyen, S. C. Baker-Finch, and D. Macdonald, Temperature dependence of the radiative recombination coefficient in crystalline silicon from spectral photoluminescence, Appl. Phys. Lett. 104, 112105 (2014).
[6] W. Bludau, A. Onton, and W. Heinke, Temperature dependence of the band gap of silicon, J. Appl. Phys. 45, 1846 (1974).
[7] J. Wagner, Photoluminescence and excitation spectroscopy in heavily doped n- and p-type silicon, Phys. Rev. B 29, 2002 (1984).
[8] J. Wagner, Band-gap narrowing in heavily doped silicon at 20 and 300 K studied by photoluminescence, Phys. Rev. B 32, 1323 (1985).
[9] P. Würfel, T. Trupke, T. Puzzer, E. Schäffer, W. Warta, and S. W. Glunz, Diffusion lengths of silicon solar cells from luminescence images, J. Appl. Phys. 101, 123110 (2007).
[10] J. A. Giesecke, M. Kasemann, M. C. Schubert, P. Würfel, and W. Warta, Separation of local bulk and surface recombination in crystalline silicon from luminescence reabsorption, Progress in Photovoltaics: Res. & Appl. 18, 10 (2011).
[11] B. Mitchell, M. K. Juhl, M. A. Green, and T. Trupke, Full spectrum photoluminescence lifetime analyses on silicon bricks, IEEE Journal of Photovoltaics 3, 962 (2013).
[12] C. Barugkin, Y. Wan, D. Macdonald, and K. R. Catchpole, Evaluating plasmonic light trapping with photoluminescence, IEEE Journal of Photovoltaics 3, 1292 (2013).
[13] C. Schinke, D. Hinken, J. Schmidt, K. Bothe, and R. Brendel, Modeling the spectral luminescence emission of silicon solar cells and wafers, IEEE Journal of Photovoltaics 3, 1038 (2013).
[14] H. T. Nguyen, F. E. Rougieux, S. C. Baker-Finch, and D. Macdonald, Impact of carrier profile and rear-side reflection on photoluminescence spectra in planar crystalline silicon wafers at different temperatures, IEEE Journal of Photovoltaics 5, 77 (2015).
[15] H. T. Nguyen, D. Yan, F. Wang, P. Zheng, Y. Han, and D. Macdonald, Micro-photoluminescence spectroscopy on heavily-doped layers of silicon solar cells, Physica Status Solidi: Rapid Research Letters 9, 230 (2015).
[16] H. Conzelmann and J. Weber, Photoluminescence from chromium-boron pair in silicon, Physica B+C 116, 291 (1983).
[17] S. Binetti, S. Pizzini, E. Leoni, R. Somaschini, A. Castaldini, and A. Cavallini, Optical properties of oxygen precipitates and dislocations in silicon, J. Appl. Phys. 92, 2437 (2002).
[18] P. Gundel, M. C. Schubert, W. Kwapil, J. Schön, M. Reiche, H. Savin, M. Yli-Koski, J. A. Sans, G. Martinez-Criado, W. Seifert, W. Warta, and E. R. Weber, Micro-photoluminescence spectroscopy on metal precipitates in silicon, Physica Status Solidi: Rapid Research Letters 3, 230 (2009).
[19] R. Sauer, J. Weber, J. Stolz, E. R. Weber, K.-H. Küsters, and H. Alexander, Dislocation-related photoluminescence in silicon, Applied Physics A 36, 1 (1985).
[20] M. Tajima, Spectroscopy and topography of deep-level luminescence in photovoltaic silicon, IEEE Journal of Photovoltaics 4, 1452 (2014).
[21] B. Sopori, P. Rupnowski, V. Mehta, V. Budhraja, S. Johnston, N. Call, H. Mountinho, M. Al-Jassim, A. Shaikh, M. Seacrist, and D. Carlson, Performance limitations of mc-si solar cells caused by defect clusters, ECS Transactions 18, 1049 (2009).

[22] H. Sugimoto, M. Inoue, M. Tajima, A. Ogura, and Y. Ohshita, Analysis of intra-grain defects in multicrystalline silicon wafers by photoluminescence mapping and spectroscopy, Japanese Journal of Applied Physics 45, L641 (2006).
[23] M. Tajima, Y. Iwata, F. Okayama, H. Toyota, H. Onodera, and T. Sekiguchi, Deep-level photoluminescence due to dislocations and oxygen precipitates in multicrystalline Si, J. Appl. Phys. 111, 113523 (2012).
[24] T. Sekiguchi and K. Sumino, Cathodoluminescence study on dislocations in silicon, J. Appl. Phys. 79, 3253 (1996).
[25] Tz. Arguirov, W. Seifert, M. Kittler, and J. Reif, Temperature behaviour of extended defects in solar grade silicon investigated by photoluminescence and EBIC, Mater. Sci. Eng. B 102, 251 (2003).
[26] W. Lee, J. Chen, B. Chen, J. Chang, and T. Sekiguchi, Cathodoluminescence study of dislocation-related luminescence from small-angle grain boundaries in multicrystalline silicon, Applied Physics Letters 94, 112103 (2009).
[27] H. T. Nguyen, F. E. Rougieux, F. Wang, H. Tan, and D. Macdonald, Micrometer-scale deep-level spectral photoluminescence from dislocations in multicrystalline silicon, IEEE Journal of Photovoltaics 5, 799 (2015).
[28] S. P. Phang and D. Macdonald, Direct comparison of boron, phosphorus, and aluminum gettering of iron in crystalline silicon, J. Appl. Phys. 109, 073521 (2011).
[29] W.C. Dash, Copper precipitation on dislocations in silicon, J. Appl. Phys 27, 1193 (1956).
[30] Y. Kashigawa, R. Shimokawa, and M. Yamanaka, Highly sensitive etchants for delineation of defects in single- and polycrystalline silicon materials, J. Electrochem. Soc. 143, 4079 (1996).
[31] S. Johnston, H. Guthrey, F. Yan, K. Zaunbrecher, M. Al-Jassim, P. Rakotoniaina, and M. Kaes, Correlating multicrystalline silicon defect types using photoluminescence, defect-band emission, and lock-in thermography imaging techniques, IEEE Journal of Photovoltaics 4, 348 (2014).

Available online at www.sciencedirect.com

ScienceDirect

Energy Procedia 92 (2016) 145 – 152

Energy Procedia

6th International Conference on Silicon Photovoltaics, SiliconPV 2016

Evaluating depth distributions of dislocations in silicon wafers using micro-photoluminescence excitation spectroscopy

Hieu T. Nguyen*, Sieu Pheng Phang, and Daniel Macdonald

Research School of Engineering, College of Engineering and Computer Science, The Australian National University, Canberra, ACT 2601, Australia

Abstract

Combining micro-photoluminescence spectroscopy and photoluminescence excitation spectroscopy, we are able to observe the evolution of the luminescence spectra from crystalline silicon wafers under various excitation wavelengths. By interpreting the relative change of the luminescence spectra, we can detect and examine the distributions of the dislocations, as well as of the defects and impurities trapped around them, segregated at different depths below the wafer surface. We show that in multicrystalline silicon wafers, the dislocations and the trapped defects and impurities, formed during the ingot growth and cooling, are distributed throughout the wafer thickness, whereas those generated in monocrystalline wafers by a post-diffusion thermal treatment are located near the wafer surface.

© 2016 The Authors. Published by Elsevier Ltd. This is an open access article under the CC BY-NC-ND license (http://creativecommons.org/licenses/by-nc-nd/4.0/).
Peer review by the scientific conference committee of SiliconPV 2016 under responsibility of PSE AG.

Keywords: Crystalline silicon; dislocations; photoluminescence (PL); photovoltaics.

1. Introduction

Photoluminescence spectroscopy (PLS) and photoluminescence imaging (PLI) have been demonstrated to be powerful characterization tools in silicon photovoltaics. Utilizing the advantages of these two techniques, the so-called hyperspectral PL imaging technique, which combines both PLS and PLI, has been employed to capture macroscopic PL images from multicrystalline silicon (mc-Si) wafers in both spatial and spectral dimensions [1,2].

* Corresponding author
E-mail address: hieu.nguyen@anu.edu.au

1876-6102 © 2016 The Authors. Published by Elsevier Ltd. This is an open access article under the CC BY-NC-ND license (http://creativecommons.org/licenses/by-nc-nd/4.0/).
Peer review by the scientific conference committee of SiliconPV 2016 under responsibility of PSE AG.
doi:10.1016/j.egypro.2016.07.013

Therefore, macroscopic properties of different radiative recombination centers at various locations in mc-Si wafers can be investigated separately. However, due to the limited number of pixels from the camera employed to detect a large area on the wafers, the spatial resolution of this hyperspectral PL-based method is on the order of several hundred micrometers [1-2]. As a result, microscopic properties of submicron features in crystalline silicon (c-Si) wafers and solar cells have not been accessible via this technique.

Recently, courtesy of the high spatial resolution from confocal optics, micro-PLS (μPLS) has been utilized to investigate electronic and optical properties of many submicron features in c-Si wafers and solar cells, such as dislocations [3-6], metal precipitates [7], or damage induced by laser-doped processes [8-10]. In addition, photoluminescence excitation (PLE) spectroscopy, in which the relative PL intensity at a certain wavelength is monitored when the excitation energy is varied, is a powerful technique to study fundamental properties of silicon and defects, such as the optical band gap in degenerate silicon [11,12] or oxygen-related deep defects in irradiated silicon [13]. Recently, we have applied a technique combining μPLS and PLE to evaluate spatial distributions of structures and defects separated at different depths inside silicon wafers [14].

Dislocation sites are an important lifetime killer in silicon solar cells [15]. The dislocations themselves are not only an effective recombination channel for free carriers, but also act as trapping sites for other defects and impurities due to the local stress and strain around them. These trapped defects and impurities, in turn, reduce the free carrier concentrations even further. The dislocations and the trapped defects and impurities can be generated either during the crystal growth of an ingot, or in subsequent solar cell fabrication steps. Due to the different natures of these two processes, the spatial distributions of the dislocations and the trapped defects and impurities are expected to be different. Therefore, in this work, we apply our recently-developed μPLS-PLE technique [14] to study the distributions of dislocations and other defects generated during these two processes. Defects formed during mc-Si ingot growth are shown to be distributed uniformly depth-wise in the silicon wafers, whereas the process-induced defects are found to reside near the wafer surfaces.

2. Experimental details

The sample investigated in Section 3 is a <100>-oriented float-zone boron-doped c-Si wafer. It was first chemically etched in an HF/HNO_3 solution to remove saw damage. It went through a thermal diffusion process in a BBr_3 gas source at 1050 ^oC for 1 hour, and was then annealed in pure nitrogen gas at 1090 ^oC for 5 hours while the borosilicate glass (BSG) and boron-rich layer (BRL) were both still present on the wafer surfaces. These process steps are aimed to generate dislocations, along with other defects and impurities, located below the wafer surfaces. After that, any residual BSG and BRL layers were finally removed prior to performing the PL measurements.

The sample investigated in Section 4 is a directionally solidified, boron-doped p-type mc-Si wafer with a background doping of about 9×10^{15} cm^{-3}. This wafer was also first chemically etched in an HF/HNO_3 solution to remove saw damage. After that, it was immersed in a defect etchant consisting of acetic/HNO_3/HF acids for 16 hours. The purpose of this second etching step is to delineate sub-grain boundaries (sub-GBs), which are otherwise not observable under a confocal microscope. These sub-GBs are known to have a high density of defects and impurities forming during the ingot growth and cooling process [5].

The setup of our μPLS system is described elsewhere [5,14]. The excitation light source is a supercontinuum laser (NKT SuperK Extreme EXR-20) with a tunable wavelength range from 490 nm to 2 μm. In this work, excitation wavelengths between 510 nm and 810 nm with a bandwidth of 10 nm were employed. The on-sample power was kept constant at 6 mW for all excitation wavelengths. The diameter of the illuminated spot on the samples varied between ~1 μm (for 510-nm excitation wavelength) and ~2 μm (for 810-nm excitation wavelength). The spectral response of the entire system was determined with a calibrated halogen-tungsten light source.

3. Dislocations and impurities distributed near the wafer surface

In this section, we apply the combined PLS-PLE technique to detect dislocations, as well as other defects and impurities, distributed near the wafer surface. Figure 1a shows the normalized PL spectra from the boron-diffused and annealed c-Si wafer, excited with different wavelengths at 79 K. There are 3 distinct components in the spectra. The first component is the Band-to-Band (BB) peak at ~1130 nm emitted from the underlying c-Si substrate. The

second component is the peak at ~1165 nm attributed to the heavily-doped layer near the surface. This second peak is also band-to-band luminescence, but shifted to longer wavelengths due to band-gap narrowing effects in the heavily-doped layer [16]. Therefore, we denoted it as Heavily-Doped Band-to-Band peak (HDBB). The HDBB peak is significantly broader than the BB peak due to the band filling and band tailing effects in heavily-doped silicon [17,18]. The third component is the deep-level luminescence at wavelengths beyond 1200 nm, emitted from defects and impurities induced by the post-diffusion thermal treatment.

In Figure 1a, the HDBB peak reduces significantly with increasing excitation wavelengths due to the reduced absorption fraction of the laser light in the heavily-doped layer. In addition, the two deep-level peaks display the same trend as the HDBB peak, initially suggesting that the defects and impurities are distributed near the wafer surface. However, there could be another possibility. The BB intensity is a quadratic function of the excess carrier density under high injection levels [19], while the deep-level intensities are less dependent on the excess carrier density [10]. Therefore, the reduction of the deep-level luminescence in Figure 1a (compared to the BB peak) could be due to the faster increment of the BB peak when the laser light penetrates more deeply into the substrate, in which case the surface recombination is reduced. To test this hypothesis, we compare the spectra in relative intensities, as depicted in Figure 1b and Figure 1c (a zoomed-in section of Figure 1b). The BB peak increases remarkably with increasing excitation wavelengths (Figure 1b), while the deep-level luminescence saturates (Figure 1c). These results also suggest that the observed defects and impurities are located near the surface.

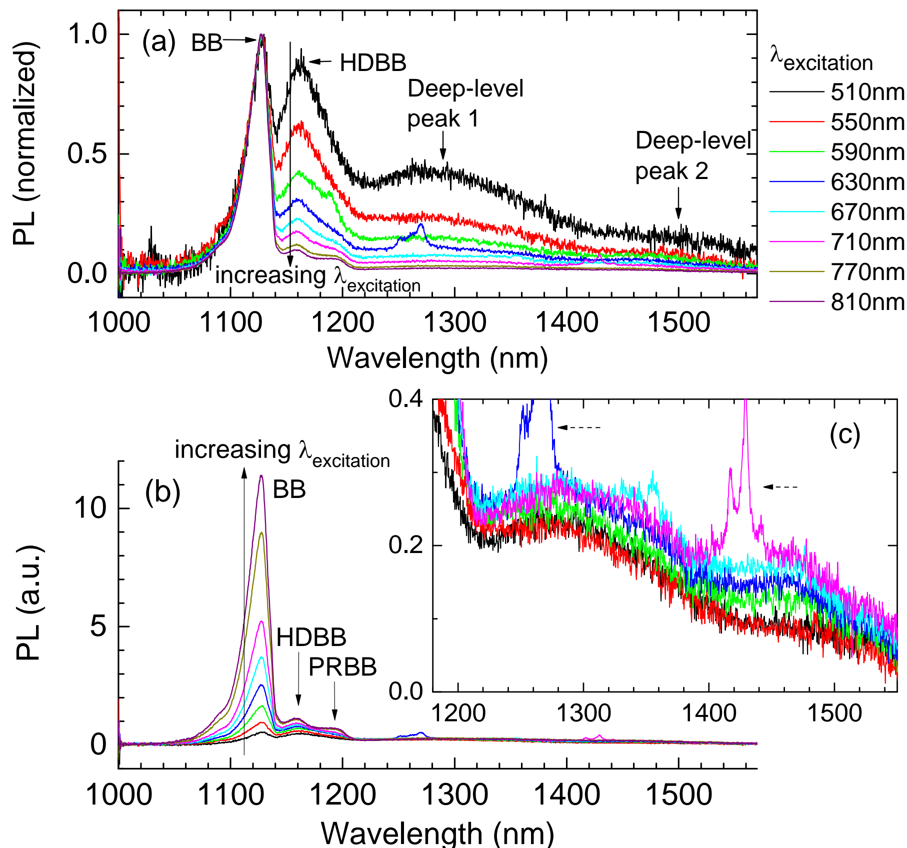

Fig. 1. PL spectra from the boron-diffused and annealed c-Si wafer, excited with different wavelengths at 79 K. The spectra were (a) normalized to the BB peak and (b) presented in relative intensities. (c) A zoom-in between 1180 and 1550nm of Figure 1b. The peak ~1200 nm is the phonon replica of the BB peak (denoted as PRBB in Figure 1b). The spurious peaks marked by broken-line arrows are artifacts due to the higher orders of the supercontinuum laser.

The very broad widths of these two deep-level peaks could be due to two reasons. The first reason is that, the doping profile is inhomogeneous across the diffused layer thickness. Thus, both deep-level peaks are, in fact, the aggregate PL emissions from different layers with different doping densities, which are shifted by varying amounts in energy due to changing band-gap narrowing. Another possibility is that, each of the two broad peaks could be possibly emitted from various defect and impurity centers locating near together inside the band gap rather than a single type of defects and impurities, and the PL emissions from these centers are also broadened due to the inhomogeneous doping profile. However, decomposing these two broad deep-level peaks into individual defect lines is difficult since these peaks are very broad and not well-defined.

Next, we continue examining the spatial distribution of the two deep-level luminescence peaks. In order to avoid the influence of the PL signal from the underlying substrate on our interpretation, we subtracted the BB component from the total spectra and normalized the resultant spectra to the HDBB peak, as depicted in Figure 2. Compared to deep-level peak 2, deep-level peak 1 is clearly suppressed with increasing excitation wavelengths, suggesting different origins and spatial distributions between the two deep-level peaks. Deep-level peak 1 is confined very near the surface while deep-level peak 2 is extended more deeply into the substrate.

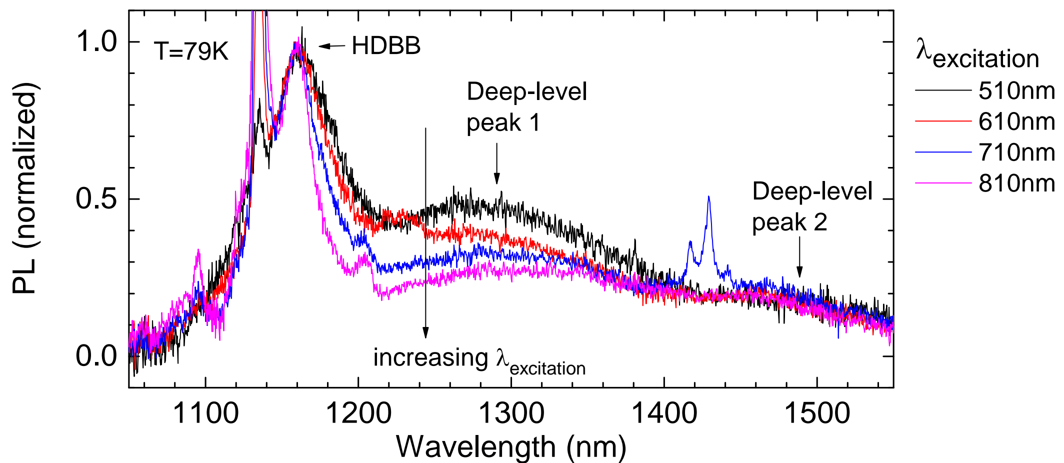

Fig. 2. PL spectra from the boron-diffused and annealed silicon wafer, excited with different wavelengths at 79 K. The BB peak from the c-Si substrate was subtracted from the original spectra, and the resultant spectra were normalized to the HDBB peak.

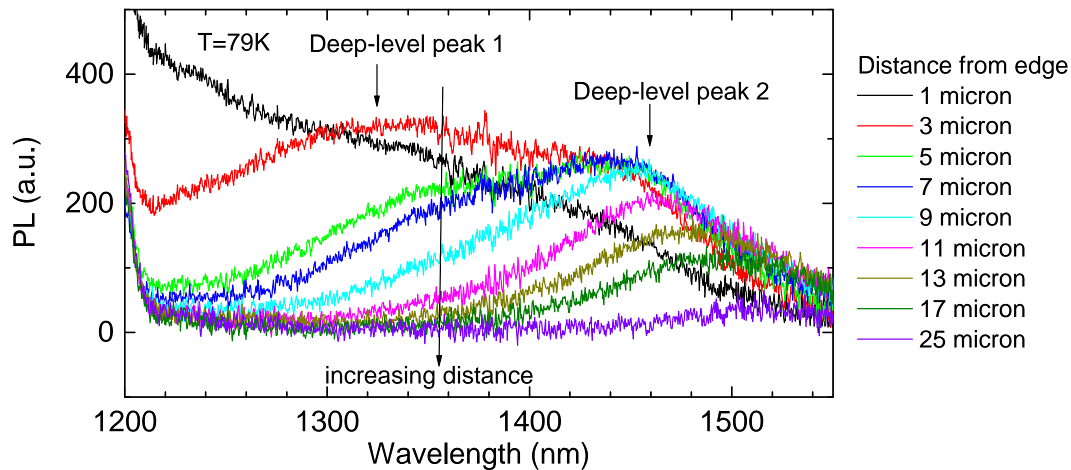

Fig. 3. PL spectra at different distances from the edge of the cross-sectional specimen (i.e. the original wafer surface) of the boron-diffused and anneal c-Si wafer. The excitation wavelength is 810 nm and the temperature is 79 K.

Now, we verify the findings on the spatial distributions of both these peaks mentioned above, using the PL spectra measured from a vertical cross-section of the boron-diffused and annealed c-Si wafer. Figure 3 plots the PL spectra at various distances from the edge of the cross-sectional specimen, i.e. the original wafer surface. Near the edge (e.g. the 3-micron curve), the intensities of both deep-level peak 1 and deep-level peak 2 are relatively high. Away from the edge of the cross-sectional specimen, deep-level peak 1's intensity is quickly diminished and eventually disappears. Meanwhile, deep-level peak 2 is still present up to a distance much further from the edge.

Furthermore, Figure 4 is a transmission electron microscope (TEM) two-beam bright-field image of the vertical cross-section. The micrograph reveals a dislocation band located about 3 microns below the surface. This dislocation band was formed during the post-diffusion thermal treatment. The dislocation band position coincides with the distance from the edge that yields the highest intensity of deep-level peak 1 (the 3-micron curve in Figure 3). Therefore, we suggest that deep-level peak 1 is likely to be related to the dislocations near the surface, while deep-level peak 2 could be attributed to the other defects and impurities trapped around the dislocation sites during the annealing and cooling process.

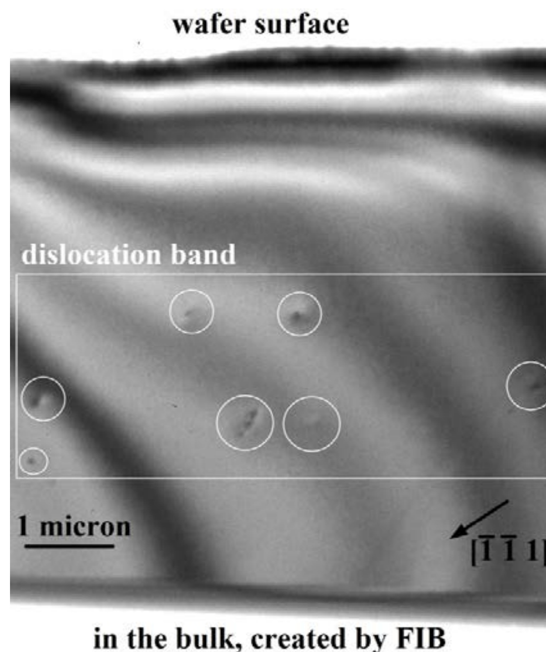

Fig. 4. TEM two-beam [-1-11] bright-field image of the (011) cross-section of the (100) boron-diffused and annealed c-Si wafer. The specimen was prepared by focus ion beam (FIB). The dislocations are marked with the white circles. The broad wavy features are bending contours due to the elastic bending of the thin TEM specimen.

4. Dislocations and impurities distributed depth-wise

In this section, we continue applying the combined PLS-PLE technique to assess dislocations and defects which are formed during the growth and cooling of a mc-Si ingot, rather than during the subsequent solar cell processing steps. In mc-Si wafers, dislocations are confined around small-angle grain boundaries or other sub-GBs, and are often decorated with other defects and impurities [3]. The dislocations themselves emit the so-called D3 and D4 lines around 1200 – 1300 nm [3-6], whereas the trapped defects and impurities are known to emit the so-called D1 and D2 lines between 1350 and 1600 nm [3-6].

Figure 5a shows the normalized PL spectra from a sub-GB of the mc-Si wafer with different excitation wavelengths at 79 K. Besides the BB peak from c-Si, we can observe deep-level luminescence peaks labeled as D4 and D3 (from dislocations) and D2 (from defects and impurities trapped around dislocations). In contrast to

Figure 1, the deep-level luminescence increases with increasing excitation wavelengths in Figure 5a. These results demonstrate that the dislocations are distributed depth-wise in the mc-Si wafer. Moreover, in Figure 5b, although the relative intensity of the defect luminescence increases, the relative BB intensity saturates. This behavior can be explained by the fact that the BB PL signal is limited by both the surface recombination and the defect density, in particular the density of dislocations in this case. Therefore, when the laser light penetrates more deeply into the wafer, although the effects of the surface recombination are suppressed, the deep-level channels still compete with the BB luminescence. We note that the D1 line is absent and the D2 line intensity is minimal in Figure 5, suggesting that the sub-GB investigated does not contains a high density of impurities and other defects, but the dislocations themselves.

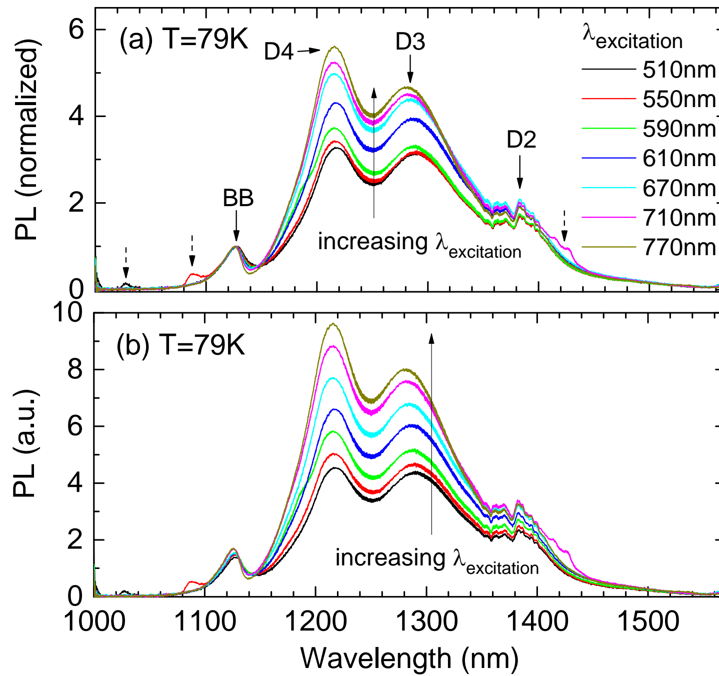

Fig. 5. PL spectra at a sub-GB, which gives strong dislocation luminescence, of the mc-Si wafer, excited with different wavelengths. The spectra were (a) normalized to the BB peak and (b) presented in relative scale. The spurious peaks marked by broken-line arrows are artifacts due to the higher orders of the supercontinuum laser.

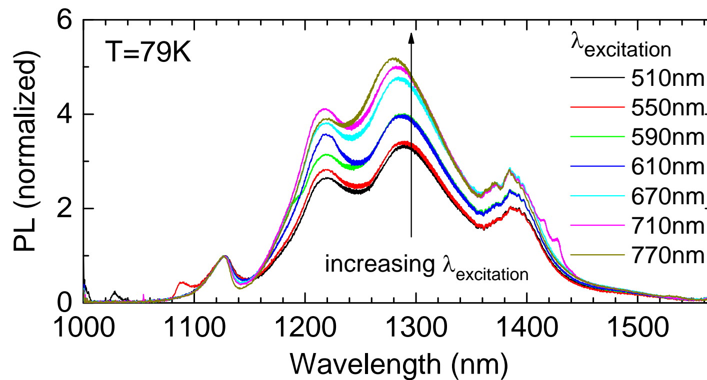

Fig. 6. PL spectra at the same sub-GB as in Figure 5, but measured from the other side of the mc-Si wafer, excited with different wavelengths.

Nevertheless, the increasing intensity of D3 and D4 with excitation wavelengths may imply a preferential increment of the dislocation density along the wafer thickness. To clarify this hypothesis, we repeated the PLE measurements on the same sub-GB, but from the other side of the wafer, and plotted the results in Figure 6. The increasing trend of D3 and D4 with increasing excitation wavelengths confirms that the higher intensity of D3 and D4 is due to a suppression of the surface recombination, rather than a higher dislocation density.

Finally, we show the results from another sub-GB, in which the dislocation sites are decorated with a high density of defects and impurities, causing strong D1 and D2 lines as depicted in Figure 7. The same as Figure 5, the dislocation luminescence intensity in Figure 7 increases with increasing excitation wavelengths. In addition, we also observe an increment of D1 and D2. The results from this figure demonstrate that, the defects and impurities are trapped around the dislocation sites during the ingot growth and cooling, and are also distributed throughout the wafer thickness.

Recently, Bauer *et al.* [20] have performed a detailed investigation on crystallographic structures of defects which are responsible for the strong recombination activities along sub-GBs in mc-Si solar cells. Combining electron beam induced current (EBIC) measurements and scanning transmission electron microscopy (STEM) images, these authors found a correlation between the increased recombination activities and the density of nonsplit Lomer dislocations along the sub-GBs. Moreover, they also showed that, the presence of partial dislocations and stacking faults at certain locations of the sub-GBs, in which perfect Lomer dislocations were absent, did not increase the EBIC contrast. Therefore, Lomer dislocations were suggested to be more detrimental to the final cell performance than partial dislocations and stacking faults. These findings can be compared to the properties of the D3 and D4 lines. The two lines have been confirmed to be due to the dislocations along the sub-GBs since the two lines are confined around the sub-GBs, in which the band-to-band intensity is found to be reduced significantly [3-5]. However, a detailed investigation on the microscopic structures of the dislocations around the sub-GBs studied in our work is required to clarify which types of dislocations emit the D3 and D4 lines. On the other hand, the D1 and D2 lines are still present at a distance far away from the sub-GBs, e.g. up to 80 μm from the sub-GBs in Ref. 5, and thus D1 and D2 are unlikely to be emitted directly from the dislocation networks at the sub-GBs.

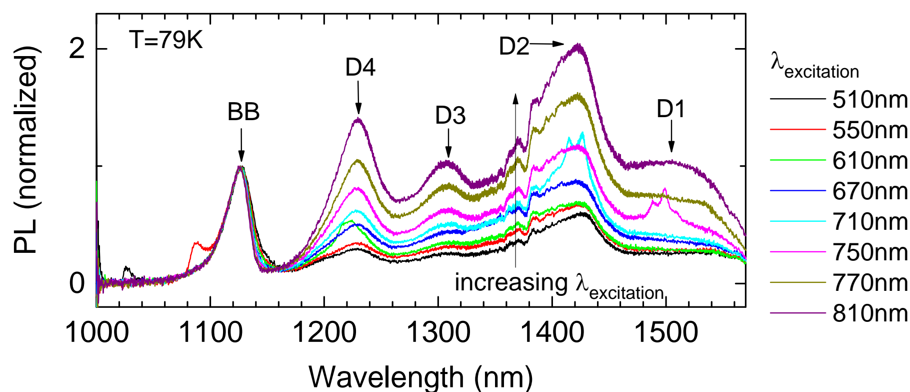

Fig. 7. Normalized PL spectra at a sub-GB, in which the dislocations sites are decorated with a high density of trapped defects and impurities, excited with different wavelengths.

5. Conclusion

We have applied the spectrally-resolved photoluminescence excitation spectroscopy technique to detect and assess the distributions of dislocations and other defects inside the silicon wafers. We have presented the results for two cases, between which the formations as well as distributions of dislocations and other defects are distinctly different. This method, in principle, can be applied for different structures and defects separated at different depths inside the silicon wafers.

Acknowledgements

This work has been supported by the Australian Research Council (ARC) and the Australian Renewable Energy Agency (ARENA) through research grant RND009. The Australian National Fabrication Facility is acknowledged for providing access to some of the facilities used in this work. The authors are in debt to Prof. H. Tan for providing access to the spectroscopic equipment.

References

[1] Olsen E, Flø AS. Spectral and spatially resolved imaging of photoluminescence in multicrystalline silicon wafers. Appl. Phys. Lett. 2011;99:011903-3.

[2] Lausch D, Mehl T, Petter K, Flø AS, Burud I, Olsen E. Classification of crystal defects in multicrystalline silicon solar cells and wafer using spectrally and spatially resolved photoluminescence. J. Appl. Phys. 2016;119:054501-6.

[3] Tajima M, Iwata Y, Okayama F, Toyota H, Onodera H, Sekiguchi T. Deep-level photoluminescence due to dislocations and oxygen precipitates in multicrystalline Si. J. Appl. Phys. 2012;111:113523-6.

[4] Tajima M. Spectroscopy and topography of deep-level luminescence in photovoltaic silicon. IEEE Journal of Photovoltatics 2014;4:1452-1458.

[5] Nguyen HT, Rougieux FE, Wang F, Tan H, Macdonald D. Micrometer-scale deep-level spectral photoluminescence from dislocations in multicrystalline silicon. IEEE Journal of Photovoltaics 2015;5:799-804.

[6] Nguyen HT, Rougieux FE, Wang F, Macdonald D. Effects of solar cell processing steps on dislocation luminescence in multicrystalline silicon. Energy Procedia 2015;77:619-625.

[7] Gundel P, Schubert MC, Kwapil W, Schön J, Reiche M, Savin H, Yli-Koski M, Sans JA, Martinez-Criado G, Seifert W, Warta W, Weber ER. Micro-photoluminescence spectroscopy on metal precipitates in silicon. Physica Status Solidi – Rapid Research Letters 2009;3:230-232.

[8] Woehl R, Gundel P, Krause J, Rühle K, Heinz FD, Rauer M, Schmiga C, Schubert MC, Warta W, Biro D. Evaluating the aluminum-alloyed p+-layer of silicon solar cells by emitter saturation current density and optical microspectroscopy measurements. IEEE Trans. Elec. Devices 2011;58:441-447.

[9] Roigé A, Alvarez J, Kleider JP, Martin I, Alcubilla R, Vega LF. Microscale spatially resolved characterization of highly doped regions in laser-fired contacts for high-efficiency crystalline Si solar cells. IEEE Journal of Photovoltatics 2015;5:545-551.

[10] Nguyen HT, Han Y, Ernst M, Fell A, Franklin E, Macdonald D. Dislocations in laser-doped silicon detected by micro-photoluminescence spectroscopy. Appl. Phys. Lett. 2015;107:022101-5.

[11] Wagner J. Photoluminescence and excitation spectroscopy in heavily doped n- and p-type silicon. Phys. Rev. B 1984;29:2002-2009.

[12] Wagner J. Heavily doped silicon studied by luminescence and selective absorption. Solid-State Electronics 1985;28:25-30.

[13] Wagner J, Thonke K, Sauer R. Excitation spectroscopy on the 0.79-eV (C) line defect in irradiated silicon. Phys. Rev. B 1984;29:7051-7053.

[14] Nguyen HT, Phang SP, Wong-Leung J, Macdonald D. Photoluminescence excitation spectroscopy of diffused layers on crystalline silicon wafers. IEEE Journal of Photovoltaics 2016;6:746-753.

[15] Sopori B, Rupnowski P, Mehta V, Budhraja V, Johnston S, Call N, Mountinho H, Al-Jassim M, Shaikh A, Seacrist M, Carlson D. Performance limitations of mc-si solar cells caused by defect clusters. ECS Transactions 2009;18:1049-1058.

[16] Nguyen HT, Yan D, Wang F, Zheng P, Han Y, Macdonald D. Micro-photoluminescence spectroscopy on heavily-doped layers of silicon solar cells. Physica Status Solidi – Rapid Research Letters 2015;9:230-235.

[17] Dumke WP. Comparison of band-gap shrinkage observed in luminescence from n+-si with that from transport and optical absorption measurements. Appl. Phys. Lett. 1983;42:196-198.

[18] Schmid PE, Thewalt MLW, Dumke WP. Photoluminescence in heavily doped Si:B and Si:As. Solid State Communications 1981;38:1091-1093.

[19]Nguyen HT, Rougieux FE, Baker-Finch SC, Macdonald D. Impact of carrier profile and rear-side reflection on photoluminescence spectra in planar crystalline silicon wafers at different temperatures. IEEE Journal of Photovoltaics 2015;5:77-81.

[20] Bauer J, Hähnel A, Werner P, Zakharov N, Blumtritt H, Zuschlag A, Breitenstein O. Recombination at Lomer dislocations in multicrystalline silicon for solar cell. IEEE Journal of Photovoltaics 2016;6:100-110.